

Reduced Order Models with Local Property Dependent Transfer Coefficients for Real Time Simulations of Single and Dual Layered Monolith Reactors

by
Mingjie Tu

A Dissertation Presented to the Department of Chemical and Biomolecular Engineering
Cullen College of Engineering
in partial fulfillment of the requirements for the degree of
Doctor of Philosophy
in Chemical Engineering

Chair of Committee: Prof. Vemuri Balakotaiah
Committee Member: Prof. Michael P. Harold
Committee Member: Prof. Praveen Bollini
Committee Member: Prof. Matthew A. Franchek
Committee Member: Prof. Birol Dindoruk
Committee Member: Prof. Karolos Grigoriadis

University of Houston

August 2021

Copyright 2021, Mingjie Tu

Acknowledgements

Foremost, I would like to express my sincere gratitude to my advisor Prof. Vemuri Balakotaiah for his continuous support of my Ph.D. research, for inspiring me to work on this excellent project, for all his patient guidance, enthusiastic encouragement, and immense knowledge. His willingness to give his time and efforts so generously have been very much appreciated. The thesis would not have been possible without his help.

Besides my advisor, I would like to thank the rest of my thesis committee: Prof. Michael P. Harold, Prof. Praveen Bollini, Prof. Matthew A. Franchek, Prof. Birol Dindoruk and Prof. Karolos Grigoriadis for making their time available to me despite their busy schedules and for their insightful comments on my work. Additionally, I would like to acknowledge the faculty and staff of the Department of Chemical Engineering at University of Houston, for their excellent support and valuable graduate courses.

I sincerely appreciate the help from my co-author of my papers, Ram Ratnakar for his useful suggestions and discussions throughout my research. I'm also indebted to Dr. Ram Ratnakar for his help in not only technical side but also work career path side. I would like to thank my mentors and teammates at Isuzu motors, in particularly, Chintan Desai and Dr. Chaitanya Sampara for sharing insights on the experimental studies of diesel oxidation catalyst. I'm particularly grateful to Dr. Yuntao Gu for recommending me the job opportunity in his group at general motors. I feel so grateful that my manger Dr. Wei Li and Dr. Patrick Szymkowicz show me their strong support during the preparation of my PhD defense.

I thank my fellow lab mates and some former lab mates that I met, Dr. Zhe Sun, Dr. Allen Ting, Dr. Imran Alam, Dr. Tian Gu, Dr. Rama Krishna Dadi, Dr. Bhaskar Sarkar, Meet Shah and Jiakang Chen for making our lab a pleasant place to work. I always enjoyed the discussions on research and other topics in daily life

with them.

Words cannot express my thanks and my love to my beloved boyfriend Zheng Dong who works in another city but tries to accompany me all the time when I need support the most to conquer all those difficulties. My sincere thanks also go to all my roommates who become my besties Yifei Ye and Ye Wang for their encouragement and support, and for all the fun we have had in these years. Without them, my life in Houston would never been so enjoyable. I would like to express my great thanks to a lovely couple Dr. Tian Gu and Chi Zhang who treat me just like their own sisters since I came to United states, during my first few years in the United States, I received a lot of debt from them. I am also very grateful to have made many good friends during my PhD life, the rich life experience from my friend Izzie Wang gave me a lot of inspiration. Humorous and interesting friend, Wenjing Liu, brings a lot of fun to my life.

The last but not the least, I would like to express my love and appreciation to my parents and family members in China for always supporting me in all my endeavors.

Abstract

Monolith reactors are widely used in catalytic after-treatment systems. Detailed mathematical models of this reactor consist of a system of coupled nonlinear partial differential equations in three spatial dimensions and time. The numerical solution of these models with complex catalytic chemistry is demanding in terms of time and memory requirements. Therefore, the development of reduced order models for these systems is important for control and optimization algorithms related to fuel economy and real time implementation of emissions constraints. The objective of this work is to develop reduced order models by simplification of the problem of multi-component diffusion and reaction in the catalytic layers.

In the first part of this work, we present a novel method for computing washcoat diffusional effects with local property dependent internal mass transfer coefficient matrix. We present a method for computing this matrix for any arbitrary washcoat geometry as a function of the Thiele matrix, defined in terms of the Jacobian of the rate vector at the local concentrations. We illustrate this method with examples for single layered monolith reactors with global kinetics, and show that it leads to accurate solutions while speeding calculations by several orders of magnitude.

In part II, we extend Thiele matrix approach to dual-layered monolith reactors, where each layer may have different catalytic or transport properties. We determine the interfacial flux vectors and mass transfer coefficient matrices in terms of Thiele matrix of each layer. We illustrate the method using a dual layered system with first layer of selective catalytic reduction (SCR) and second layer of lean NOx trap (LNT) catalyst. We also investigate the mesh size dependency of the solution and note that the detailed model leads to sufficiently accurate solution only when the number of mesh points is about equal to or greater than the largest eigenvalue (in magnitude) of the Thiele matrix. We compare the speed and accuracy of the reduced order model solution and show that it is closer to detailed model which

has sufficient mesh points.

In part III, we extend the Thiele matrix approach to micro-kinetic models. First, we show that the short time scales associated with the adsorption/desorption steps requires the use of a large number of mesh points to obtain a mesh independent solution. We present a multi-mode coarse-grained model using the internal mass transfer coefficient matrix. This matrix is shown to be diagonal for most micro-kinetic models of practical interest. We illustrate the method with $\text{H}_2/\text{CO}/\text{C}_3\text{H}_6$ oxidation over a $\text{Pt}/\text{Al}_2\text{O}_3$ catalyst with a detailed micro-kinetic model. While the computation of the mesh independent solution of the detailed model is tedious, the reduced order model leads to an accurate solution while speeding-up calculations by about three orders of magnitude.

Table of Contents

Acknowledgements	iii
Abstract	v
Table of Contents	vii
List of Tables	xi
List of Figures	xiii
Nomenclature	xviii
Chapter 1 Introduction	1
1.1 Introduction	1
1.2 Automotive	4
1.3 Physical characteristics of monoliths	5
1.4 Hierarchies of models of monolith reactors	7
1.4.1 3-D model	7
1.4.2 Reduced order model	9
1.5 Outline of the Thesis	14
Chapter 2 Introduction to various reduced order model approaches	16
2.1 Literature review	16
2.2 Detailed and Reduced Order Models of Monolith Reactors	19
2.2.1 Detailed(1+1D) washcoat diffusion model	20
2.2.2 Two-Mode Form of Reduced-order Model	24
2.2.3 Reduced Order Model with Storage on Catalyst:	26
2.2.4 Computation of the Internal and External Mass Transfer Co-efficient Matrices	27
2.3 The Thiele matrix approach for the internal mass transfer coefficient matrix	31

Chapter 3 Comparison of accuracy of various reduced order models in a single layered monolith reactor	38
3.1 Comparison of accuracy of various reduced order models in a single layered monolith reactor	38
3.1.1 Example 1: Four reactions model of a TWC	39
3.1.2 Example 2: TWC Model with Oxygen Storage and Release	47
3.1.3 Example 3: Reversible Reactions with Linear Kinetics	50
3.2 Conclusions	57
Chapter 4 Reduced order models for real time simulations of monolith reactors with dual washcoat layers	59
4.1 Introduction and literature review for dual layered monolith reactors	59
4.2 Detailed and reduced order models of single and dual layered monolith reactors	61
4.2.1 Detailed(1+1D) Washcoat Diffusion Model	62
4.2.2 Review of Thiele matrix approach for single layered monolith reactor	67
4.2.3 Reduced-order model for dual layered monolith reactors	70
4.2.4 Computation of the internal and external Sherwood matrices	71
4.3 Accuracy of reduced order model	75
4.3.1 Reaction mechanism of SCR and LNT catalyst	76
4.3.2 Results	76
4.3.3 Mesh size dependency of detailed Short Monolith model	79
4.3.4 Comparison of detailed and reduced order model results	80
4.4 Conclusions and Discussion	90
Chapter 5 Reduced order model for real time simulation of monolith reactor with micro-kinetics	96
5.1 Introduction	96

5.2	Mathematical Modeling	98
5.2.1	Detailed(1+1D) washcoat diffusion model	99
5.2.2	Reduced-order model	104
5.3	Example: Micro-kinetics of CO/H ₂ /C ₃ H ₆ adsorption, desorption and oxidation on Pt/Al ₂ O ₃ monolith catalysts	109
5.4	Results	111
5.5	Conclusions and discussion	120
Chapter 6 A novel asymptotic approach for computing washcoat diffu-		
sional effects in monolith reactors		122
6.1	Introduction	122
6.2	Mathematical Modeling	124
6.2.1	Detailed 1+1D Model	125
6.2.2	Reduced Order Model with Domain Decomposition	127
6.3	Validation of the Workflow with Linear Kinetics.	130
6.3.1	Exact solution of 1+1D Model	131
6.3.2	Solution of ROM	132
6.3.3	Comparison for Single-component system	133
6.3.4	Comparison for multicomponent system	134
6.4	Real time simulation of three-way catalytic converter	138
6.5	Conclusions and Discussion	144
Chapter 7 Summary and Suggestions for Future Work		146
7.1	Summary	146
7.2	Suggestions for Future Work	148
References		151
Appendices		157
Appendix A: Calculation of matrix functions and some details of Thiele		
matrix approach		158

Appendix B: Vector form of the reduced order model for a dual layered monolith reactor	167
Appendix C: Sherwood and Cross-Sherwood Numbers for Standard Geome- tries	176

List of Tables

Table 3.1	Numerical constants and parameters used in model simulation	39
Table 3.2	Reactions that are applied in Joshi's model for the real time simulation of a TWC	40
Table 3.3	Kinetic parameters for example1	40
Table 3.4	Reactions that are applied in Kumar's model for the oxygen storage and release of a TWC	40
Table 3.5	Kinetic parameters for example2	40
Table 3.6	Reaction scheme used in example 1	41
Table 3.7	Simulation conditions for example 1	41
Table 3.8	Reaction scheme in example 2 of TWC with oxygen storage .	48
Table 3.9	Simulation conditions for example 2	48
Table 3.10	Reversible reaction scheme and rate constants for example 3 .	52
Table 3.11	Inlet conditions and other parameters used in example 3 . . .	53
Table 4.1	Effective diffusion lengths, asymptotic internal Sherwood number and Λ^* for some common channel and washcoat shapes	92
Table 4.2	Effective diffusion lengths, asymptotic internal Sherwood and cross-Sherwood numbers for some common washcoat shapes	93
Table 4.3	Temperature dependent parameters used in the simulation . .	93
Table 4.4	Numerical constants and parameters used in model simulation	94
Table 4.5	Reaction scheme used in the Shakya et al. model for the SCR layer	94
Table 4.6	Reaction scheme used in the Shakya et al. model for the LNT layer	94
Table 4.7	Simulation conditions	95

Table 4.8	Catalyst properties	95
Table 5.1	Numerical constants and parameters used in model simulation	110
Table 5.2	Temperature dependent parameters used in the second example	111
Table 5.3	Reactions and rate expression in the second example	111
Table 5.4	Kinetic parameters for reaction rates	112
Table 6.1	Numerical constants and parameters used in model simulation	136
Table 6.2	Four reaction model for TWC: rates and kinetic parameters . .	138
Table 6.3	Numerical constants and parameters used in model simulation	139
Table A.1	Effective diffusion lengths, asymptotic internal Sherwood number and Λ for some common channel and washcoat shapes for the case of first order kinetics	166
Table C.1	Effective diffusion lengths, asymptotic internal Sherwood and cross-Sherwood numbers for some common washcoat shapes	177

List of Figures

Figure 1.1	Ceramic monolith (up) and catalyst deposition(down left) and	2
Figure 1.2	Transversal section of square-channel monolith with the pa- rameters employed to characterize the monolith geometry .	2
Figure 1.3	Implementation timeline of heavy-duty emissions standards in major vehicle markets	5
Figure 1.4	Schematic diagram of a monolith reactor, a representative channel, and catalyst layer illustrating various length scales.	6
Figure 1.5	Schematic diagram of the cross-section of square and cir- cular channels with washcoat with various effective length scales.	6
Figure 2.1	Comparison between exact Sherwood number and approx- imate Sherwood number	35
Figure 3.1	Computed dimensionless CO exit concentration versus time for a four reaction TWC model with (a) thin washcoat (b) thick washcoat	43
Figure 3.2	Computed dimensionless CO exit concentration versus time for a four reaction TWC model with (a) diluted inlet condition (b) concentrated inlet condition	44
Figure 3.3	(a) Computed dimensionless HC exit concentration predicted by various approximations with concentrated inlet condition (b) Comparison of exit fluid temperature versus time with concentrated inlet condition	45

Figure 3.4	(a) Comparison of computed dimensionless exit concentration of reductant species A predicted by various approximations for a TWC model with oxygen storage and non-isothermal condition (b) Comparison of exit concentration of A predicted by the Thiele matrix approximation with Jacobian matrix evaluated at different local concentrations.	51
Figure 3.5	Comparison of dimensionless exit concentration of reductant species A predicted by various approximations for a TWC model with oxygen storage under isothermal conditions.	52
Figure 3.6	(a) Computed exit concentration of species A versus inlet temperature (b) Exit concentration of species B versus inlet temperature for the three species reversible reaction scheme.	55
Figure 3.7	Comparison of calculated exit fluid phase concentration of species C versus inlet temperature (b) Different concentrations of C at exit for the three species reversible reaction scheme.	56
Figure 4.1	Schematic diagram of a single layered (a), and dual layered monolith channels (b), and examples of dual layered systems (c).	63
Figure 4.2	Comparison of approximated and exact internal/external and cross-exchange Sherwood numbers	74
Figure 4.3	Comparison of effluent NO _x concentrations predicted by various approximations to washcoat diffusion during storage at 300 °C (1+1D model results are with 10 mesh points).	78
Figure 4.4	Comparison of predicted NO and NO ₂ exit concentrations during storage with different number of mesh points for the Short Monolith model.	81

Figure 4.5	Comparison of NO exit concentrations predicted by the reduced order and detailed models	82
Figure 4.6	Comparison of NO ₂ exit concentrations predicted by reduced order and detailed models	83
Figure 4.7	Comparison of NO and NO ₂ exit concentrations with lean-rich cycling using reduced order and detailed models.	86
Figure 4.8	Comparison of exit NO concentration predicted by 1+1D model and reduced order model solutions in a short monolith reactor with higher temperature and space velocity	87
Figure 4.9	Comparison of exit NO ₂ concentration between 1+1D model and reduced order model solutions in a short monolith reactor with higher temperature and space velocity	88
Figure 4.10	Comparison between different reduced order model solutions with a lower $D_e (D_{e,j} = D_{f,j}/1000)$: (a) Exit NO concentration (b) Exit NO ₂ concentration	89
Figure 5.1	Schematic of a monolith channel with a single washcoat layer	98
Figure 5.2	Exit conversion versus inlet temperature for CO oxidation with micro kinetics in a long channel model (a) exit CO conversion (b) exit O ₂ conversion	114
Figure 5.3	Exit conversion versus inlet temperature for CO oxidation with micro kinetics in a short monolith model	115
Figure 5.4	Exit conversion versus inlet temperature for CO and H ₂ co-oxidation in a long channel model (a) exit CO conversion (b) exit H ₂ conversion	117
Figure 5.5	CO/H ₂ /C ₃ H ₆ co-oxidation in a long channel model (a) Exit conversion versus inlet temperature (b) Solid temperature rise versus inlet temperature	118

Figure 5.6	Inlet temperature ramp up and down for $\text{CO}/\text{H}_2/\text{C}_3\text{H}_6$ co-oxidation in a long channel model (a) Exit conversion versus inlet temperature with asymptotic solution (b) Solid temperature versus inlet temperature with asymptotic solution (c) and (d) are results of Thiele matrix solution	119
Figure 6.1	Schematic of half of a monolith channel with a single washcoat layer, along with an artificial intermediate interface.	125
Figure 6.2	Effectiveness factor of the washcoat from the exact solution and the proposed ROM-coupled with domain decomposition using only asymptotic transfer coefficients.	134
Figure 6.3	Dimensionless interface flux at the fluid-washcoat interface from the exact solution and the proposed method using only asymptotic transfer coefficients.	135
Figure 6.4	Exit concentrations (dimensionless) from 1+1D model and proposed ROM for linear kinetics.	137
Figure 6.5	Temporal profile of dimensionless exit concentrations \mathbf{X}_f^e for TWC obtained from 1+1D model (solid lines) and proposed method (dashed line) for CO , H_2 , NO and hydrocarbon (HC).	140
Figure 6.6	Temporal profile of exit fluid temperature T_f^e for TWC obtained from 1+1D model (solid lines) and proposed method (dashed line) for CO , H_2 , NO and hydrocarbon (HC).	141
Figure 6.7	Axial profiles of dimensionless exit concentrations \mathbf{X}_f of NO versus dimensionless axial coordinate (x/L) obtained from 1+1D model (solid lines) and proposed method (dashed line) for TWC at various times.	142

Figure 6.8	Cross-plot between exit dimensionless concentrations X_f^e of all species obtained from 1+1D model (solid lines) and proposed method (dashed line) for TWC.	143
Figure B.1	Figure S1: Schematic cross-section of a monolith channel with dual washcoat layers and various concentration modes.	169
Figure B.2	Figure S2: Schematic cross-section of a monolith channel with dual washcoat layers and various length scales.	170
Figure B.3	Figure S3: Mesh point distribution in the washcoat layer . . .	175

Nomenclature

Roman Letters

- a pore radius (m)
- A pre-exponential factor ($\text{mol} \cdot \text{m}^{-3} \cdot \text{s}^{-1}$)
- C_p specific heat capacity ($\text{J} \cdot \text{kg}^{-1} \cdot \text{K}^{-1}$)
- C_T total concentration of gas phase species ($\text{mol} \cdot \text{m}^{-3}$)
- D diffusivity ($\text{m}^2 \cdot \text{s}^{-1}$)
- E activation energy ($\text{J} \cdot \text{mol}^{-1}$)
- h heat transfer coefficient ($\text{W} \cdot \text{m}^{-2} \cdot \text{K}^{-1}$)
- \mathbf{k}_{me} external mass transfer coefficient matrix ($\text{m} \cdot \text{s}^{-1}$)
- \mathbf{k}_{mi} internal mass transfer coefficient matrix ($\text{m} \cdot \text{s}^{-1}$)
- \mathbf{k}_{mo} overall mass transfer coefficient matrix ($\text{m} \cdot \text{s}^{-1}$)
- L length of the monolith channel (m)
- Le lewis number
- M molecular mass ($\text{g} \cdot \text{mol}^{-1}$)
- N number of species
- Nu Nusselt number
- p pressure (Pa)
- P transverse mass Péclet number
- Pe_h axial heat Péclet number
- \mathbf{r} vector of reaction rates ($\text{mol} \cdot \text{m}^{-3} \cdot \text{s}^{-1}$)
- R gas constant ($\text{J} \cdot \text{mol}^{-1} \cdot \text{K}$)
- R_Ω hydraulic radius of monolith channel (m)
- R_d hydraulic diameter of monolith channel (m)
- \mathbf{Sh} Sherwood number matrix

\mathbf{Sh}_i	internal Sherwood number matrix
Sh_e	external Sherwood number
Sh_{e1}	external Sherwood number for layer 1
Sh_{i1}	internal Sherwood number for layer 1
Sh_{i2}	internal Sherwood number for layer 2
\widehat{Sh}_{e1}	cross-exchange external Sherwood number for layer 1
\widehat{Sh}_{i1}	cross-exchange internal Sherwood number for layer 1
t	time (s)
T	temperature (K)
$\langle u \rangle$	average feed gas velocity ($\text{m} \cdot \text{s}^{-1}$)
x	coordinate along the length of the monolith channel (m)
\mathbf{X}	vector of mole fractions
\mathbf{X}_{fm}	vector of cup-mixing mole fractions in fluid phase
$\langle \mathbf{X}_{wc} \rangle$	vector of volume averaged mole fractions in washcoat
\mathbf{X}_s	vector of mole fractions at gas-solid interface
y	transverse coordinate (m)
x	dimensionless coordinate along the length of the monolith channel

Greek Letters

δ_w	effective wall thickness (m)
δ_c	washcoat thickness (m)
ϵ_w	void fraction (porosity) of washcoat
$\partial\Omega_{k:k+1}$	interface between k^{th} and $(k + 1)^{th}$ domain of washcoat
Ω_k	k^{th} domain of washcoat
θ	fractional oxidation state of catalyst
λ	normalized air/fuel ratio
ν	matrix of stoichiometric coefficients
ρ	density ($\text{kg} \cdot \text{m}^{-3}$)

τ tortuosity

Φ thiele matrix

Subscript

k k^{th} layer of washcoat

i reaction index

j gaseous component index

f fluid phase

s solid phase

w/wc washcoat

Superscript

in inlet condition

0 initial condition

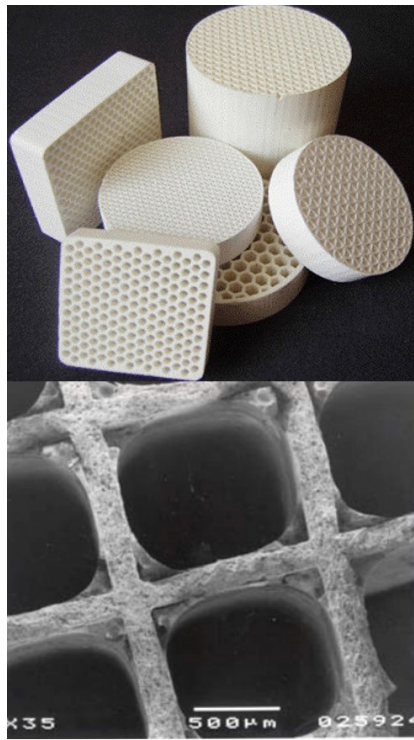
Chapter 1

Introduction

1.1 Introduction

In the past 30 years or so, there has been a gradual increase in the use of monoliths as catalyst supports. During this period, monoliths have mostly been used in environmental applications where high gas throughput and low pressure drop are required. Some of the applications in which these benefits have proven useful include exhaust gas treatment. Examples include three-way converters (TWCs) used in the treatment of emissions from gasoline engines, diesel oxidation catalysts (DOCs) used for treating emissions from diesel and lean burn engines, selective catalyst reduction (SCR) reactors used in reducing nitrogen oxides (NO_x) from light and heavy-duty diesel engines, and so forth. Other applications of monolith reactors include volatile organic chemical (VOC) combustion, removal of ozone from the cabin air of commercial aircraft, carbon monoxide and hydrocarbon abatement from the exhaust streams of gas turbines and catalytic partial oxidation of hydrocarbons to syngas and chemicals.

Monoliths are structures that contain various types of interconnected or separated channels (straight, wavy, or crimped) in a single block of material (e.g., honeycombs, foams, or interconnected fibers). Most monolith reactors consist of one piece of ceramic material. This ceramic block contains a large number of parallel channels extending over the entire length of the block, separated by thin walls. The channels normally have circular, square, or triangular cross sections but also channel geometries produced by wrapping up flat metal sheets with corrugated metal sheets in between (*Fig. 1.1*). Monolithic reactors are those filled with monoliths that are either made of porous catalytic material or the catalytic material is deposited (washcoated) in the channels of an inert monolithic support. In both



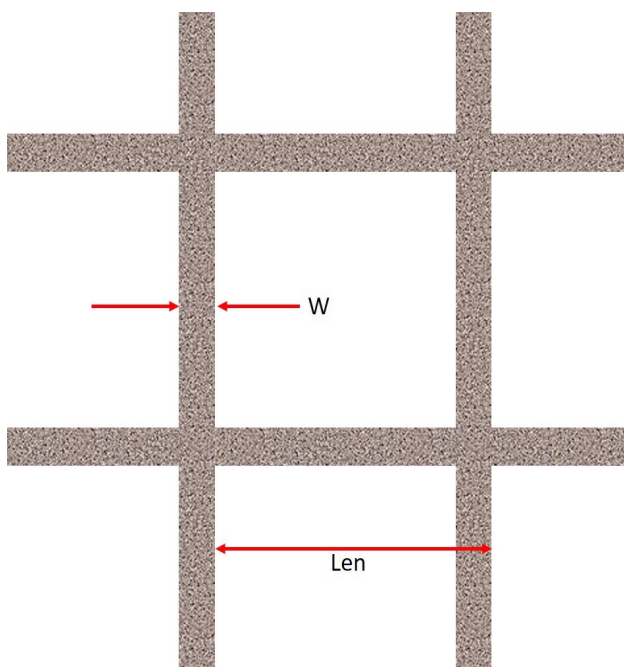
Ceramic monolith



Metallic monolith



Figure 1.1: Ceramic monolith (up) and catalyst deposition(down left) and



$$N = \frac{1}{Len^2}$$

$$OFA = N \times (Len - W)^2 = \frac{(Len - W)^2}{Len^2}$$

$$SA = 4N \times (Len - W) = \frac{4 \times (Len - W)}{Len^2}$$

Len: repeat distance
W: wall thickness
N: cell density
OFA: open frontal area
GSA: geometric surface area

Figure 1.2: Transversal section of square-channel monolith with the parameters employed to characterize the monolith geometry

arrangements, the channel walls function as catalyst and the channels provide space for flow of gas and/or liquid. Another type of monolithic reactors are those where the thin walls act directly as membranes or are used as a substrate for depositing materials that serve as membranes for separation and/or purification purposes. Currently, ceramic and metallic monoliths (*Fig. 1.1*) are the two major types of monolith supports used. Ceramic monoliths are mostly prepared by extrusion while metallic monoliths are normally made by corrugation. The ceramic material cordierite (magnesium aluminum silicate) is commonly used because it is cheap, it can be easily manufactured with high porosity, and it has a very small thermal expansion coefficient. Channel size and shape affect the pressure drop across the channel and the hydrodynamics of the fluid phases. The monolith themselves have a square, oval, racetrack, or round geometry, depending on the application. Larger volumes of monolith structures are obtained by stacking smaller building blocks. Different types of distributors can be used to achieve the desired uniform flow distribution over the monolith cross section, such as spray nozzles, shower heads, hole plates, glass frits, and static mixers. In the case of the square-channel monoliths, the monolith geometry is fully defined by two parameters: the channel size or repeat distance (L), and either the wall thickness (w , usually between 0.06 and 0.5 mm) or cell density (N), which is defined as number of cells per square inch (cpsi) and typically ranges between 100 and 1200 (*Fig. 1.2*). Other parameters commonly used to characterize the monolith structure are the void fraction, which varies between 0.5 and 0.9 and is frequently expressed as the open frontal area (OPA), the geometric surface area (GSA), and the surface-to-volume ratio. Monolithic reactors have some common features in most of the applications for which they are used. Compared with other types of reactors commonly used in industry they have numerous advantages, such as low pressure drop, especially under high fluid throughputs; high specific external surface area for mass transfer; elimination

of internal diffusion limitations when thin walls are used; low axial dispersion and back-mixing, and therefore high product selectivity; reduction of fouling and plugging, and thus extended lifetime; and as a result of the application of a regular structure, the scale-up to industrial relevant size is considerably easier. The main disadvantages are potential low radial heat transfer rate, and thus difficulty in temperature control, especially for ceramic monolith supports. Monolith reactors were developed for the cleaning of exhaust gases from combustion processes, both in cars and large power plants. For these processes, monolith reactors offer an irresistible combination of low pressure drop and high surface area. The combination of high cell density, 31–186 cells/cm² (200–1200 cells/in²), with thin walls, 0.051–0.27 mm (0.002–0.0105 in), give rise to low backpressure in automotive exhaust systems. This combination also yields high open frontal area (OFA), 72–87%, which is a necessary condition for low backpressure. Due to their significant advantages over conventional types of reactors, monoliths have also applications in gas phase, gas-liquid phase, liquid phase, or gas-liquid-solid phase reactions in the environmental and chemical, petrochemical, biochemical, and energy industries.

1.2 Automotive

As countries around the globe adapt more stringent emissions standards set by Real Driving Emissions (RDE) legislation (*Fig. 1.3*, reference from wikipedia), mathematical models of monolith reactors are becoming ever more widely used tools for devising vehicle control strategies. It is important for the model to be not only an accurate predictor but also run on Hardware-in-Loop (HIL) and engine control unit (ECU) systems which have significantly less computational power and memory than modern personal computers. The interactions between fluid flow, heat and mass transfer, catalytic chemistry at various length and time scales coupled with transient inputs to the monolith reactors used in after-treatment makes the simulation of these system in real time challenging.

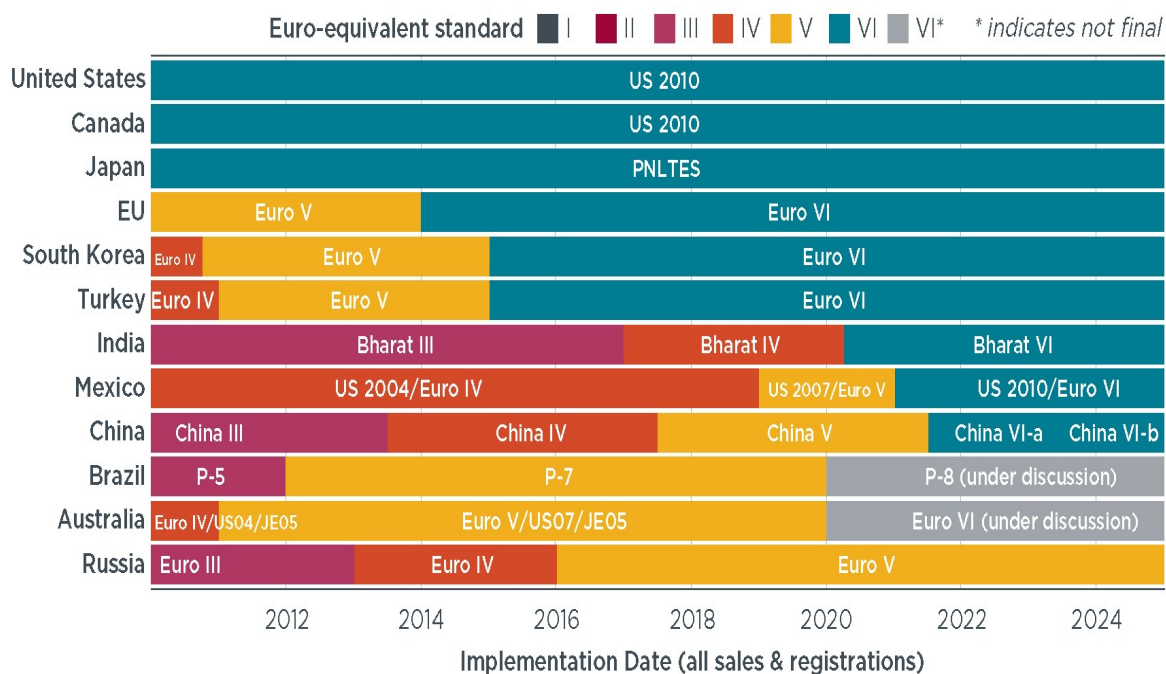


Figure 1.3: Implementation timeline of heavy-duty emissions standards in major vehicle markets

1.3 Physical characteristics of monoliths

The existence of multiple length and time scales in monolith reactors as shown in *Fig. 1.4* is well recognized (the effective length scales used in the model equations are shown in *Fig. 1.5*). At the larger scales (e.g., length and diameter of monolith and hydraulic diameter of the channels), the convection effects (flow distribution and velocity profile) are dominant while at the smaller scales (e.g., washcoat, pore and crystallite), diffusion and reaction phenomena dominate. Since the processes occurring at the various scales are intimately coupled and inlet composition and flow conditions vary with time in most after-treatment systems, simulation of the detailed mathematical models describing these systems may be time consuming. Although the numerical solution of the detailed mathematical models of monolith reactors with detailed kinetics (consisting of several coupled partial differential equations in two or three spatial coordinates and time) is possible with

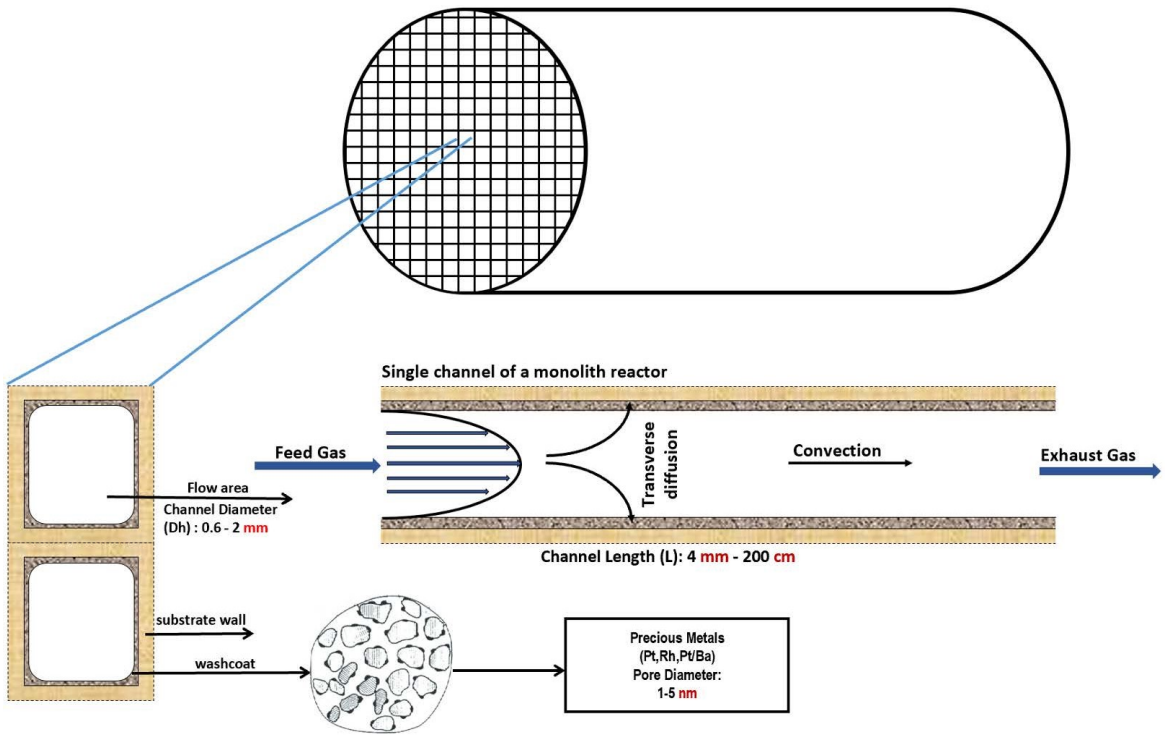


Figure 1.4: Schematic diagram of a monolith reactor, a representative channel, and catalyst layer illustrating various length scales.

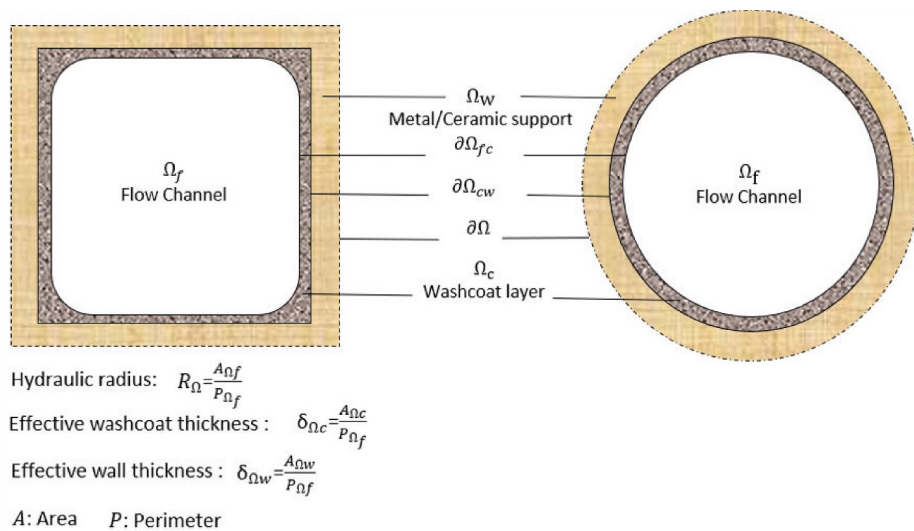


Figure 1.5: Schematic diagram of the cross-section of square and circular channels with washcoat with various effective length scales.

present day computers, it may be demanding in terms of time and memory requirements. Thus, it is preferable to eliminate the small scales and develop reduced order models in terms of measurable quantities for real time (or faster than real time) simulation of these systems. Below we review from detailed model to reduced order model but only emphasize in species balance equations because the main point of this work is to discuss the simplification of washcoat diffusion problem.

1.4 Hierarchies of models of monolith reactors

1.4.1 3-D model

The detailed mathematical models for describing transport and reaction processes occurring in a monolith reactor are obtained from the continuity, species, momentum and energy conservation equations, which are often complex and may be in form of several partial differential equations in terms of two or three spatial coordinates and time. These conservation equations may be highly nonlinear and may contain local property dependent transport and reaction parameters (e.g., dependent on temperature, concentration, or spatial coordinates etc.). For example, under certain assumptions, the species conservation equation in fluid and solid phases may be expressed as follows (without homogenous reactions in the fluid phase)

$$\frac{\partial \mathbf{X}_f}{\partial t} + \vec{\nabla} \cdot (\vec{u} \mathbf{X}_f) - \vec{\nabla} \cdot (\mathbf{D}_f \vec{\nabla} \cdot \mathbf{X}_f) = 0; \text{ in } \Omega_f \quad (1.1)$$

$$\text{and } \epsilon_w \frac{\partial \mathbf{X}_{wc}}{\partial t} - \vec{\nabla} \cdot (\mathbf{D}_e \vec{\nabla} \cdot \mathbf{X}_{wc}) = \frac{1}{C_T} \boldsymbol{\nu}^T \mathbf{r}(\mathbf{X}_{wc}, T_{wc}); \text{ in } \Omega_{wc}. \quad (1.2)$$

[Remarks: In the equations, bold symbols are used to represent matrices and vectors. We choose to write the model equations in terms of species mole fractions, which is convenient for after-treatment application. They could also be expressed in terms of concentrations as in the traditional formulation]. where subscripts f and

wc represent quantities in fluid phase (Ω_f) and catalyst or washcoat phase (Ω_{wc}), respectively; Here, the column vectors, \mathbf{X}_f and $\mathbf{X}_{wc} \in \mathbb{R}^N$, represent the mole fractions in the fluid phase and the mole fractions in the washcoat, respectively; \vec{u} is the (interstitial) fluid velocity; \mathbf{D}_f is the diffusivity matrix in fluid phase and \mathbf{D}_e is the effective diffusivity matrix in catalytic/solid phase; \mathbf{r} is the reaction rate vector; $\mathbf{r}(\mathbf{X}_{wc}, T_{wc}) \in \mathbb{R}^{N_r}$ is the reaction rate vector, where each element r_i represents the rate of the i^{th} reaction, the parameters N and N_r represent the total numbers of gaseous species and reactions, respectively. The matrix, $\nu \in \mathbb{R}^{N_r \times N}$, is a matrix of stoichiometric coefficients with rows representing the reaction index while the columns representing species index; ϵ_w is the porosity of the catalytic phase. The overall mass balance or continuity equation may be expressed as follows:

$$\frac{\partial \rho_f}{\partial t} + \vec{\nabla} \cdot (\vec{u} \rho_f) = 0 \quad (1.3)$$

where ρ_f is the fluid density. Similarly, under certain assumptions, the energy conservation equation may be expressed as follows:

$$\rho_f C_{p_f} \left(\frac{\partial T_f}{\partial t} + \vec{u} \vec{\nabla} \cdot T_f \right) - \vec{\nabla} \cdot (k_f \vec{\nabla} \cdot T_f) = 0; \text{ in } \Omega_f, \quad (1.4)$$

$$\rho_{wc} C_{p_{wc}} \frac{\partial T_{wc}}{\partial t} - \vec{\nabla} \cdot (k_{wc} \vec{\nabla} \cdot T_{wc}) = (-\Delta H)^T \mathbf{r}(\mathbf{X}_{wc}, T_{wc}); \text{ in } \Omega_{wc} \quad (1.5)$$

$$\text{and } \rho_w C_{p_w} \frac{\partial T_w}{\partial t} - \vec{\nabla} \cdot (k_w \vec{\nabla} \cdot T_w) = 0; \text{ in } \Omega_w \quad (1.6)$$

where ρ and C_p are the density and specific heat capacity; T is the temperature; k is the thermal conductivity; ΔH is the heat of reaction vector; and subscripts ' w ' represents the solid wall (substrate). The velocity profile along with pressure profiles is obtained using continuity equation (Eq. 1.3) and momentum conservation equations. In most applications of interest, a simplified velocity profiles is assumed, considering a fully developed or developing profile in the catalyst bed or

monolith channels. In such cases, the momentum balance can be decoupled from the species and energy balances.

The model equations described above (Eqs. 1.4-1.5) are solved using appropriate inlet, initial and boundary conditions. It may be noted that the transport and reaction parameters (such as viscosity, density, diffusivity, heat of reaction, heat capacities, reaction rate constants etc.) depend on temperature and concentration, and vary in spatial coordinates due to non-uniform catalyst/reaction activity profiles. In addition, the non-linearity due to reaction can be extremely strong, especially the temperature dependence. Further, the coupling of transport and reaction processes with many physicochemical parameters at multiple length/time scales (corresponding to diffusion/conduction, convection and reaction time scales) can lead to complex steady-state and transient behaviors (e.g., multiple steady-states, ignition-extinction and hysteresis behavior, spatial and temporal patterns, traveling reaction fronts and so forth). Analysis of such behavior using the 3-dimensional models can be extremely difficult and exploring the different types of solutions (that may exist in the multi-dimensional parameter space) may be impractical through direct numerical solutions of these 3D models. Therefore, the development of reduced order coarse-grained models is essential to enable real time simulations and to obtain various solutions in the parameter space.

1.4.2 Reduced order model

1+2D model

For a parallel plate geometry, with the limiting case of transverse diffusion time scale is much less than the axial convection time scale: $\frac{R^2}{D_f} \ll \frac{L}{u}$, we can average the species balance equations over the transverse direction as followed equations, so that 3-D model can be reduced to 1+2D model by using two concentrations modes X_{fm} and X_s , with an external mass transfer coefficient k_{me} , Fluid phase species balance equations are given by

$$\frac{\partial \mathbf{X}_f}{\partial t} + \langle u \rangle \frac{\partial \mathbf{X}_f}{\partial x} = \mathbf{D}_f \frac{\partial^2 \mathbf{X}_f}{\partial x^2} - \frac{\mathbf{k}_{me}(\mathbf{X}_{fm} - \mathbf{X}_s)}{R_\Omega}; \text{ in } \Omega_f. \quad (1.7)$$

\mathbf{X}_{fm} here is the fluid cup mixing fraction and \mathbf{X}_s is the interfacial mole fraction between fluid and solid phase. R_Ω represents the hydraulic radius of the monolith channel, $\langle u \rangle$ is the average velocity in the channel. The species balance equations in the washcoat is

$$\epsilon_w \frac{\partial \mathbf{X}_{wc}}{\partial t} = \frac{1}{C_T} \boldsymbol{\nu}^T \mathbf{r}(\mathbf{X}_{wc}) + \vec{\nabla} \cdot (\mathbf{D}_e \vec{\nabla} \cdot \mathbf{X}_{wc}); \text{ in } \Omega_{wc}. \quad (1.8)$$

with continuity equation expressed as follows:

$$\mathbf{j}_{fw} = \mathbf{k}_{me}(\mathbf{X}_{fm} - \mathbf{X}_s) = -\mathbf{D}_e \vec{\nabla} \cdot \mathbf{X}_{wc}; \text{ in } \partial\Omega_{fwc}. \quad (1.9)$$

Here, 1+2D means the we have one direction along the reactor axial length, 2D comes when we have a asymmetric cross section of the washcoat(*Fig. 1.5*).

1+1D model

1+2D model can be reduced to 1+1D model by the shape normalization of the washcoat cross section, so here comes the effective washcoat thickness δ_c which equals to the area of the cross section of the catalyst over the perimeter of the flow channel. And the fluid and catalyst phase species balance equations are given by

$$\frac{\partial \mathbf{X}_f}{\partial t} + \langle u \rangle \frac{\partial \mathbf{X}_f}{\partial x} = \mathbf{D}_f \frac{\partial^2 \mathbf{X}_f}{\partial x^2} - \frac{\mathbf{k}_{me}(\mathbf{X}_{fm} - \mathbf{X}_s)}{R_\Omega}; \text{ in } \Omega_f, \quad (1.10)$$

$$\epsilon_w \frac{\partial \mathbf{X}_{wc}}{\partial t} = \frac{1}{C_T} \boldsymbol{\nu}^T \mathbf{r}(\mathbf{X}_{wc}) + \mathbf{D}_e \frac{\partial^2 \mathbf{X}_{wc}}{\partial y^2}; \text{ in } \Omega_{wc} \quad (1.11)$$

$$\text{and } \mathbf{j}_{fw} = \mathbf{k}_{me}(\mathbf{X}_{fm} - \mathbf{X}_s) = -\mathbf{D}_e \frac{\partial \mathbf{X}_{wc}}{\partial y}; \text{ in } \partial\Omega_{fwc}. \quad (1.12)$$

Assume the wall is non-porous, the species fluxes at the wall-washcoat interface vanish, i.e.

$$\left. \frac{\partial \mathbf{X}_{wc}}{\partial y} \right|_{y=\delta_c} = \mathbf{0}. \quad (1.13)$$

The continuity of the species fluxes at the fluid-washcoat interface leads to the interfacial boundary condition:

$$\frac{\mathbf{j}_{fw}}{C_T} = \mathbf{k}_{me} (\mathbf{X}_{fm} - \mathbf{X}_s) = -\mathbf{D}_e \left. \frac{\partial \mathbf{X}_{wc}}{\partial y} \right|_{y=R_\Omega}. \quad (1.14)$$

In our work, we focus on short monolith model and long channel model, with a short monolith model, heat and species dispersion times are much smaller than the space time, the spatial gradient in temperature and concentration within the bed are negligible (complete axial mixing). For a long channel model, heat and mass dispersion times are much greater than the space time (i.e., negligible axial heat and mass dispersion). This lead to the traditional 1+1D model without axial dispersion term, fluid phase species balance equations become as

$$\frac{\partial \mathbf{X}_f}{\partial t} = -\langle u \rangle \frac{\partial \mathbf{X}_f}{\partial x} - \frac{\mathbf{k}_{me} (\mathbf{X}_{fm} - \mathbf{X}_s)}{R_\Omega}; \text{ in } \Omega_f.$$

Length and time scales: In order to determine the numerical effort involved in obtaining an accurate (and mesh size independent solution) of the full 1+1D model, we examine the various length and time scales represented in the model. The time scales associated with convection (τ), external mass transfer (t_{mj}) and washcoat diffusion or internal mass transfer (t_{Dj}) are defined by

$$\tau = \frac{L}{\langle u \rangle}; \quad t_{mj} = \frac{R_\Omega^2}{D_{f,j}}; \quad t_{Djk} = \frac{\delta_{ck}^2}{D_{ek,j}}, \quad (1.15)$$

where R_Ω (δ_{ck}) is the channel hydraulic radius (effective washcoat layer thickness), and $D_{f,j}$ ($D_{ek,j}$) is the diffusivity of species j in the gas phase (effective diffusivity in

the washcoat layer k). In after-treatment applications, the space time τ is usually in the range 0.01 to 1s, the external mass transfer time is in the range 0.001 to 0.01s, while the washcoat diffusion time is in the range 0.001 to 0.01s. However, depending on the washcoat layer properties, the latter time can vary in a wider range of 10^{-5} to 1s, with the smaller value corresponding to thinner washcoats with larger pores and the larger value corresponding to thicker washcoats with small or partially blocked pores. [The larger values of washcoat diffusion time may also be realized either with aged catalysts or when species are stored in one of the layers and effective diffusivity in that layer decreases with increased storage]. In addition to these transport time scales, those associated with the gas phase species interactions with the catalytic sites are determined by the eigenvalues of the Jacobian of the species formation rate vector $\boldsymbol{\nu}_k^T \mathbf{r}_{gk}(\mathbf{X}_{wk}, \boldsymbol{\theta}_{wk})$ with respect to the species mole fractions. Specifically, the stiffness in the spatial coordinate y (or washcoat depth) is determined by the largest eigenvalue of the Thiele matrix (squared) of layer k defined by

$$\Phi_k^2 = \delta_{ck}^2 (\mathbf{D}_{ek})^{-1} \left(-\frac{1}{C_T} \frac{d(\boldsymbol{\nu}_k^T \mathbf{r}_{gk}(\mathbf{X}_{wk}, \boldsymbol{\theta}_{wk}))}{d\mathbf{X}_{wk}} \right); \quad k = 1, 2. \quad (1.16)$$

We note that in some applications, the magnitude of the largest eigenvalue of Φ_k^2 can be in the range 10^4 to 10^8 , which indicates that pore diffusional effects are very strong and a large number of mesh points (of the order of the square root of the largest eigenvalue in magnitude, e.g., 10^2 to 10^4) may be required to obtain mesh size independent solution of the detailed 1+1D model. This fact will be illustrated in the numerical calculations presented in this work.

To summarize, while there are only four relevant length scales in monolith reactors (the macro length scales such as reactor/channel length L , the channel hydraulic radius R_{Ω} , the meso length scales such as the washcoat depths or ef-

fective diffusional lengths δ_{ck} , and micro-length scales such as the pore diameter (d_p) or crystallite size (d_c), which determine the effective diffusivity and reactivity, there are many more time scales. For a single layered system, the number of time scales is approximately equal to three times the number of gas phase species plus the number of surface species while for a dual layered system, it is about four times the number of gas phase species plus the number of surface species. It is mostly these time scales that determine the system behavior and also the numerical effort involved in obtaining a mesh size independent solution of the monolith models.

Two-mode form of the 1-D model

The only difference between the 1+1D model and the two mode form of the reduced order model is that the two-mode form of the reduced order model replace the problem of solving detailed washcoat diffusion problem by adding another washcoat averaged mass balance equation and using the internal mass transfer coefficient matrix \mathbf{k}_{mi} . This lead to the traditional two mode form of the reduced order model without axial dispersion term

$$\frac{\partial \mathbf{X}_{fm}}{\partial t} = -\langle u \rangle \frac{\partial \mathbf{X}_{fm}}{\partial x} - \frac{\mathbf{k}_{mo} (\mathbf{X}_{fm} - \langle \mathbf{X}_{wc} \rangle)}{R_\Omega}, \quad (1.17)$$

$$\epsilon_w \frac{\partial \langle \mathbf{X}_{wc} \rangle}{\partial t} = \frac{1}{C_T} \boldsymbol{\nu}^T \mathbf{r}(\langle \mathbf{X}_{wc} \rangle) + \frac{\mathbf{k}_{mo} (\mathbf{X}_{fm} - \langle \mathbf{X}_{wc} \rangle)}{\delta_c}, \quad (1.18)$$

$$\mathbf{k}_{mo} (\mathbf{X}_{fm} - \langle \mathbf{X}_{wc} \rangle) = \mathbf{J}_{fw} \quad (1.19)$$

$$\text{and } \mathbf{k}_{me}^{-1} = \frac{\mathbf{t}_{Df}}{Sh_{e,\infty} R_\Omega}; \quad \mathbf{k}_{mi}^{-1} = \frac{\mathbf{t}_{wc}}{Sh_{i,\infty} \delta_c}; \quad \mathbf{k}_{mo}^{-1} = \mathbf{k}_{me}^{-1} + \mathbf{k}_{mi}^{-1}, \quad (1.20)$$

where \mathbf{k}_{mi} and \mathbf{k}_{mo} are internal and overall mass transfer coefficient matrices, respectively. So the problem becomes how to find an appropriate expression for \mathbf{k}_{mi} . The objective of our work is to simplify the solution of diffusion-reaction equations in the washcoat to avoid the computational demand of the full numerical solution so that in the next few chapters we showed different approximations of \mathbf{k}_{mi} and propose a novel approach to calculate \mathbf{k}_{mi} .

1.5 Outline of the Thesis

In chapter II and III, we present a novel method for computing washcoat diffusional effects in reduced order models with local property dependent internal and external transfer coefficients for real time simulations of monolith reactors. The method, called "Thiele matrix approach" includes washcoat diffusional effects by computing the internal Sherwood matrix which depends on the local Thiele matrix, defined in terms of the Jacobian of the rate vector at the local concentrations. The accuracy and speed-up of the method is illustrated for single layered monolith reactors with global kinetics, and it is also compared with other existing methods in literature. It is shown that this method leads to the best match with detailed model while speeding calculations by orders of magnitude.

In chapter IV, we extend Thiele matrix approach further to include dual washcoat layers. For the case of dual-layered monolith reactors, except the traditional external and internal Sherwood matrices, cross-exchange Sherwood matrices also arise in layer one of the washcoat due to the coupling between fluxes at the two interfaces. We illustrate the method using a dual layered LNT-SCR model with multi-component system. We also investigate the mesh size dependency in the transverse direction on detailed model accuracy and note that the detailed model has sufficient accuracy when the number of mesh points is about equal to the square root of the largest eigenvalue of the Thiele matrix Φ^2 . The speed and accuracy of the reduced order model solution haven been compared with the detailed model and show that Thiele matrix solution is closer to detailed model which has sufficient mesh points.

In chapter V, we extend Thiele matrix approach to include detailed micro-kinetic models. First, we show that the short time scales associated with the adsorption/desorption steps of micro-kinetic models requires the use of a very large number of mesh points within the washcoat to obtain a mesh independent solution.

Next, we present a multi-mode reduced order model using the Thiele matrix dependent internal mass transfer coefficient matrix. This matrix is shown to be diagonal for most micro-kinetic models of practical interest and can be calculated very accurately. We illustrate the method with an example of $\text{H}_2/\text{CO}/\text{C}_3\text{H}_6$ oxidation over a $\text{Pt}/\text{Al}_2\text{O}_3$ catalyst with a 20 step micro-kinetic model. Even for this simple single site model, we show that the small time (and length) scales associated with the species adsorption steps make the computation of the mesh independent solution of the 1+1D model very time consuming. However, the reduced order model leads to an accurate solution while speeding-up calculations by about three orders of magnitude.

We found that evaluation of the Sherwood matrix as a function of the Thiele modulus matrices is cumbersome and computationally costly in some cases. Therefore, in chapter VI, we propose and validate a methodology based on coupling of ROM and domain decomposition method for single and multicomponent systems, which simplifies the evaluation of transfer coefficients and speed-up the real time simulation significantly. We simulated a real system of three-way catalytic converter (TWC) with four reaction model for comparing the results with the detail model. The results show a very good match between the two while increasing the simulation speed by about three orders of magnitude.

In the last chapter, we summarize the main results of the thesis and discuss some possible extensions of this work.

Chapter 2

Introduction to various reduced order model approaches

2.1 Literature review

The reduced order models that can be used to simulate the system behavior in real time are also useful for implementation of the various control and optimization algorithms related to fuel economy and the more stringent emissions constraints. Finally, the reduced order models are most useful in parametric and bifurcation studies and solution of the inverse problems, i.e., the estimation of the kinetic and other parameters from a limited set of experimental data. There have already been many reduced order models proposed for monolith reactors in the literature. Most of these are based on the assumption of adiabatic reactor and a single channel being representative of the entire reactor. The simplest of these models is the so called pseudo-homogeneous model that ignores the temperature and concentration gradients in the directions perpendicular to the flow and also concentration gradients in the washcoat. The next hierarchy of models are the two-phase or two-mode models that use two concentrations and temperatures at each axial position to describe the local (transverse) gradients in the channel. Since these two-phase models were found to be adequate to describe most of the observed experimental features, several modifications are suggested to improve further the accuracy of these models. Most of these modifications have to do with improved correlations for the external heat and mass transfer coefficients and inclusion of the washcoat diffusional effects so that various regimes of operation of the monolith reactor (e.g., kinetic, pore/washcoat diffusion and external mass transfer control) can be described accurately. We review briefly below these modifications with a focus on the description of the washcoat diffusional effects.

The approach proposed by Balakotaiah [1] was used by Joshi et al., [2] to de-

velop and demonstrate the utility of low-dimensional models in the transient simulations of monolith reactors with a single washcoat layer. For the isothermal case, their model consisted of two (phase averaged global) equations for each gas phase species, one for the fluid phase cup-mixing concentration and one for the average concentration in the washcoat layer. The fluid-washcoat interfacial concentration was eliminated in this model by use of an overall mass transfer coefficient that is defined in terms of the usual external transfer coefficient and an asymptotic internal mass transfer coefficient (which depends only on the effective thickness of the washcoat, effective diffusivity of the species in the washcoat and shape/geometry of the washcoat). While the use of asymptotic internal mass transfer coefficient was adequate for many applications, especially those involving cold-start transient simulations of various after-treatment systems, Kumar et al., [3] noted that it was inadequate (or may have significant error) for describing ignited branches on which strong washcoat diffusional limitations may exist. They recommended using a local property (Thiele matrix) dependent internal mass transfer coefficient with a diagonal approximation. This work was later followed by Bissett [4] and Gundlapally et al., [5] who developed an asymptotic solution for washcoat pore diffusion (that is valid only when the gradients in the washcoat are small). In related work, Ratnakar et al., [6] and Ratnakar and Balakotaiah [7] used the Liapunov-Schmidt (L-S) averaging technique to obtain reduced order models for monoliths with a single washcoat layer and compared the same with the existing literature models. Their conclusion was that most literature models, including the classical two-phase models of catalytic reactors and the 1+1D models of monolith reactors, do not distinguish between the cup-mixing and the averaged concentration in the channel, and neglect the Taylor dispersion term that arises due to velocity gradients and transverse molecular diffusion in the channel. However, the Taylor dispersion term becomes negligible when the velocity profile is flat and/or inlet conditions vary slowly (com-

pared to the space time). It should be noted that the L-S method of averaging gives the correct structure of the reduced order models but is only applicable when the transverse gradients in the channel and washcoat are small. This deficiency was removed by Ratnakar et al., [8], where they used Thiele modulus dependent Sherwood number as suggested by Balakotaiah [1], and expanded the range of validity of the multi-mode reduced order models.

The accuracy of the diagonal approximation for washcoat diffusion was tested by Kumar et al., [9] using a three reaction model for describing the spatio-temporal dynamics of oxygen storage and release in a three-way converter (TWC). The main conclusion of these authors was that for the kinetic model studied, the reduced order model describes the spatio-temporal dynamics with sufficient accuracy, the exception being very high inlet forcing frequency. Following this observation, reduced order models with diagonal approximation were used by Ting et al., ([10], [11]) to simulate the lean-rich cycling behavior of LNTs with more complex chemistry (32 reactions) and Daneshvar et al., [12] to simulate the light-off behavior of DOCs with feed streams containing CO and several hydrocarbons.

In recent years, monolith reactors with two (or more) washcoat layers are used in many applications and reduced order models for such systems have also been developed. Mozaffari et al., [13] and Rink et al., [14] extended the earlier approach of Joshi et al., [2] to develop reduced order models for dual layered systems and illustrated their use with several applications. More recently, Ratnakar et al., [8] developed reduced order models for dual and multi-layered systems using the L-S method of averaging and showed the structure of the local equations is different from the earlier intuitively written models. It should be noted that in both single and dual layered monolith reactors, the main criterion that determines the accuracy of the reduced order model is the approximation(s) used for describing the washcoat diffusion problem, specifically the internal mass transfer coefficient. Ac-

accurate correlations for describing the external mass transfer coefficients are available in the literature for both fully developed and simultaneously developing flows [5]. The main goal of this work is to examine in detail the various approximations for describing the internal mass transfer coefficient for the case of single layered monolith reactors. We propose a novel, fast and accurate method for this purpose and compare its accuracy and speed of computation with existing methods as well as exact (numerical) solutions.

This chapter is organized as follows: in the next section, we give a brief review of the detailed and reduced order models for a monolith reactor with single washcoat layer and various approximations used for describing the internal mass transfer coefficient. In section 2 and 3, we present the Thiele matrix approach for computing the (non-diagonal) matrix of internal mass transfer coefficients for the case of multiple reactions in a single washcoat layer.

2.2 Detailed and Reduced Order Models of Monolith Reactors

As stated in chapter 1, the most detailed models of monolith reactors consist of continuity, momentum, species and energy balances in three spatial coordinates and time. However, such detailed models are not needed in most applications and the most common simplifications used assume a velocity profile and consider only the species and energy balances. Further, as the transverse gradients in the channel are usually small, and the time scale for the variation of the inlet conditions is much larger than the space time (slowly varying inputs), the species balance is further simplified by neglecting the Taylor dispersion term and using two concentrations modes with an external mass transfer coefficient (that depends on the flow conditions in the channel). This leads to the so called 1+1D models, which couple the washcoat diffusion problem to the flux at the fluid-washcoat interface (For further details on this simplification, we refer to the articles by Ratnakar and Balakotaiah [8] and Gu and Balakotaiah [16]). Since the main focus of this work

is on the approximation of the washcoat diffusion problem, we shall use the 1+1D model as our basis (detailed) model in all comparisons.

Since the transverse temperature gradient in the washcoat and wall are negligible (due to much higher thermal conductivity of these solid materials compared to gas phase and smaller thickness compared to channel hydraulic radius), the standard two-phase model with lumped capacitances will be used to describe the temperature variations of the fluid and solid phases along the monolith length. We review here again the standard 1+1D model for the species balances and two-phase model for the energy balance and also show here various approximations for the washcoat diffusion problem.

2.2.1 Detailed(1+1D) washcoat diffusion model

Under the assumption of slowly varying inputs, the gas phase species balances are same as that of the standard two-phase model and are described by conservation equations in the channel with interfacial transfer terms. They are given by the vector equation

$$\frac{\partial \mathbf{X}_{fm}}{\partial t} + \langle u \rangle \frac{\partial \mathbf{X}_{fm}}{\partial x} = -\frac{\mathbf{k}_{me}}{R_{\Omega}} (\mathbf{X}_{fm} - \mathbf{X}_s); \quad x > 0, t > 0, \quad (2.1)$$

while the species balances in the washcoat are given by

$$\epsilon_w \frac{\partial \mathbf{X}_{wc}}{\partial t} = \frac{1}{C_T} \boldsymbol{\nu}^T \mathbf{r}(\mathbf{X}_{wc}) + \mathbf{D}_e \frac{\partial^2 \mathbf{X}_{wc}}{\partial y^2}; \quad 0 < y < \delta_c. \quad (2.2)$$

Since the wall is assumed to be non-porous, the species fluxes at the wall-washcoat interface vanish, i.e.,

$$\left. \frac{\partial \mathbf{X}_{wc}}{\partial y} \right|_{y=\delta_c} = \mathbf{0}. \quad (2.3)$$

The continuity of the species fluxes at the fluid-washcoat interface leads to the interfacial boundary condition:

$$\frac{\mathbf{j}_{fw}}{C_T} = \mathbf{k}_{me} (\mathbf{X}_{fm} - \mathbf{X}_s) = -\mathbf{D}_e \left. \frac{\partial \mathbf{X}_{wc}}{\partial y} \right|_{y=0}. \quad (2.4)$$

[Remarks: In the equations, bold symbols are used to represent matrices and vectors. We choose to write the model equations in terms of species mole fractions, which is convenient for after-treatment application. They could also be expressed in terms of concentrations as in the traditional formulation, see the Appendix A. For a derivation of the 1+1D model from the full partial differential equations and the assumptions involved, we refer to the article by Ratnakar et al., [8]]. Here, the column vectors, \mathbf{X}_{fm} and $\mathbf{X}_{wc} \in \mathbb{R}^N$, represent the cup-mixing mole fractions in the fluid phase and the mole fractions in the washcoat, respectively; R_Ω represents the hydraulic radius of the monolith channel, $\langle u \rangle$ is the average velocity in the channel, the column vector $\mathbf{X}_s \in \mathbb{R}^N$ is the mole fraction vector at the fluid-washcoat interface and \mathbf{k}_{me} is the matrix of external mass transfer coefficients defined by the first equality of Eq. 2.4. In Eq. 2.2, ϵ_w is the porosity of the washcoat, $\mathbf{r}(\mathbf{X}_{wc}) \in \mathbb{R}^{N_r}$ is the reaction rate vector, where each element r_i represents the rate of the i^{th} reaction, the parameters N and N_r represent the total numbers of gaseous species and reactions, respectively. The matrix, $\nu \in \mathbb{R}^{N_r \times N}$, is a matrix of stoichiometric coefficients with rows representing the reaction index while the columns representing species index. The vector \mathbf{j}_{fw} represents the species fluxes at the fluid-washcoat interface. The parameter δ_c is the effective thickness of the washcoat, \mathbf{D}_e is assumed to be a diagonal matrix of effective (Knudsen) diffusivities of various species in the washcoat. The total concentration (C_T) is computed using the ideal gas law

$$C_T = \frac{p}{RT_f(t)}. \quad (2.5)$$

Here, p represents the total gas pressure, assumed constant at 1 atm, T_f is the fluid temperature. In most after-treatment applications, the external mass transfer coefficient matrix is assumed to be diagonal as the reactive species concentrations are small compared to the major inert species (which is usually nitrogen).

The energy balance in the fluid phase is given by

$$\rho_f C p_f \frac{\partial T_f}{\partial t} + \langle u \rangle \rho_f C p_f \frac{\partial T_f}{\partial x} = \frac{h}{R_\Omega} (T_s - T_f). \quad (2.6)$$

As stated above, with the assumption that the solid temperature is uniform in the transverse direction, the solid phase energy balance is given by

$$\delta_w \rho_w C p_w \frac{\partial T_s}{\partial t} = \delta_w k_w \frac{\partial^2 T_s}{\partial x^2} - h (T_s - T_f) + \int_0^{\delta_c} \mathbf{r}^T (-\Delta \mathbf{H}) dy. \quad (2.7)$$

Here, T_f is the fluid (cup-mixing) temperature, ρ_f and $C p_f$ are the density and specific heat capacity of the fluid phase, T_s is the solid temperature and δ_w represents the effective wall thickness (defined as $\delta_w = \delta_s + \delta_c$, where δ_s is the effective half-thickness of the wall and δ_c is the effective thickness of the washcoat.) , ρ_w and $C p_w$ are the effective density and specific heat capacity of the washcoat, respectively, defined as $\delta_w \rho_w C p_w = \delta_c \rho_c C p_c + \delta_s \rho_s C p_s$ and $\delta_w k_w = \delta_c k_c + \delta_s k_s$, where the subscript s and c represent the support and catalyst/washcoat, respectively; h in *Eq.* 2.6 and 2.7 represents the local heat transfer coefficient at the fluid-washcoat interface. The last term in *Eq.* 2.7 represents the total heat generated by various reactions with ΔH_i being the enthalpy change of reaction i .

The inlet, initial and boundary conditions for the above model are of the form

$$\text{Inlet.C. : } \mathbf{X}_{fm}(0, t) = \mathbf{X}_{fm,in}(t) ; T_f(0, t) = T_{f,in}(t), \quad (2.8)$$

$$\text{Initial.C. : } \mathbf{X}_{fm}(x, 0) = \mathbf{X}_{fm}^0(x) ; \mathbf{X}_{wc}(x, y, 0) = \mathbf{X}_{wc}^0(x, y), \quad (2.9)$$

$$\text{Initial.C. : } T_f(x, 0) = T_f^0(x) ; T_s(x, 0) = T_s^0(x) \quad (2.10)$$

$$\text{and Boundary.C. : } \frac{\partial T_s}{\partial x}(0, t) = 0 ; \frac{\partial T_s}{\partial x}(L, t) = 0. \quad (2.11)$$

We note that to solve the above 1+1D model for the isothermal case, we need to discretize the transverse length (y) scale using $M (\geq 1)$ interior mesh points. For example, discretization using second order finite difference (or finite volume) method leads to $N(M + 2)$ partial differential equations in length (x) and time (t), where N is the number of species, plus N linear algebraic equations relating the interfacial flux vector (\mathbf{j}_{fw}) and the interfacial mole fractions ($\mathbf{X}_s = \mathbf{X}_{wc}|_{y=0}$). [For the non-isothermal case, the number of equations increases by two, as fluid and solid energy balances are added. Also, the number of mesh points can be much higher if diffusion in the washcoat is two-dimensional]. We also note that if the gradients in the washcoat are assumed to be negligible, then the solid phase species balance may be integrated across the washcoat depth to obtain the equation

$$\epsilon_w \frac{\partial \mathbf{X}_s}{\partial t} = \frac{1}{C_T} \boldsymbol{\nu}^T \mathbf{r}(\mathbf{X}_s) + \frac{\mathbf{k}_{me}}{\delta_c} (\mathbf{X}_{fm} - \mathbf{X}_s). \quad (2.12)$$

Eqs. 2.1 and 2.12 along with appropriate inlet, initial and boundary conditions define the standard two-phase model (which ignores completely the gradients in the washcoat) and the solution requires integration of $2N$ equations for the isothermal case. Thus, the major effort in solving the 1+1D model is due to the washcoat diffusion problem.

If both external and internal gradients are neglected, we obtain the pseudo-homogeneous model, for which the species balances are given by

$$\left(1 + \frac{\epsilon_w \delta_c}{R_\Omega}\right) \frac{\partial \mathbf{X}}{\partial t} + \langle u \rangle \frac{\partial \mathbf{X}}{\partial x} = \frac{\delta_c}{R_\Omega} \frac{1}{C_T} \boldsymbol{\nu}^T \mathbf{r}(\mathbf{X}, T), \quad (2.13)$$

while the energy balance is

$$\left(1 + \frac{\delta_w \rho_w C_{p_w}}{R_\Omega \rho_f C_{p_f}}\right) \frac{\partial T}{\partial t} + \langle u \rangle \frac{\partial T}{\partial x} = \frac{\delta_w k_w}{R_\Omega \rho_f C_{p_f}} \frac{\partial^2 T}{\partial x^2} + \frac{\delta_c}{R_\Omega \rho_f C_{p_f}} \mathbf{r}(\mathbf{X}, T)^T (-\Delta \mathbf{H}), \quad (2.14)$$

with appropriate inlet, initial and boundary conditions. This pseudo-homogeneous model is described by $N + 1$ partial differential equations in x and t for the non-isothermal case. As is well known, this pseudo-homogeneous model can describe the monolith reactor behavior only in the kinetic regime or at low operating temperatures or when cell density is high and washcoat thickness is small.

2.2.2 Two-Mode Form of Reduced-order Model

Balakotaiah [1] and Joshi et al., [2] integrated the species balance Eq. 2.2 over the volume of the washcoat and expressed it in terms of volume averaged mole fraction vector $\langle \mathbf{X}_{wc} \rangle$. This is defined by

$$\langle \mathbf{X}_{wc} \rangle = \frac{1}{\delta_c} \int_0^{\delta_c} \mathbf{X}_{wc}(x, y, t) dy. \quad (2.15)$$

They also introduced the concept of internal mass transfer coefficient so that the interfacial flux vector may be expressed as

$$\frac{\mathbf{j}_{fw}}{C_T} = \mathbf{k}_{me} (\mathbf{X}_{fm} - \mathbf{X}_s) = \mathbf{k}_{mi} (\mathbf{X}_s - \langle \mathbf{X}_{wc} \rangle). \quad (2.16)$$

The above flux continuity equation may be solved for the fluid-washcoat interfacial concentration (mole fraction) vector \mathbf{X}_s explicitly as

$$\mathbf{X}_s = (\mathbf{k}_{me} + \mathbf{k}_{mi})^{-1} (\mathbf{k}_{me} \mathbf{X}_{fm} + \mathbf{k}_{mi} \langle \mathbf{X}_{wc} \rangle). \quad (2.17)$$

Eliminating \mathbf{X}_s , the species balance in the fluid phase may now be written as

$$\frac{\partial \mathbf{X}_{fm}}{\partial t} + \langle u \rangle \frac{\partial \mathbf{X}_{fm}}{\partial x} = -\frac{\mathbf{k}_{mo}}{R\Omega} (\mathbf{X}_{fm} - \langle \mathbf{X}_{wc} \rangle), \quad (2.18)$$

while the volume averaged species balance equation for the washcoat (for gas phase species) becomes

$$\epsilon_w \frac{\partial \langle \mathbf{X}_{wc} \rangle}{\partial t} = \frac{1}{C_T} \boldsymbol{\nu}^T \mathbf{r}(\langle \mathbf{X}_{wc} \rangle) + \frac{\mathbf{k}_{mo}}{\delta_c} (\mathbf{X}_{fm} - \langle \mathbf{X}_{wc} \rangle). \quad (2.19)$$

Here, the overall mass transfer coefficient matrix (\mathbf{k}_{mo}) is given by

$$\mathbf{k}_{mo}^{-1} = \mathbf{k}_{me}^{-1} + \mathbf{k}_{mi}^{-1}, \quad (2.20)$$

where \mathbf{k}_{mi} is the internal mass transfer coefficient matrix, which is defined below:

$$\mathbf{k}_{mi} (\mathbf{X}_s - \langle \mathbf{X}_{wc} \rangle) = -\mathbf{D}_e \left. \frac{\partial \mathbf{X}_{wc}}{\partial y} \right|_{y=0} = \frac{\mathbf{j}_{fw}}{C_T}. \quad (2.21)$$

[Remark: From this definition, it is clear that the determination of \mathbf{k}_{mi} is equivalent to determining the interfacial flux vector \mathbf{j}_{fw} and requires the solution of the washcoat diffusion problem. For further details, please see the Appendix A].

The fluid phase energy balance remains unchanged with averaging over the washcoat volume but the solid phase energy balance becomes

$$\delta_w \rho_w C_p \frac{\partial T_s}{\partial t} = \delta_w k_w \frac{\partial^2 T_s}{\partial x^2} + h (T_f - T_s) + \delta_c \mathbf{r}(\langle \mathbf{X}_{wc} \rangle)^T (-\Delta \mathbf{H}). \quad (2.22)$$

We note that the structure of this averaged model is identical to the standard two-phase model (except that it includes washcoat diffusional effect) and we only need to solve $2N + 2$ partial differential equations in x and t for the non-isothermal case. The initial, inlet and boundary conditions remain the same except for the initial

condition of the washcoat mole fraction vector:

$$\langle \mathbf{X}_{wc} \rangle (x, 0) = \langle \mathbf{X}_{wc}^0(x, y) \rangle. \quad (2.23)$$

Thus, the most appealing feature of this reduced order model with internal (and overall) mass transfer coefficient matrix concept is that it has the same structure as that of the standard two-phase model but accounts for gradients at small scales, i.e. both in the washcoat as well as external mass transfer effect in the channel (as in the traditional two-phase model). The major task now is the computation of the overall mass transfer coefficient matrix \mathbf{k}_{mo} which could be local property (composition, position and time) dependent.

2.2.3 Reduced Order Model with Storage on Catalyst:

The above approach can be extended to include detailed kinetic models that account for adsorption, desorption and reaction between adsorbed species or when one or more catalytic sites can store the reactants. In this case, the balance equation for the gas phase species vector (Eq. 2.18) remains the same, the averaged balance equation for the gas phase species in the washcoat (Eq. 2.19) also remains the same except now $\mathbf{r}(\langle \mathbf{X}_{wc} \rangle)$ is replaced by $\mathbf{r}(\langle \mathbf{X}_{wc} \rangle, \langle \boldsymbol{\theta}_w \rangle)$ where $\langle \boldsymbol{\theta}_w \rangle$ is the washcoat (volume) averaged fractional coverage (or storage) vector for the catalytic sites. The vector $\mathbf{r}(\langle \mathbf{X}_{wc} \rangle, \langle \boldsymbol{\theta}_w \rangle)$ now represents the rate of reaction of the gas phase species within the washcoat volume either by reactions in the washcoat or removal (or addition) of gas phase species to surface species through adsorption and/or desorption. In addition, to complete the reduced order model we also append the washcoat averaged equation for the coverage vector:

$$C_S \frac{\partial \langle \boldsymbol{\theta}_w \rangle}{\partial t} = \mathbf{r}_w(\langle \mathbf{X}_{wc} \rangle, \langle \boldsymbol{\theta}_w \rangle). \quad (2.24)$$

Here, C_S is the total concentration of the catalytic sites and $\mathbf{r}_w(\langle \mathbf{X}_{wc} \rangle, \langle \boldsymbol{\theta}_w \rangle)$ represents the net rate of production of surface species (assuming that the diffusivity of the surface species is zero). Thus, the reduced order model for the isothermal case with N gas phase species and S surface species consists of $(2N + S - 1)$ partial differential equations (using the fact that the sum of all coverage fractions is unity). [For the non-isothermal case, it will be $2N + S + 1$ equations]. The model can also be extended to cases in which there are multiple catalytic or storage sites.

2.2.4 Computation of the Internal and External Mass Transfer Coefficient Matrices

We now discuss various literature approximations for the internal and external mass transfer coefficient matrices in the reduced order models reviewed above.

Asymptotic approximation:

The work of Balakotaiah [1] showed that the internal mass transfer coefficient matrix becomes diagonal in the limit of slow reactions or small gradient in the washcoat. Thus, Joshi et al., [2] approximated the internal mass transfer coefficient using an asymptotic internal Sherwood number $Sh_{i,\infty}$ times the effective diffusivity in the washcoat D_e over the washcoat thickness δ_c as given in Eq. 2.25. The internal asymptotic Sherwood number depends only on the washcoat geometric shape and is tabulated for common washcoat shapes [17]. For long channels, the external mass transfer coefficient can also be approximated using an external asymptotic Sherwood number $Sh_{e,\infty}$ times the fluid phase diffusivity D_f over the channel hydraulic diameter $4R_\Omega$. The external asymptotic Sherwood number depends only on the geometric shape of the flow channel and is tabulated for various standard flow geometries [5]. For example, for a rounded square channel, $Sh_{e,\infty} = 3.2$ and $Sh_{i,\infty} = 2.65$, while for a circular channel with a parabolic velocity and thin washcoat, $Sh_{e,\infty} = 4.36$ and $Sh_{i,\infty} = 3.0$. Thus, in the simplest approximation both the internal and the external mass transfer coefficient matrices are

assumed to be diagonal with diagonal elements given by

$$k_{mi,j} = \frac{D_{e,j}Sh_{i,\infty}}{\delta_c}, \quad k_{me,j} = \frac{D_{f,j}Sh_{e,\infty}}{4R_\Omega}. \quad (2.25)$$

In this case, the overall mass transfer coefficient matrix is also diagonal with diagonal elements given by

$$\frac{1}{k_{mo,j}} = \frac{1}{k_{me,j}} + \frac{1}{k_{mi,j}}. \quad (2.26)$$

The simulations of Joshi et al., [2] and Kumar et al., ([3], [9]) showed that while the use of asymptotic internal and external transfer coefficients was adequate for many applications, especially those involving cold-start transient simulations of various after-treatment systems when the washcoat Thiele moduli are small (thin washcoat and/or low temperature), it was inadequate or may have significant error for describing ignited (and/or high temperature) branches on which strong washcoat diffusional limitations may exist.

Diagonal approximation with position dependent transfer coefficients:

While position (and local property) dependent external transfer coefficients were discussed by several authors in the literature, they were combined with local property dependent internal mass transfer coefficients by Kumar et al., [3] to simulate monolith reactor steady-state and transient behavior using reduced order models. In this approach, the external Sherwood matrix is assumed to be diagonal with each diagonal element taken to be a function of the Schmidt number and local position or the Graetz number $\frac{P_j}{z}$, where $z = x/L$ is the dimensionless axial position and P_j is the transverse mass Péclet number defined by

$$P_j = \frac{R_\Omega^2 \langle u \rangle}{LD_{f,j}}, \quad (2.27)$$

where $\langle u \rangle$ and $D_{f,j}$ are the average gas velocity and gas phase diffusivity of species j , respectively. Expressions for the external Sherwood numbers for fully developed or simultaneously developing flow with constant flux boundary condition were given by Gundlapally and Balakotaiah [5]. The internal Sherwood number is also assumed to be diagonal and depending only on the diagonal elements of the local Thiele matrix (Φ^2), where the j -th Thiele modulus Φ_j^2 is computed using the net rate of (consumption of) each species $R_j(\mathbf{X})$ evaluated at \mathbf{X}_{fm} . Thus, in this approach k_{mo} , k_{me} and k_{mi} are diagonal and the j^{th} diagonal element of k_{mo} is defined by Eqs. 2.28 to 2.32:

$$\frac{1}{k_{mo,j}} = \frac{1}{k_{me,j}} + \frac{1}{k_{mi,j}}, \quad (2.28)$$

$$k_{mi,j} = \frac{D_{e,j} Sh_{i,j}}{\delta_c}, \quad k_{me,j} = \frac{D_{f,j} Sh_{e,j}}{4R_\Omega}, \quad (2.29)$$

$$Sh_{i,j} = Sh_{i,\infty} + (1 + \Lambda \Phi_j)^{-1} \Lambda \Phi_j^2, \quad (2.30)$$

$$\Phi_j^2 = \frac{\delta_c^2}{D_{e,j}} k_{j,eff} \quad (2.31)$$

$$\text{and } k_{j,eff} = -\frac{1}{C_T} \frac{R_j(\mathbf{X})}{X_j} \Big|_{X=X_{wc,j}} ; \quad R_j(\mathbf{X}) = \sum_{i=1}^{Nr} \nu_{ij} r_i(\mathbf{X}). \quad (2.32)$$

The parameters $Sh_{i,\infty}$ and Λ depend only on the geometric shape of the washcoat and have been tabulated by Joshi et al. [17] for some common washcoat shapes. The external Sherwood number for the case of fully developed flow in a channel is given by [5]

$$Sh_{e,j} = Sh_{H_2,\infty} + \frac{0.108(fRe)^{1/3} \left(\frac{P_j}{z}\right)}{1 + 0.083 \left(\frac{P_j}{z}\right)^{2/3}} ; \quad P_j = \frac{R_\Omega^2 \langle u \rangle}{LD_{f,j}} ; \quad z = \frac{x}{L}, \quad (2.33)$$

where fRe is the friction factor times Reynolds number for the flow channel (with fully developed laminar flow). Similarly, for simultaneously developing flow,

$$Sh_{e,j} = Sh_{H_2,\infty} + \frac{0.98Sc_j^{-1/6}(\frac{P_j}{z})}{1 + 0.512(\frac{P_j}{z})^{1/2}}; \quad Sc_j = \frac{\nu}{D_{f,j}}, \quad (2.34)$$

where Sc_j is the Schmidt number for species j . To simulate the non-isothermal case, the above expressions have to be combined with the local (position dependent) heat transfer coefficient h , which is computed using the Nusselt number (Nu) correlation as

$$h = \frac{Nu(z)k_f}{4R_\Omega}. \quad (2.35)$$

Similar to the calculation of the Sherwood number, we use a position dependent Nusselt number (Nu) [5]

$$Nu(z) = Nu_{H_2,\infty} + \frac{0.108(fRe)^{1/3}(\frac{P_h}{z})}{1 + 0.083(\frac{P_h}{z})^{2/3}}; \quad P_h = \frac{R_\Omega^2 \langle u \rangle}{L\alpha_f}, \quad (2.36)$$

for fully developed laminar flow in the channel [Here, α_f is the effective thermal diffusivity of the fluid]. For simultaneously developing flow, we have [5]

$$Nu(z) = Nu_{H_2,\infty} + \frac{0.98Pr^{-1/6}(\frac{P_h}{z})}{1 + 0.512(\frac{P_h}{z})^{1/2}}, \quad Pr = \frac{\nu}{\alpha_f}, \quad (2.37)$$

where Pr is the Prandtl number.

The diagonal approximation for the internal Sherwood matrix Sh_i combined with position (or local property) dependent diagonal external transfer coefficients has been used in the past few years for modeling several after-treatment systems. As already mentioned, Kumar et al., (2014) used it to model the experimental data from a TWC and found it to have sufficient accuracy. They also compared the solutions obtained with the diagonal approximation with the 1+1D model and found good agreement except for the case of high cycling frequency of the inputs. More recently, Daneshvar et al., (2017) used it to model the DOC with five oxidation reactions and found good agreement with experimental results and more detailed

model. Ting et al., (2019) used it for a 32 reaction scheme of a Lean NO_x Trap (LNT) with fast cycling to explain all the observed experimental trends. As mentioned in the introduction, the solution of the full 1+1D model with detailed reaction schemes (e.g., 50 or more global reactions and/or micro-kinetics) and verification of the grid independence of the solution could be very difficult when simulating monolith reactors over a wide temperature range. It is exactly in such cases, the asymptotic and diagonal approximations make the simulations possible in real time. However, their accuracy cannot be assessed without comparison to the solution of the full 1+1D model].

The main criticism of the diagonal approximation is that it was mostly tested for uncoupled parallel oxidation reactions which are irreversible for all practical purposes. It may not be a good approximation when there is strong coupling among competing oxidations or in the presence of reversible reactions, exo or endothermic. Further, the diagonal elements of Φ^2 have to be positive numbers for calculation of the internal mass transfer coefficients, and if they are not, Sh_i will become complex and this approach breaks down. The proposed modification discussed in the next section remedies this defect of the diagonal approximation (at the expense of slightly increased computation time). [Remark: *Eqs.* 2.30 to 2.32 assume that all Φ_j^2 are positive numbers but this may not be the case in many applications].

2.3 The Thiele matrix approach for the internal mass transfer coefficient matrix

As explained in the previous section, the external mass transfer coefficient matrix can be approximated by a diagonal matrix in most after-treatment systems (in the absence of any homogeneous reactions). However, the internal mass transfer coefficient matrix, in general, is a non-diagonal matrix. This brings to the main idea of the proposed method in this work for approximating the washcoat diffusional effects. This method is based on the exact solution of the washcoat diffusion problem

for the case of linear kinetics for which the effectiveness matrix as well as the internal mass transfer coefficient matrix can be determined exactly [1]. We note that k_{mi} is non-diagonal even when the D_e is diagonal because the matrix of first order rate constants \mathbf{K} is not diagonal. Thus, instead of using the diagonal approximation for \mathbf{Sh}_i (or k_{mi}), we use a full calculated matrix for the internal Sherwood matrix and also take advantage of the fact that it is an even function of the (non-diagonal) Thiele matrix Φ . Thus, in our approach, the eigenvalues of Φ^2 can be positive or negative or complex, and the fact that Φ^2 is a matrix of real numbers and \mathbf{Sh}_i is an even function of Φ eliminates the problem of dealing with complex values for the mass transfer coefficients (Please see Appendix A for details). Further, to deal with nonlinear kinetics, we linearize the washcoat reaction-diffusion problem at the local fluid phase concentration (or interfacial or volume averaged washcoat concentration) so that the effective first-order rate constant matrix is the Jacobian matrix of the rate vector evaluated at these local conditions. For example, if the Jacobian of the rate vector is evaluated at the interfacial conditions \mathbf{X}_s , we have

$$\Phi^2 = \delta_c^2 (\mathbf{D}_e)^{-1} \left(-\frac{1}{C_T} \frac{d(\mathbf{R}(\mathbf{X}))}{d\mathbf{X}} \right)_{\mathbf{x}=\mathbf{X}_s}, \quad (2.38)$$

where $\mathbf{R}(\mathbf{X}) = \nu^T \mathbf{r}(\mathbf{X})$ is the net rate vector, where each element $R_j(\mathbf{X})$ represents the net rate of formation of the j^{th} species. The expressions for the overall mass transfer coefficient matrix and the external mass transfer matrix remain the same but the internal mass transfer matrix is now given by [1]

$$\mathbf{k}_{mi} = \frac{1}{\delta_c} \mathbf{D}_e \cdot \mathbf{Sh}_i \quad (2.39)$$

$$\text{and } \mathbf{Sh}_i = \left[(\Phi \tanh \Phi)^{-1} - (\Phi^2)^{-1} \right]^{-1}. \quad (2.40)$$

[For a derivation of these and related expressions, see [1] and also the Appendix A]. For computational simplification, the full Thiele matrix defined in Eq. 2.38 can

be evaluated either at \mathbf{X}_{fm} or $\langle \mathbf{X}_{wc} \rangle$, which are the variables appearing in the reduced order model. It should be pointed out that this approach has also some limitations, especially when the steady-state diffusion-reaction problem in the wash-coat has multiple solutions. This occurs when an eigenvalue of Φ^2 changes sign, and in this case multiple values (solutions) are possible for \mathbf{Sh}_i . This situation could occur for strongly nonlinear and reactant or product inhibited kinetics (such as CO oxidation on Pt/Al_2O_3 at high CO concentrations). However, this is not an issue for transient simulations as in this case we are solving an initial value problem (after discretization in the spatial coordinate x) that always has a unique solution. We refer to the articles by Kumar et al. [3] and Joshi et al., [2] for further discussion on this topic.

The numerical calculation of \mathbf{Sh}_i (or \mathbf{k}_{mi}) from Φ^2 may lead to some difficulties, when Φ^2 has several zero eigenvalues (due to existence of stoichiometric invariants when the number of species is larger than the number of reactions) and/or for low temperatures at which many eigenvalues of Φ^2 can be very small in magnitude as the effective rate constants (or reaction rates) are very small. In fact, we have found that the existing codes (in MATLAB, Mathematica, etc.) for computing functions of a matrix are not useful or accurate when the matrix has multiple zero and/or small eigenvalues (typically smaller than 10^{-5}). In such cases, we have used the Cayley-Hamilton theorem for computing \mathbf{Sh}_i from Φ^2 . To illustrate this, we first note that if we define

$$f(x) = \left(\frac{1}{\sqrt{x} \tanh[\sqrt{x}]} - \frac{1}{x} \right)^{-1}. \quad (2.41)$$

Taylor series expansion of this function at the base point $x = 0$ leads to

$$f(x) \approx 3 + \frac{x}{5} - \frac{x^2}{175} + \frac{2}{7875}x^3 + \dots \quad (2.42)$$

This expression may be used to approximate $f(x)$ to better than three decimal accuracy for x values below unity. Thus, if all the eigenvalues of Φ^2 are smaller than unity in absolute value (or modulus for complex eigenvalues), we can compute \mathbf{Sh}_i from the expression

$$\mathbf{Sh}_i \approx 3\mathbf{I} + \frac{1}{5}\Phi^2 - \frac{1}{175}\Phi^4 + \frac{2}{7875}\Phi^6. \quad (2.43)$$

[Remark: The above expression reduces to the asymptotic approximation if we use only the first term]. For the case in which Φ^2 has eigenvalues that are much larger than unity in absolute value (which is the case when washcoat diffusion becomes important or the main controlling factor or some characteristic reaction times are very small compared to diffusion time), we replace the function $f(x)$ by another even function (in \sqrt{x}) that is also an excellent approximation, namely

$$g(x) = 3 + \sqrt{x} \tanh\left[\frac{1}{5}\sqrt{x}\right]. \quad (2.44)$$

[Remark: It can be verified that $f(x)$ and $g(x)$ agree to order x in their Taylor series expansion, and also approach \sqrt{x} for large x . By plotting $f(x)$ and $g(x)$, it may be seen that $g(x)$ is a very good approximation to $f(x)$, and is even in \sqrt{x} as is $f(x)$, for all values of $x \geq 0$]. Now, the Cayley-Hamilton theorem, spectral theorem or any other algorithm for calculating the function of a matrix can be employed as $g(x)$ is even (in \sqrt{x}) and the numerical problems associated with small as well as negative or complex eigenvalues of Φ^2 disappear [please see the Appendix A for details and numerical examples]. Thus,

$$\mathbf{Sh}_i = \left[(\Phi \tanh \Phi)^{-1} - (\Phi^2)^{-1} \right]^{-1} \quad (2.45)$$

$$\text{and } \approx 3\mathbf{I} + \Phi \tanh\left[\frac{1}{5}\Phi\right]. \quad (2.46)$$

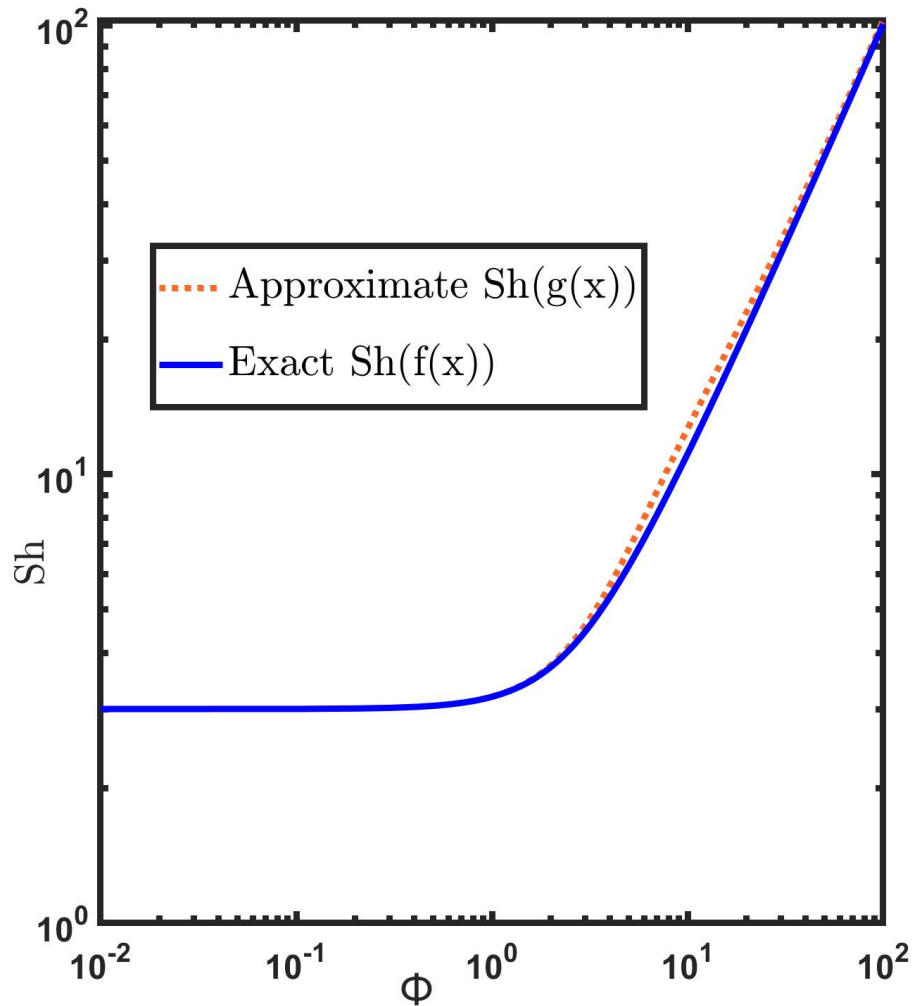


Figure 2.1: Comparison between exact Sherwood number and approximate Sherwood number

Fig. 2.1 shows the comparison between the exact formula and approximate formula for Sherwood number, red dotted line which is the approximate Sherwood number can be seen is a perfect approximation to the blue solid line which is the exact Sherwood number. As a simple illustrative example, we consider the case in which $\mathbf{A} = \Phi^2$ is a 3×3 matrix with two zero (or very small) eigenvalues ($\lambda_1 \approx \lambda_2 \approx 0$) and one non-zero (or large) eigenvalue ($\lambda_3 \neq 0$). In this case, it follows

from the Cayley-Hamilton theorem, the exact Sherwood matrix is given by

$$\mathbf{Sh}_i = \sum_{i=1}^3 c_i \mathbf{A}^{i-1} = c_1 \mathbf{I} + c_2 \mathbf{\Phi}^2 + c_3 \mathbf{\Phi}^4 \quad (2.47)$$

$$\text{and } c_1 = 3, c_2 = \frac{1}{5}, c_3 = \frac{g(\lambda_3) - c_1 - c_2 \lambda_3}{\lambda_3^2} \text{ or } c_3 = \frac{f(\lambda_3) - c_1 - c_2 \lambda_3}{\lambda_3^2}. \quad (2.48)$$

When $\mathbf{\Phi}^2$ is a 3×3 matrix with three zero (or very small) eigenvalues, we have

$$c_1 = f(0) = 3; c_2 = \frac{1}{5}; c_3 = -\frac{1}{175}.$$

In the general case in which $\mathbf{\Phi}^2$ is a $N \times N$ matrix and all eigenvalues of $\mathbf{\Phi}^2$ are of the same order of magnitude and large, the computation of \mathbf{Sh}_i involves determining the eigenvalues of $\mathbf{\Phi}^2$ and solving N linear algebraic equations for the coefficients c_i . Thus, the amount of additional work involved in using the Thiele matrix approach is justified compared to the accuracy gained, and much less than that required to solve the full washcoat diffusion problem as illustrated with examples in the next section. [See also the Appendix A for calculation of \mathbf{Sh}_i from $\mathbf{\Phi}^2$ for further illustration and examples].

We close this chapter by noting that the above formulas for computing the internal mass transfer coefficients can be extended easily to other washcoat shapes. In the general case, we write

$$\mathbf{Sh}_i = Sh_{i\infty} \mathbf{I} + \mathbf{\Phi} \tanh[\Lambda^* \mathbf{\Phi}], \quad (2.49)$$

where $\mathbf{\Phi}^2$ is the square of the shape normalized Thiele matrix. The two constants $Sh_{i\infty}$ and Λ^* that characterize the washcoat can be evaluated using the procedure of Joshi et al., [17]. These constants are listed in the Appendix A for some common washcoat geometric shapes. [Remarks: The parameters $Sh_{i\infty}$ and Λ^* are only functions of the washcoat shape or geometry, and $Sh_{i\infty}$ is the same as that

tabulated by Joshi et al., [17], while Λ^* is different. Both are empirical parameters that lead to a good fit of the Sh_i versus Φ curve near Φ values of order unity. The main difference between *Eq.* 2.30 and (the scalar version of) *Eq.* 2.49 is that the former is not an even function of Φ , which creates numerical difficulties cited above].

In this chapter, we presented a novel reduced order model with local property dependent internal and external mass transfer coefficients for real time simulations of monolith reactors. In the next chapter we compare the accuracy of the present approach with other reduced order models in the literature and with exact (numerical) solution of the detailed washcoat diffusion model and illustrate the application of the reduced order models to three-way catalytic converter using three different examples.

Chapter 3

Comparison of accuracy of various reduced order models in a single layered monolith reactor

3.1 Comparison of accuracy of various reduced order models in a single layered monolith reactor

In this chapter, we provide examples illustrating the Thiele matrix approach for treating the washcoat diffusion problem. We also compare the accuracy of the proposed method with those in the literature and also with exact (numerical) solution of the full washcoat diffusion model. In all the examples of this section, we assume that the reacting gases are diluted in nitrogen, the gas phase diffusivity matrix, $\mathbf{D}_f \in \mathbb{R}^{N \times N}$ is a diagonal matrix with the j^{th} diagonal element $D_{f,j}$ representing the diffusivity of the j^{th} species in nitrogen. To compute the diffusivity as a function of temperature, we calculated binary diffusion coefficients by using the Fuller correlation based on species atomic diffusion volumes [18] and varying with the temperature as $T^{1.75}$. The effective diffusivity of each species in the washcoat is computed by assuming Knudsen diffusion regime prevails in the washcoat. Hence, the washcoat effective diffusivity matrix (\mathbf{D}_e) is a diagonal matrix with the diagonal elements ($D_{e,j}$) representing diffusivity of the j^{th} species,

$$D_{e,j} = \frac{\epsilon_w}{\tau_c} 97a \sqrt{\frac{T_s}{M_j}}, \quad (3.1)$$

where M_j is the molecular mass of the j^{th} species, ϵ_w is the washcoat porosity, τ_c is the tortuosity and a is the mean pore radius (in meters, and $D_{e,j}$ is in units of $\text{m}^2 \cdot \text{s}^{-1}$). Effective diffusivities for examples one and two were computed by using Eq. 3.1. In example two, the molecular mass of the reductant is taken as 28 $\text{g} \cdot \text{mol}^{-1}$ while that for the oxidant is 32 $\text{g} \cdot \text{mol}^{-1}$. In example 3, equal and constant

D_e is used for all species with $D_e = 10^{-7} \text{ m}^2 \cdot \text{s}^{-1}$. The values of various other parameters used in the simulations are listed in *Table 3.1*:

Table 3.1: Numerical constants and parameters used in model simulation

Constant	Value
a	$10 \times 10^{-9} \text{ m}$
R_Ω	$181 \times 10^{-6} \text{ m}$
δ_c	$30 \times 10^{-6} \text{ m}$
R_{Ω_large}	$300 \times 10^{-6} \text{ m}$
δ_{c_thin}	$15 \times 10^{-6} \text{ m}$
δ_w	$63.5 \times 10^{-6} \text{ m}$
L	$7.85 \times 10^{-2} \text{ m}$
k_f	$0.0386 \text{ W} \cdot \text{m}^{-1} \cdot \text{K}^{-1}$
k_w	$1.5 \text{ W} \cdot \text{m}^{-1} \cdot \text{K}^{-1}$
Cp_f	$1068 \text{ J} \cdot \text{kg}^{-1} \cdot \text{K}^{-1}$
Cp_w	$1000 \text{ J} \cdot \text{kg}^{-1} \cdot \text{K}^{-1}$
ρ_w	$2000 \text{ kg} \cdot \text{m}^{-3}$
ϵ_w	0.41
τ_c	8
$Sh_{e,\infty}$	3.2
$Nu_{e,\infty}$	3.2
$Sh_{i,\infty}$	3
Λ	0.32

Rate Expressions Used in Examples:

For completeness, we list below the empirical rate expressions used in examples 1 and 2 in *Tables 3.2 to 3.5*. In these expressions, the rates are based on washcoat volume, i.e., having units of $\text{moles}/(\text{m}^3 \text{wc} \cdot \text{s})$:

3.1.1 Example 1: Four reactions model of a TWC

The first example we consider is the four reaction model of a three-way converter (TWC), which is same as that used by Joshi et al., (2009) to illustrate the usefulness of reduced order models for real time simulations. The reactions used

Table 3.2: Reactions that are applied in Joshi's model for the real time simulation of a TWC

No.	Reaction	Reaction rate (mol·m ⁻³ ·s ⁻¹)	-ΔH (kJ/mol)
1	$CO + 0.5O_2 \longrightarrow CO_2$	$r_1 = \frac{A_1 \exp(\frac{-E_1}{RT}) X_{O_2} X_{CO}}{G}$	283
2	$H_2 + 0.5O_2 \longrightarrow H_2O$	$r_2 = \frac{A_2 \exp(\frac{-E_2}{RT}) X_{O_2} X_{H_2}}{G}$	242
3	$C_3H_6 + 4.5O_2 \longrightarrow 3CO_2 + 3H_2O$	$r_3 = \frac{A_3 \exp(\frac{-E_3}{RT}) X_{O_2} X_{C_3H_6}}{G}$	1926
4	$NO + CO \longrightarrow CO_2 + 0.5N_2$	$r_4 = A_4 \exp(\frac{-E_4}{RT}) X_{NO} X_{CO}$	373
$G = T_s (1 + K_{a1} X_{CO} + K_{a1} X_{HC})^2 (1 + K_{a3} X_{CO}^2 X_{HC}^2) (1 + K_{a4} X_{NO}^{0.7})$			
$K_{ai} = A_{ai} \exp(\frac{-E_{ai}}{RT})$			

Table 3.3: Kinetic parameters for example1

No.	A_i (mol·m ⁻³ ·s ⁻¹ ·K)	E_i (kJ·mol ⁻¹)	A_{ai} (mol·m ⁻³ ·s ⁻¹ ·K)	E_{ai} (J/mol)
1	1×10^{19}	10.825	65.5	-961
2	1×10^{19}	10.825	2080	-361
3	2×10^{19}	11.427	3.98	-11611
4	4×10^{14}	10.825	4.79×10^5	3733

Table 3.4: Reactions that are applied in Kumar's model for the oxygen storage and release of a TWC

No.	Reaction	Reaction rate (mol·m ⁻³ ·s ⁻¹)	-ΔH (kJ/mol)
1	$A + 0.5O_2 \longrightarrow AO$	$r_1 = a_c \frac{A_1 \exp(\frac{-E_1}{RT}) X_{O_2} X_A}{T_s (1 + K_{a1} X_A)^2}$	283
2	$Ce_2O_3 + 0.5O_2 \longrightarrow Ce_2O_4$	$r_2 = a_c A_2 \exp(\frac{-E_2}{RT}) X_{O_2} (1 - \theta) TOSC_{green}$	100
3	$A + Ce_2O_4 \longrightarrow Ce_2O_3 + AO$	$r_3 = a_c A_3 \exp(\frac{-E_3}{RT}) X_A \theta TOSC_{green}$	183

Table 3.5: Kinetic parameters for example2

No.	Reaction	A_i	E_i (kJ/mol)
1	$A + 0.5O_2 \longrightarrow AO$	9.8×10^{18}	mol·m ⁻³ ·s ⁻¹ ·K
2	$Ce_2O_3 + 0.5O_2 \longrightarrow Ce_2O_4$	9.2×10^{13}	s ⁻¹
3	$A + Ce_2O_4 \longrightarrow Ce_2O_3 + AO$	1.8×10^7	s ⁻¹
Adsorption constant		A_{a1}	E_a (kJ/mol)
$K_{a1} = A_{a1} \exp(-E_a/RT)$		65.5	-7.99
$TOSC_{green} = 200 \text{ mol} \cdot \text{m}^{-3} \text{ washcoat}$			

Table 3.6: Reaction scheme used in example 1

No.	Reaction
1	$CO + 0.5O_2 \longrightarrow CO_2$
2	$C_3H_6 + 4.5O_2 \longrightarrow 3CO_2 + 3H_2O$
3	$NO + CO \longrightarrow CO_2 + 0.5N_2$
4	$H_2 + 0.5O_2 \longrightarrow H_2O$

Table 3.7: Simulation conditions for example 1

Variable	Concentrated Inlet	Diluted Inlet
$\langle u \rangle$	$2 \text{ m} \cdot \text{s}^{-1}$	$2 \text{ m} \cdot \text{s}^{-1}$
T_f^0	300 K	300 K
T_s^0	300 K	300 K
$X_{f,CO}^{in}$	1%	400 ppm
X_{f,O_2}^{in}	0.85%	1%
$X_{f,HC}^{in}$	500 ppm	12 ppm
X_{f,H_2}^{in}	0.3%	133 ppm
$X_{f,NO}^{in}$	300 ppm	200 ppm
T_f^{in}	540 K	540 K

are listed in *Table 3.6*. [The rate expressions and kinetic constants may be found in the cited references or Appendix A].

As explained earlier, the gas phase diffusivities (in units of $\text{m}^2 \cdot \text{s}^{-1}$ and T_f in K) are computed using the following equations:

$$D_{f,j} = a_j \times 10^{-10} \times T_f^{1.75} \text{ [m}^2 \cdot \text{s}^{-1}\text{]},$$

$$\text{and } a_{CO} = 9.56, a_{C_3H_6} = 5.56, a_{NO} = 8.78, a_{H_2} = 44.5, a_{O_2} = 9.55. \quad (3.2)$$

Results:

Shown in *Fig. 3.1* (a) and (b) are the comparisons between the detailed (1+1D) model and the 1-D model using the asymptotic approximation for CO exit concentration versus time. [Remark: Unless specified otherwise, 10 interior mesh points were used in the simulation of the 1+1D model. This number of mesh points is sufficient only if the largest eigenvalue of the matrix Φ^2 is less than 100 in absolute value. Otherwise, more mesh points, approximately equal to the square

root of the largest eigenvalue in modulus of Φ^2 are needed. This was checked in the numerical calculations]. To highlight the differences between the different models, we plot the dimensionless exit mole fraction Y_{CO} instead of the conversion (which approaches unity at higher times or temperatures). We also use semilogarithmic coordinate for the exit concentration of CO. In case (a), $\delta_c = 15 \mu\text{m}$ and $R_\Omega = 300 \mu\text{m}$, in case (b), $\delta_c = 30 \mu\text{m}$ and $R_\Omega = 181 \mu\text{m}$. For other cases including examples 2 and 3, we use $\delta_c = 30 \mu\text{m}$ and $R_\Omega = 181 \mu\text{m}$ in the simulations. Other constant parameter values used are listed in *Tables* 3.1 and 3.7. The solid (green) and dotted (blue) curves in (a) and (b) represent the results of the 1+1 D model. The dashed (red) and dash-dotted (black) curves show the results of the reduced order model with asymptotic approximation for the internal Sherwood number. The asymptotic approximation works as good as the detailed model when washcoat thickness is $15 \mu\text{m}$ because with a thin washcoat layer, the Thiele moduli are either less than unity or do not exceed values corresponding to the (small gradient) asymptote. However, when we double the washcoat thickness and reduce the channel hydraulic radius, the asymptotic approximation shows large error, the reason is that with a very thin washcoat and larger hydraulic diameter, reactions go from kinetic control to external mass transfer control, as the washcoat diffusion controlled regime is very small in duration (or in temperature) or non-existent. When the washcoat thickness increases, the reactions go through kinetic control, washcoat diffusion control, and to external mass transfer control. In this case, if the description of the washcoat diffusion controlled regime is not accurate, the asymptotic approximation leads to significant error at large times or higher temperatures. [Remark: We note that for the case of thicker washcoat, the predicted exit concentration is off by an order of magnitude if washcoat diffusion is completely ignored, i.e., taking $k_{mi} = \infty$].

Fig. 3.2 (a) and (b) show comparisons of the dimensionless exit concentration

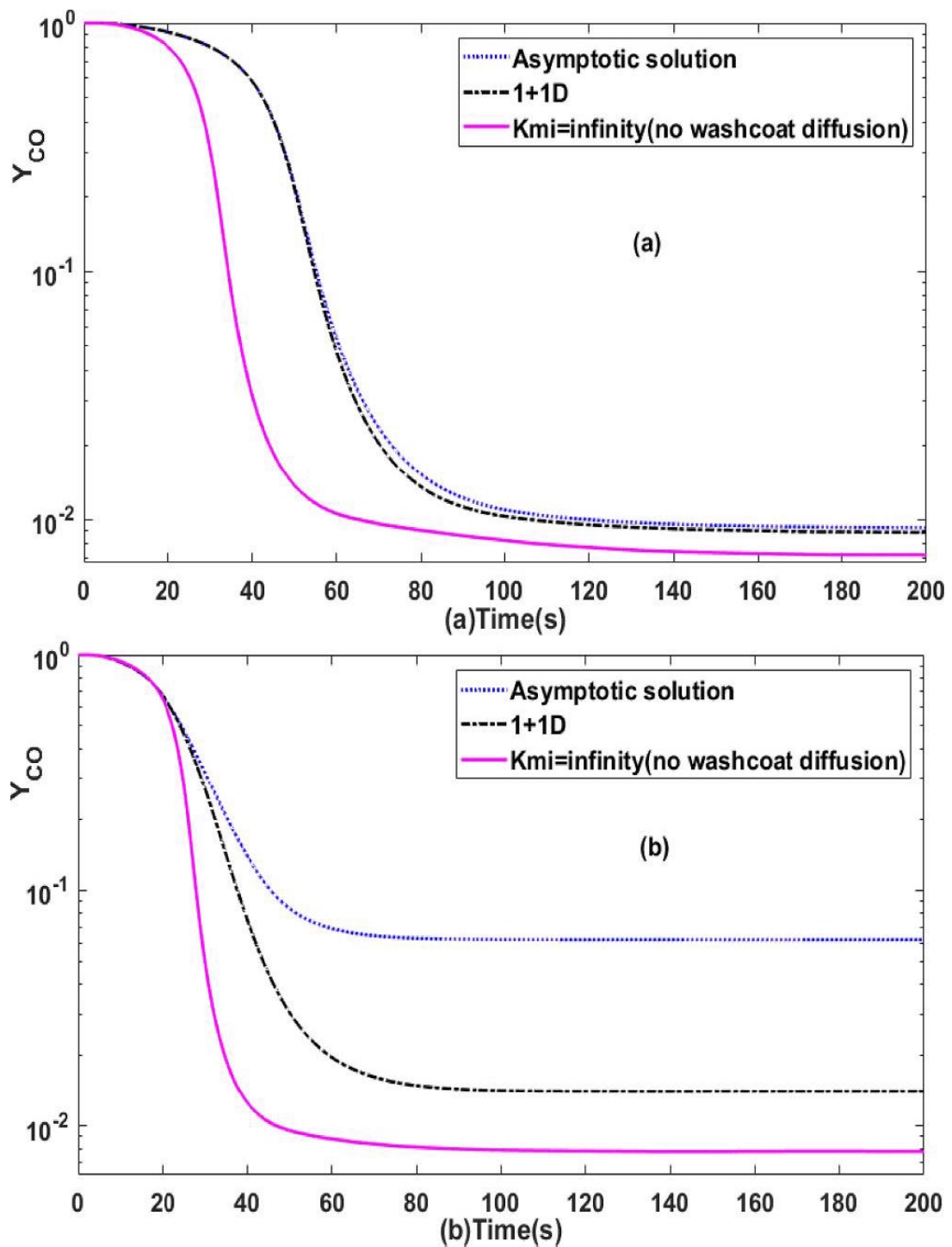


Figure 3.1: Computed dimensionless CO exit concentration versus time for a four reaction TWC model with (a) thin washcoat (b) thick washcoat

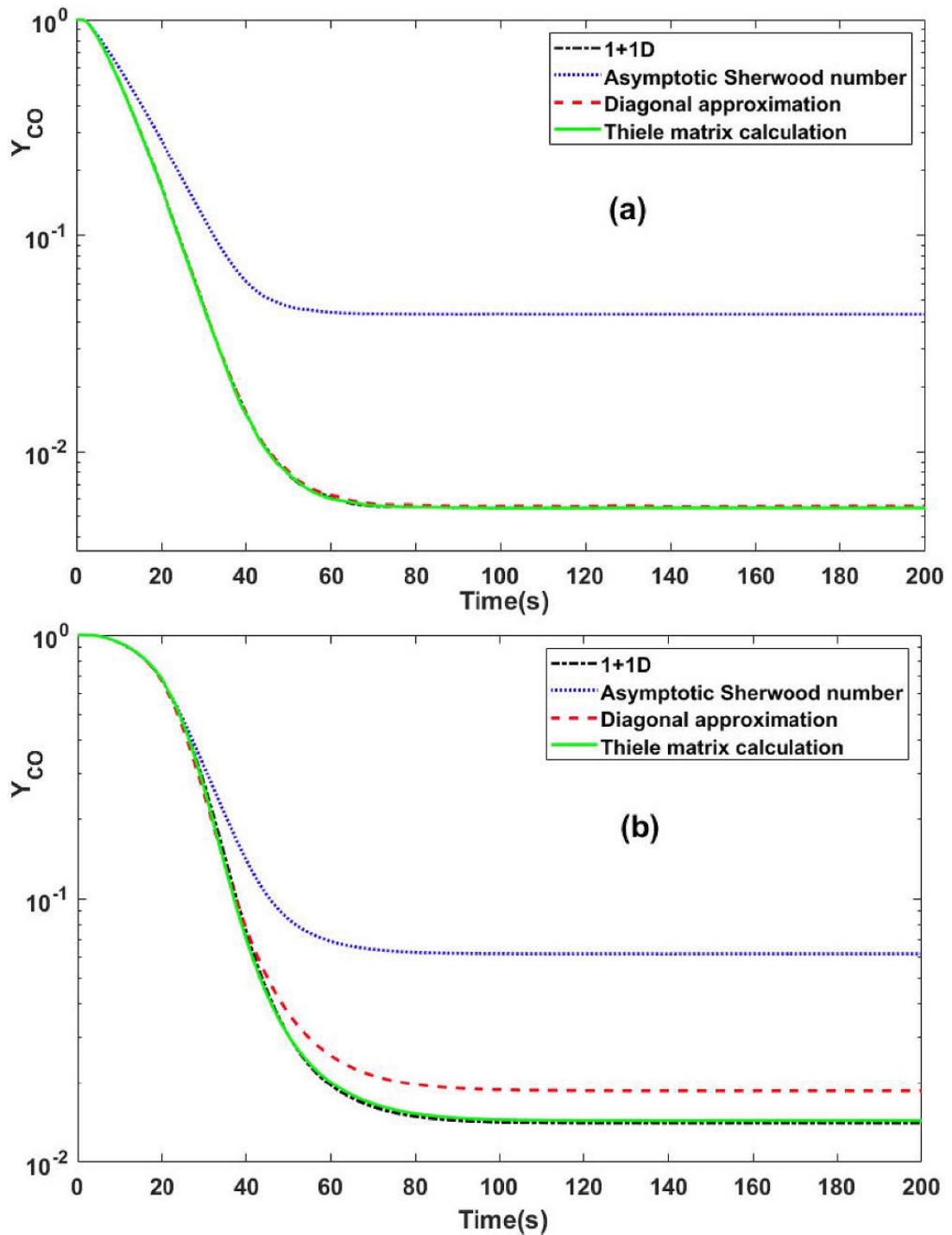


Figure 3.2: Computed dimensionless CO exit concentration versus time for a four reaction TWC model with (a) diluted inlet condition (b) concentrated inlet condition

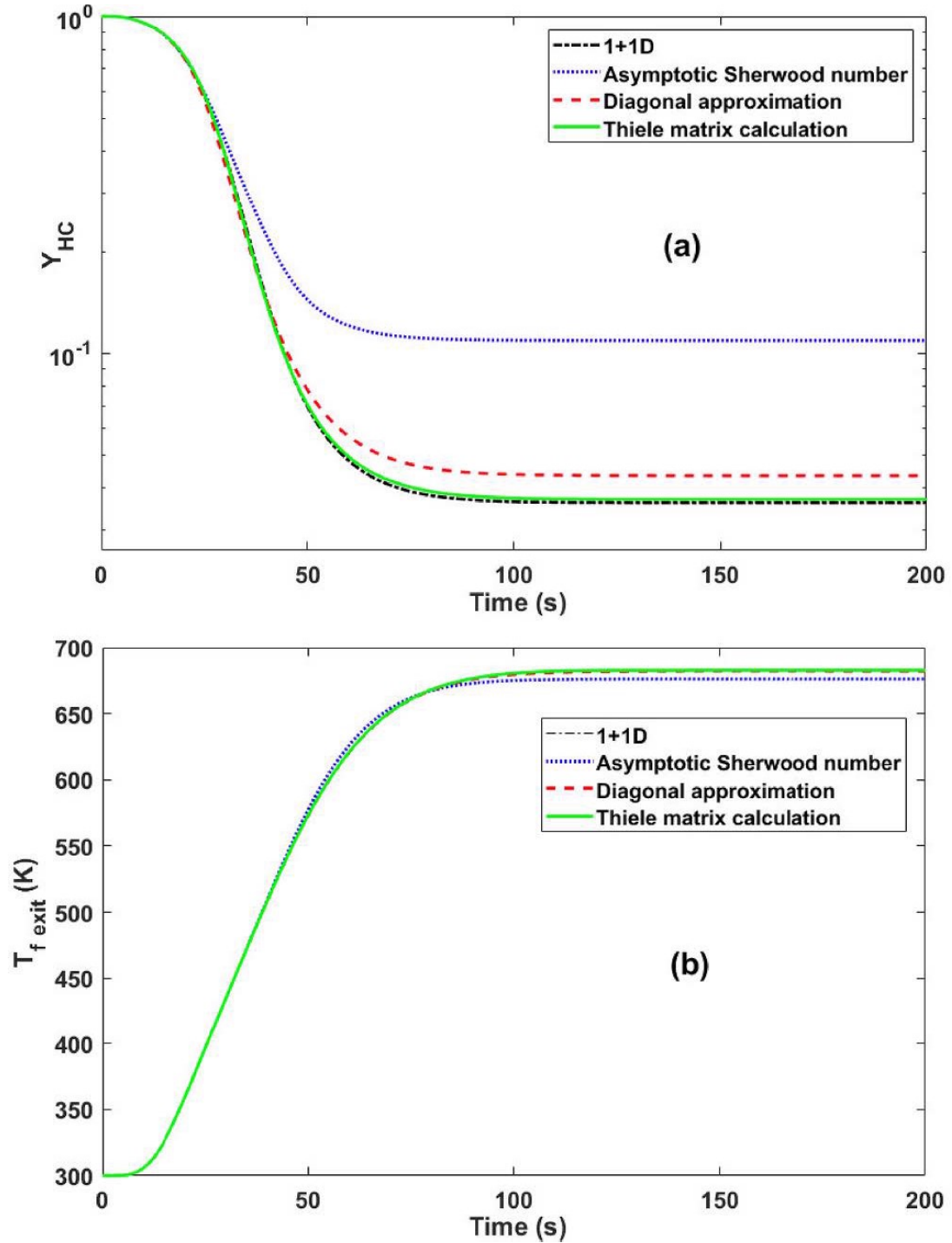


Figure 3.3: (a) Computed dimensionless HC exit concentration predicted by various approximations with concentrated inlet condition (b) Comparison of exit fluid temperature versus time with concentrated inlet condition

of CO predicted by various reduced order models and the detailed model with diluted inlet and concentrated inlet conditions, respectively. The inlet conditions used are shown in *Table 3.7*. The dotted (blue) curve represents the result predicted by reduced-order model using asymptotic approximation, while dashed (red) curve and solid (green) curve denote the reduced-order model results using diagonal approximation and full calculated Thiele matrix, respectively. The dash-dotted (black) curve shows the detailed (1+1D) model prediction. For diluted inlet condition, where the nonlinearities of reaction kinetics are weak, all these approximations are good except asymptotic approximation because a $30\ \mu\text{m}$ thick washcoat layer is used in this case. In concentrated inlet case, we have strong non-linear kinetics (and stronger coupling between the reactions), deviations among these approximations become more significant, the asymptotic approximation is not good again, the diagonal approximation performs not as good as in the diluted inlet case, only the full Thiele matrix calculation which uses a local concentration dependent Jacobian matrix predicts the exit concentration accurately. Similar results are observed for exit HC concentration and temperature profile as shown in *Fig. 3.3*. Since the external mass transfer coefficients are the same among these approximations, the error is mainly from the approximation of internal mass transfer coefficients. The diagonal approximation does not predict well due to the fact that with multiple and strongly coupled reactions, some off-diagonal elements of the Thiele matrix are either comparable or exceed the diagonal elements and hence they cannot be ignored. As mentioned before, this is one of the main limitations of the diagonal approximation [See Appendix A for numerical values and further details].

The computation time for each solution on a desktop computer is: 1+1D model: 2279 s, Thiele matrix calculation: 23 s, Diagonal approximation : 3.2 s and the asymptotic approximation: 2.0 s. Thus, for this simple four reaction case, the Thiele matrix approach is about a hundred times faster than the calculation that

uses the detailed washcoat diffusion solution. We also note that the Thiele matrix solution is also about ten times faster than real time.

3.1.2 Example 2: TWC Model with Oxygen Storage and Release

As our second example, we consider the case of oxygen storage and release reactions of a three-way catalytic converter shown in *Table 3.8*. The constant parameter values used in the simulations are listed in *Table 3.1*. Here, species A is the lumped reductant (which is a weighted combination of CO , H_2 and HC) and O_2 is the lumped oxidant (weighted combination of O_2 and NO). In this example, we take $D_{f,A} = D_{f,O_2} = 9.56 \times 10^{-10} \times T_f^{1.75} [\text{m}^2 \cdot \text{s}^{-1}]$. This is the same example used by Kumar et al., ([3], [9]) in their study of the spatio-temporal dynamics of oxygen storage and release in a TWC. The main difference between this and the previous example is that the model used here involves two gaseous species and accounts for the oxygen storage capacity of the catalyst. It consists of seven PDEs: two species balances for each gas phase reactants, two energy balance equations and a catalyst (storage) site balance equation for oxidation state of ceria given by

$$\theta = \frac{[Ce_2O_4]}{[Ce_2O_4] + [Ce_2O_3]} \quad (3.3)$$

$$\text{and } \frac{\partial \theta}{\partial t} = \frac{1}{2TOSC} (R_{storage} - R_{release}), \quad (3.4)$$

where θ is the fractional oxidation state of ceria and $TOSC$ is the total oxygen storage capacity. [Remark: The numerical factor 2 in *Eq. 3.4* arises due to the stoichiometric coefficient of oxygen in reactions listed in *Table 3.8*. The rate expression used are listed in the Appendix A].

The kinetics used in the work is similar to detailed micro-kinetics hence this model can be extended to the case with adsorption, desorption and reactions. [Note: In this example, $N = 2$, $S = 2$ so that the simulation of the isothermal model requires solving 5 equations while the non-isothermal model requires 7 equations].

Table 3.8: Reaction scheme in example 2 of TWC with oxygen storage

No.	Reaction
1	$A + 0.5O_2 \longrightarrow AO$
2	$Ce_2O_3 + 0.5O_2 \longrightarrow Ce_2O_4$
3	$A + Ce_2O_4 \longrightarrow Ce_2O_3 + AO$

Table 3.9: Simulation conditions for example 2

Variable	Value
$\langle u \rangle$	$2 \text{ m} \cdot \text{s}^{-1}$
T_f^0	300 K
T_s^0	300 K
θ^0	0
$X_{f,A}^{in}$	2%
X_{f,O_2}^{in}	1%
T_f^{in}	650 K

We simulated both the cold-start that includes the thermal effects (with heat of reaction equal to that of CO oxidation) as well as the isothermal light-off behavior with lower concentration of the reactants (and negligible heat effects).

Results

For the non-isothermal result shown in *Fig. 3.4* (a) is a comparison of exit concentration of species A predicted by various models under non-isothermal condition and (b) is a comparison of exit concentration of A predicted by detailed model and Thiele matrix approximation with Jacobian matrix evaluated at different local concentrations. In *Fig. 3.4(a)*, dotted blue curve is the asymptotic approximation, which is very different and far from all the others, the dashed red curve which is diagonal approximation also deviates from other model solutions. In the middle, the dotted green curve is the Thiele matrix approximation which remains close to the detailed solution(dash-dotted black and solid magenta curves) but we can also notice a gap among them. Two possible reasons can be accounted for this deviation. First, because of the higher inlet temperature, more active catalyst and thermal effect, we have very strong pore diffusion. The Thiele moduli are very large and can reach to the order of 1000 at the higher temperatures reached in

this example, so that simulation of the detailed model actually requires a lot more mesh points (~ 1000) to describe the concentration profile in the washcoat accurately. [Remark: The interfacial flux can be evaluated more accurately with a smaller number of mesh points, in this example, about 50]. It can be noticed that when we change the number of mesh points from 10 to 50, the computed solution of the 1+1D model comes closer to the Thiele matrix calculation curve. A second reason is that we evaluated the Jacobian matrix at the averaged washcoat concentration instead of evaluating it at the gas-solid interfacial concentration. To clarify this, we evaluated the Jacobian at cup-mixing fluid concentration \mathbf{X}_{fm} , averaged washcoat concentration $\langle \mathbf{X}_{wc} \rangle$ and interfacial concentration \mathbf{X}_s , respectively, and show the results in *Fig. 3.4(b)*. As expected, evaluating the Jacobian matrix at the interfacial concentration \mathbf{X}_s increases the accuracy of reduced order model in this example with strong nonlinear kinetics. In *Fig. 3.4(b)*, for the first 15 seconds where reactions are still in kinetic regime, all the solutions are accurate because the Thiele moduli are small during the cold start period and $\mathbf{X}_{fm} \approx \mathbf{X}_s \approx \langle \mathbf{X}_{wc} \rangle$. From 15 to 30 seconds where reactions are in the washcoat diffusion controlled regime: $\mathbf{X}_{fm} \approx \mathbf{X}_s > \langle \mathbf{X}_{wc} \rangle$, evaluating the Jacobian at \mathbf{X}_{fm} and \mathbf{X}_s shows a slightly lower conversion than evaluating it at $\langle \mathbf{X}_{wc} \rangle$. In this transition stage, species concentration are still high and hence the inhibition terms are large which will lead to an effective negative reaction order. With a negative order reaction, some diagonal elements of the Jacobian matrix are smaller when the concentration of species is larger, therefore, the internal mass transfer coefficient is smaller and causes a lower exit conversion (or higher exit concentration). After 30 seconds, where the system is in external mass transfer regime, with a strong pore diffusion: $\mathbf{X}_{fm} > \mathbf{X}_s \gg \langle \mathbf{X}_{wc} \rangle$. Since the non-linearity becomes weak, the reaction order gradually changes from negative to positive and evaluating Jacobian at \mathbf{X}_{fm} and \mathbf{X}_s show a higher conversion than evaluating it at $\langle \mathbf{X}_{wc} \rangle$. Generally speaking, eval-

uating Jacobian at \mathbf{X}_s is more accurate than that at $\langle \mathbf{X}_{wc} \rangle$ or \mathbf{X}_{fm} . This can be also observed in the isothermal light-off behavior (with dilute feed, where the concentrations are ten times lower) shown in *Fig. 3.5* (inlet temperature ramp up rate is 1K per minute), without thermal effects, all these curves are close to each other except that the asymptotic approximation is not good.

For this example, we also note the computation times for each method (on a desktop): 1+1D model (with 50 mesh points in washcoat): 10454 s, Thiele matrix approach: 40 s, Diagonal approximation : 6.3 s, and the Asymptotic approximation: 5.1 s. Based on these computation times, we note that the Thiele matrix approach for describing washcoat diffusion has not only high accuracy but is also faster by about three orders of magnitude even in this simple example of two gas phase and two surface species ($N = S = 2$).

3.1.3 Example 3: Reversible Reactions with Linear Kinetics

The last example we consider is that of a reversible reaction scheme between three species with linear kinetics. The reaction scheme and the kinetic constants are shown in *Table 3.10*. Other parameter values used in the simulations can be located in *Table 3.1*. The aim here is to examine the accuracy of the diagonal approximation in the presence of reversible or equilibrium limited reactions. We note that reversible reaction schemes are common in more detailed kinetic models of after-treatment systems, e.g. kinetic models of TWC that include water-gas shift, reforming and dehydrogenation reactions or kinetic models of LNT that include reversible exothermic NO oxidation reaction along with other endothermic or reversible (storage and release) reactions. Since this is an illustrative example, we have fixed the ratios of the various rate constants and the temperature dependence so that the equilibrium composition is independent of temperature. We also use constant and equal D_f values for all species with $D_f = 10^{-4} \text{ m}^2 \cdot \text{s}^{-1}$. The inlet conditions and other parameters used are listed in *Table 3.11*.

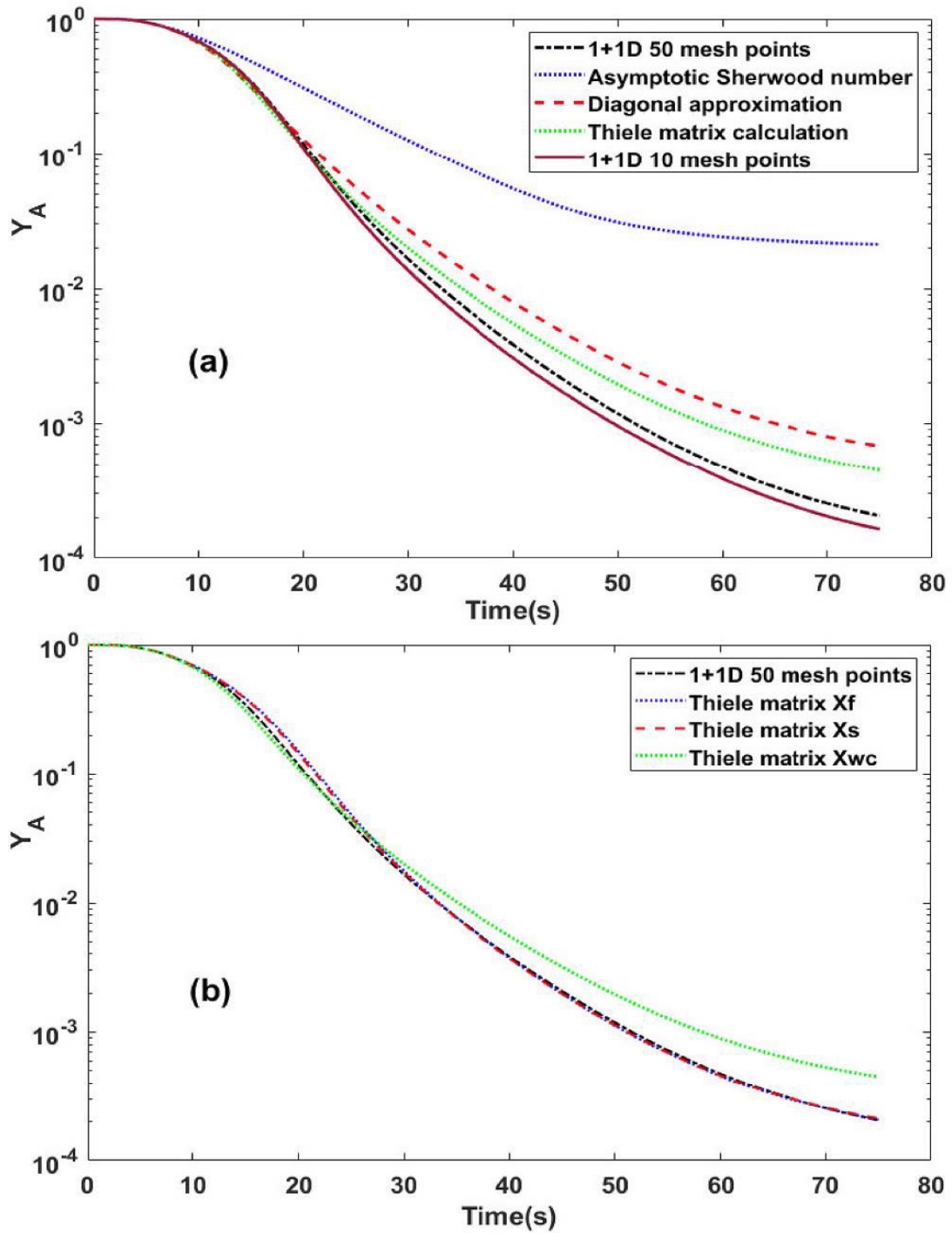


Figure 3.4: (a) Comparison of computed dimensionless exit concentration of reductant species A predicted by various approximations for a TWC model with oxygen storage and non-isothermal condition (b) Comparison of exit concentration of A predicted by the Thiele matrix approximation with Jacobian matrix evaluated at different local concentrations.

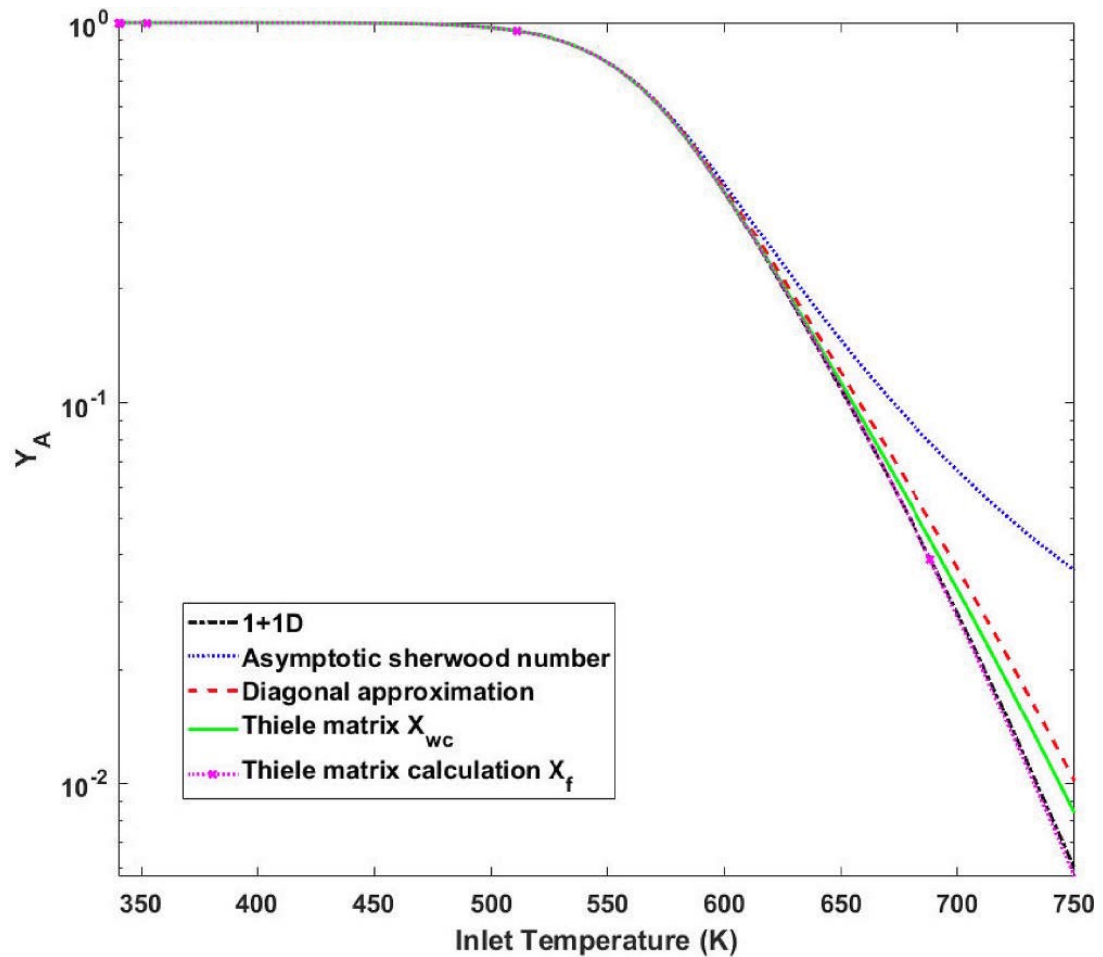


Figure 3.5: Comparison of dimensionless exit concentration of reductant species A predicted by various approximations for a TWC model with oxygen storage under isothermal conditions.

Table 3.10: Reversible reaction scheme and rate constants for example 3

No.	Reaction	Rate
1	$A \longrightarrow B$	kC_A
2	$B \longrightarrow A$	$\frac{1}{2}kC_B$
3	$B \longrightarrow C$	$\frac{1}{2}kC_B$
4	$C \longrightarrow B$	$\frac{1}{4}kC_C$
$k = 10^{12} \exp(-12000/T) \text{ s}^{-1}$		

Table 3.11: Inlet conditions and other parameters used in example 3

Variable	Value
$\langle u \rangle$	$20 \text{ m} \cdot \text{s}^{-1}$
$X_{f,A}^{in}$	0.99
$X_{f,B}^{in}$	0.005
$X_{f,C}^{in}$	0.005
L	$3 \times 10^{-2} \text{ m}$
T_{in} ramp up rate	1 K/min

We note that for this reaction scheme, the net rate of formation of the intermediate product B can be either positive or negative. Thus, the diagonal approximation only makes sense when absolute values are taken for the diagonal elements of Φ^2 . In this example, as the kinetics is linear, we can calculate the internal mass transfer coefficient matrix as well as the exit mole fraction vector analytically. The Thiele matrix is independent of composition and may be expressed as

$$\Phi^2 = \phi^2 \begin{pmatrix} 1 & -\frac{1}{2} & 0 \\ -1 & 1 & -\frac{1}{4} \\ 0 & -\frac{1}{2} & \frac{1}{4} \end{pmatrix}, \quad \phi^2 = \frac{\delta_c^2 k(T)}{D_e}, \quad (3.5)$$

while the diagonal approximation gives

$$\Phi^2 = \phi^2 \begin{pmatrix} \frac{X_A - \frac{X_B}{2}}{X_A} & 0 & 0 \\ 0 & \frac{-X_A + X_B - \frac{X_C}{4}}{X_B} & 0 \\ 0 & 0 & \frac{-\frac{X_B}{2} + \frac{X_C}{4}}{X_C} \end{pmatrix}.$$

Analytical model results

As stated earlier, in this example, the Thiele matrix approximation and the detailed model solutions are identical and are given by the vector equation

$$\mathbf{X}_{fe} = \exp \left\{ -\delta_c \mathbf{K} (\mathbf{k}_{mo} + \delta_c \mathbf{K})^{-1} \mathbf{k}_{mo} a_v \tau \right\} \mathbf{X}_{f,in}, \quad (3.6)$$

where

$$\mathbf{k}_{mo}^{-1} = \mathbf{k}_{mi}^{-1} + \mathbf{k}_{me}^{-1} \quad (3.7)$$

$$\text{and } \mathbf{k}_{me} = \frac{1}{4R_\Omega} \mathbf{D}_f \cdot \mathbf{Sh}_e, \quad \mathbf{k}_{mi} = \frac{1}{\delta_c} \mathbf{D}_e \cdot \mathbf{Sh}_i, \quad a_v = \frac{1}{R_\Omega}. \quad (3.8)$$

Asymptotic approximation takes $\mathbf{Sh}_i = Sh_{i,\infty} \mathbf{I}$, while diagonal approximation takes \mathbf{K} and hence \mathbf{Sh}_i as a diagonal matrix. Since diagonal elements of \mathbf{K} can be negative, we used absolute value in calculating \mathbf{Sh}_i using the diagonal approximation.

Numerical results

Fig.?? (a) and (b) are the results of computed dimensionless exit composition of A and B versus inlet temperature with the dotted (blue) curve representing the asymptotic approximation, dashed (red) curve representing diagonal approximation, solid (green) and dash-dotted (black) curves representing the Thiele matrix approximation and detailed solutions, respectively. As stated earlier, in this example, the equilibrium mole fractions are independent of temperature and given by $C_{A,eq} = \frac{1}{7}, C_{B,eq} = \frac{2}{7}, C_{C,eq} = \frac{4}{7}$. We note that the asymptotic approximation performs bad because of the inaccurate washcoat diffusion prediction, and although absolute values were taken in the diagonal approximation, we get positive numbers but the approximation is still incorrect, where as the results of detailed and the Thiele matrix calculation are identical, we can not see the difference between these two curves because of the linear kinetics. Similar results are observed from prediction for composition of species C as shown in *Fig. 3.7* and this conclusion is consistent with analytical results.

The computation time for each solution is (desktop): 1+1D model(50 mesh points in the washcoat): 295 s, Thiele matrix calculation: 5.5 s, Diagonal approximation : 1.6 s and the asymptotic approximation: 0.9 s. Again, the computation time of Thiele matrix is lower by about a factor fifty for this simple example with

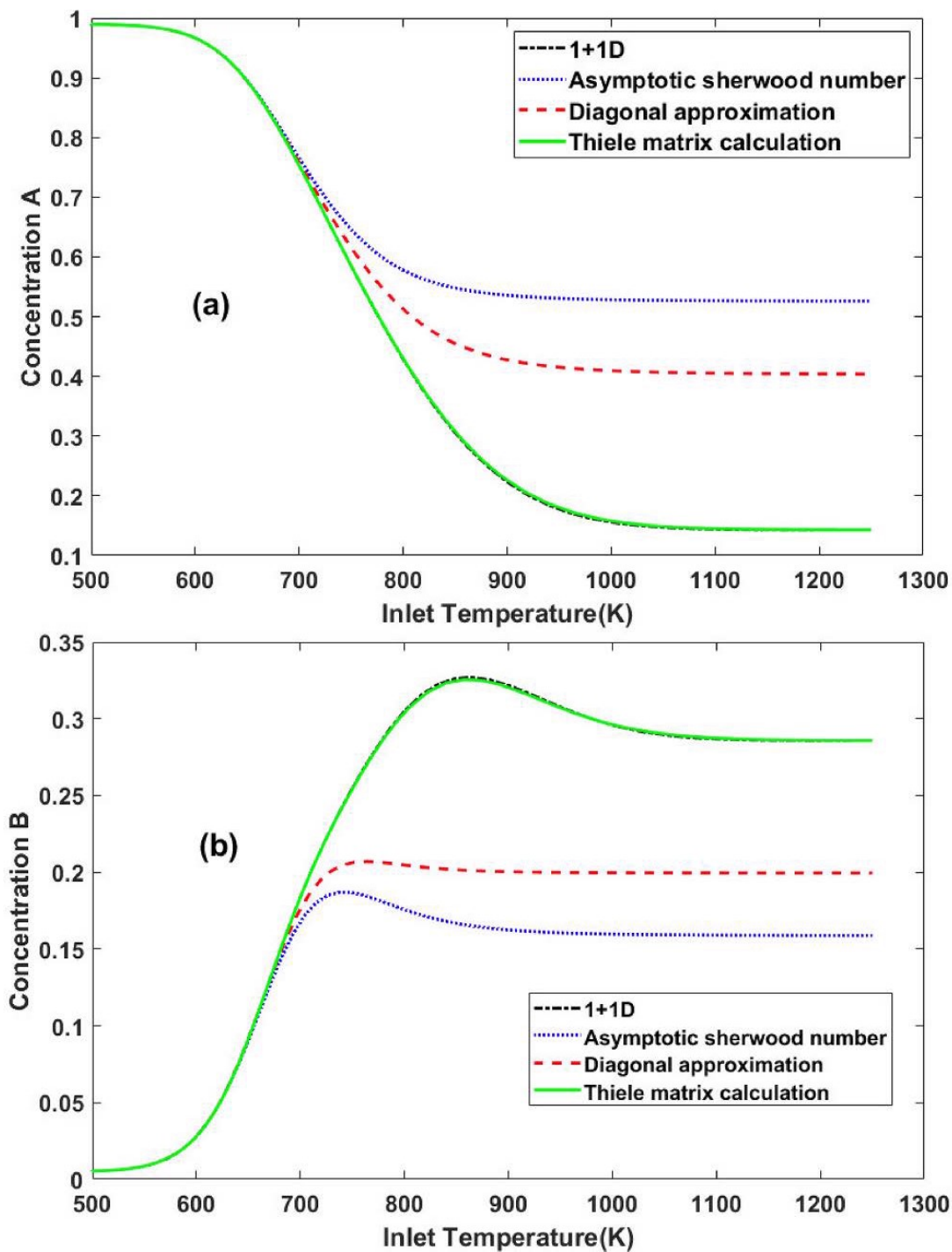


Figure 3.6: (a) Computed exit concentration of species A versus inlet temperature (b) Exit concentration of species B versus inlet temperature for the three species reversible reaction scheme.

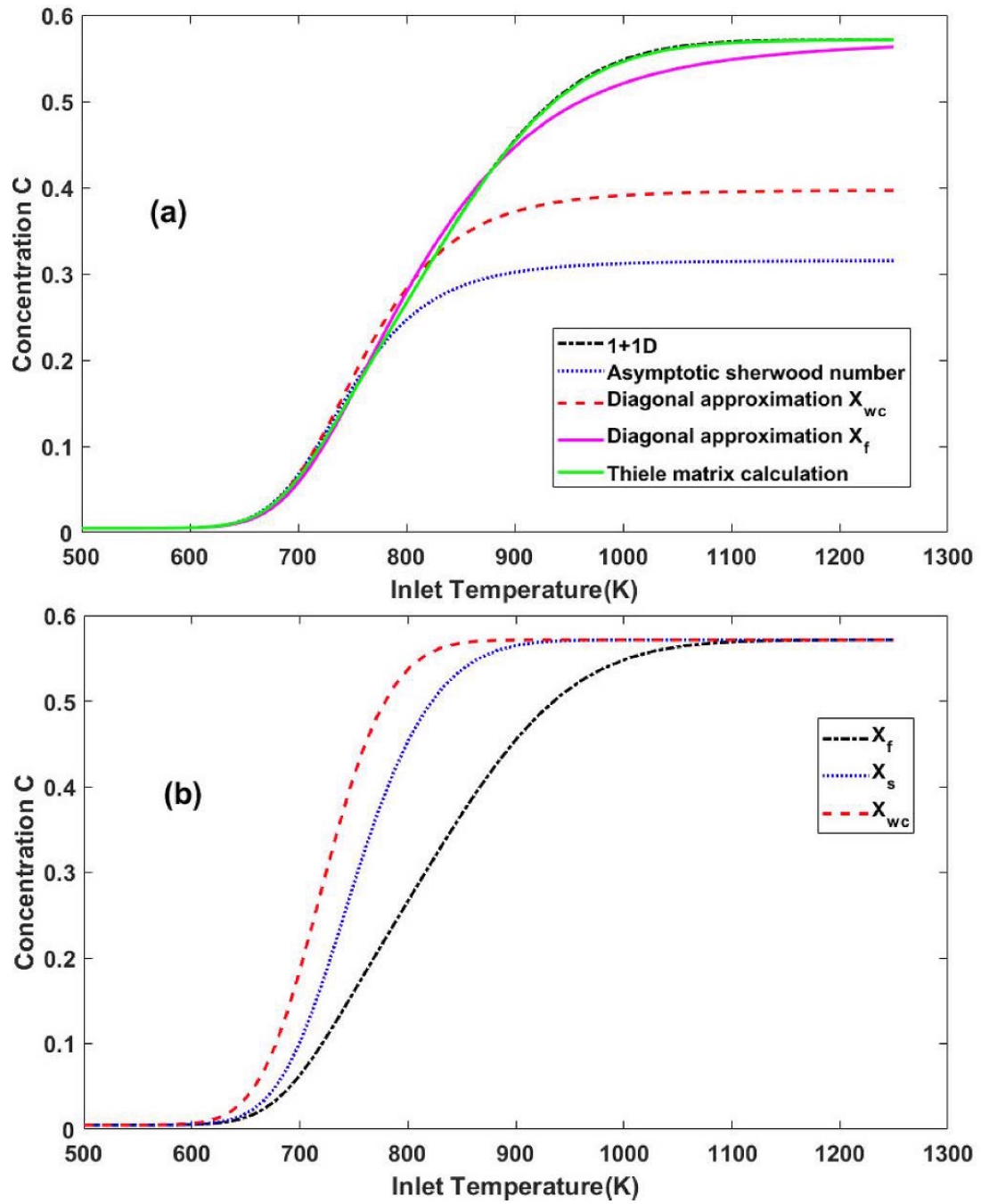


Figure 3.7: Comparison of calculated exit fluid phase concentration of species C versus inlet temperature (b) Different concentrations of C at exit for the three species reversible reaction scheme.

reversible reactions with linear kinetics.

3.2 Conclusions

As our goal is to present and compare the Thiele matrix method, we have illustrated it here with only simple examples of three to four reactions. Even in these simple cases, it is found that this new method can speed-up the transient simulation of monolith reactors by two to three orders of magnitude compared to detailed washcoat diffusion models, while retaining excellent accuracy. We have also compared our method of estimating the washcoat diffusional effect with existing methods (asymptotic approximation, diagonal approximation and detailed 1+1D model) in terms of accuracy and simulation time requirements. As can be expected, and illustrated in the four reaction TWC model of example 1, all three methods work good for slow reactions, and/or thin washcoat and/or low temperature (kinetic regime) or when the eigenvalue of the Thiele matrix Φ^2 are much smaller than unity. In this regime, Sh_i can be approximated as a diagonal matrix $Sh_{i,\infty}\mathbf{I}$. When the concentration gradients in the washcoat become significant or equivalently, some eigenvalues of the Thiele matrix Φ^2 are much greater than unity (or some fast reactions or thicker washcoat or the ratio $D_f/D_e > 100$ so that pore diffusional effects become important), the asymptotic approximation of constant internal Sherwood number is not accurate and may lead to large errors (examples 1, 2 and 3). The diagonal approximation may have sufficient accuracy (for practical purpose) and is much simpler to implement but is applicable only for special types of reaction networks such as parallel irreversible reactions with very small or zero species coupling (or equivalently very small off-diagonal elements compared to diagonal elements in the Jacobian matrix of the rate vector). The diagonal approximation also breaks down (or has poor accuracy) for reversible reactions or when there is strong coupling between the species through the reaction network. This is clearly illustrated in example 3. In contrast to the prior methods, the Thiele

matrix approach is exact for linear kinetics and has acceptable accuracy for non-linear kinetics while speeding-up calculations by two to three orders of magnitude compared to the solution of the 1+1 D model in the examples studied (up to 4 reactions). Though we have not illustrated here, our experience indicates that the speed-up factor could be several orders of magnitude higher for realistic cases of large number of reactions and/or with detailed (micro) kinetic models. Therefore, in next two chapters, we extended the method to include more detailed kinetics.

Chapter 4

Reduced order models for real time simulations of monolith reactors with dual washcoat layers

4.1 Introduction and literature review for dual layered monolith reactors

In chapter 2, we presented the Thiele matrix approach for computing washcoat diffusional effects which is based on the computation of the local property dependent internal transfer coefficient matrix as a function of the local Thiele matrix, defined in terms of the Jacobian of the species formation vector at the local concentrations. In chapter 3, the accuracy and speed-up factor for this method was illustrated for single layered monolith reactors with global kinetics, and it was also compared with other existing methods (or reduced order models) in the literature. It was shown that Thiele matrix approach leads to the best match with the mesh size independent solution of the detailed model while speeding calculations by orders of magnitude. In this chapter, we extend the Thiele matrix approach further to include monolith reactors with dual washcoat layers. This extension is important as multi-functional monolith reactors consisting of two or more washcoat layers with different functionalities are used in many after-treatment systems. Examples include dual layered selective catalytic reduction (SCR) units with Cu and Fe zeolite layers, reactors with a lean NO_x trap (LNT) and SCR layers, reactors with a hydrocarbon (HC) trap and an oxidation layer, diesel oxidation catalysts (DOCs) with two different oxidation layers (e.g. Pd and Pt containing washcoats), ammonia slip catalyst (ASC) with NH₃ oxidation function (Pt/Al₂O₃) and a selective catalytic NO_x reduction function (Cu/zeolite), and four-way catalysts with spinel layer (for oxygen storage) and a precious group metal (PGM) based oxidation layer (see *Figure 4.1*).

It should be pointed out that reduced order models of dual-layered monolith reactors have been presented by other researchers. Mozaffari et al., [13] and Rink et al., [14] extended the earlier approach of Joshi et al., [2] to develop reduced order models for dual layered systems and illustrated their use with several applications. More recently, Picardo and Pushpavanam [20] used the Lyapunov-Schmidt (L-S) method to derive reduced order models for two-phase stratified flow with reaction in the top layer. An asymptotic solution for the washcoat pore diffusion problem for dual layered monoliths was also presented by Bissett [4]. Finally, Ratnakar et al., [8] developed reduced order models for dual and multi-layered systems using the L-S method of averaging and showed the structure of the local equations is different from the earlier intuitively written models. The work of Ratnakar et al., [8] presented the correct structure of the reduced order models for dual (as well as multi) layered systems, but the application was confined to the case of a single reaction. It is also noted that most of the modeling studies of dual-layered monolith reactors in the literature use 1+1 D models described by partial differential equations in both x (axial/flow), y (transverse to flow) directions and t (time) to perform the simulations. Therefore, to make the simulation workable (in a reasonable time using a desktop computer), mesh points are normally taken to be about 20 to 50 in the axial direction and 5 to 10 in the transverse direction ([21] [22] [23]) to obtain a system of differential equations in time. When such discretized models are used (without verifying mesh independency of the computed solutions) to interpret experimental results and estimate kinetic or transport parameters, the accuracy of the estimated parameters may be poor. In the present work, we investigate the mesh size dependency (in the transverse direction) of the dual layered model and note that the discretized model describes the washcoat diffusional effects accurately only when the number of mesh points in each washcoat layer is about equal to the square root of the magnitude of the largest eigenvalue of the Thiele matrix

Φ^2 . We also compare the speed and accuracy of the reduced order model solution with the detailed model and show that Thiele matrix solution is closer to detailed model which has sufficient mesh points.

This chapter is organized as follows: in the next section, we review the detailed (1+1D) diffusion–convection–reaction model for a catalytic monolith reactor with dual washcoat layers and present a reduced order model for a dual layered system in terms of phase averaged concentration modes and inter and intra-phase fluxes. We also discuss the detailed steps involved in the computation of the interfacial fluxes, and the local property dependent mass transfer coefficient matrices. In section 3, we illustrate the application of the reduced order model with a specific example of a dual layered system with a lean NO_x trap (LNT) layer and selective reduction catalyst (SCR) layer. We illustrate the results of mesh size dependency and comparisons between the detailed solution and reduced order model solution. In the last section, we summarize the results.

4.2 Detailed and reduced order models of single and dual layered monolith reactors

For a discussion of hierarchies of models of monolith reactors, we refer to the articles by Ratnakar et. al., [8] and Tu et al., [19]. In this chapter, we consider only the single channel model of a monolith reactor consisting of continuity, momentum, species and energy balances in three spatial coordinates and time. However, as discussed in the literature, such detailed models are not needed in most after-treatment applications and the single channel model is further simplified by decoupling the momentum equation from the species and energy balances. Under the assumption of slowly varying inputs, the model is further simplified to a transient 1+1D model (or one axial and one transverse direction), which is shown to capture all the qualitative features of the monolith reactor. We shall use the standard 1+1D model as our basis model for model accuracy comparison.

In the following sections, we present the model equations for the standard 1+1D model for the isothermal case, followed by a review of the reduced order models proposed in the literature. This is followed by a review of the Thiele matrix approach for single layer monolith (*Figure 4.1(a)*) and then our procedure for extending it to dual-layered monolith reactors (*Figure 4.1(b)*). Since our goal is to explain the main concepts using the simplest geometry (i.e. parallel plate channel) we present the various formulas and results for this case, and indicate briefly extension to other geometries.

4.2.1 Detailed(1+1D) Washcoat Diffusion Model

Under the assumption of slowly varying inputs, the gas phase species balances are same as that of the standard two-phase model and are described by conservation equations in the channel with interfacial flux (or transfer) terms. The vector form of the species balance equation for the fluid phase is given by

$$\frac{\partial \mathbf{X}_{fm}}{\partial t} + \langle u \rangle \frac{\partial \mathbf{X}_{fm}}{\partial x} = -\frac{\mathbf{k}_{me}}{R_{\Omega}} (\mathbf{X}_{fm} - \mathbf{X}_s); \quad x > 0, t > 0, \quad (4.1)$$

while the species balances in the washcoat layers are described by

$$\epsilon_{w1} \frac{\partial \mathbf{X}_{w1}}{\partial t} = \frac{1}{C_T} \boldsymbol{\nu}_1^T \mathbf{r}_{g1}(\mathbf{X}_{w1}, \boldsymbol{\theta}_{w1}) + \mathbf{D}_{e1} \frac{\partial^2 \mathbf{X}_{w1}}{\partial y^2} \quad \text{in } \Omega_1, \quad 0 < y < \delta_{c1} \quad (4.2)$$

$$\text{and } \epsilon_{w2} \frac{\partial \mathbf{X}_{w2}}{\partial t} = \frac{1}{C_T} \boldsymbol{\nu}_2^T \mathbf{r}_{g2}(\mathbf{X}_{w2}, \boldsymbol{\theta}_{w2}) \quad (4.3)$$

$$+ \mathbf{D}_{e2} \frac{\partial^2 \mathbf{X}_{w2}}{\partial y^2} \quad \text{in } \Omega_2, \quad \delta_{c1} < y < \delta_{c1} + \delta_{c2}. \quad (4.4)$$

When kinetic models that account for adsorption, desorption, storage and surface reactions are used to describe the chemistries occurring in the catalytic layers, the model equations should also account for surface species coverages. Assuming that each layer has a single type of catalytic sites on which gas phase species can interact (adsorb/desorb, store or react), the species coverage vectors for the

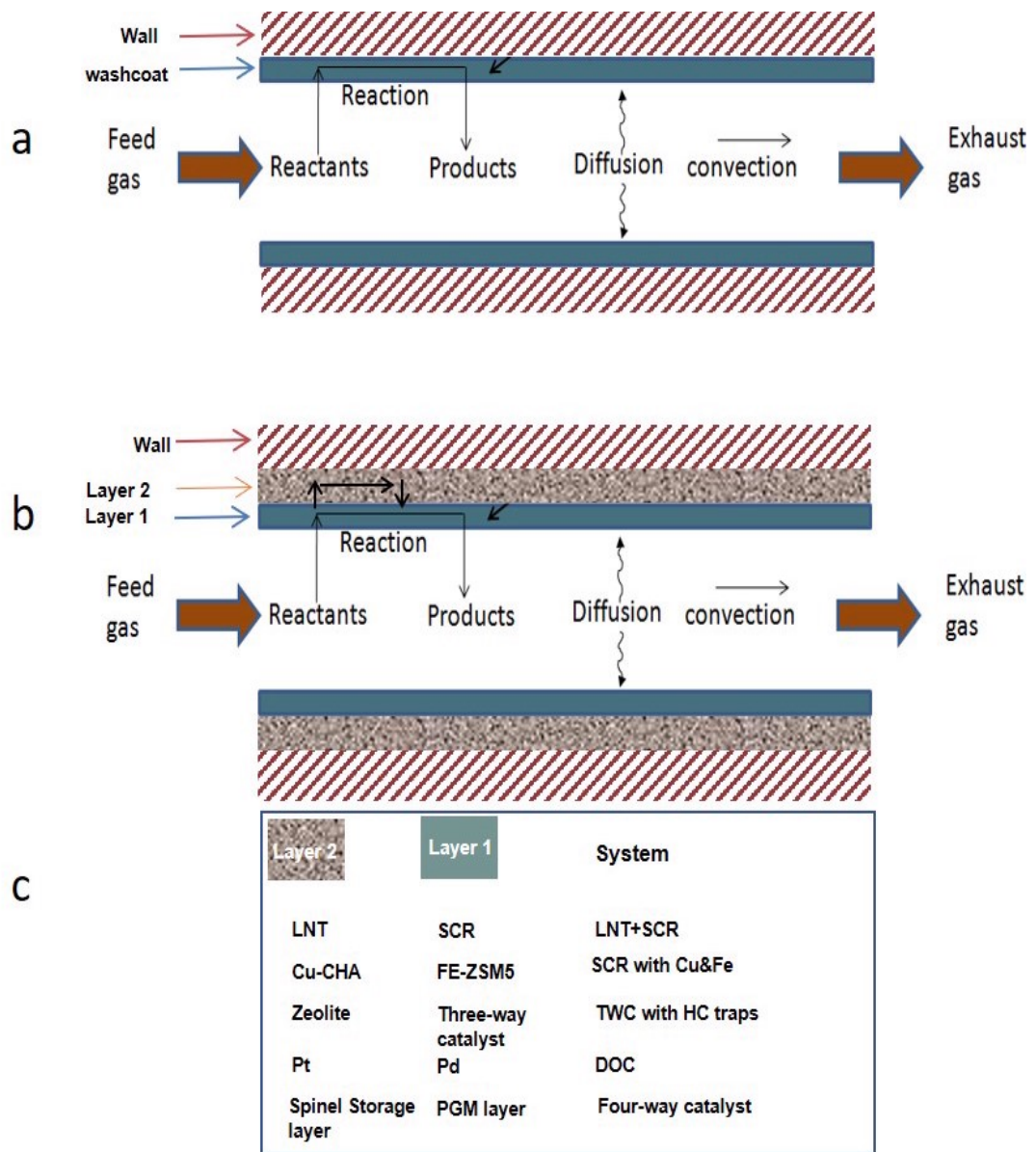


Figure 4.1: Schematic diagram of a single layered (a), and dual layered monolith channels (b), and examples of dual layered systems (c).

surface species of the layers are given by

$$C_{S1} \frac{\partial \theta_{w1}}{\partial t} = \mathbf{r}_{s1}(\mathbf{X}_{w1}, \theta_{w1}) \quad \text{in } \Omega_1, 0 < y < \delta_{c1} \quad (4.5)$$

$$\text{and } C_{S2} \frac{\partial \theta_{w2}}{\partial t} = \mathbf{r}_{s2}(\mathbf{X}_{w2}, \theta_{w2}) \quad \text{in } \Omega_2, \delta_{c1} < y < \delta_{c1} + \delta_{c2}. \quad (4.6)$$

[Remark: The generalization of the model when each layer has several different types of catalytic or storage sites is straightforward and can be done by including additional balance equations of the same type]. Since the wall is assumed to be non-porous, the species fluxes at the wall-washcoat interface vanish, i.e.,

$$\left. \frac{\partial \mathbf{X}_{w2}}{\partial y} \right|_{y=\delta_{c1}+\delta_{c2}} = \mathbf{0}. \quad (4.7)$$

The continuity of the species fluxes at the fluid-washcoat and interfaces layers leads to the interfacial boundary conditions:

$$\mathbf{J}_{01} = \frac{\mathbf{j}_{fw}}{C_T} = \mathbf{k}_{me} (\mathbf{X}_{fm} - \mathbf{X}_s) = -\mathbf{D}_{e1} \frac{\partial \mathbf{X}_{w1}}{\partial y} \quad @ \quad y = 0; \mathbf{X}_s = \mathbf{X}_{w1}|_{y=0} \quad (4.8)$$

$$\mathbf{X}_{w1} = \mathbf{X}_{w2}, \text{ on } \partial\Omega_{12} \quad @ \quad y = \delta_{c1} \quad (4.9)$$

$$\text{and } \mathbf{J}_{12} = -\mathbf{D}_{e1} \frac{\partial \mathbf{X}_{w1}}{\partial y} = -\mathbf{D}_{e2} \frac{\partial \mathbf{X}_{w2}}{\partial y} \quad @ \quad y = \delta_{c1}. \quad (4.10)$$

In the above model equations, bold symbols are used to represent matrices and vectors. We choose to write the model equations in terms of species mole fractions but note that they may also be expressed in terms of species concentrations (see Supporting Material). Here, the column vectors, \mathbf{X}_{fm} and $\mathbf{X}_{wk} \in \mathbb{R}^N$, represent the cup-mixing mole fractions in the fluid phase and the mole fractions in the k^{th} layer of washcoat ($k = 1, 2$), respectively; $\partial\Omega_{01}$ ($y = 0$) is the interface between fluid and washcoat layer 1, and $\partial\Omega_{12}$ ($y = \delta_{c1}$) is the interface between washcoat layer 1 and 2; R_{Ω} represents the hydraulic radius of the monolith flow channel, $\langle u \rangle$ is the average velocity in the flow channel, the column vector $\mathbf{X}_s \in \mathbb{R}^N$ is the mole

fraction vector at the fluid-washcoat interface and \mathbf{k}_{me} is the matrix of external mass transfer coefficients defined by the first equality of Eq. 4.8. In Eq. 4.2, ϵ_{wk} is the porosity in the k^{th} layer of washcoat, $\mathbf{r}_{gk}(\mathbf{X}_{wk}, \boldsymbol{\theta}_{wk}) \in \mathbb{R}^{N_{rk}}$ is the reaction rate vector in the k^{th} layer of washcoat, where the i -th element of this vector represents the rate of the i^{th} reaction, the parameters N and N_{rk} represent the total numbers of gaseous species and reactions, respectively. The matrix, $\boldsymbol{\nu}_k \in \mathbb{R}^{N_{rk} \times N}$, is a matrix of stoichiometric coefficients with rows representing the reaction index while the columns representing species index. The m^{th} element of the vector $\mathbf{r}_{sk}(\mathbf{X}_{wk}, \boldsymbol{\theta}_{wk})$ represent the net rate of formation of surface species m in layer k . The vector \mathbf{j}_{fw} represents the species fluxes at the fluid-washcoat interface. The parameter δ_{ck} is the effective thickness of layer k , while \mathbf{D}_{ek} is assumed to be a diagonal matrix of effective (Knudsen) diffusivities of various gas phase species in the k^{th} layer of washcoat (and the diffusivities of all surface species are assumed to be zero). The total concentration (C_T) is computed using the ideal gas law

$$C_T = \frac{p}{RT_f}, \quad (4.11)$$

where, p represents the total pressure in gas phase, assumed constant at 1 atm, and T_f is the local fluid temperature. In most after-treatment applications, the external mass transfer coefficient matrix is assumed to be diagonal as the reactive species concentrations are small compared to the major inert species (which is usually nitrogen, but it is argon in the examples used in this work).

The inlet, initial and boundary conditions for the above model are of the form

$$\mathbf{X}_{fm}(0, t) = \mathbf{X}_{fm,in}(t), \quad (4.12)$$

$$\mathbf{X}_{fm}(x, 0) = \mathbf{X}_{fm}^0(x); \quad \mathbf{X}_{wk}(x, y, 0) = \mathbf{X}_{wk}^0(x, y); \quad k = 1, 2 \quad (4.13)$$

$$\text{and } \boldsymbol{\theta}_{wk}(x, y, 0) = \boldsymbol{\theta}_{wk}^0(x, y); \quad k = 1, 2. \quad (4.14)$$

As explained by Tu et al., [19] for the case of a single layered monolith, the numerical solution of the above model is usually obtained by discretization of the washcoat species balance equation using difference methods and integrating the resulting partial differential equations in x and t using further discretization in the axial coordinate. For example, if the upwind method is used to discretize the convective derivative in the species balance, we obtain a sequence of Short Monolith (SM) models (analogous to the so called cell or tanks-in-series model for the homogeneous case):

$$\frac{d\mathbf{X}_{fm,j}}{dt} = \langle u \rangle \frac{(\mathbf{X}_{fm,j-1} - \mathbf{X}_{fm,j})}{\Delta x} - \frac{\mathbf{k}_{me}}{R_{\Omega}} (\mathbf{X}_{fm,j} - \mathbf{X}_{s,j}); \quad j = 1, 2, \dots, M, \quad (4.15)$$

where M is the number of cells (or $M-1$ is the number of axial interior mesh points) and $\Delta x = \frac{L}{M}$. In the extreme case of a single cell ($M = 1$), Eq. 4.15 becomes

$$\frac{d\mathbf{X}_{fm}}{dt} = \frac{\langle u \rangle}{L} (\mathbf{X}_{fm} - \mathbf{X}_{fm,in}(t)) - \frac{\mathbf{k}_{me}}{R_{\Omega}} (\mathbf{X}_{fm} - \mathbf{X}_s); \quad t > 0. \quad (4.16)$$

Eq. 4.16 along with Eqs. 4.2-4.6 and appropriate inlet and initial conditions define the SM model. This model is defined by a set of parabolic partial differential equations in y and t and is ideal for comparing the impact of washcoat diffusional effect as the complete long monolith (LM) model is represented by a sequence of SM models.

We note that if the diffusional effects in the layers are neglected and gas phase species mole fractions are assumed to be independent of depth in the washcoat, $\mathbf{X}_{w1} = \mathbf{X}_{w2} = \mathbf{X}_w$, the balance equations reduce to

$$\frac{(\delta_{c1}\epsilon_{w1} + \delta_{c2}\epsilon_{w2})}{(\delta_{c1} + \delta_{c2})} \frac{\partial \mathbf{X}_w}{\partial t} = \frac{\delta_{c1}}{(\delta_{c1} + \delta_{c2})} \frac{1}{C_T} \boldsymbol{\nu}_1^T \mathbf{r}_{g1}(\mathbf{X}_w, \boldsymbol{\theta}_{w1}) + \frac{\delta_{c2}}{(\delta_{c1} + \delta_{c2})} \frac{1}{C_T} \boldsymbol{\nu}_2^T \mathbf{r}_{g2}(\mathbf{X}_w, \boldsymbol{\theta}_{w2}) \quad (4.17)$$

$$+ \frac{\mathbf{k}_{me}}{(\delta_{c1} + \delta_{c2})} (\mathbf{X}_{fm} - \mathbf{X}_w), \quad (4.18)$$

$$C_{S1} \frac{\partial \boldsymbol{\theta}_{w1}}{\partial t} = \mathbf{r}_{s1}(\mathbf{X}_w, \boldsymbol{\theta}_{w1}), \quad 0 < y < \delta_{c1} \quad (4.19)$$

$$\text{and } C_{S2} \frac{\partial \boldsymbol{\theta}_{w2}}{\partial t} = \mathbf{r}_{s2}(\mathbf{X}_w, \boldsymbol{\theta}_{w2}), \quad \delta_{c1} < y < \delta_{c1} + \delta_{c2}. \quad (4.20)$$

Eq. 4.1 along with Eqs. 4.17-4.20 and appropriate inlet and initial conditions define the limiting model that completely ignores the washcoat diffusional effects (but includes external mass transfer effects). This model consists of a set of hyperbolic partial differential equations in x and t .

4.2.2 Review of Thiele matrix approach for single layered monolith reactor

We review here briefly the Thiele matrix approach for the calculation of the washcoat diffusional effect for the case of a single layer, and refer to the work of Tu et al., [19] for further details. The specie balance in fluid phase of Thiele matrix approach remains the same as other approximations and may be expressed as

$$\frac{\partial \mathbf{X}_{fm}}{\partial t} + \langle u \rangle \frac{\partial \mathbf{X}_{fm}}{\partial x} = -\frac{\mathbf{J}_{0,1}}{R_\Omega}, \quad (4.21)$$

while the volume averaged species balance equations for the washcoat (for gas phase species) become

$$\epsilon_w \frac{\partial \langle \mathbf{X}_w \rangle}{\partial t} = \frac{1}{C_T} \boldsymbol{\nu}^T \mathbf{r}_g(\langle \mathbf{X}_w \rangle, \langle \boldsymbol{\theta}_w \rangle) + \frac{\mathbf{J}_{01}}{\delta_c} \quad (4.22)$$

$$\text{and } C_S \frac{\partial \langle \boldsymbol{\theta}_w \rangle}{\partial t} = \mathbf{r}_s(\langle \mathbf{X}_w \rangle, \langle \boldsymbol{\theta}_w \rangle).$$

The interfacial flux is given by

$$\mathbf{J}_{01} = \mathbf{k}_{mo}(\mathbf{X}_{fm} - \langle \mathbf{X}_w \rangle), \quad (4.23)$$

$$\mathbf{k}_{mo}^{-1} = \mathbf{k}_{me}^{-1} + \mathbf{k}_{mi}^{-1}, \quad (4.24)$$

$$\mathbf{k}_{mi} = \frac{1}{\delta_c} \mathbf{D}_e \cdot \mathbf{Sh}_i, \quad (4.25)$$

$$\mathbf{Sh}_i = \left[(\Phi \tanh \Phi)^{-1} - (\Phi^2)^{-1} \right]^{-1} \quad (4.26)$$

$$\text{and } \approx 3\mathbf{I} + \Phi \tanh\left[\frac{1}{5}\Phi\right], \quad (4.27)$$

where $\langle \mathbf{X}_w \rangle$ is the (volume or phase) averaged species mole fraction vector, \mathbf{k}_{mo} , \mathbf{k}_{mi} , \mathbf{k}_{me} are the overall, internal, and external mass transfer coefficients matrices, respectively. \mathbf{Sh}_i is the internal Sherwood matrix, and Φ^2 is the square of the shape normalized Thiele matrix.

The external mass transfer coefficient matrix can be approximated by a diagonal matrix in most after-treatment systems (in the absence of any homogeneous reactions) while the internal mass transfer coefficient matrix is a non-diagonal matrix in the general case. This brings to the main idea of Thiele matrix approach [19]: this method is based on the exact solution of the washcoat diffusion problem for the case of linear kinetics for which the effectiveness factor matrix as well as the internal mass transfer coefficient matrix can be determined exactly [1]. Because \mathbf{k}_{mi} is non-diagonal even when \mathbf{D}_e is diagonal, and the matrix of first order rate constants \mathbf{K} is not diagonal, a full calculated matrix is used for the internal Sherwood matrix, with the non-diagonal elements in Φ^2 standing for the coupling relationship among reactions:

$$\Phi^2 = \delta_c^2 (\mathbf{D}_e)^{-1} \left(-\frac{1}{C_T} \frac{d(\boldsymbol{\nu}^T \mathbf{r}_g(\mathbf{X}_w, \boldsymbol{\theta}_w))}{d\mathbf{X}_w} \right)_{\mathbf{X}_w = \mathbf{X}_s}. \quad (4.28)$$

[Remark: As discussed by Tu et al.[19], evaluation of Φ^2 at the fluid-washcoat interfacial mole fraction vector \mathbf{X}_s leads to better accuracy of the reduced order model. This vector can be related to the mixing-cup and volume averaged mole fraction vectors by $\mathbf{X}_s = (\mathbf{k}_{me} + \mathbf{k}_{mi})^{-1} (\mathbf{k}_{me} \mathbf{X}_{fm} + \mathbf{k}_{mi} \langle \mathbf{X}_w \rangle)$. Further, we note that in Eq. 4.27, the \mathbf{Sh}_i matrix is an even function of the (non-diagonal) Thiele

matrix Φ (defined by Eq. 4.28). Hence, the eigenvalues of Φ^2 can be positive or negative or complex, and the fact that Φ^2 is a matrix of real numbers and Sh_i is an even function of Φ eliminates the problem of dealing with complex values for the mass transfer coefficients. Further, to deal with nonlinear kinetics, we linearize the washcoat reaction-diffusion problem at the local interfacial conditions \mathbf{X}_s , so that the Jacobian matrix plays the same role as that of the first-order rate constant matrix for linear kinetics. As explained by Tu et al., [19], Sh_i can be computed from Φ^2 , using the Cayley-Hamilton theorem. In addition, the internal mass transfer coefficient can be computed for any general washcoat shape, using the relation

$$\mathbf{Sh}_i = Sh_{i\infty} \mathbf{I} + \Phi \tanh[\Lambda^* \Phi], \quad (4.29)$$

where the two constants $Sh_{i\infty}$ and Λ^* depend only the washcoat shape. These constants are listed in *Table 4.1* for some common washcoat geometric shapes. [Remarks: The parameters $Sh_{i\infty}$ and Λ^* are only functions of the washcoat shape or geometry, and $Sh_{i\infty}$ is the same as that tabulated by Joshi et al., [17], while Λ^* is different. Both are empirical parameters that lead to a good fit of the Sh_i versus Φ curve near Φ values of order unity. *Table 4.1* also corrects a couple of typographical errors in row 5 (rounded square) of Tu et al., [19] and other prior work.

To summarize, the Thiele matrix approach simplifies the 1+1D model by solving the washcoat diffusion problem at the local conditions and computing the fluid-washcoat interfacial flux vector \mathbf{J}_{01} through the $N \times N$ matrix \mathbf{k}_{mi} (or \mathbf{Sh}_i), where N is the number of gas phase species. The two main appealing features of this method compared to direct numerical solution of the 1+1D model are: (i) examination of the eigenvalues of Φ^2 provides physical insight on the time scales involved and stiffness of the local diffusion-reaction problem (or the associated spatial gradients) as well as a method for computing \mathbf{k}_{mi} , and (ii) the method can speed-up

the transient simulations by a factor that is approximately equal to the square root of the largest eigenvalue (in magnitude) of Φ^2 .

4.2.3 Reduced-order model for dual layered monolith reactors

The article by Ratnakar et al., [8], lists the scalar equations of the low-dimensional model for dual-layered monolith for a single component system. We present here the vector form of the same so that it can be used for multi-component systems. The vector form of the species balance in the fluid phase is same as that for single layer and may be written as

$$\frac{\partial \mathbf{X}_{fm}}{\partial t} + \langle u \rangle \frac{\partial \mathbf{X}_{fm}}{\partial x} = -\frac{\mathbf{J}_{0,1}}{R_\Omega}, \quad (4.30)$$

while the volume averaged species balance equations for the washcoat layers (for gas phase species) become

$$\epsilon_{w1} \frac{\partial \langle \mathbf{X}_{wc} \rangle_1}{\partial t} - \frac{1}{C_T} \boldsymbol{\nu}_1^T \mathbf{r}_1(\langle \mathbf{X}_{wc} \rangle_1) = \frac{\mathbf{J}_{0,1} - \mathbf{J}_{1,2}}{\delta_{c1}} \quad (4.31)$$

$$\text{and } \epsilon_{w2} \frac{\partial \langle \mathbf{X}_{wc} \rangle_2}{\partial t} - \frac{1}{C_T} \boldsymbol{\nu}_2^T \mathbf{r}_2(\langle \mathbf{X}_{wc} \rangle_2) = \frac{\mathbf{J}_{1,2}}{\delta_{c2}}. \quad (4.32)$$

The local equations relating the interfacial fluxes to the cup-mixing and volume averaged mole fraction (or concentration) vectors are given by

$$\begin{bmatrix} \mathbf{X}_{fm} - \langle \mathbf{X}_w \rangle_1 \\ \langle \mathbf{X}_w \rangle_1 - \langle \mathbf{X}_w \rangle_2 \end{bmatrix} = \begin{bmatrix} \mathbf{k}_{01}^{-1} \cdot \mathbf{J}_{01} + \widehat{\mathbf{k}}_{i1}^{-1} \cdot \mathbf{J}_{12} \\ \widehat{\mathbf{k}}_{e1}^{-1} \cdot \mathbf{J}_{01} + \mathbf{k}_{02}^{-1} \cdot \mathbf{J}_{12} \end{bmatrix}, \quad (4.33)$$

$$\mathbf{k}_{01}^{-1} = R_\Omega * (\mathbf{D}_f * \mathbf{Sh}_{e0})^{-1} + \delta_{c1} * (\mathbf{D}_{e1} * \mathbf{Sh}_{i1})^{-1}, \quad (4.34)$$

$$\widehat{\mathbf{k}}_{i1}^{-1} = \delta_{c1} * (\mathbf{D}_{e1} * \widehat{\mathbf{Sh}}_{i1})^{-1}, \quad (4.35)$$

$$\widehat{\mathbf{k}}_{e1}^{-1} = \delta_{c1} * (\mathbf{D}_{e1} * \widehat{\mathbf{Sh}}_{e1})^{-1} \quad (4.36)$$

$$\text{and } \mathbf{k}_{02}^{-1} = \delta_{c1} * (\mathbf{D}_{e1} * \mathbf{Sh}_{e1})^{-1} + \delta_{c2} * (\mathbf{D}_{e2} * \mathbf{Sh}_{i2})^{-1}, \quad (4.37)$$

where subscripts 1 and 2 (except in mass transfer coefficient matrices \mathbf{k}) stand for layer 1 and layer 2, respectively. The vector \mathbf{J}_{01} denotes the species fluxes at the fluid-washcoat interface, while \mathbf{J}_{12} is the species flux vector at the interface between washcoat layer 1 and 2; $\langle \mathbf{X}_w \rangle_k$ is washcoat (volume) averaged mole fraction vector, \mathbf{k}_{01} is the overall mass transfer coefficients matrix for fluid phase and washcoat layer1, and \mathbf{k}_{02} is the overall mass transfer coefficient matrix for washcoat layer 1 and 2; $\widehat{\mathbf{k}}_{i1}$ and $\widehat{\mathbf{k}}_{e1}$ are the two cross-exchange mass transfer coefficient matrices that arise in layer 1 due to the coupling between fluxes at the two interfaces $\partial\Omega_{01}$ and $\partial\Omega_{12}$ [8]. $\mathbf{Sh}_{e,0}$ is the traditional external Sherwood matrix at the fluid-washcoat interface, while $\mathbf{Sh}_{i,1}$ and $\mathbf{Sh}_{i,2}$ are the internal Sherwood number matrices for each washcoat layer and $\mathbf{Sh}_{e,1}$ is the external Sherwood number matrix for the first washcoat layer. $\widehat{\mathbf{Sh}}_{i,1}$ and $\widehat{\mathbf{Sh}}_{e,1}$ are the cross-coupling Sherwood matrices. [Please refer to the article of Ratnakar et al., [8] for details and for explanation of the physical meaning of these Sherwood matrices. The Appendix B also provides a brief review of these equations in terms of the various mass transfer coefficient matrices].

4.2.4 Computation of the internal and external Sherwood matrices

In this section, we discuss the computation of the five Sherwood matrices ($\mathbf{Sh}_{i,1}$, $\mathbf{Sh}_{i,2}$, $\mathbf{Sh}_{e,1}$, $\widehat{\mathbf{Sh}}_{i,1}$ and $\widehat{\mathbf{Sh}}_{e,1}$) as functions of the Thiele matrices for each layer defined by

$$\Phi_1^2 = \delta_{c1}^2 (\mathbf{D}_{e1})^{-1} \left(-\frac{1}{C_T} \frac{d(\boldsymbol{\nu}_1^T \mathbf{r}_{g1}(\mathbf{X}_{w1}, \boldsymbol{\theta}_{w1}))}{d\mathbf{X}_{w1}} \right)_{\mathbf{X}_{w1}=\mathbf{X}_{s1}} \quad (4.38)$$

$$\text{and } \Phi_2^2 = \delta_{c2}^2 (\mathbf{D}_{e2})^{-1} \left(-\frac{1}{C_T} \frac{d(\boldsymbol{\nu}_2^T \mathbf{r}_{g2}(\mathbf{X}_{w2}, \boldsymbol{\theta}_{w2}))}{d\mathbf{X}_{w2}} \right)_{\mathbf{X}_{w2}=\mathbf{X}_{s2}}. \quad (4.39)$$

First, we note that the external Sherwood matrix $\mathbf{Sh}_{e,0}$ is diagonal and depends only on the shape of the flow channel and velocity profile. The computation of the elements of this matrix has already been discussed by Tu et al., [19] as well as other

literature studies[5]. We also note that the matrix \mathbf{Sh}_{i2} depends only on the properties of layer 2 and hence can be estimated using the single layer formula discussed in the previous section. For example, when layer 2 is thin (or slab geometry), we have

$$\mathbf{Sh}_{i2} = \left[(\Phi_2 \tanh \Phi_2)^{-1} - (\Phi_2^2)^{-1} \right]^{-1} \quad (4.40)$$

$$\text{and } \approx 3\mathbf{I} + \Phi_2 \tanh\left[\frac{1}{5}\Phi_2\right]. \quad (4.41)$$

The remaining four Sherwood matrices depend on the properties of layer 1 (which has non-zero species fluxes at both boundaries). For the case of thin layer 1 (or slab geometry), the four Sherwood matrices may be expressed as[8]

$$\mathbf{Sh}_{i1} = \mathbf{Sh}_{e1} = \left[(\Phi_1 \tanh \Phi_1)^{-1} - (\Phi_1^2)^{-1} \right]^{-1}, \quad (4.42)$$

$$\approx 3\mathbf{I} + \Phi_1 \tanh\left[\frac{1}{5}\Phi_1\right], \quad (4.43)$$

$$\widehat{\mathbf{Sh}}_{i1} = \widehat{\mathbf{Sh}}_{e1} = \left[(\Phi_1^2)^{-1} - (\Phi_1 \sinh \Phi_1)^{-1} \right]^{-1} \quad (4.44)$$

$$\text{and } \approx 6\mathbf{I} + \Phi_1^2. \quad (4.45)$$

We note that even though there are four Sherwood numbers, there are only two distinct matrix functions to be computed. Further, as in the case of single layered monolith, the Cayley-Hamilton theorem may be used to compute these functions or their approximations. For example, we can approximate Eq. 4.44 to Eq. 4.45, so that it becomes much simpler to compute cross-coupled Sherwood matrices. Fig. 4.2 shows a comparison of the exact cross-coupled Sherwood number and its approximation, solid red line is the result of approximated solution (Eq. 4.45) and dotted blue line is the result of exact expression (Eq. 4.44), we can see that the approximation is excellent while simplifying the computations (avoiding the computation of matrix functions for $\widehat{\mathbf{Sh}}_{i1}$ and $\widehat{\mathbf{Sh}}_{e1}$). Similarly, Fig. 4.2 shows a com-

parison between approximate internal/external Sherwood number and the exact expression. The dotted yellow line is the result of the approximation (Eq. 4.43) and solid green line is the result of exact expression (Eq. 4.42). For other washcoat geometries the various Sherwood matrices may be approximated by

$$\mathbf{Sh}_{i1} = Sh_{i1\infty}\mathbf{I} + \Phi_1 \tanh[\Lambda^* \Phi_1], \quad (4.46)$$

$$\widehat{\mathbf{Sh}}_{i1} = \widehat{Sh}_{i1\infty}\mathbf{I} + \Phi_1^2, \quad (4.47)$$

$$\widehat{\mathbf{Sh}}_{e1} = \widehat{Sh}_{e1\infty}\mathbf{I} + \Phi_1^2, \quad (4.48)$$

$$\mathbf{Sh}_{e1} = Sh_{e1\infty}\mathbf{I} + \Phi_1 \tanh[\Lambda^* \Phi_1] \quad (4.49)$$

$$\text{and } \mathbf{Sh}_{i2} = Sh_{i2\infty}\mathbf{I} + \Phi_2 \tanh[\Lambda^* \Phi_2]. \quad (4.50)$$

where $\Lambda^* \approx 0.2$ with a thin washcoat layer.

In the above expressions, the first term represents the asymptotic value while the second term represents the Thiele matrix dependence. We list in *Table C.1* the constants appearing in these expressions for some common geometries of layer 1 [37]. As stated earlier, in addition to these four Sherwood numbers for layer 1 and one Sherwood number for layer 2 (\mathbf{Sh}_{i2}), the external Sherwood number Sh_{e0} depends on the geometry of the flow channel, velocity profile and local flow conditions. For example, for the case of a circular flow geometry, the asymptotic external Sherwood number (based on channel hydraulic diameter) 4.364 for parabolic velocity profile. For other geometric shapes and flow conditions, the asymptotic Sherwood number may be found in the literature [see for example, Balakotaiah [1], Gundlapally and Balakotaiah [5], Tu et al., [19]]. Also, as discussed in these studies, for irregular channel geometries with a flow geometry that is close to a circle and thin washcoat layers (e.g., rounded square), the various Sherwood numbers can be approximated by that of circular flow geometry with thin washcoat layers (see also Appendix B for the details).

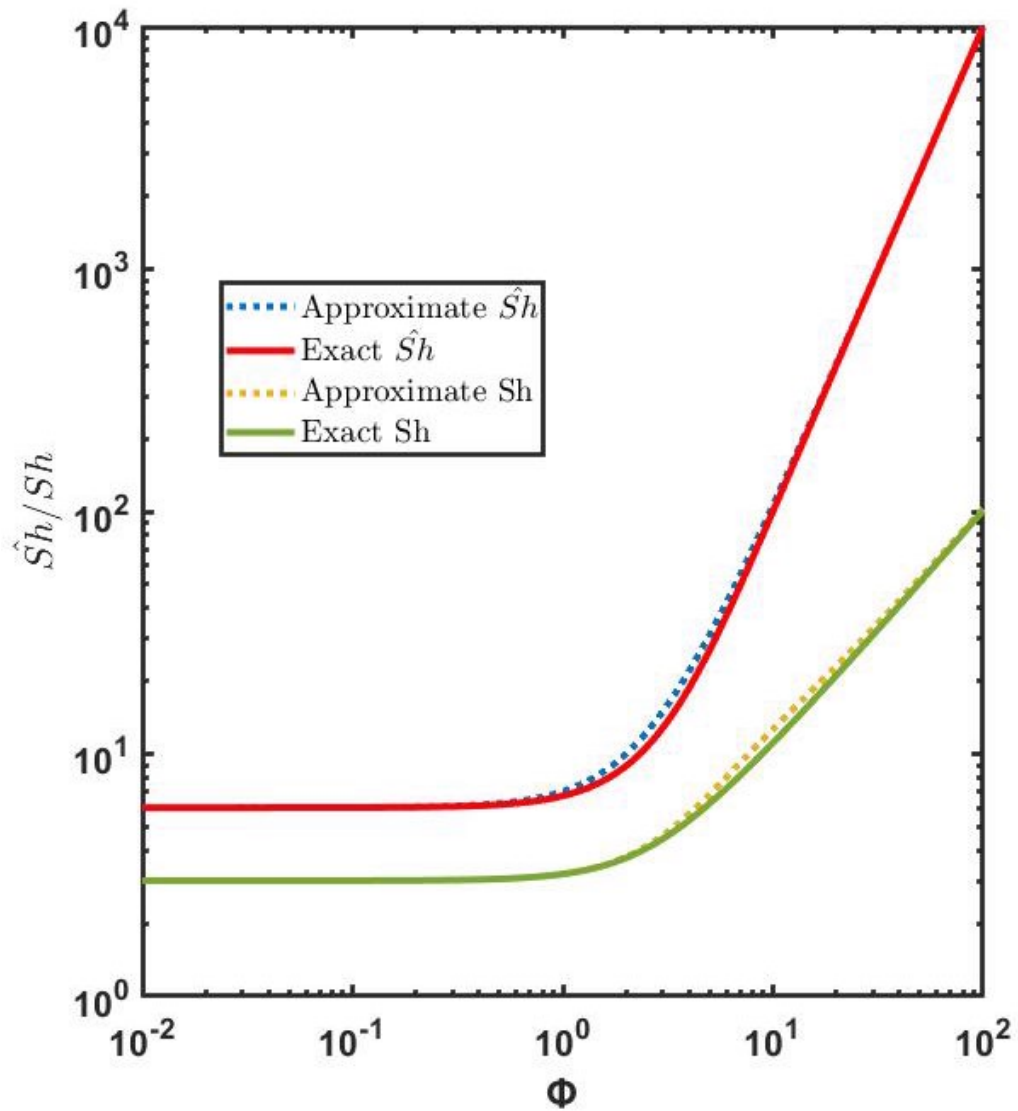


Figure 4.2: Comparison of approximated and exact internal/external and cross-exchange Sherwood numbers

To summarize, the reduced order Thiele matrix based approach for dual layered monolith reactors replaces the problem of solving the washcoat diffusion and reaction in the layers by that of computing some matrix functions and solving the local linear equations for the species interfacial fluxes. As in the case of single layer, the two main appealing features of this method compared to direct numerical solution of the 1+1D model are: (i) physical insight provided by examining the eigenvalues of Φ_k^2 on the time scales and/or stiffness of the local diffusion-reaction problem in layer k , and (ii) speed-up of the transient simulations by a factor that is approximately equal to the square root of the largest eigenvalue (in magnitude) of Φ_k^2 .

4.3 Accuracy of reduced order model

In this section, we provide an example illustrating the Thiele matrix approach for treating the dual layer washcoat diffusion problem. We also compare the accuracy of the reduced order Thiele matrix based calculation with that of detailed model with various mesh sizes as well as the method based only on the asymptotic values (for the various Sherwood numbers) or completely neglecting washcoat diffusion effects. In the example below, we assume that the reacting gases are diluted in argon, the gas phase diffusivity matrix, $\mathbf{D}_f \in \mathbb{R}^{N \times N}$ is a diagonal matrix with the j^{th} diagonal element $D_{f,j}$ representing the diffusivity of the j^{th} species in argon. To compute the diffusivity as a function of temperature, binary diffusion coefficients were calculated by using the Fuller correlation based on species atomic diffusion volumes [18] and varying with the temperature. The effective diffusivity of each species in the washcoat is estimated by assuming a diffusivity ratio, $\lambda (= D_f/D_e)$, of 100. This λ -value corresponds to the effective diffusivity (assuming Knudsen regime) in the porous catalyst with pore radius of ca. 5 nm which is typical for γ -alumina washcoat (porosity $\epsilon_{wc} = 0.4$, density $\rho_{wc} = 1700 \text{ kg/m}^3$, surface area $S_g = 100 \text{ m}^2/\text{g}_{wc}$, and tortuosity $\tau = 1.5$ [21]). Hence, the washcoat effective diffusivity

matrix (D_e) is also a diagonal matrix with the diagonal elements ($D_{e,j}$) representing diffusivity of the j^{th} species,

$$D_{e1,j} = D_{e2,j} = D_{f,j}/100,$$

Table 4.3 shows the temperature dependent parameters used in this simulation, the values of various other parameters used in the simulations are listed in *Table 5.1*,

4.3.1 Reaction mechanism of SCR and LNT catalyst

As stated earlier, the kinetic model used in this study is taken from the work of Shakya et al., [21] and Metkar et al., [38]. Here, we only summarize the SCR and LNT reaction scheme and refer to [21] for more details. The SCR reactions considered in this study are listed in *Table 4.5*, the LNT reactions considered in this study are listed in *Table 4.6*, for other constant parameter values and inlet conditions used are listed in *Table 4.7*. [Remark: The $S1$ in the SCR chemistry denotes the ammonia adsorption/reaction sites in the Cu-chabazite catalyst layer while the s and f letters denote the slow and fast storage Ba sites in the LNT layer. In this model, there is no storage on the Pt sites of the LNT layer, though the Pt loading impacts the kinetics of the NO oxidation reaction]. Catalyst compositions can be found in *Table 4.8*.

Before we present results, it should be mentioned that for these reaction networks, the number of gas phase species that are reactants in the SCR layer are five, i.e. NO , NO_2 , O_2 , NH_3 and NH_4NO_3 (as H_2O , N_2 and N_2O are only products and their concentrations do not enter any kinetic expression). Thus, the Thiele (and Sherwood) matrices are of order five for this layer. Similarly, for the LNT layer, the Thiele (and Sherwood) matrices are of order three during storage and five during storage and reduction (cycling). [The Appendix B lists numerical values of the Thiele and Sherwood matrices for some typical cases during the simulations].

4.3.2 Results

We first reproduce the results of the storage experiment of Shakya et al., [21]. *Fig. 4.3* shows a comparison of the results computed by various models, namely the detailed 1+1D model (with 30 mesh points in the axial and 10 mesh points in transverse directions) and the various reduced order models (with same number of axial mesh points but approximation of the washcoat diffusion problem) at 300 °C. In *Fig. 4.3*, the dashed pink and green lines are results of Thiele matrix approximation of NO and NO₂ exit concentrations, respectively. The dash-dotted purple and light blue lines are results of asymptotic approximation of NO and NO₂ exit concentrations, respectively. The solid red and blue lines are results of the detailed 1+1D model with 10 (uniformly spaced) mesh points in the washcoat layer (2 interior mesh points in the SCR layer, 5 interior mesh points in LNT and one mesh point at each boundary, see Appendix B for further details). We observe that there is a gap between the Thiele matrix solution and others in both NO and NO₂ computed effluent profiles. First, it would appear that the Thiele matrix solution is not accurate. However, we also note that at 300 °C, the reactions in the LNT layer are strongly influenced by washcoat diffusion, and hence the asymptotic solution is not valid (as the largest eigenvalue of Thiele matrix Φ_2^2 is much larger than 1). Even though detailed model takes 10 mesh points in the washcoat layer, the number of mesh points is actually not sufficient to obtain an accurate (and mesh size independent) solution of the detailed model. In this case, the detailed model takes 567 s, the Thiele matrix approach takes 2.3 s and the asymptotic approximation takes 0.8 s. Our reduced order model is approximately 246 times faster than the detailed 1+1D model.

In the next section, we discuss the mesh size dependency of the detailed model using the short monolith model (as obtaining the mesh independent solution of the full length monolith even for the isothermal case requires considerable effort, of

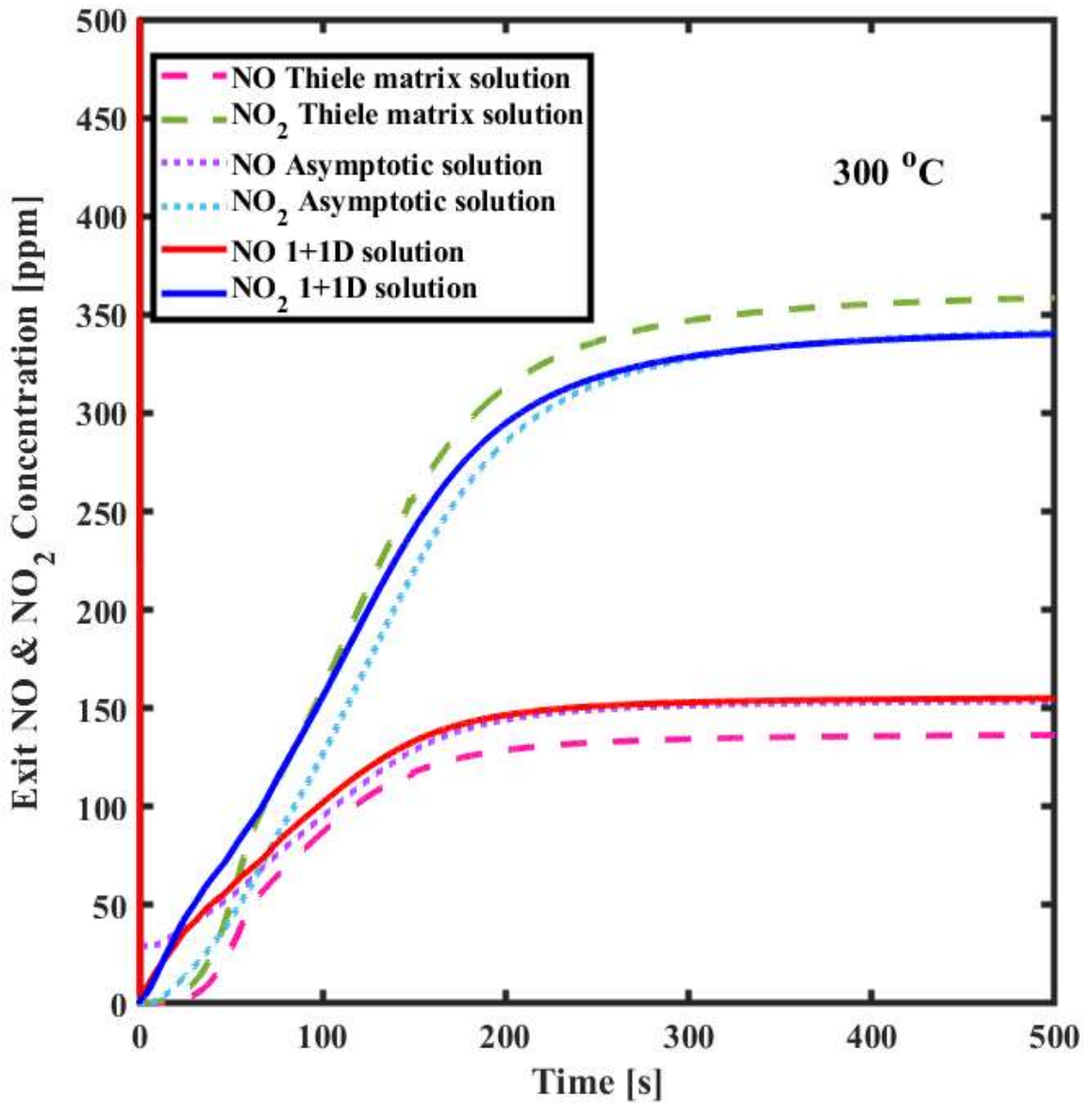


Figure 4.3: Comparison of effluent NO_x concentrations predicted by various approximations to washcoat diffusion during storage at 300 °C (1+1D model results are with 10 mesh points).

the order of several days on a desktop computer). The rest of the simulations are run at 300 °C since this is where the washcoat diffusion becomes important [At lower temperatures, the washcoat diffusional effects are not important while at much higher temperatures, the external mass transfer will diminish the impact of washcoat diffusion.]. Further, since the objective is to compare the Thiele matrix approach to the mesh size independent solution with washcoat diffusion, we do this comparison using a short monolith model for the rest of the simulations. This is justified as detailed in the previous section, the long monolith reactor model (1+1D) with M mesh points in the axial direction is equivalent to a series of M short monolith models, so instead of distributing mesh points in the axial direction, we can save the time and use more mesh points in the transverse direction to get the washcoat diffusion described more accurately.

4.3.3 Mesh size dependency of detailed Short Monolith model

Fig. 4.4 shows the comparisons of the solutions of the detailed model with different number of mesh points in the washcoat. The lines of NO results, from top to the bottom show the exit concentration of NO with 6 mesh points, 10 mesh points, 30 mesh points, 100 mesh points and 200 mesh points in the washcoat layer (In all cases, the mesh is uniform]. We note that with the increase in the number of mesh points, the NO conversion also increases, until the number of mesh points reaches about 100. The results of 100 and 200 mesh points almost overlap. A similar trend can also be observed in NO₂ effluent profiles. [Again, it should be pointed out that most simulations of single or dual layered monolith reactors do not take this many mesh points to obtain mesh size independent solution and this computation of mesh size independent solution is done more easily for the short monolith model than the long channel model]. We also note that according to our calculation results, in this specific example, the largest eigenvalue (in magnitude) of Φ_2^2 changes from 10³ to 10⁴ during this calculation (see Appendix B for further details). *Fig. 4.4*

validates that the approximate number of mesh points beyond which the solution becomes mesh independent is approximately equal to (or higher than) the square root of the largest eigenvalue (in magnitude) of Φ_2^2 , as can be expected from the general theory of multi-component diffusion-reaction in the washcoat, see ?. [Remark: In this specific application, washcoat diffusional impact is higher in the LNT layer as the reaction time scales in the SCR layer are much larger than those in the LNT layer. In other applications, washcoat diffusional effect can be important in either layer or both].

We also record the computation times for each case (Desktop Computer: Intel Core i7-8700 CPU, installed RAM: 16GB): 6 mesh points in washcoat: 13.5 s , 10 mesh points in washcoat: 23.0 s , 15 mesh points in washcoat: 55.1 s , 30 mesh points in washcoat: 162.8 s , 100 mesh points in washcoat: 452.7 s, 200 mesh points in washcoat: 1192.0 s. The main observation here is that the computation time increases more than linearly with the number of mesh points.

4.3.4 Comparison of detailed and reduced order model results

According to *Fig. 4.4*, exit NO and NO₂ concentrations basically remain the same after increasing the number of mesh points to 100. Thus, in this section we compare the results of detailed model with 100 points in the washcoat layer with the reduced order model with the Thiele matrix based Sherwood numbers as well as with constant (asymptotic) internal Sherwood numbers.

Fig. 4.5 and *4.6* show the comparison between asymptotic approximation, Thiele matrix solution and detailed solution with 100 mesh points in the washcoat layer. *Fig. 4.5* shows the result of exit NO concentration while *Fig. 4.6* shows the result of exit NO₂ concentration.

In *Fig. 4.5*, the NO result of the Thiele matrix solution which is the blue line with 'x' marker is almost identical with the red line which is the detailed solution. We can also observe similar results for NO₂ in *Fig. 4.6*. The Thiele matrix solu-

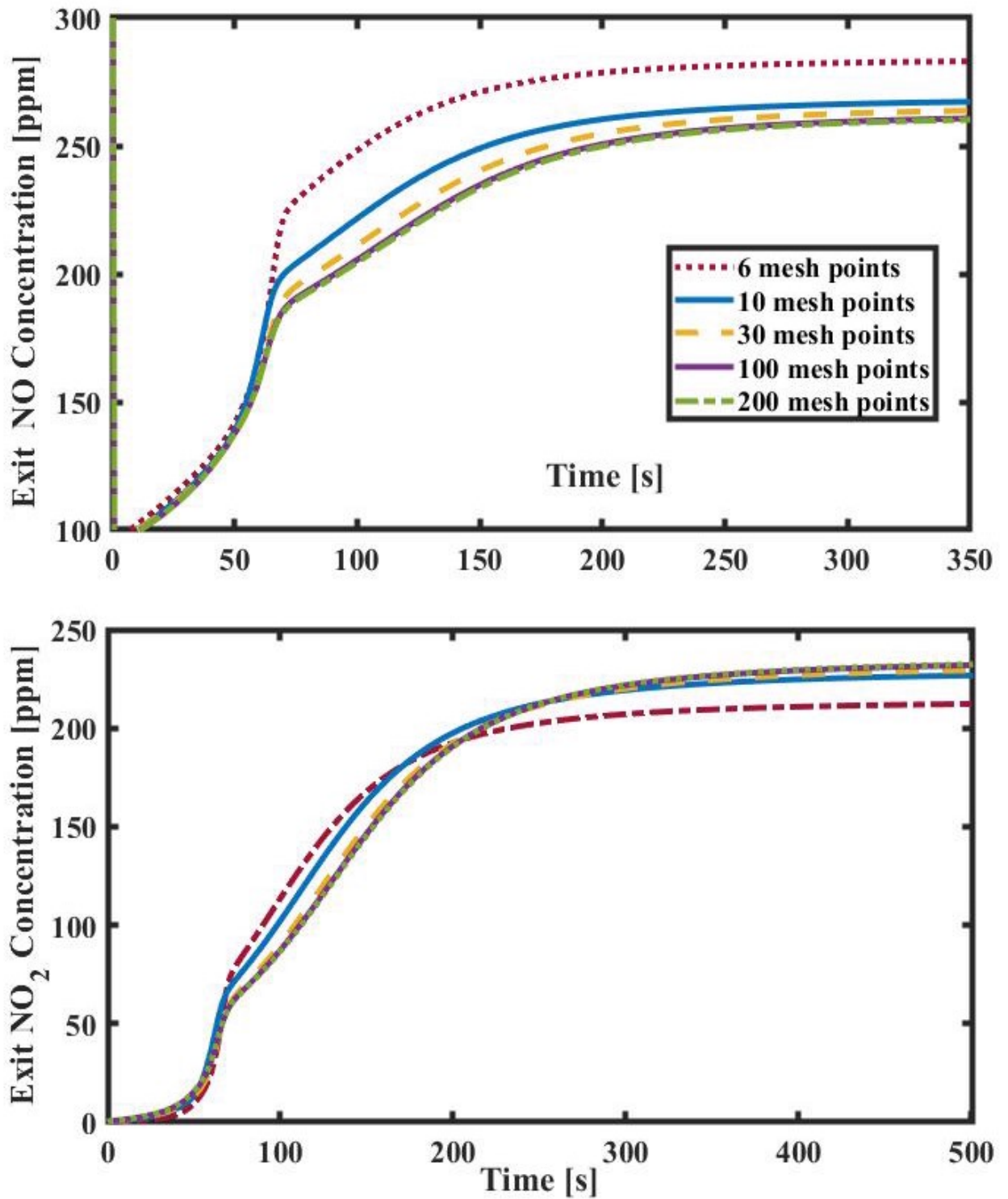


Figure 4.4: Comparison of predicted NO and NO₂ exit concentrations during storage with different number of mesh points for the Short Monolith model.

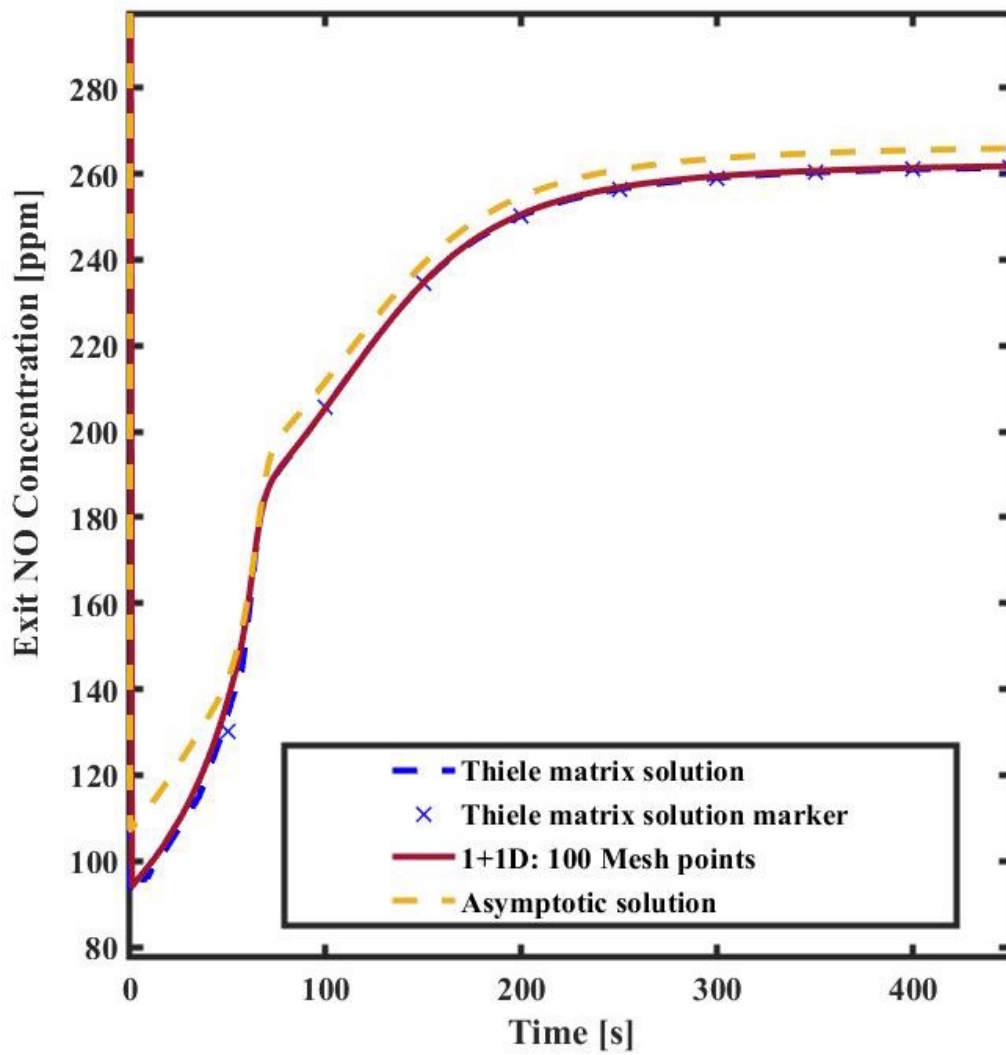


Figure 4.5: Comparison of NO exit concentrations predicted by the reduced order and detailed models

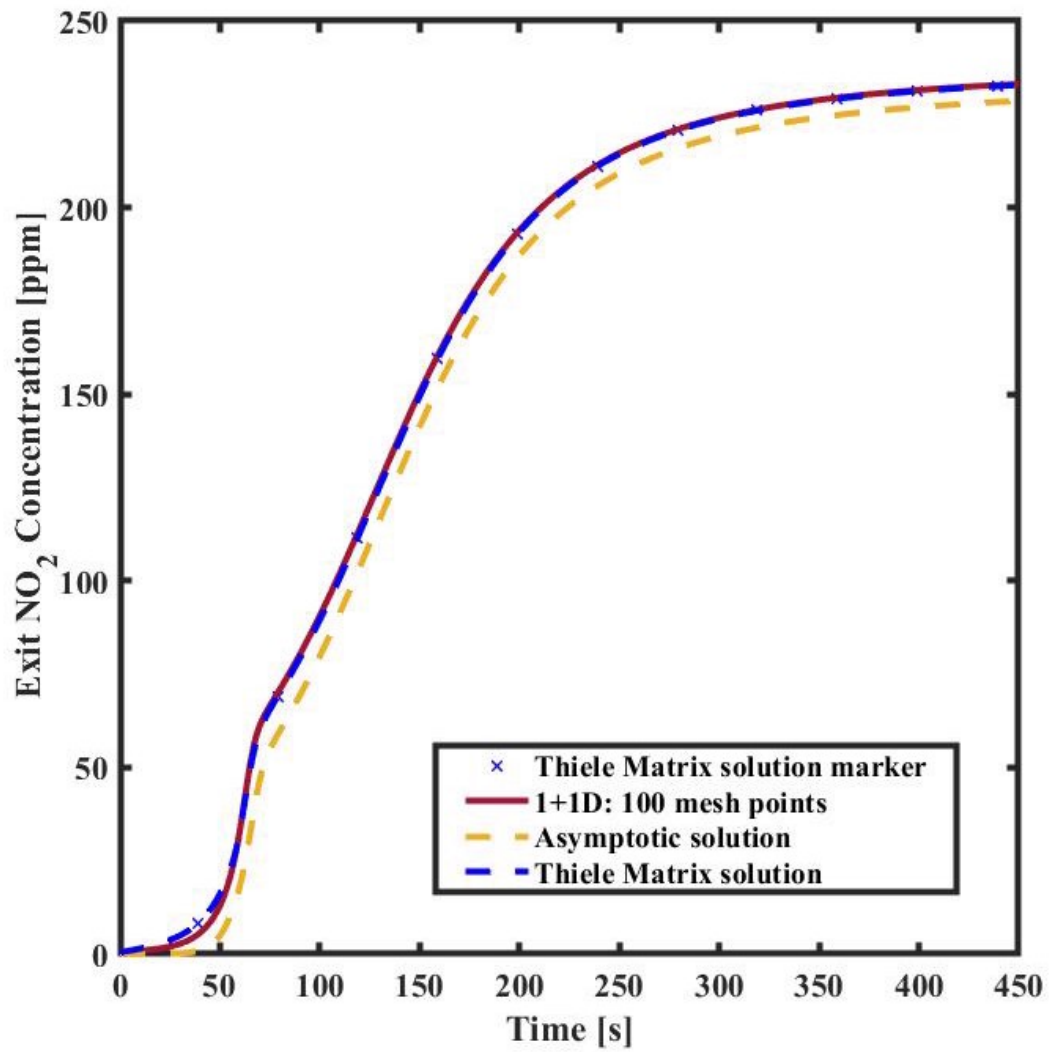


Figure 4.6: Comparison of NO₂ exit concentrations predicted by reduced order and detailed models

tion is closer to the detailed model solution which has sufficient mesh points. This observation also applies to the lean-rich cycling simulations. *Fig. 4.7* shows the lean-rich cycling results of different approximations. For each cycle, we run 80 seconds lean phase and 20 seconds rich phase [While the figures show the comparison over two cycles after a periodic steady-state is attained, the simulations are run for a duration of about eight cycles]. The inlet conditions for the lean-rich cycling are shown in *Table 4.7*. Again, the Thiele matrix solution shows higher accuracy compared to the asymptotic solution and sufficient accuracy when compared to the detailed model with sufficient number of mesh points. What should be noted is that except the case with cycling input, *Fig. 4.4* to *4.6* only involve NOx storage reactions in the LNT layer, so that we have a 3×3 Thiele matrix in LNT layer and reaction rate is negligible in the SCR layer. Hence, the SCR layer acts as an inert diffusion layer and Sh_{i1} , \widehat{Sh}_{i1} , \widehat{Sh}_{e1} and Sh_{i1} depends on the asymptotic Sherwood number. While in the case with cycling input condition, both LNT and SCR layers become active with NOx storage, regeneration and reduction steps, Φ_2^2 is a 5×5 matrix which involves the species NO , NO_2 , O_2 , H_2 and NH_3 ; Φ_1^2 is also a 5×5 matrix that includes NH_4NO_3 but excludes H_2 . The asymptotic solution also shows good approximation because in this specific example, the reactions are not fast in the SCR layer [This may also be due to lower temperature selected or smaller value used for the thickness of the SCR layer]. Asymptotic approximation can perform very bad when washcoat diffusion control is the dominant regime or when the washcoat diffusion limitation is very strong. To clarify this, we show two more cases at 370°C and higher space velocity ($\langle u \rangle = 4.9 \times \left(\frac{T}{273.15}\right) \times \left(\frac{a}{a-2 \times \delta_c}\right)^2$ m/s) with only storage reactions in the LNT layer since LNT layer contains fast kinetics. *Fig. 4.8* and *4.9* are the comparison of 1+1D model and reduced order model results in a short monolith reactor. Solid purple and light blue lines are results of ignoring washcoat diffusion limitation and asymptotic solution, respectively. It can

be observed that these two lines are far from the middle lines. Dashed pink, dotted yellow, dash-dotted green, solid red and dashed blue lines are the results of 1+1D model with 20, 30, 60, 100 and 200 mesh points in the LNT layer, respectively. The Thiele matrix result is denoted by the solid black line. As the number of mesh points increases, the 1+1D solution comes closer to the Thiele matrix solution and as mentioned before, the largest eigenvalue of Thiele matrix Φ_2^2 is about 4×10^4 . Compared to the Thiele matrix solution, both ignoring the washcoat diffusion limitation and asymptotic solution give about 30% to 40% error. *Fig. 4.10* shows a comparison of different reduced order models with a lower diffusivities $D_e(D_{e,j} = D_{f,j}/1000)$. In this case, the largest eigenvalue of the Thiele matrix Φ_2^2 increases by another factor of 10 which means the diffusion in the washcoat layer become stronger and the concentration gradient is even larger than previous case. Asymptotic solution which is the solid green line and ignoring washcoat diffusion which is the dashed blue line in *Fig. 4.10* give more than 80% error compared to the Thiele matrix solution. Asymptotic solution performs bad because of the lower estimation of concentration gradient which leads to a smaller mass transfer coefficient.

The computation time for each solution in *Fig. 4.5* to *4.7* is: Asymptotic solution with steady state input : 0.67 s , Thiele matrix solution with steady state input: 2.5 s, asymptotic solution with lean rich cycling input: 5.4 s, Thiele matrix solution with lean rich cycling input: 16.0 s. Detailed model (100 mesh points) with lean rich cycling input: 11388 s. Thus, the computation time of Thiele matrix is lower by about a factor 700 compared to the detailed model with 100 mesh points in both steady state and cycling input case.

These comparisons may be used to obtain an estimate of the simulation time for the reduced order model using the Thiele matrix approach versus obtaining mesh independent solution of the full length (long channel) detailed model. For ex-

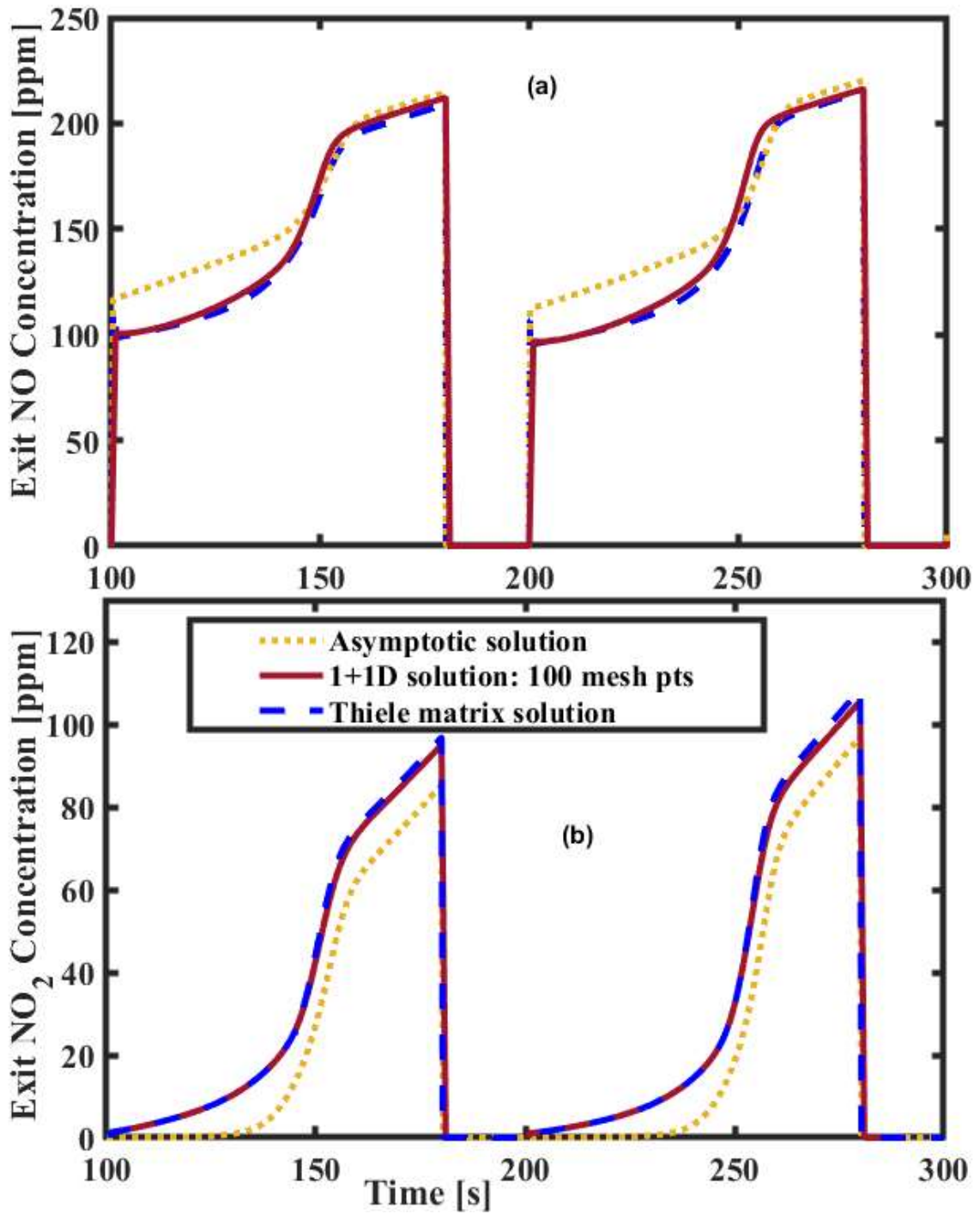


Figure 4.7: Comparison of NO and NO₂ exit concentrations with lean-rich cycling using reduced order and detailed models.

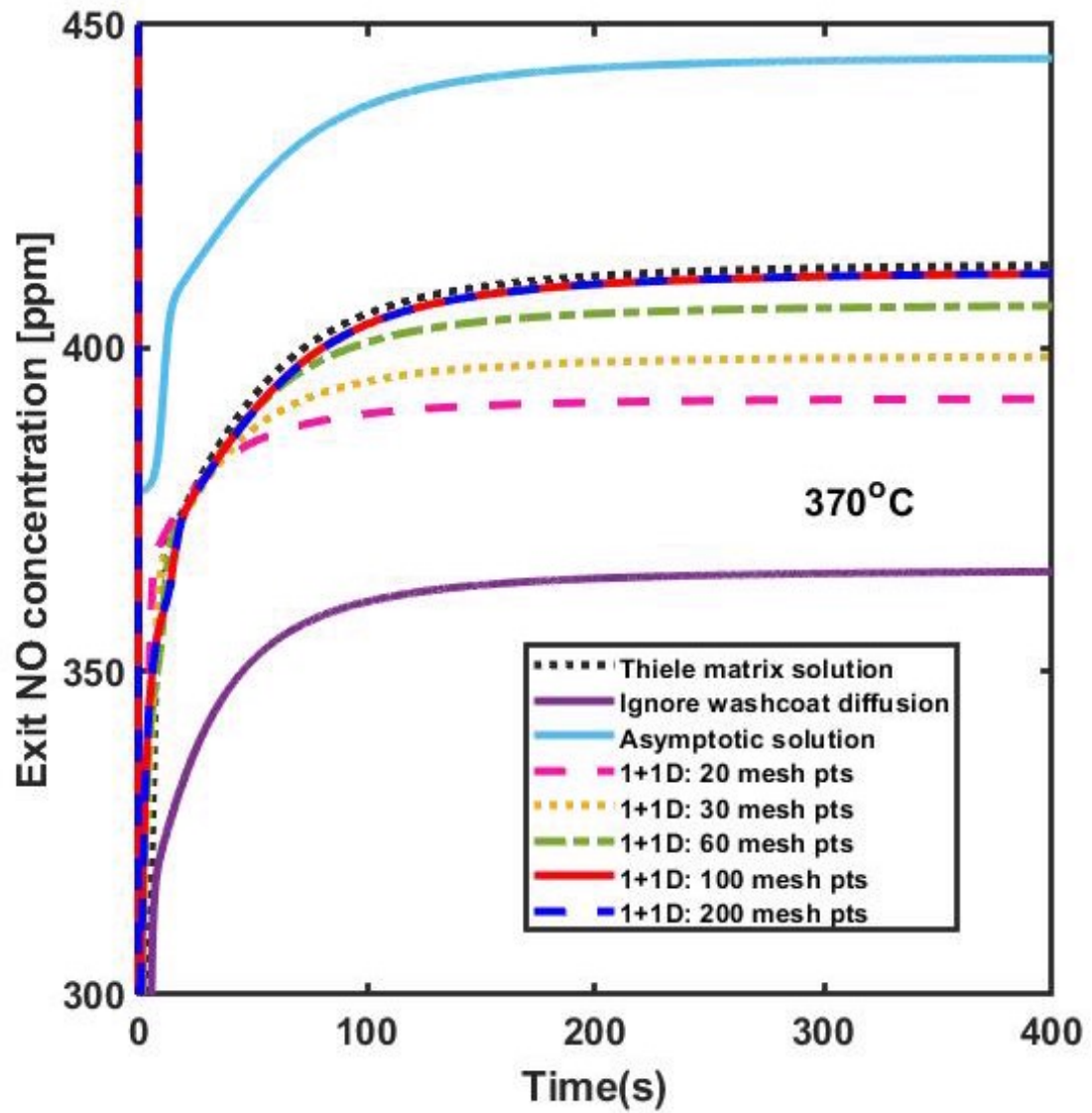


Figure 4.8: Comparison of exit NO concentration predicted by 1+1D model and reduced order model solutions in a short monolith reactor with higher temperature and space velocity

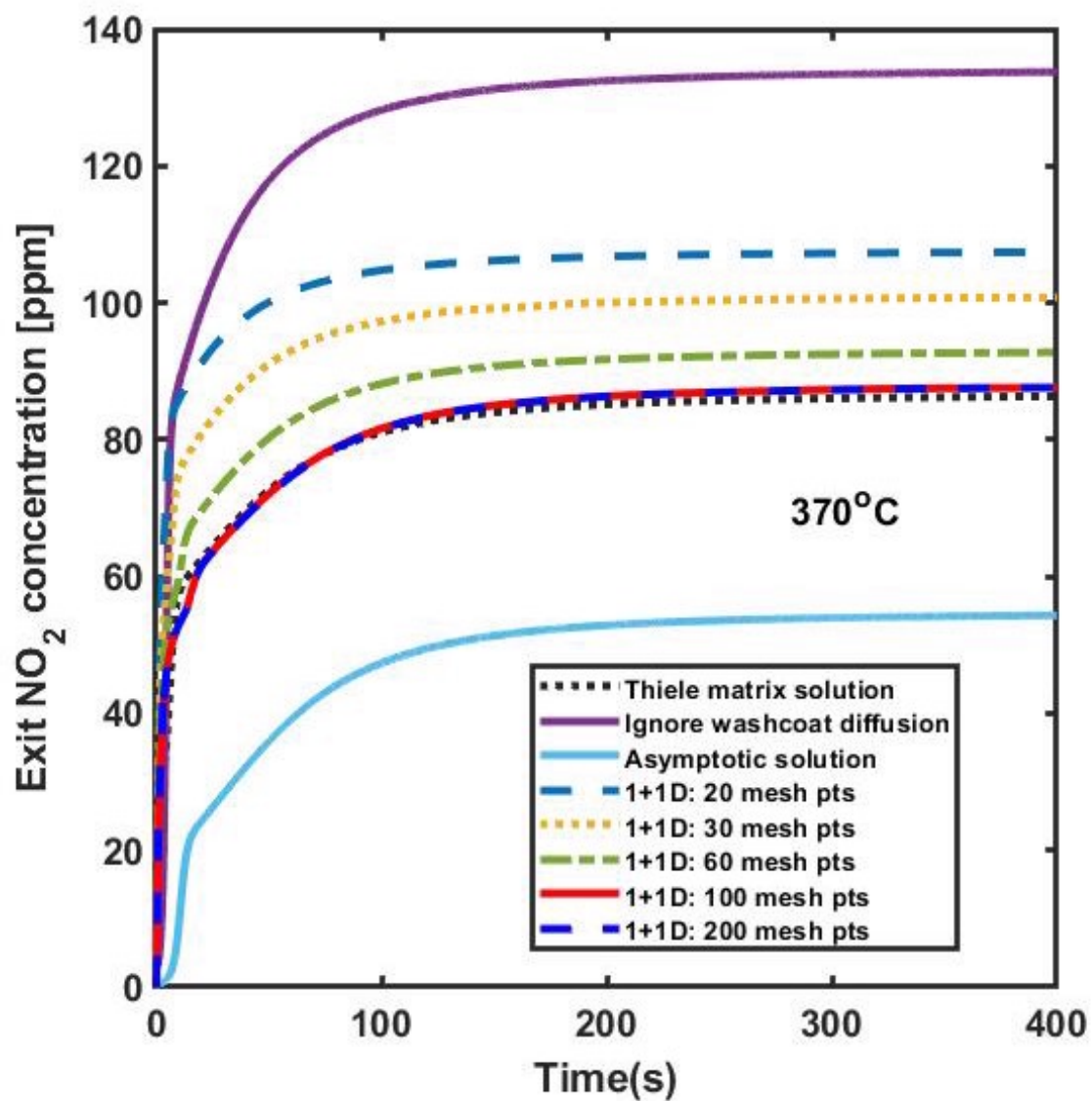


Figure 4.9: Comparison of exit NO₂ concentration between 1+1D model and reduced order model solutions in a short monolith reactor with higher temperature and space velocity

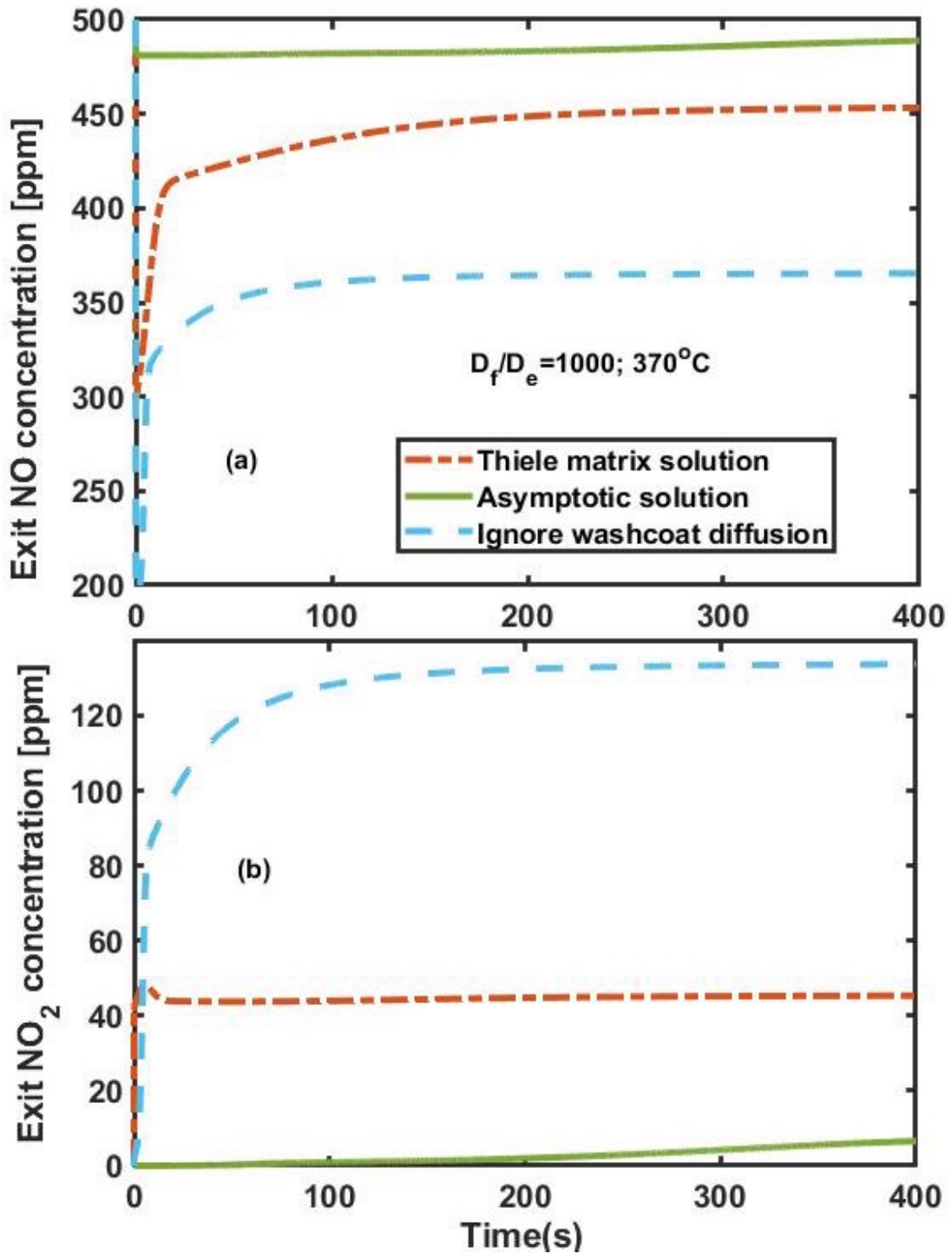


Figure 4.10: Comparison between different reduced order model solutions with a lower D_e ($D_{e,j} = D_{f,j}/1000$): (a) Exit NO concentration (b) Exit NO₂ concentration

ample, if 100 mesh points are also used in the axial direction, then the simulation time for both increases by factor 100 (while the speed-up factor remains approximately the same if memory requirements are not a problem), which indicates that the computations for the detailed model cannot be done in real time using a desktop computer. We expect the speed up factor to increase further with increase in temperature and/or more complex micro-kinetic models containing much shorter adsorption/desorption or reaction time scales.

4.4 Conclusions and Discussion

In this chapter, we present a reduced order model for real time simulations of dual layered monolith reactors. As stated in the introduction, it is a common practice in the literature to use detailed and/or micro-kinetic models to describe the various reactions occurring in the washcoat layers. However, an accurate assessment of the washcoat diffusional effects with such detailed kinetic models also requires extremely fine mesh (within the washcoat layer) and the number of mesh points (at which the computed solution becomes independent of the mesh size) depends on the characteristic time scales associated with the kinetic model or the washcoat Thiele modulus based on the largest eigenvalue of the Jacobian matrix of the local species formation rate vector. For example, a typical value for species effective diffusivity in a washcoat layer is of the order $10^{-6} m^2/s$, while adsorption and/or reaction time scales could be as small as $10^{-8} s$, which leads to an associated length scale of $0.1 \mu m$ (based on Thiele modulus of unity). This leads to a washcoat Thiele modulus of 300 for a layer of thickness of $30 \mu m$ and requiring as many mesh points (or higher) for an accurate solution. In our view, most literature studies that use detailed or micro-kinetic models either do not take such fine mesh or do not verify the mesh size independence of the computed solutions, and if verified, real time simulations of such systems may be impractical. The approach presented here can speed up calculations by orders of magnitude while retaining

the accuracy of the computed solutions. We have illustrated the method for the case of a dual layered LNT+SCR system with 8 reactions in the SCR layer and 11 reactions in the LNT layer. Obviously, the power of the method is enhanced in systems with more reactions and/or much smaller chemistry time scales in one of the catalyst layers and/or at higher temperatures. Actually, it may be shown that for the case of first principles based micro-kinetic models (instead of global or empirical or pseudo micro-kinetic models), the Thiele matrix method is even more powerful because the Thiele matrix becomes diagonal, so that the speed of Thiele matrix approach is same as the asymptotic solution but much more accurate than the asymptotic solution. The details of the computations are discussed in next chapter.

Table 4.1: Effective diffusion lengths, asymptotic internal Sherwood number and Λ^* for some common channel and washcoat shapes

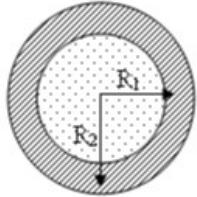
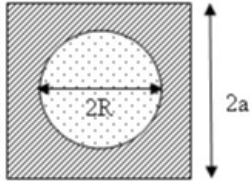
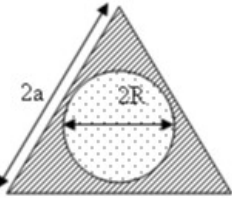
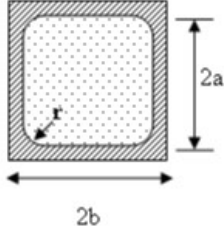
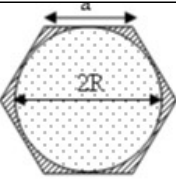
Channel Shape	R_{Ω_1}	δ_{Ω_c}	$Sh_{i\infty}$ and Λ^*												
	a	b-a	$Sh_{i\infty} = 3$ and $\Lambda^* = 0.18$												
	$R_1/2$	$(R_2^2 - R_1^2)/(2R_1)$	<table border="1"> <thead> <tr> <th>R_2/R_1</th> <th>$Sh_{i\infty}$</th> <th>Λ^*</th> </tr> </thead> <tbody> <tr> <td>1.01</td> <td>3.0125</td> <td>0.20</td> </tr> <tr> <td>1.1</td> <td>3.153</td> <td>0.19</td> </tr> <tr> <td>1.2</td> <td>3.311</td> <td>0.18</td> </tr> </tbody> </table>	R_2/R_1	$Sh_{i\infty}$	Λ^*	1.01	3.0125	0.20	1.1	3.153	0.19	1.2	3.311	0.18
R_2/R_1	$Sh_{i\infty}$	Λ^*													
1.01	3.0125	0.20													
1.1	3.153	0.19													
1.2	3.311	0.18													
	$R/2$	$(4a^2 - \pi R^2)/(2\pi R)$	<table border="1"> <thead> <tr> <th>a/R</th> <th>$Sh_{i\infty}$</th> <th>Λ^*</th> </tr> </thead> <tbody> <tr> <td>1</td> <td>0.826</td> <td>0.45</td> </tr> <tr> <td>1.1</td> <td>1.836</td> <td>0.46</td> </tr> <tr> <td>1.2</td> <td>2.533</td> <td>0.31</td> </tr> </tbody> </table>	a/R	$Sh_{i\infty}$	Λ^*	1	0.826	0.45	1.1	1.836	0.46	1.2	2.533	0.31
a/R	$Sh_{i\infty}$	Λ^*													
1	0.826	0.45													
1.1	1.836	0.46													
1.2	2.533	0.31													
	$R/2$	$(\sqrt{3}a^2 - \pi R^2)/(2\pi R)$	<table border="1"> <thead> <tr> <th>a/R</th> <th>$Sh_{i\infty}$</th> <th>Λ^*</th> </tr> </thead> <tbody> <tr> <td>1.7321</td> <td>0.84</td> <td>0.42</td> </tr> <tr> <td>1.9245</td> <td>1.45</td> <td>0.53</td> </tr> <tr> <td>2.4744</td> <td>2.92</td> <td>0.31</td> </tr> </tbody> </table>	a/R	$Sh_{i\infty}$	Λ^*	1.7321	0.84	0.42	1.9245	1.45	0.53	2.4744	2.92	0.31
a/R	$Sh_{i\infty}$	Λ^*													
1.7321	0.84	0.42													
1.9245	1.45	0.53													
2.4744	2.92	0.31													
	$\frac{(4a^2 - 4r^2 + \pi r^2)}{(2\pi r + 8a - 8r)}$	$\frac{(4b^2 - 4a^2 + 4r^2 - \pi r^2)}{(2\pi r + 8a - 8r)}$	<table border="1"> <thead> <tr> <th>b/a</th> <th>b/r</th> <th>$Sh_{i\infty}$</th> <th>Λ^*</th> </tr> </thead> <tbody> <tr> <td>1.11</td> <td>5</td> <td>2.65</td> <td>0.21</td> </tr> <tr> <td>1.25</td> <td>10</td> <td>3.09</td> <td>0.20</td> </tr> </tbody> </table>	b/a	b/r	$Sh_{i\infty}$	Λ^*	1.11	5	2.65	0.21	1.25	10	3.09	0.20
b/a	b/r	$Sh_{i\infty}$	Λ^*												
1.11	5	2.65	0.21												
1.25	10	3.09	0.20												
	$R/2$	$(3\sqrt{3}a^2 - 2\pi R^2)/(4\pi R)$	<table border="1"> <thead> <tr> <th>a/R</th> <th>$Sh_{i\infty}$</th> <th>Λ^*</th> </tr> </thead> <tbody> <tr> <td>1.155</td> <td>0.814</td> <td>0.50</td> </tr> <tr> <td>1.17</td> <td>1.16</td> <td>0.76</td> </tr> <tr> <td>1.2</td> <td>1.74</td> <td>0.54</td> </tr> </tbody> </table>	a/R	$Sh_{i\infty}$	Λ^*	1.155	0.814	0.50	1.17	1.16	0.76	1.2	1.74	0.54
a/R	$Sh_{i\infty}$	Λ^*													
1.155	0.814	0.50													
1.17	1.16	0.76													
1.2	1.74	0.54													
Where washcoat and flow area are designated as shown below:															
															

Table 4.2: Effective diffusion lengths, asymptotic internal Sherwood and cross-Sherwood numbers for some common washcoat shapes

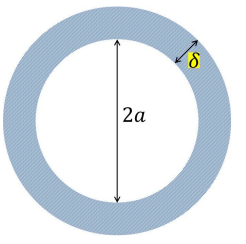
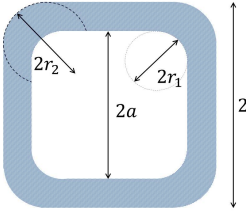
Channel Shape	$\delta_{\Omega w} = \frac{2A_{\Omega w}}{P_{\Omega_1} + P_{\Omega_2}}$	$Sh_{\Omega\infty}$																				
	δ	<table border="1"> <thead> <tr> <th>$Sh_{i\infty}$</th> <th>$\widehat{Sh}_{i\infty}$</th> <th>$Sh_{e\infty}$</th> <th>$\widehat{Sh}_{e\infty}$</th> </tr> </thead> <tbody> <tr> <td>3</td> <td>6</td> <td>3</td> <td>6</td> </tr> </tbody> </table>	$Sh_{i\infty}$	$\widehat{Sh}_{i\infty}$	$Sh_{e\infty}$	$\widehat{Sh}_{e\infty}$	3	6	3	6												
$Sh_{i\infty}$	$\widehat{Sh}_{i\infty}$	$Sh_{e\infty}$	$\widehat{Sh}_{e\infty}$																			
3	6	3	6																			
	$(b - a)$	<table border="1"> <thead> <tr> <th>b/a</th> <th>$Sh_{i\infty}$</th> <th>$\widehat{Sh}_{i\infty}$</th> <th>$Sh_{e\infty}$</th> <th>$\widehat{Sh}_{e\infty}$</th> </tr> </thead> <tbody> <tr> <td>1.01</td> <td>3.00</td> <td>5.97</td> <td>3.00</td> <td>6.03</td> </tr> <tr> <td>1.1</td> <td>3.00</td> <td>5.73</td> <td>3.00</td> <td>6.30</td> </tr> <tr> <td>1.2</td> <td>3.01</td> <td>5.51</td> <td>3.01</td> <td>6.61</td> </tr> </tbody> </table>	b/a	$Sh_{i\infty}$	$\widehat{Sh}_{i\infty}$	$Sh_{e\infty}$	$\widehat{Sh}_{e\infty}$	1.01	3.00	5.97	3.00	6.03	1.1	3.00	5.73	3.00	6.30	1.2	3.01	5.51	3.01	6.61
b/a	$Sh_{i\infty}$	$\widehat{Sh}_{i\infty}$	$Sh_{e\infty}$	$\widehat{Sh}_{e\infty}$																		
1.01	3.00	5.97	3.00	6.03																		
1.1	3.00	5.73	3.00	6.30																		
1.2	3.01	5.51	3.01	6.61																		
	$\frac{b^2 - a^2 - (1 - \frac{\pi}{4})(r_2^2 - r_1^2)}{b + a - (1 - \frac{\pi}{4})(r_2 + r_1)}$	<table border="1"> <thead> <tr> <th>$\frac{b}{a}$</th> <th>$\frac{r_1}{a} = \frac{r_2}{b}$</th> <th>$Sh_{i\infty}$</th> <th>$\widehat{Sh}_{i\infty}$</th> <th>$Sh_{e\infty}$</th> <th>$\widehat{Sh}_{e\infty}$</th> </tr> </thead> <tbody> <tr> <td>1.1</td> <td>0.2</td> <td>2.9</td> <td>5.9</td> <td>3.0</td> <td>6.1</td> </tr> <tr> <td>1.1</td> <td>0.5</td> <td>2.9</td> <td>5.9</td> <td>3.0</td> <td>6.3</td> </tr> </tbody> </table>	$\frac{b}{a}$	$\frac{r_1}{a} = \frac{r_2}{b}$	$Sh_{i\infty}$	$\widehat{Sh}_{i\infty}$	$Sh_{e\infty}$	$\widehat{Sh}_{e\infty}$	1.1	0.2	2.9	5.9	3.0	6.1	1.1	0.5	2.9	5.9	3.0	6.3		
$\frac{b}{a}$	$\frac{r_1}{a} = \frac{r_2}{b}$	$Sh_{i\infty}$	$\widehat{Sh}_{i\infty}$	$Sh_{e\infty}$	$\widehat{Sh}_{e\infty}$																	
1.1	0.2	2.9	5.9	3.0	6.1																	
1.1	0.5	2.9	5.9	3.0	6.3																	

Table 4.3: Temperature dependent parameters used in the simulation

Constant	Value/Expression
$\langle u \rangle$	$4.9 \times 10^{-1} \times \left(\frac{T}{273.15}\right) \times \left(\frac{R_d}{R_d - 2 \times R_{\Omega}}\right)^2 \text{ m/s}$
C_T	$\frac{1 \text{ bar}}{8.314 \times T} \text{ mol/m}^3$
$D_{f,NO}$	$1.13 \times 10^{-9} \times T^{1.7148} \text{ m}^2/\text{s}$
D_{f,NO_2}	$0.91 \times 10^{-9} \times T^{1.7148} \text{ m}^2/\text{s}$
D_{f,O_2}	$1.13 \times 10^{-9} \times T^{1.7019} \text{ m}^2/\text{s}$
D_{f,H_2}	$5.83 \times 10^{-9} \times T^{1.6725} \text{ m}^2/\text{s}$
D_{f,NH_3}	$1.62 \times 10^{-9} \times T^{1.7033} \text{ m}^2/\text{s}$
D_{f,NH_4NO_3}	$0.75 \times 10^{-9} \times T^{1.7033} \text{ m}^2/\text{s}$

Table 4.4: Numerical constants and parameters used in model simulation

Constant	Value
a	1.1 mm
R_{Ω}	250×10^{-6} m
$\delta_{c1(SCR)}$	10×10^{-6} m
$\delta_{c2(LNT)}$	20×10^{-6} m
L	2×10^{-2} m
$\epsilon_{w1(SCR)}$	0.4
$\epsilon_{w2(LNT)}$	0.4

Table 4.5: Reaction scheme used in the Shakya et al. model for the SCR layer

No.	SCR Reaction
1	$NH_3(g) + S1 \leftrightarrow NH_3 - S1$
2	$2NH_3 - S1 + 1.5O_2(g) \leftrightarrow 3H_2O(g) + 2S1$
3	$NO(g) + 0.5O_2(g) \leftrightarrow NO_2(g)$
4	$4NH_3 - S1 + 4NO(g) + O_2(g) \longrightarrow 4N_2(g) + 6H_2O(g) + 4S1$
5	$2NH_3 - S1 + NO(g) + NO_2(g) \longrightarrow 2N_2(g) + 3H_2O(g) + 2S1$
6	$4NH_3 - S1 + 3NO_2(g) \longrightarrow 3.5N_2(g) + 6H_2O(g) + 4S1$
7	$2NH_3 - S1 + NO_2(g) \longrightarrow N_2(g) + NH_4NO_3(g) + H_2O(g) + 2S1$
8	$NH_4NO_3(g) \longrightarrow N_2O(g) + 2H_2O(g)$

Table 4.6: Reaction scheme used in the Shakya et al. model for the LNT layer

No.	LNT Reaction
1	$NO(g) + 0.5O_2(g) \leftrightarrow NO_2(g)$
2	$2NO_2(g) + 0.5O_2(g) + BaO_{(f)} \leftrightarrow Ba(NO_3)_{2(f)}$
3	$3NO_2(g) + BaO_{(s)} \leftrightarrow Ba(NO_3)_{2(s)} + NO(g)$
4	$Ba(NO_3)_{2(f)} \longrightarrow 2NO(g) + 1.5O_2(g) + BaO_{(f)}$
5	$Ba(NO_3)_{2(f)} + H_2(g) \longrightarrow 2NO(g) + 3H_2O(g) + BaO_{(f)}$
6	$Ba(NO_3)_{2(s)} + H_2(g) \longrightarrow 2NO(g) + 3H_2O(g) + BaO_{(s)}$
7	$Ba(NO_3)_{2(f)} + 10/3NH_3(g) \longrightarrow 8/3N_2(g) + 5H_2O(g) + BaO_{(f)}$
8	$Ba(NO_3)_{2(s)} + 10/3NH_3(g) \longrightarrow 8/3N_2(g) + 5H_2O(g) + BaO_{(s)}$
9	$2NO(g) + H_2(g) \longrightarrow N_2O(g)$
10	$NO(g) + 5/2H_2(g) \longrightarrow NH_3(g) + H_2O(g)$
11	$3/2NO(g) + NH_3(g) \longrightarrow 5/4N_2(g) + 3/2H_2O(g)$

Table 4.7: Simulation conditions

Variable	Lean Inlet	Rich Inlet
T	300 °C	
$X_{f,NO}^{in}$	500 ppm	0
X_{f,NO_2}^{in}	0	0
X_{f,O_2}^{in}	5%	0
X_{f,H_2}^{in}	0	5000 ppm
X_{f,NH_3}^{in}	0	0
$X_{f,NH_4NO_3}^{in}$	0	0
$C_{BaO(f)}$	75 mol/ m ³ wc	
$C_{BaO(s)}$	250 mol/ m ³ wc	
C_{pt}	14.9 mol/ m ³ wc	
C_s	4000 mol/ m ³ wc	

Table 4.8: Catalyst properties

Catalyst	Components	Composition(%wt of washcoat)
LNT	Pt/BaO/Al ₂ O ₃	2.48% Pt (dispersion = 8%); 13.0% BaO
SCR	Cu-chabazite	2.5% Cu

Chapter 5

Reduced order model for real time simulation of monolith reactor with micro-kinetics

5.1 Introduction

In chapter 2, we presented a novel method for computing washcoat diffusional effects in reduced order models with local property dependent internal and external transfer coefficients. The method includes washcoat diffusional effects by computing the internal Sherwood matrix which depends on the local Thiele matrix, defined in terms of the Jacobian of the rate vector at the local concentrations. In this chapter, we extend Thiele matrix approach further to include more detailed micro-kinetics. Micro-kinetics models have also been studied by many researchers for different catalysts, dating back to 1998, Nibbelke et al., [24] proposed a micro-kinetics model for CO oxidation over platinum catalyst in a monolith reactor, the model consists of species balance equations in the gas phase and catalyst site balance equations on the surface. Diffusion limitations were neglected in radial direction, convection is also dominant than diffusion in the axial direction. This model was later used by Harmsen et al., [25] in his micro-kinetics study of acetylene and CO oxidation over a Pt/Rh/CeO₂/γ-Al₂O₃ catalyst. In 2004, Koci et al., [26] used a spatially pseudo-dimensional, heterogeneous model to study the micro-kinetics of three-way catalysts. The model Koci et al. used is a so-called 1+1 model which consists of a two-form mass balance equation in the gas phase, a mass balance equation in the washcoat with a detailed washcoat pore diffusion term and catalyst site balance for absorbed species, the model also includes enthalpy balance in gas and washcoat layer. In 2011, Rankovic et al., [27] studied the micro-kinetics model of oxidation of CO/H₂ mixture over Pt/Al₂O₃ and Rh/Al₂O₃ with more than a hundred reaction steps, they simplified the model as a stirred reactor model which

is like a short monolith model and ignored the mass transfer limitation in the radial direction. Recently, Keller et al., [28] and Stotz et al., [29] studied surface reaction of methane oxidation over PdO catalyst using a steady state micro-kinetics model with detailed species, energy and momentum balance equations. We found that the models in the literature either ignore the washcoat diffusion limitation term or include the internal diffusion effect but do not show mesh size dependency on the model accuracy.

To summarize, it is our view that most literature studies that use micro-kinetics models either ignore the washcoat diffusional effects or do not show the mesh size independency of the computed solutions. As is well known, kinetic parameters that are derived from a mesh size dependent model are diffusion disguised. Our experience indicates that due to the short time and length scales associated with the micro-kinetics models, the computation of the mesh size independent solutions of the monolith models requires a large number of mesh points within the washcoat and is demanding in terms of time and memory requirements. In this work, we show that the discretized model describes the washcoat diffusional effects accurately only when the number of mesh points in washcoat layer is about equal to the square root of the magnitude of the largest eigenvalue of the Thiele matrix Φ^2 . We present a multi-mode reduced order model that eliminates the degrees of freedom associated with species diffusion in the washcoat using the internal mass transfer coefficient matrix. This matrix is shown to be diagonal for most micro-kinetics models of practical interest and can be calculated very accurately. We compare the speed and accuracy of the reduced order model solution with the detailed model and show that Thiele matrix solution is not only closer to detailed model which has sufficient mesh points but can speed up calculations by about three orders of magnitude.

This chapter is organized as follows: in the next section, we review the detailed

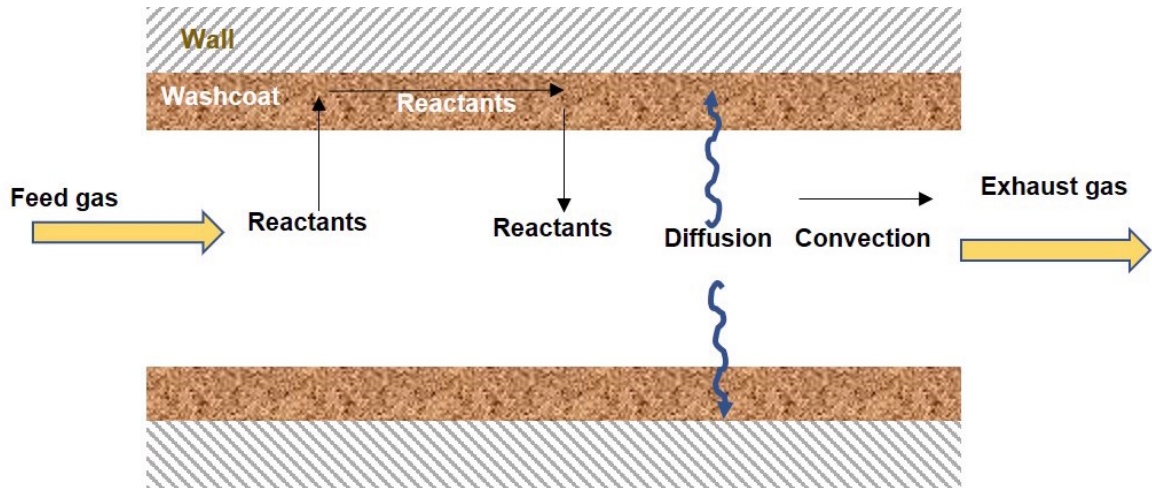


Figure 5.1: Schematic of a monolith channel with a single washcoat layer

(1+1D) diffusion–convection–reaction model for a catalytic monolith reactor with single washcoat layers and present the reduced order model equations. We also discuss the detailed steps involved in the computation of the local property dependent mass transfer coefficient matrices. In section 3, we illustrate the application of the reduced order model with a specific example of $H_2/CO/C_3H_6$ oxidation Pt/Al_2O_3 . We illustrate the results of mesh size dependency and comparisons between the detailed solution and reduced order model solution. In the last section, we summarize the main contributions of this work and discuss some possible extensions.

5.2 Mathematical Modeling

In the following sections, we present the model equations for the standard 1+1D model and a traditional two-mode form of reduced-order model. This is followed by a review of the Thiele matrix approach and then our procedure for extending it to the case of micro-kinetics. Since our goal is to explain the main concepts using the simplest geometry (i.e., parallel plate channel: *Fig. 5.1*) we present the various formulas and results for this case, and indicate only briefly extension to other geometries.

5.2.1 Detailed(1+1D) washcoat diffusion model

For the traditional 1+1D model, the gas phase and washcoat species balances and are given by the vector equations

$$\frac{\partial \mathbf{C}_{fm}}{\partial t} + \langle u \rangle \frac{\partial \mathbf{C}_{fm}}{\partial x} = -\frac{\mathbf{k}_{me}}{R_{\Omega}} (\mathbf{C}_{fm} - \mathbf{C}_s); \quad x > 0, t > 0 \quad (5.1)$$

$$\text{and } \epsilon_w \frac{\partial \mathbf{C}_{wc}}{\partial t} = \mathbf{r}_g(\mathbf{C}_{wc}, \boldsymbol{\theta}_w) + \mathbf{D}_e \frac{\partial^2 \mathbf{C}_{wc}}{\partial y^2}; \quad 0 < y < \delta_c, \quad (5.2)$$

while the species coverage vector on the catalytic sites is given by

$$C_M \frac{\partial \boldsymbol{\theta}_w}{\partial t} = \mathbf{r}_s(\mathbf{C}_{wc}, \boldsymbol{\theta}_w). \quad (5.3)$$

Since the wall is assumed to be non-porous, the species fluxes at the wall-washcoat interface vanish, i.e.,

$$\left. \frac{\partial \mathbf{C}_{wc}}{\partial y} \right|_{y=\delta_c} = \mathbf{0}. \quad (5.4)$$

The continuity of the species fluxes at the fluid-washcoat interface leads to the interfacial boundary condition:

$$\mathbf{j}_{fw} = \mathbf{k}_{me} (\mathbf{C}_{fm} - \mathbf{C}_s) = -\mathbf{D}_e \left. \frac{\partial \mathbf{C}_{wc}}{\partial y} \right|_{y=0}; \quad \mathbf{C}_s = \mathbf{C}_{wc}|_{y=0}. \quad (5.5)$$

In these equations, bold symbols are used to represent matrices and vectors. We choose to write the model equations in terms of species concentrations, though in after-treatment applications, it may be convenient to express them in terms of species mole fractions. Here, the column vectors, \mathbf{C}_{fm} and $\mathbf{C}_{wc} \in \mathbb{R}^N$, represent the cup-mixing concentration in the fluid phase and the species concentration vector in the washcoat, respectively; R_{Ω} represents the hydraulic radius of the monolith channel, $\langle u \rangle$ is the average velocity in the channel, the column vector $\mathbf{C}_s \in \mathbb{R}^N$ is the species concentration vector at the fluid-washcoat interface and \mathbf{k}_{me} is the ma-

trix of external mass transfer coefficients defined by the first equality of *Eq. 5.5*. In *Eq. 5.3*, C_M is the total concentration of the catalytic sites and the j -th component of $\mathbf{r}_s(\mathbf{C}_{wc}, \boldsymbol{\theta}_w)$ represents the net rate of formation of surface species j at a particular position in the washcoat. Similarly, the i -th component of $\mathbf{r}_g(\mathbf{C}_{wc}, \boldsymbol{\theta}_w)$ represents the net rate of formation of gas phase species i at a particular position within the washcoat. In writing the balance equations for the gas phase species, it is assumed that the micro-kinetic model is such that any species can react with vacant or adsorbed species on the catalyst surface (or no direct reaction between gas phase species), which is valid for Langmuir-Hinshelwood and Eley-Rideal type kinetics. Similarly, in writing the surface species balance, it is assumed that all surface species have zero diffusivity.

We note that the number of independent components in the coverage vector is equal to the number of surface species. [The fraction of vacant sites can be obtained by using the fact that the sum of all coverages is unity]. In *Eq. 5.2*, ϵ_w is the porosity of the washcoat, N is the total number of reacting gaseous species and the vector \mathbf{j}_{fw} represents the species fluxes at the fluid-washcoat interface. The parameter δ_c is the effective thickness of the washcoat, \mathbf{D}_e is assumed to be a diagonal matrix of effective (Knudsen) diffusivities of various species in the washcoat. In most after-treatment applications, the external mass transfer coefficient matrix is assumed to be diagonal as the reactive species concentrations are small compared to the major inert species (which is usually nitrogen).

The inlet and initial conditions for the above model are of the form

$$\text{Inlet.C. : } \mathbf{C}_{fm}(0, t) = \mathbf{C}_{f,in}(t) \quad (5.6)$$

$$\text{and Initial.C. : } \mathbf{C}_{fm}(x, 0) = \mathbf{C}_{fm}^0(x) ; \mathbf{C}_{wc}(x, y, 0) = \mathbf{C}_{wc}^0(x, y) ; \boldsymbol{\theta}_w(x, y, 0) = \boldsymbol{\theta}_w^0(x, y). \quad (5.7)$$

We shall refer to the isothermal model defined by *Eqs. 5.1-5.7* as the long channel

model. We note that the total number of (partial differential) equations in this model is $2N + N_s$, where N is the number of reacting gaseous species and N_s is the number of surface species. If washcoat diffusion is completely ignored (and C_{wc} and θ_w are assumed to be dependent only on x and t , Eq. 5.2 simplifies to

$$\epsilon_w \frac{\partial C_{wc}}{\partial t} = \mathbf{r}_g(C_{wc}, \theta_w) + \frac{k_{me}}{\delta_c} (C_{fm} - C_{wc}). \quad (5.8)$$

Eq. 5.1 with ($C_s = C_{wc}$), Eq. 5.8 and Eq. 5.3 define the two-phase plug flow model. This model is described by $(2N + N_s)$ hyperbolic partial differential equations in x and t .

If the upwind method is used to discretize the convective derivative in the gas phase species balance, the long channel model becomes a sequence of Short Monolith (SM) models (analogous to the so-called cell or tanks-in-series model for the homogeneous case):

$$\frac{\partial C_{fm,j}}{\partial t} = \langle u \rangle \frac{(C_{fm,j-1} - C_{fm,j})}{\Delta x} - \frac{k_{me}}{R_\Omega} (C_{fm,j} - C_{s,j}); \quad j = 1, 2, \dots, (5.9)$$

$$\epsilon_w \frac{\partial C_{wc,j}}{\partial t} = \mathbf{r}_g(C_{wc,j}, \theta_{w,j}) + D_e \frac{\partial^2 C_{wc,j}}{\partial y^2} \quad (5.10)$$

$$\text{and } C_M \frac{\partial \theta_{w,j}}{\partial t} = \mathbf{r}_s(C_{wc,j}, \theta_{w,j}), \quad (5.11)$$

where N_x is the number of cells (or $N_x - 1$ is the number of axial interior mesh points) and $\Delta x = \frac{L}{N_x}$. [Note that for $j = 1$ in Eq. 5.9, $C_{fm,0} = C_{fm,in}(t)$]. In the extreme case of a single cell ($N_x = 1$), the spatial dependence on x is eliminated and we get the SM model (similar to the two-phase CSTR model except for accounting for diffusion in the washcoat layer):

$$\frac{\partial C_{fm}}{\partial t} = -\frac{\langle u \rangle}{L} (C_{fm} - C_{fm,in}(t)) - \frac{k_{me}}{R_\Omega} (C_{fm} - C_s); \quad t > 0, \quad (5.12)$$

$$\epsilon_w \frac{\partial \mathbf{C}_{wc}}{\partial t} = \mathbf{r}_g(\mathbf{C}_{wc,j}, \boldsymbol{\theta}_{w,j}) + \mathbf{D}_e \frac{\partial^2 \mathbf{C}_{wc}}{\partial y^2}; 0 < y < \delta_c \quad (5.13)$$

$$\text{and } C_M \frac{\partial \boldsymbol{\theta}_w}{\partial t} = \mathbf{r}_s(\mathbf{C}_{wc}, \boldsymbol{\theta}_w), \quad (5.14)$$

with appropriate initial and boundary conditions. In this limiting case (of parabolic model), C_{fm} depends only on t while C_{wc} and $\boldsymbol{\theta}_w$ dependent on y and t . As discussed in the literature [1], this model retains all the qualitative features of the full system and is ideal for comparing the impact of washcoat diffusional effect as the complete monolith model is represented by a sequence of SM models. Finally, we note that when washcoat diffusion is completely ignored, the SM model reduces to a two-phase CSTR model described by $(2N + N_s)$ ordinary differential equations in time.

We note that if the washcoat diffusion term in the SM model is discretized using second order finite differences using N_y mesh points ($N_y > 2$), we obtain $[N+(N + N_s)N_y]$ ordinary differential equations in time, whereas for the long channel model this number becomes $[N+(N + N_s)N_y]N_x$. Thus, the simplification of the washcoat diffusion problem can speed up the calculations by a factor that is approximately equal to the number of mesh points needed in the washcoat to obtain a mesh independent solution.

Length and Time Scales:

In order to determine the difficulty involved in obtaining mesh independent solution of the full 1+1D model with micro-kinetics, it is instructive to examine the various length and time scales represented in the model. The time scales associated with convection (τ), external mass transfer (t_{mj}) and washcoat diffusion or internal mass transfer (t_{Dj}) are defined by

$$\tau = \frac{L}{\langle u \rangle}; \quad t_{mj} = \frac{R_\Omega^2}{D_{m,j}}; \quad t_{Dj} = \frac{\delta_c^2}{D_{e,j}}, \quad (5.15)$$

where R_Ω (δ_c) is the channel hydraulic radius (effective washcoat thickness), and $D_{m,j}$ ($D_{e,j}$) is the diffusivity of species j in the gas phase (effective diffusivity in the washcoat). In most after-treatment applications, the space time τ is in the range 0.01 to 1s, the external mass transfer time is in the range 0.001 to 0.01s, while the washcoat diffusion time varies in a wider range 10^{-5} to 1s (with the smaller value corresponding to thinner washcoats with larger pores and the larger value corresponding to thicker washcoats with small or partially blocked pores). In addition to these transport time scales, those associated with adsorption/desorption of the gas phase species on the catalytic sites are determined by the eigenvalues of the Jacobian of the rate vector $\mathbf{r}_g(\mathbf{C}_{wc}, \boldsymbol{\theta}_w)$ with respect to the species concentrations. As shown in the next section, this Jacobian matrix is diagonal for most micro-kinetic models of interest with typical eigenvalue (or effective first order rate constant for species adsorption, k_{aj}) is in the range 10^6 to $10^9 s^{-1}$, or the associated time scale ($t_{aj} = 1/k_{aj}$) is in the range 10^{-9} to $10^{-6} s$. [Remark: The lower bound corresponds to higher concentration of catalytic sites and a high value for sticking coefficient while the higher value is for the opposite case]. In addition to these N time scales, we also have N_s time scales associated with the reactions between surface species determined by the eigenvalues of the Jacobian of the rate vector $\mathbf{r}_s(\mathbf{C}_{wc}, \boldsymbol{\theta}_w)$ with respect to the coverage vector $\boldsymbol{\theta}_w$ (and the total concentration of catalytic sites in the washcoat). If the adsorbed species diffusivity is assumed to be zero then these surface reaction time scales only determine the system stiffness in time. In contrast, the stiffness in the spatial coordinate y (or washcoat depth) is determined by the Thiele modulus (squared) based on the effective adsorption rate constant defined by

$$\phi_{aj}^2 = \frac{k_{aj} \delta_c^2}{D_{e,j}} = \frac{t_{Dj}}{t_{aj}}. \quad (5.16)$$

[Equivalently, the length scale associated with species adsorption is $\sqrt{\frac{D_{e,j}}{k_{aj}}}$]. We note that for most micro-kinetic models of interest, this parameter is in the range

10^4 to 10^8 , which indicates that a large number of mesh points N_y (of the order of 10^2 to 10^4) are required to obtain mesh independent solution of the detailed model. This is illustrated in the numerical calculations presented in the next section.

5.2.2 Reduced-order model

To obtain the reduced order model, we average *Eqs. 5.2 and 5.3* over the depth of the washcoat, leading to

$$\epsilon_w \frac{\partial \langle \mathbf{C}_{wc} \rangle}{\partial t} = \frac{1}{\delta_c} \int_0^{\delta_c} \mathbf{r}_g(\mathbf{C}_{wc}, \boldsymbol{\theta}_w) dy - \frac{\mathbf{D}_e}{\delta_c} \frac{\partial \mathbf{C}_{wc}}{\partial y} \Big|_0 \quad (5.17)$$

$$\text{and} = \frac{1}{\delta_c} \int_0^{\delta_c} \mathbf{r}_g(\mathbf{C}_{wc}, \boldsymbol{\theta}_w) dy - \frac{\mathbf{j}_{fw}}{\delta_c}, \quad (5.18)$$

where the washcoat averaged quantities are defined by

$$\langle \mathbf{C}_{wc} \rangle = \frac{1}{\delta_c} \int_0^{\delta_c} \mathbf{C}_{wc}(y, t) dy ; \quad \langle \boldsymbol{\theta}_w \rangle = \frac{1}{\delta_c} \int_0^{\delta_c} \boldsymbol{\theta}_w(y, t) dy. \quad (5.19)$$

Now,

$$\langle \mathbf{r}_g(\mathbf{C}_{wc}, \boldsymbol{\theta}_w) \rangle = \frac{1}{\delta_c} \int_0^{\delta_c} \mathbf{r}_g(\mathbf{C}_{wc}, \boldsymbol{\theta}_w) dy. \quad (5.20)$$

Expanding the integrand around the average values,

$$\mathbf{r}_g(\mathbf{C}_{wc}, \boldsymbol{\theta}_w) = \mathbf{r}_g(\langle \mathbf{C}_{wc} \rangle, \langle \boldsymbol{\theta}_w \rangle) + \frac{\partial \mathbf{r}_g}{\partial \mathbf{C}_{wc}} (\mathbf{C}_{wc} - \langle \mathbf{C}_{wc} \rangle) + \frac{\partial \mathbf{r}_g}{\partial \boldsymbol{\theta}_w} (\boldsymbol{\theta}_w - \langle \boldsymbol{\theta}_w \rangle) + \text{higher order terms}, \quad (5.21)$$

where the Jacobian matrices in *Eq. 5.21* are evaluated at $\langle \mathbf{C}_{wc} \rangle$ and $\langle \boldsymbol{\theta}_w \rangle$. Substituting this in *Eq. 5.20* and simplification gives

$$\langle \mathbf{r}_g(\mathbf{C}_{wc}, \boldsymbol{\theta}_w) \rangle = \mathbf{r}_g(\langle \mathbf{C}_{wc} \rangle, \langle \boldsymbol{\theta}_w \rangle) + 0 + 0 + \text{higher order terms}. \quad (5.22)$$

Thus, to leading order, the average value of \mathbf{r}_g is same as \mathbf{r}_g evaluated at the average values $\langle \mathbf{C}_{wc} \rangle$ and $\langle \boldsymbol{\theta}_w \rangle$. Now the Eq. (5.18) becomes

$$\epsilon_w \frac{\partial \langle \mathbf{C}_{wc} \rangle}{\partial t} = \mathbf{r}_g(\langle \mathbf{C}_{wc} \rangle, \langle \boldsymbol{\theta}_w \rangle) - \frac{\mathbf{j}_{fw}}{\delta_c}. \quad (5.23)$$

Similarly, averaging of Eq. 5.3 gives

$$C_M \frac{\partial \langle \boldsymbol{\theta}_w \rangle}{\partial t} = \mathbf{r}_s(\langle \mathbf{C}_{wc} \rangle, \langle \boldsymbol{\theta}_w \rangle). \quad (5.24)$$

From the definition of internal mass transfer coefficient matrix, we have

$$\mathbf{j}_{fw} = \mathbf{k}_{me} (\mathbf{C}_{fm} - \mathbf{C}_s) = \mathbf{k}_{mi} (\mathbf{C}_s - \langle \mathbf{C}_{wc} \rangle). \quad (5.25)$$

Thus, Eqs. 5.1, 5.23, 5.24 and 5.25 define the averaged model. After eliminating the interfacial concentration vector \mathbf{C}_s , we get

$$\mathbf{C}_s = (\mathbf{k}_{me} + \mathbf{k}_{mi})^{-1} (\mathbf{k}_{me} \mathbf{C}_{fm} + \mathbf{k}_{mi} \langle \mathbf{C}_{wc} \rangle), \quad (5.26)$$

$$\mathbf{k}_{mo}^{-1} = \mathbf{k}_{me}^{-1} + \mathbf{k}_{mi}^{-1} \quad (5.27)$$

$$\text{and } \mathbf{j}_{fw} = \mathbf{k}_{mo} (\mathbf{C}_{fm} - \langle \mathbf{C}_{wc} \rangle). \quad (5.28)$$

Thus, the averaged model may be expressed as

$$\frac{\partial \mathbf{C}_{fm}}{\partial t} + \langle u \rangle \frac{\partial \mathbf{C}_{fm}}{\partial x} = -\frac{\mathbf{k}_{mo}}{R_\Omega} (\mathbf{C}_{fm} - \langle \mathbf{C}_{wc} \rangle), \quad (5.29)$$

$$\epsilon_w \frac{\partial \langle \mathbf{C}_{wc} \rangle}{\partial t} = \mathbf{r}_g(\langle \mathbf{C}_{wc} \rangle, \langle \boldsymbol{\theta}_w \rangle) + \frac{\mathbf{k}_{mo}}{\delta_c} (\mathbf{C}_{fm} - \langle \mathbf{C}_{wc} \rangle) \quad (5.30)$$

$$\text{and } C_M \frac{\partial \langle \boldsymbol{\theta}_w \rangle}{\partial t} = \mathbf{r}_s(\langle \mathbf{C}_{wc} \rangle, \langle \boldsymbol{\theta}_w \rangle), \quad (5.31)$$

while the averaged inlet and initial conditions are given by

$$\mathbf{C}_{fm}(0, t) = \mathbf{C}_{f,in}(t); \quad \langle \mathbf{C}_{wc} \rangle(x, 0) = \langle \mathbf{C}_{wc}^0(x) \rangle; \quad \langle \boldsymbol{\theta}_w \rangle(x, 0) = \langle \boldsymbol{\theta}_w^0(x) \rangle.$$

The most appealing feature of the averaged model is that the total number of equations for isothermal case is same as that when washcoat diffusion is completely neglected, i.e. $2N + N_s$, where N is the number of gas phase species, N_s is the number of surface species. However, the averaged model includes washcoat diffusional effects through the dependence of the internal mass transfer coefficient matrix \mathbf{k}_{mi} on the washcoat properties, species local concentrations and coverages. A very important observation is that this matrix is diagonal and the diagonal elements (internal mass transfer coefficients) can be computed exactly when the net rate of adsorption of any gas phase species onto the catalytic sites does not depend on the concentrations of other gas phase species (which is a good assumption that applies to most micro-kinetic models). For example, the Jacobian matrix for the micro-kinetic model of CO oxidation (described in the next section with reaction steps are R1-R5 in *Table 5.3*) is given by

$$\mathbf{J}(X_{CO}, X_{CO_2}, X_{O_2}) = \begin{bmatrix} \frac{\partial R_{CO,net}}{\partial X_{CO}} & \frac{\partial R_{CO,net}}{\partial X_{CO_2}} & \frac{\partial R_{CO,net}}{\partial X_{O_2}} \\ \frac{\partial R_{CO_2,net}}{\partial X_{CO}} & \frac{\partial R_{CO_2,net}}{\partial X_{CO_2}} & \frac{\partial R_{CO_2,net}}{\partial X_{O_2}} \\ \frac{\partial R_{O_2,net}}{\partial X_{CO}} & \frac{\partial R_{O_2,net}}{\partial X_{CO_2}} & \frac{\partial R_{O_2,net}}{\partial X_{O_2}} \end{bmatrix}. \quad (5.32)$$

where the net rates of the species adsorption are given by

$$R_{CO,net} = -k_{CO_{ads}}X_{CO}\theta_{Pt} + k_{CO_{des}}\theta_{CO}, \quad (5.33)$$

$$R_{CO_2,net} = -k_{CO_2_{ads}}X_{CO_2}\theta_{Pt} + k_{CO_2_{des}}\theta_{CO_2} \quad (5.34)$$

$$\text{and } R_{O_2,net} = -k_{O_2_{ads}}X_{O_2}\theta_{Pt} + k_{O_2_{des}}\theta_{O_2}. \quad (5.35)$$

Since the net rate of each species depends only on that species fraction, the Jacobian matrix becomes diagonal:

$$\mathbf{J}(X_{CO}, X_{CO_2}, X_{O_2}) = \begin{bmatrix} -k_{CO_ads}\theta_{Pt} & 0 & 0 \\ 0 & -k_{CO_2_ads}\theta_{Pt} & 0 \\ 0 & 0 & -k_{O_2_ads}\theta_{Pt} \end{bmatrix}. \quad (5.36)$$

Hence, the Thiele matrix also becomes diagonal and the computation of the internal mass transfer coefficient for each gas phase species is decoupled from the other species. [Remarks:(a) If the \mathbf{k}_{me} is diagonal and \mathbf{k}_{mi} is diagonal, \mathbf{k}_{mo} is also diagonal (b) \mathbf{k}_{mi} is diagonal for Langmuir-Hinshelwood and Eley-Rideal kinetics].

A second important observation is that when the net rate of adsorption of any gas phase species j is linear in the mole fraction (or concentration), the internal mass transfer coefficient (or Sherwood number) can be computed exactly and is given by

$$\frac{1}{Sh_j} = \frac{1}{\Phi_j \tanh \Phi_j} - \frac{1}{\Phi_j^2}; \Phi_j^2 = \frac{\delta_c^2}{D_{e,j}} \frac{\partial R_{j,net}}{\partial X_j}; Sh_j = \frac{k_{c,j}\delta_c}{D_{e,j}}.$$

Before closing this section, we present the reduced order model for the non-isothermal case and in a form that is more convenient for computations, using only species mole fractions:

$$\frac{\partial \mathbf{X}_{fm}}{\partial t} + \langle u \rangle \frac{\partial \mathbf{X}_{fm}}{\partial x} = -\frac{\mathbf{k}_{mo}}{R_\Omega} (\mathbf{X}_{fm} - \langle \mathbf{X}_{wc} \rangle); \quad (5.37)$$

$$\begin{aligned} \epsilon_w \frac{\partial \langle \mathbf{X}_{wc} \rangle}{\partial t} &= \frac{1}{C_T} \mathbf{r}_g(\langle \mathbf{X}_{wc} \rangle, \langle \boldsymbol{\theta}_w \rangle, T_s) + \frac{\mathbf{k}_{mo}}{\delta_c} (\mathbf{X}_{fm} - \langle \mathbf{X}_{wc} \rangle), \\ C_M \frac{\partial \langle \boldsymbol{\theta}_w \rangle}{\partial t} &= \mathbf{r}_s(\langle \mathbf{C}_{wc} \rangle, \langle \boldsymbol{\theta}_w \rangle, T_s), \end{aligned} \quad (5.38)$$

$$\rho_f C_{p_f} \frac{\partial T_f}{\partial t} + \langle u \rangle \rho_f C_{p_f} \frac{\partial T_f}{\partial x} = \frac{h}{R_\Omega} (T_s - T_f); h = \frac{Nu_\infty \cdot k_f}{4R_\Omega} \quad (5.39)$$

$$\text{and } \delta_w \rho_w C_{p_w} \frac{\partial T_s}{\partial t} = \delta_w k_w \frac{\partial^2 T_s}{\partial x^2} + h (T_f - T_s) \quad (5.40)$$

$$\begin{aligned}
& +\delta_c \mathbf{r}_g(\langle \mathbf{X}_{wc} \rangle, \langle \boldsymbol{\theta}_w \rangle, T_s)^T (-\Delta \mathbf{H}_g) \\
& +\delta_c \mathbf{r}_s(\langle \mathbf{X}_{wc} \rangle, \langle \boldsymbol{\theta}_w \rangle, T_s)^T (-\Delta \mathbf{H}_s).
\end{aligned} \tag{5.41}$$

Here, T_f is the fluid (cup-mixing) temperature, ρ_f and Cp_f are the density and specific heat capacity of the fluid phase, T_s is the solid temperature and δ_w represents the effective wall thickness (defined as $\delta_w = \delta_s + \delta_c$, where δ_s is the effective half-thickness of the wall and δ_c is the effective thickness of the washcoat.), ρ_w and Cp_w are the effective density and specific heat capacity of the washcoat, respectively, defined as $\delta_w \rho_w Cp_w = \delta_c \rho_c Cp_c + \delta_s \rho_s Cp_s$ and $\delta_w k_w = \delta_c k_c + \delta_s k_s$, where the subscript s and c represent the support and catalyst/washcoat, respectively; h in *Eqs.* 5.39 and 5.40 represent the local heat transfer coefficient at the fluid-washcoat interface (in both detailed and reduced order model, we use an asymptotic Nu_∞ to compute h for a rounded square channel). The last term in *Eq.* 5.40 represents the total heat generated by various reactions with ΔH_i being the enthalpy change of reaction i . The total concentration (C_T) is computed using the ideal gas law

$$C_T = \frac{p}{RT_f(t)}. \tag{5.42}$$

Here, p represents the total gas pressure, assumed constant at 1 atm, T_f is the fluid temperature. In most after-treatment applications, the external mass transfer coefficient matrix is assumed to be diagonal as the reactive species concentrations are small compared to the major inert species (which is usually nitrogen).

The inlet, initial and boundary conditions for the above model are of the form

$$Inlet.C. : \mathbf{X}_{fm}(0, t) = \mathbf{X}_{fm,in}(t); T_f(0, t) = T_{f,in}(t), \tag{5.43}$$

$$Initial.C. : \mathbf{X}_{fm}(x, 0) = \mathbf{X}_{fm}^0(x); \langle \mathbf{X}_{wc} \rangle(x, 0) = \langle \mathbf{X}_{wc}^0(x) \rangle; \langle \boldsymbol{\theta}_w \rangle(x, 0) = \langle \boldsymbol{\theta}_w^0(x) \rangle, \tag{5.44}$$

$$Initial.C. : T_f(x, 0) = T_f^0(x); T_s(x, 0) = T_s^0(x) \tag{5.45}$$

$$\text{and Boundary.C. : } \frac{\partial T_s}{\partial x}(0, t) = 0 ; \frac{\partial T_s}{\partial x}(L, t) = 0. \quad (5.46)$$

As discussed in the literature [19], the above model is also applicable for any channel flow geometry and washcoat shape provided appropriate values are used for the effective diffusion lengths and the various constants appearing in the Sherwood and Nusselt numbers. For example, the internal mass transfer coefficient matrix for any washcoat shape can be expressed as

$$\mathbf{Sh}_i = Sh_{i\infty} \mathbf{I} + \Phi \tanh[\Lambda^* \Phi], \quad (5.47)$$

where Φ^2 is the square of the shape normalized Thiele matrix. The two constants $Sh_{i\infty}$ and Λ^* for many common washcoat geometric shapes can be found in the literature [19].

5.3 Example: Micro-kinetics of CO/H₂/C₃H₆ adsorption, desorption and oxidation on Pt/Al₂O₃ monolith catalysts

As our illustrative example, we consider the oxidation of CO/H₂/C₃H₆ mixture on a Pt/Al₂O₃ monolith catalyst using a micro-kinetic model. The reaction mechanism for this was taken from the work of Kota et al., [31]. Unless specified otherwise, the constant parameter values used in the simulations are listed in *Table 5.1*. The gas phase diffusivity matrix, $\mathbf{D}_f \in \mathbb{R}^{N \times N}$ is a diagonal matrix and values are shown in *Table 5.2*. The effective diffusivity of each species in the washcoat is estimated by assuming a diffusivity ratio, $\lambda (= D_f/D_e)$, of 100 and the rate expressions are shown in *Table 5.3*. The rate constant is described by the Arrhenius type expression

$$k_{f/r} = A_{f/r} \exp\left(-\frac{E_{f/r}}{R_g T}\right). \quad (5.48)$$

All the adsorption steps are considered to be non-activated with an adsorption rate constant of

$$k_i = S_{0i} \alpha_\nu \left[C_T \left(\frac{R_g T}{2\pi M_i} \right)^{0.5} \right], \quad (5.49)$$

where S_{0i} is the sticking coefficient of gas phase species i at zero coverage, M_i is the molecular weight of the species, C_T is the total gas phase concentration, α_ν is the active platinum surface area per unit volume of washcoat and its value is taken as $1.5 \times 10^6 \text{ m}^2 \text{Pt} / \text{m}^3 \text{wc}$. The kinetic parameters and sticking coefficients used in the simulation are listed in *Table 5.4*.

In this example, we have 6 gas phase species and 14 adsorbed surface species in total. It should be noted that even in this simple example, the simulation of the 1+1D model with 80 mesh points in the axial and 30 mesh points in the transverse directions takes more than two weeks on a desktop computer, and the solution is not mesh independent! The time required to obtain a mesh independent solution is about ten to fifteen times longer (provided memory requirement is not a problem). In contrast, the reduced order model with 80 mesh points in the axial direction only takes around 5 mins. Therefore, we only investigate the mesh size dependency of the computed solution using short monolith model.

Table 5.1: Numerical constants and parameters used in model simulation

Constant	Value
R_Ω	$261 \times 10^{-6} \text{ m}$
δ_c	$30 \times 10^{-6} \text{ m}$
L	$5 \times 10^{-2} \text{ m}$
ϵ_w	0.41
ρ_f, ρ_c, ρ_s	1.109, 1675, 1369 kg/m ³
Cp_f, Cp_c, Cp_s	1009, 1000, 880 J/kg/K
k_f, k_s, k_c	0.0386, 2, 1.5 W/m/K
$Nu_e = Sh_e$	4.364
$C_M = C_{pt}$	40 mol/m ³ WC
θ_{Pt}^0	1
α	$1.5 \times 10^6 \text{ m}^2 \text{Pt} / \text{m}^3 \text{WC}$

Table 5.2: Temperature dependent parameters used in the second example

Constant	Value/Expression
$\langle u \rangle$	$6 \times 10^{-1} \times \left(\frac{T}{273.15}\right)$ m/s
C_T	$\frac{1 \text{ bar}}{8.314 \times T}$ mol/m ³
D_{f,O_2}	$9.24 \times 10^{-10} \times T^{1.75}$ m ² /s
D_{f,H_2}	$4.7 \times 10^{-9} \times T^{1.75}$ m ² /s
D_{f,H_2O}	$1.19 \times 10^{-9} \times T^{1.75}$ m ² /s
$D_{f,CO}$	$9.29 \times 10^{-10} \times T^{1.75}$ m ² /s
D_{f,CO_2}	$7.15 \times 10^{-10} \times T^{1.75}$ m ² /s
D_{f,C_3H_6}	$5.36 \times 10^{-10} \times T^{1.75}$ m ² /s

Table 5.3: Reactions and rate expression in the second example

No.	Reaction	
1	CO (g) + Pt \leftrightarrow CO-Pt	$k_{1f}X_{CO}\theta_\nu - k_{1r}\theta_{CO}$
2	CO-Pt + O-Pt \leftrightarrow CO ₂ -Pt + Pt	$k_{2f}\theta_{CO}\theta_O - k_{2r}\theta_{CO_2}\theta_\nu$
3	CO ₂ -Pt \leftrightarrow CO ₂ (g) + Pt	$k_{3f}\theta_{CO_2} - k_{3r}X_{CO_2}\theta_\nu$
4	O ₂ (g) + Pt \leftrightarrow O ₂ -Pt	$k_{4f}X_{O_2}\theta_\nu - k_{4r}\theta_{O_2}$
5	O ₂ -Pt + Pt \rightarrow 2O-Pt	$k_{5f}\theta_{O_2}\theta_\nu - k_{5r}\theta_O^2$
6	CO-Pt + OH-Pt \leftrightarrow CO ₂ -Pt + H-Pt	$k_{6f}\theta_{CO}\theta_{OH} - k_{6r}\theta_{CO_2}\theta_H$
7	H ₂ (g) + 2Pt \leftrightarrow 2H-Pt	$k_{7f}X_{H_2}\theta_\nu^2 - k_{7r}\theta_H^2$
8	H-Pt + O-Pt \leftrightarrow OH-Pt + Pt	$k_{8f}\theta_H\theta_O - k_{8r}\theta_{OH}\theta_\nu$
9	H-Pt + OH-Pt \leftrightarrow H ₂ O-Pt + Pt	$k_{9f}\theta_{OH}\theta_H - k_{9r}\theta_{H_2O}\theta_\nu$
10	H ₂ O-Pt \leftrightarrow H ₂ O (g) + Pt	$k_{10f}\theta_{H_2O} - k_{10r}X_{H_2O}\theta_\nu$
11	2OH-Pt \leftrightarrow H ₂ O-Pt + O-Pt	$k_{11f}\theta_{OH}^2 - k_{11r}\theta_{H_2O}\theta_O$
12	C ₃ H ₆ (g) + Pt \leftrightarrow C ₃ H ₆ -Pt	$k_{12f}X_{C_3H_6}\theta_\nu - k_{12r}\theta_{C_3H_6}$
13	C ₃ H ₆ -Pt + O-Pt \leftrightarrow C ₃ H ₅ -Pt + OH-Pt	$k_{13f}\theta_{C_3H_6}\theta_O - k_{13r}\theta_{C_3H_5}\theta_{OH}$
14	C ₃ H ₅ -Pt + O-Pt \leftrightarrow C ₃ H ₄ -Pt + OH-Pt	$k_{14f}\theta_{C_3H_5}\theta_O - k_{14r}\theta_{C_3H_4}\theta_{OH}$
15	C ₃ H ₄ -Pt + Pt \leftrightarrow C ₂ H ₃ -Pt + CH-Pt	$k_{15f}\theta_{C_3H_4}\theta_\nu - k_{15r}\theta_{C_2H_3}\theta_{CH}$
16	C ₂ H ₃ -Pt + 2O-Pt \leftrightarrow CO ₂ -Pt + CH ₃ -Pt+Pt	$k_{16f}\theta_{C_2H_3}\theta_O - k_{16r}\theta_{CO_2}\theta_{CH_3}$
17	CH ₃ -Pt + O-Pt \leftrightarrow CH ₂ -Pt + OH-Pt	$k_{17f}\theta_{CH_3}\theta_O - k_{17r}\theta_{CH_2}\theta_{OH}$
18	CH ₂ -Pt + O-Pt \leftrightarrow CH-Pt + OH-Pt	$k_{18f}\theta_{CH_2}\theta_O - k_{18r}\theta_{CH}\theta_{OH}$
19	CH-Pt + O-Pt \leftrightarrow CO-Pt + H-Pt	$k_{19f}\theta_{CH}\theta_O - k_{19r}\theta_{CO}\theta_H$
20	CH-Pt + 2O-Pt \leftrightarrow CO ₂ -Pt + H-Pt+Pt	$k_{20f}\theta_{CH}\theta_O^2 - k_{20r}\theta_H\theta_{CO_2}$

5.4 Results

Simulations of CO oxidation were performed using a feed of 0.55% CO and 1% O₂. The feed temperature is ramped from 350 K to 650 K at a ramp rate of 8 K/min. *Fig. 5.2* shows the results of CO oxidation based on reaction steps R1 to R5. We compared 1+1D model solution with various approximations of 1D reduced

Table 5.4: Kinetic parameters for reaction rates

No.	A_f (mol/ m ³ s)	A_r (mol/ m ³ s)	E_r (kJ/ mol)	E_r (kJ/ mol)
1	$S_0=0.85$	$1.6*10^{16}$	0	136
2	$8*10^{15}$	$2.2*10^{15}$	170	219
3	$4*10^{13}$	$S_0=0.005$	10	0
4	$S_0=0.07$	$8*10^{15}$	0	102
5	$4*10^{11}$	$1*10^{14}$	50	164
6	$9.7*10^{18}$	$4*10^{13}$	31	89
7	$S_0=0.046$	$4*10^{13}$	0	78
8	$3*10^{12}$	$1.27*10^{15}$	25	63
9	$7*10^{12}$	$4*10^{13}$	20	81
10	$1*10^{13}$	$S_0=0.075$	43	0
11	$4*10^{12}$	$4*10^{12}$	48	75
12	$S_0=0.8$	$4*10^{17}$	0	69.7
13	$4*10^{13}$	$4*10^{11}$	29	199
14	$7*10^{13}$	$4*10^{13}$	23	131
15	$2*10^{14}$	$4*10^{13}$	78	165
16	$3*10^{13}$	$4*10^{12}$	56	171
17	$1*10^{14}$	$4*10^8$	70	28
18	$4*10^{13}$	$4*10^8$	52	69
19	$3*10^{12}$	$4*10^{11}$	70	370
20	$1.7*10^{15}$	$1*10^{13}$	42	170

order model. *Fig. 5.2* shows the exit conversion of CO versus inlet temperature. In this simulation, 30 mesh points were used in the axial direction for both the detailed (1+1D) and reduced order model in the long channel limit. The solid red line is the result of 1D model without the washcoat diffusion limitation effect, dashed blue line is the 1+1 D model results with 15 mesh points in the washcoat. Dotted green line is the result of Thiele matrix approach and dash-dotted line is the result of asymptotic approximation. We observe that the asymptotic approximation is far away from other lines because of the inaccurate washcoat diffusion description, this method only valid when the reaction is slow or the washcoat layer is very thin. There are also gaps between the light-off curves computed ignoring washcoat diffusion, 1+1D model and Thiele matrix solution. Totally ignoring the washcoat diffusion resistance gives a higher conversion than others because it assumes there is no washcoat diffusion limitation and the overall mass transfer coefficient matrix $k_{mo} = k_{me}$. Even

though there is a gap between 1+1D model results and Thiele matrix approach, it does not imply that the Thiele matrix approach is not accurate, on the contrary, 1+1D model actually needs a lot more mesh points inside washcoat to get the washcoat diffusion effect described accurately according to the largest eigenvalue of Φ^2 which in this example is about 10^5 . We also note that the computation time for 1+1D model is 2602 s, Thiele matrix approach takes 6.5 s, while the asymptotic approximation takes 5.9 s. As stated earlier, the Thiele matrix solution is as fast as the asymptotic approximation.

In *Fig.5.3*, we investigate the mesh size dependency in the transverse direction on the model accuracy. Feed composition is the same as the long channel model. This figure shows the results of exit conversion of CO in a short monolith model. From top to bottom, the pink solid line is the result of totally neglecting washcoat diffusion and again this solution gives a higher conversion than others. Other curves shown are the results of detailed model with 5, 15, 100, 200, and 400 mesh points in the washcoat. After the detailed model results, there is Thiele matrix solution which is dashed yellow line and very close to the detailed model with 400 mesh points in the washcoat. The separation between the first three lines: from the dash-dotted green line to the blue solid line is very significant, but after the blue solid line, the separation becomes very small so we enlarge the corner of the figure to better distinguish the lines. As can be seen from the enlarged picture (inset), the results of detailed model come closer to the Thiele matrix approximation and the Thiele matrix solution is almost identical when the detailed model has 400 mesh points. In this case, 5 or 15 mesh points are not enough to get an accurate detailed model, we need to take at least 400 mesh points. Again, as stated in the previous section, the number of mesh points in the transverse direction needs to be close to the square root of largest eigenvalue in Φ^2 . One main conclusion from the results shown is that the asymptotic solution gives about 50% error compared to the most

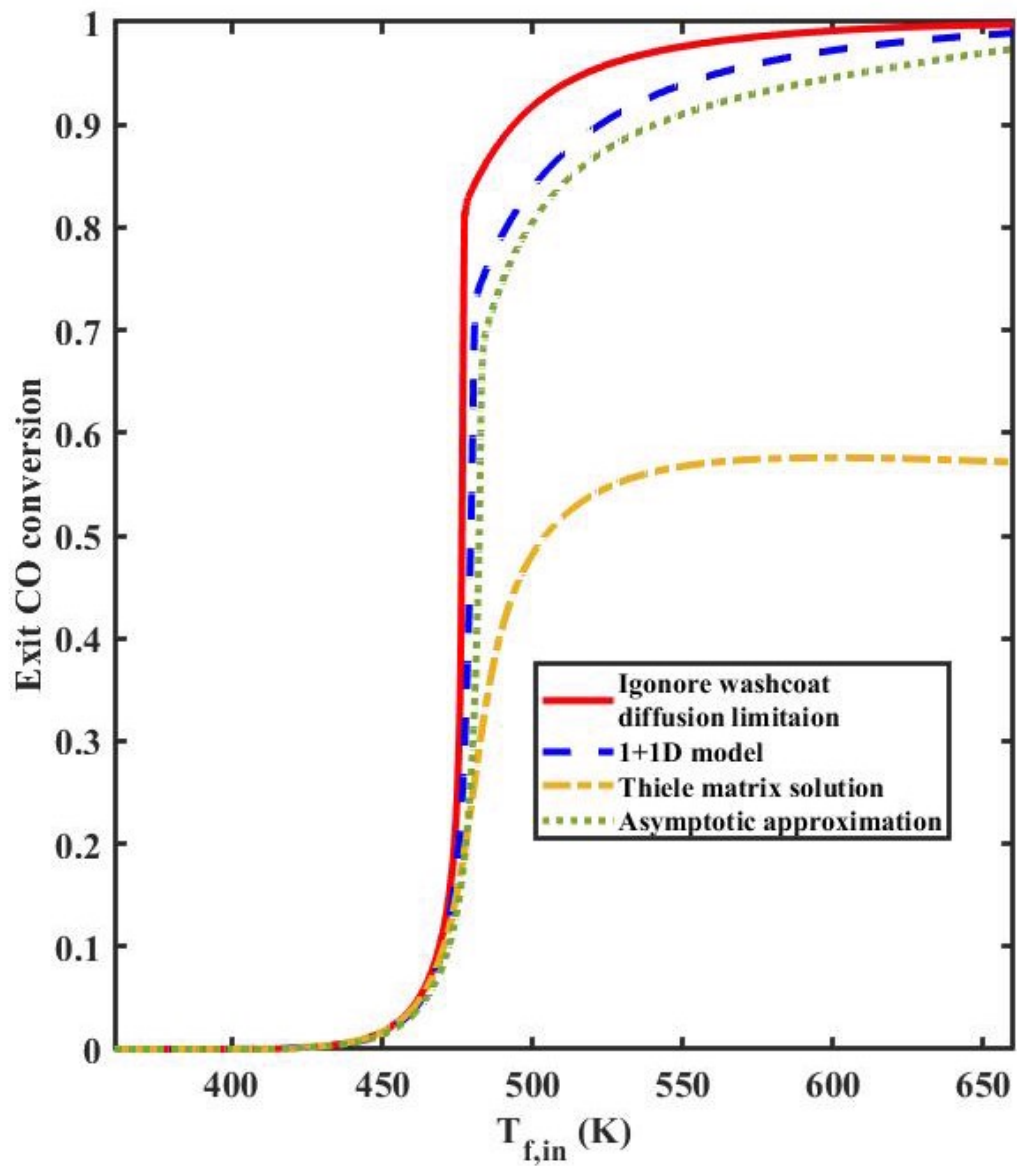


Figure 5.2: Exit conversion versus inlet temperature for CO oxidation with micro kinetics in a long channel model (a) exit CO conversion (b) exit O₂ conversion

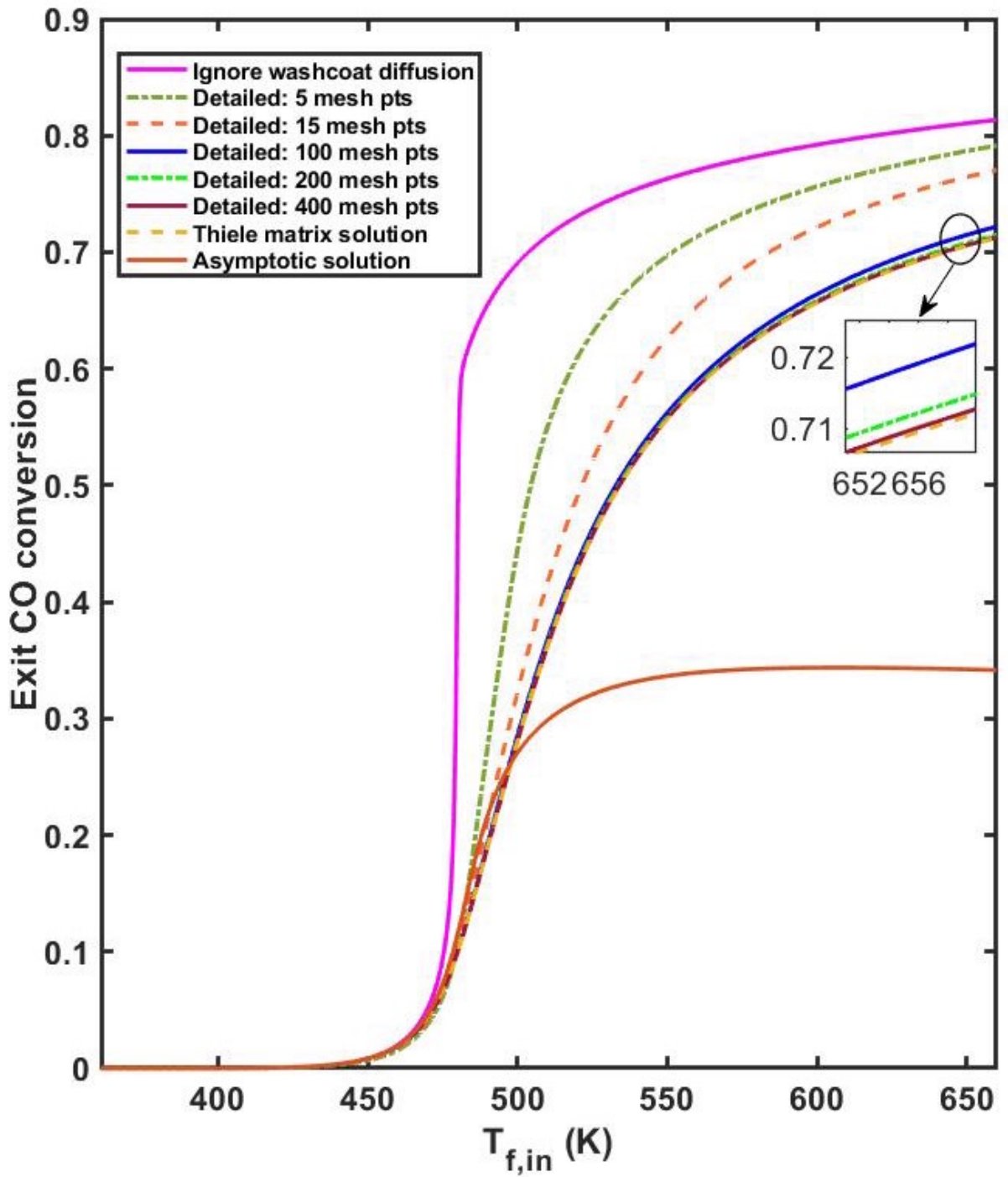


Figure 5.3: Exit conversion versus inlet temperature for CO oxidation with micro kinetics in a short monolith model

detailed model. In this case, asymptotic solution takes 0.46 s to while Thiele matrix solution takes 0.54 s and is about 10^3 times faster than detailed solution with 400 mesh points in the washcoat. From these comparisons, it is clear that the Thiele matrix solution with reduced order model is very accurate with micro kinetics. This is a great advantage because most micro-kinetic models account for a large number of reactions and species, and if the Thiele matrix is non-diagonal, there will be substantial effort in computing matrix functions that deal with high dimensional matrices. Since the Thiele matrix solution has been proved to accurately predict the exit effluent composition in previous case and the examples in previous chapter, in next few cases, we only compare different reduced order model approaches with a full length monolith model.

Fig. 5.4 shows the 1D (reduced order) model results for CO/H₂ co-oxidation based on reaction steps R1 to R11. Simulation inlet composition is: 0.55% CO, 0.25% H₂ and 6% O₂. In this case, the feed temperature is ramped from 360 K to 800 K at a rate of 8 K/min. Cases (a) and (b) show the exit conversion of CO and H₂, respectively. Yellow dashed line is the result of ignoring the washcoat diffusion effect, followed is the dash-dotted blue line which is the Thiele matrix solution and the last is the asymptotic solution. Again, ignoring the washcoat diffusion resistance always accounts for a higher conversion and the asymptotic solution acts like a lower bound because of the lower estimation of the internal mass transfer coefficient.

Fig. 5.5 shows the 1D (reduced order) model results for CO/H₂/C₃H₆ oxidation, Simulation inlet composition is: 1% CO, 0.33% C₃H₆, 0.33% H₂ and 1% O₂. Feed temperature is ramped from 450 K to 650 K at a rate of 8 K/min. (a) and (b) show the exit conversion of each species and the solid temperature rise versus the inlet temperature. in figure (a), from top to the bottom, the first two lines are H₂ conversions of Thiele matrix solution and asymptotic solution, respectively. Followed two

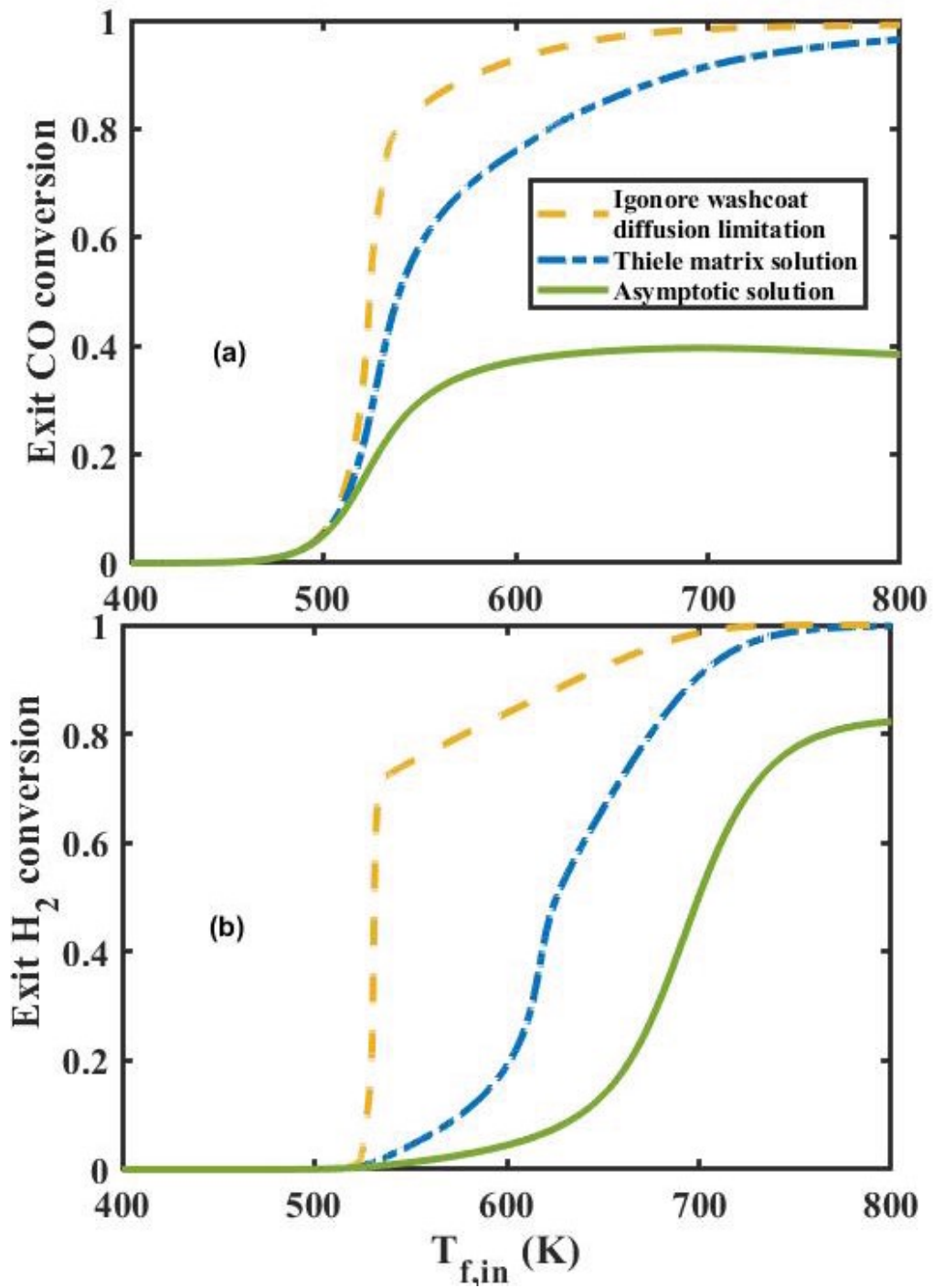


Figure 5.4: Exit conversion versus inlet temperature for CO and H₂ co-oxidation in a long channel model (a) exit CO conversion (b) exit H₂ conversion

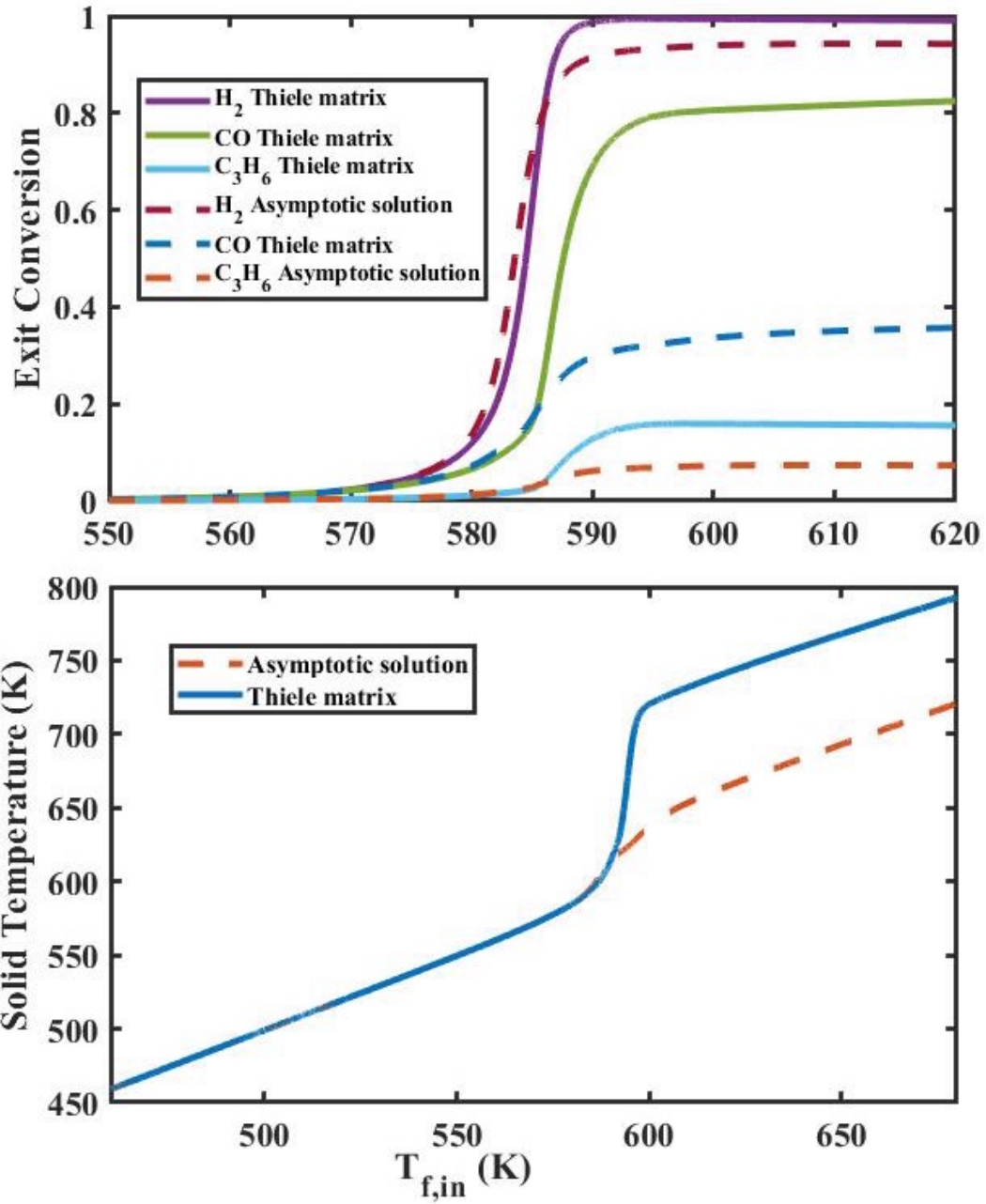


Figure 5.5: CO/H₂/C₃H₆ co-oxidation in a long channel model (a) Exit conversion versus inlet temperature (b) Solid temperature rise versus inlet temperature

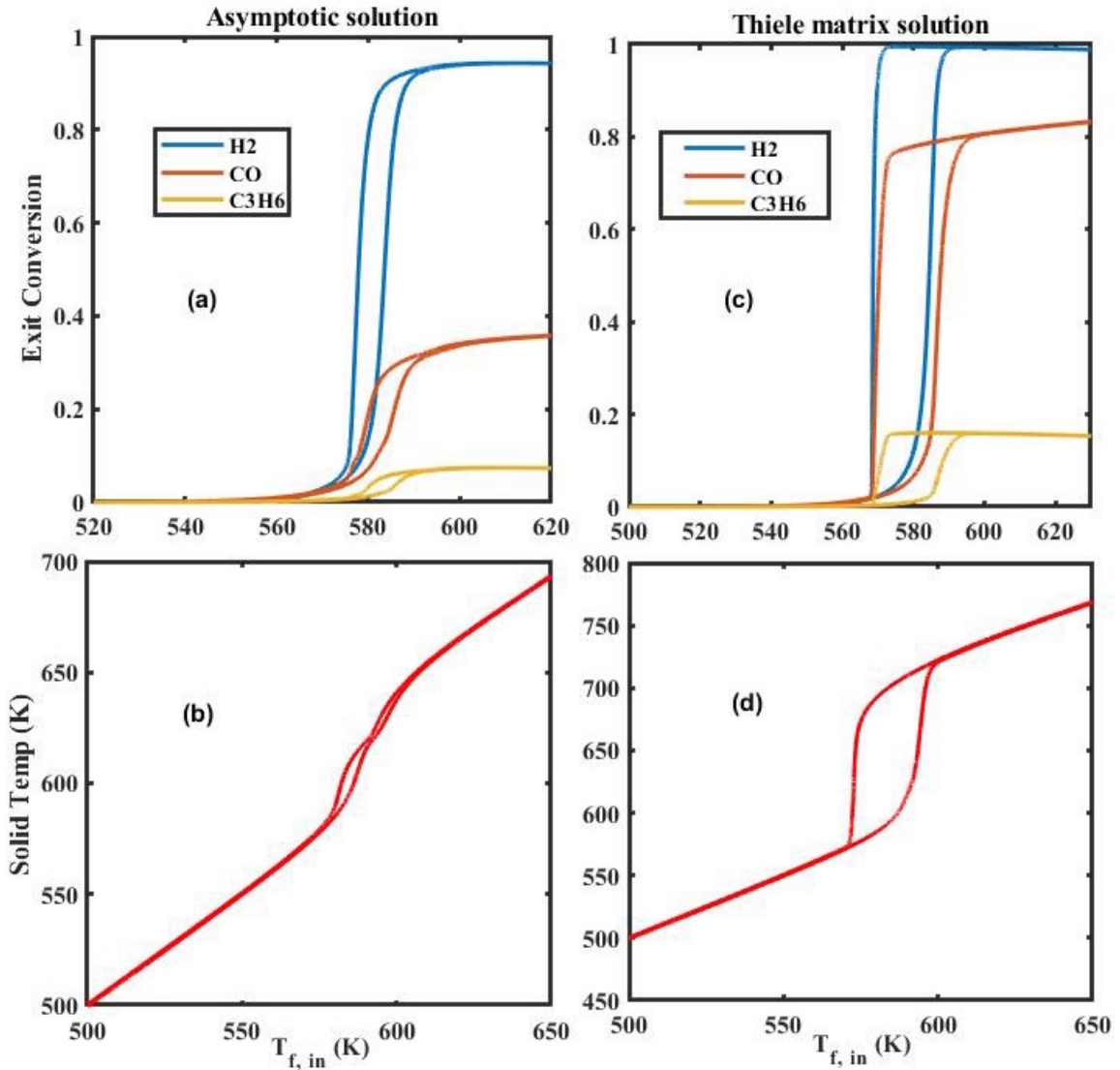


Figure 5.6: Inlet temperature ramp up and down for CO/H₂/C₃H₆ co-oxidation in a long channel model (a) Exit conversion versus inlet temperature with asymptotic solution (b) Solid temperature versus inlet temperature with asymptotic solution (c) and (d) are results of Thiele matrix solution

lines are the exit CO conversions and the bottom two lines are results of exit C₃H₆ conversion. We can observe a same trend as *Fig. 5.4*, the asymptotic solution gives a lower conversion and in figure (b) we notice that the heat release in the washcoat of asymptotic solution is also lower than the Thiele matrix solution.

Fig. 5.6 is the simulation results of hysteresis study of CO/H₂/C₃H₆ co-oxidation in a long channel model. simulation inlet composition is: 1% CO, 0.33% C₃H₆,

0.33% H₂ and 1% O₂. Inlet temperature is ramped up from 450 K to 650 K at a rate of 8 K/min and then ramped down to 450 K at a rate of 1 K/min. (a) and (c) are the exit conversion versus inlet temperature with asymptotic solution and Thiele matrix solution, respectively, (b) and (d) are the solid temperature versus inlet temperature with asymptotic solution and Thiele matrix solution, respectively. We can notice that not only the conversion of the asymptotic solution predicts lower than the Thiele matrix solution but also the ignition and extinction temperature show a large difference. Thus, it's important to use an accurate reduced order model to predict the effluent concentration accurately since it also affects light off and light down temperature which is a very important factor in aftertreatment area.

As for the computation time, as stated earlier, the Thiele matrix method is as fast as the asymptotic method in all of the co-oxidation cases. For example, in the case of CO/H₂ co-oxidation, the computation times of Thiele matrix and asymptotic solutions are 16.5 s and 15.2 s, respectively.

5.5 Conclusions and discussion

In this chapter, we present a novel method for including washcoat diffusional effect in reduced order models of monolith reactors with micro-kinetics. As stated in the introduction, it is a common practice in the literature to use micro-kinetic models to describe the various reactions occurring in the catalytic layer. However, an accurate assessment of the washcoat diffusional effects with such detailed micro-kinetic models also requires extremely fine mesh (within the washcoat layer) and the number of mesh points (at which the computed solution becomes independent of the mesh size) depends on the characteristic time scales associated with the micro-kinetic model or the washcoat Thiele modulus based on the smallest time scale associated with the kinetic model. For example, a typical adsorption and/or reaction time scale is of the order of 10^{-7} s, while a typical value for species effective diffusivity in the washcoat in the Knudsen regime is of the order 10^{-6} m²/s, which

leads to an associated length scale of $0.3 \mu m$ (based on Thiele modulus of unity). This leads to a washcoat Thiele modulus of 316 for a washcoat of thickness of $100 \mu m$ and requiring as many mesh points for an accurate solution. In our view, most literature studies that use detailed or micro-kinetic models either do not take such fine mesh or do not verify the mesh independence of the computed solutions, and if verified, real time simulations of such systems may be impractical. The approach presented here can speed up calculations by about two to three orders of magnitude while retaining the accuracy of the computed solutions. We have illustrated the method with an example of $H_2/CO/C_3H_6$ oxidation over Pt/Al_2O_3 catalyst with a 20 step micro-kinetic model. Obviously, the power of the method is enhanced in systems with more reaction steps and/or much smaller chemistry time scales or at higher temperatures or thicker washcoat layers.

Chapter 6

A novel asymptotic approach for computing wash-coat diffusional effects in monolith reactors

6.1 Introduction

In this chapter, we propose and validate a methodology based on coupling of ROM and domain decomposition method for single and multicomponent systems, which simplifies the evaluation of transfer coefficients and speed-up the real time simulation significantly. We also present simulation of a system of three-way catalytic converter (TWC) with four reaction model for comparing the results with the detail model. The results show a very good match between the two while increasing the simulation speed by about three orders of magnitude.

In the literature, even though various ROM are proposed, the most used ones are 1D two-phase models (see the more recent ones in Joshi et al., [2], Tu et al., [19], Ratnakar et al., [8], Sarkar et al., [35]), which use transfer coefficients concepts approach (Balakotaiah [1]) in retaining small-scale physics. While these ROMs have been proven for simulation of monolith reactors by retaining essential physics at smaller scales, the transfer coefficients used in the model depend strongly on kinetics/transport parameters, especially for fast reactions. For example, for thin washcoats where geometrical effects can be ignored, the internal transfer coefficients (\mathbf{k}_{mi}) and cross-transfer coefficients ($\widehat{\mathbf{k}}_{mi}$) are given by (Ratnakar et al., [8], Sarkar et al., [35], Tu et al., [19])

$$\mathbf{k}_{mi} = \frac{D_e \mathbf{S}\mathbf{h}_i}{\delta_c}; \quad \mathbf{S}\mathbf{h}_i = \left[(\Phi \tanh \Phi)^{-1} - (\Phi^2)^{-1} \right]^{-1} \quad (6.1)$$

and

$$\widehat{\mathbf{k}}_{mi} = \frac{D_e \widehat{\mathbf{S}}\mathbf{h}_i}{\delta_c}; \quad \widehat{\mathbf{S}}\mathbf{h}_i = \left[(\Phi^2)^{-1} - (\Phi \sinh \Phi)^{-1} \right]^{-1}, \quad (6.2)$$

where the Thiele modulus matrix is given by

$$\Phi^2 = \delta_c^2 (\mathbf{D}_e)^{-1} \mathbf{J}^R; \quad \mathbf{J}^R = \frac{\partial \mathbf{R}}{\partial \mathbf{c}}. \quad (6.3)$$

Here \mathbf{D}_e is effective diffusivity in the washcoat; δ_c is the mean washcoat thickness; \mathbf{Sh}_i and $\widehat{\mathbf{Sh}}_i$ are Sherwood and cross-Sherwood number matrices, respectively; \mathbf{J}^R is the Jacobian matrix for the net reaction vectors \mathbf{r} (i.e. net rate of consumption) with respect to concentration vector \mathbf{C} . For other geometries, the expressions can be simplified as follows:

$$\mathbf{Sh}_i = Sh_{i\infty} \mathbf{I} + \Phi \tanh(\Lambda^* \Phi) \quad (6.4)$$

$$\text{and } \widehat{\mathbf{Sh}}_i = \widehat{Sh}_{i\infty} \mathbf{I} + \Phi^2, \quad (6.5)$$

where Λ^* is the shape factor (see Appendix C) for Λ^* corresponding to few standard geometries) and subscript ' ∞ ' denotes the asymptotic value. The accuracies of these ROM depend on how accurately the transfer coefficients are determined as we explained in the third chapter. For example, asymptotic transfer coefficients may be adequate for many applications where gradient in the washcoat is negligible, but not when strong washcoat diffusion limitation is present. For such cases, the transfer coefficients are expressed as a functions of Thiele matrix, which are applied and illustrated by many researchers recently (Joshi et al., [2], Kumar et al., [3], Kumar et al., [9], Mozaffari et al., [13], Rink et al., [14], Ratnakar et al., [8], Sarkar et al., [35], Tu et al., [19]) [Note: functional forms used for \mathbf{Sh}_i in some of the cited literature are different and may not be valid when Φ^2 is a negative definite matrix]. In addition, the traditional form of ROM containing binary transfer coefficients are not adequate for multi-layer washcoat and may require additional cross-transfer coefficients (Eq.6.2 or 6.5) as shown in Ratnakar et al., [8] and applied in Sarkar et al., [35].

The determination of cross-transfer and transfer coefficient (k_{mi} and \hat{k}_{mi}) for multicomponent systems require evaluation of non-linear functions of Thiele modulus matrices (Ratnakar et al., [8], Sarkar et al., [35], Tu et al., [19]), which could be cumbersome and computationally costly in some cases, and may also be difficult depending on the nature of Thiele modulus matrices and computer accuracies. Avoiding such computation of function of matrices can further speed up the real time simulation. Therefore, in this chapter, we present a methodology that couples the reduced order model (ROM) with domain decomposition with retained accuracies, where the determination of the transfer coefficients are simplified (i.e. not requiring the evaluation of function of matrices). In our approach, use of asymptotic transfer coefficients (first term in *Eqs.6.4* and *6.5*) are sufficient for most practical purposes, significantly simplifies the model simulation. This approach can also be extended to many other similar diffusion-convection-reaction systems such as packed-bed reactors, tubular reactors and porous catalysts. Thus, this chapter is arranged as follows: In the next section, we present the main concept of our approach and mathematical modeling. In section 3, we validate our approach with exact solution for steady-state single and multicomponent systems with linear kinetics. In section 4, we consider a realistic system of three-way catalytic converter (TWC) with four reaction model and compare the results from our approach and detailed model for transient simulation. Finally, we summarize our main findings in the last section.

6.2 Mathematical Modeling

Our proposed approach to speed up real time simulation of monolith is based on coupling of ROM with domain decomposition method. Since our objective is to explain the main concepts, we consider a simple monolith with a single washcoat layer as shown schematically in *Figure 6.1* and start with 1+1D model to describe multicomponent diffusion-convection in the flow channel (Ω_f) and diffusion-reaction

in the washcoat (Ω_w). We could also start with the detailed 3D model with any geometry, but the workflow does not change.

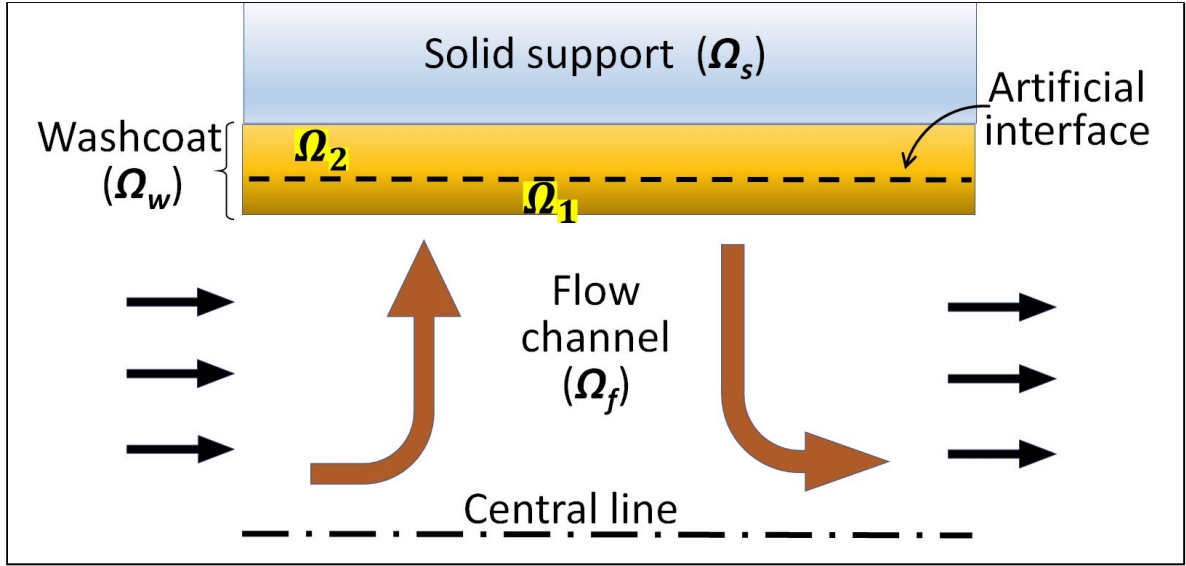


Figure 6.1: Schematic of half of a monolith channel with a single washcoat layer, along with an artificial intermediate interface.

6.2.1 Detailed 1+1D Model

In 1+1D model, the species and energy balances in the flow channel (Ω_f) are represented by 1D model (as the dispersion effects are negligible), where transverse gradients are captured by external heat and mass-transfer coefficients. The energy balance in the washcoat (Ω_w) is also simplified and represented by 1D model since the temperature gradient in the washcoat is negligible due to higher thermal diffusivity for most practical applications. The species balance in the washcoat (Ω_w), on the other hand, is described by detailed 3D diffusion-reaction model due to strong washcoat diffusional limitations. Thus, the 1+1D model for system shown in *Figure 6.1* can be expressed as

$$\frac{\partial \mathbf{C}_f}{\partial t} + \langle u \rangle \frac{\partial \mathbf{C}_f}{\partial x} = \frac{-1}{R_{\Omega_f}} \mathbf{j}_0 = \frac{-1}{R_{\Omega}} \mathbf{k}_{me} (\mathbf{C}_f - \mathbf{C}_s) \quad \text{in } \Omega_f \quad (6.6)$$

$$\varepsilon_w \frac{\partial \mathbf{C}_w}{\partial t} = \mathbf{D}_e \nabla_{\perp}^2 \mathbf{C}_w + \nu^T \mathbf{r}(\mathbf{C}_w, T_w) \quad \text{in } \Omega_w, \quad (6.7)$$

$$\rho_f C_{pf} \left(\frac{\partial T_f}{\partial t} + u_f \frac{\partial T_f}{\partial x} \right) = \frac{-1}{R_{\Omega_f}} q_0 = \frac{-1}{R_{\Omega_f}} h_{f,ext} (T_f - T_s) \quad \text{in } \Omega_f \quad (6.8)$$

$$\text{and } \rho_w C_{pw} \frac{\partial T_w}{\partial t} - \kappa_w \frac{\partial^2 T_w}{\partial x^2} = \frac{1}{\delta_T} q_0 - \frac{\delta_w}{\delta_T} \Delta \mathbf{H}^T \mathbf{r}(\mathbf{C}_w, T_w) \quad \text{in } \Omega_w, \quad (6.9)$$

where the subscript 'f' and 'w' represent the flow channel Ω_f and washcoat Ω_w , respectively; \mathbf{C} is concentration vector; \mathbf{r} is the reaction vector in the washcoat; ν is the stoichiometric coefficient matrix; $\Delta \mathbf{H}$ is the enthalpy vector; \mathbf{D} is the diffusivity matrix; $\langle u \rangle$ is the fluid velocity in the flow channel; ε_w is the washcoat porosity; ρ is the density of the phase, C_p is the specific heat capacity; T is temperature; and κ is the thermal conductivity; \mathbf{j}_0 and q_0 are molar-flux vector and heat flux at the fluid washcoat interface $\partial\Omega_{fw}$; \mathbf{k}_{me} and $h_{f,ext}$ are the external mass-transfer coefficient matrix and heat-transfer coefficient in the fluid phase; R_{Ω_f} is the hydraulic radius of the flow channel; δ_w is the mean thicknesses of the washcoat layer; and δ_T is the total thickness of the solid layers including washcoat and solid support. The transverse boundary condition for washcoat concentration vector \mathbf{C}_w are given as

$$\mathbf{C}_w = \mathbf{C}_s \quad \text{and} \quad \mathbf{j}_0 = -\mathbf{D}_w n \cdot \nabla_{\perp} \mathbf{C}_w \quad @ \partial\Omega_{fw}; \quad \text{and} \quad n \cdot \nabla_{\perp} \mathbf{C}_w = 0 \quad @ \partial\Omega_w. \quad (6.10)$$

Similarly, the inlet and exit conditions are given by

$$\mathbf{C}_f(0, t) = \mathbf{C}_{f,in}(t); \quad T_f(0, t) = T_{f,in}(t); \quad \frac{\partial T_w}{\partial x}(0, t) = 0; \quad \frac{\partial T_w}{\partial x}(L, t) = 0. \quad (6.11)$$

while initial conditions as

$$\mathbf{C}_f = \mathbf{C}_f^0, \quad \mathbf{C}_w = \mathbf{C}_w^0, \quad T_f = T_f^0, \quad T_w = T_w^0 \quad @ t = 0. \quad (6.12)$$

6.2.2 Reduced Order Model with Domain Decomposition

The reduced-order model for the example considered earlier has been developed by many researchers (see the brief review in our recent works Ratnakar et al., [8], Sarkar et al., [35], Tu et al., [19]). These reduced order models are represented by phase averaged global equations in each domain (flow channel and washcoat), where interface heat or mass fluxes are expressed in terms of the overall transfer coefficients. Various efforts have been made following the work Balakotaiah [1] to improve the determination of these transfer coefficients (see the brief reviews in Tu et al., [19]). As shown in our recent work Tu et al., [19], the most accurate determination of transfer coefficients are obtained by using *Eq.* (6.1 or 6.2), which lead to exact solution for linear kinetics and acceptable accuracy for non-linear kinetics. However, as explain in earlier section, those ROM require the use of function of Thiele matrix Φ , which may increase the computation time tremendously, especially for highly non-linear kinetics.

In the current approach, we divide the washcoat (Ω_w) into two artificial domains Ω_1 and Ω_2 using an artificial intermediate layer as schematically shown in *Figure* 6.1. The main idea for domain decomposition is to capture the washcoat diffusion limitation more accurately, therefore we explain it first for single component system and then describe for multicomponent system. Note that for the scalar case (i.e for a single component system), the Sherwood number expressed in *Eq.* (6.1 or 6.2) may be given by its asymptotic values when Thiele modulus is small (i.e. $\phi \ll 1$). But when Thiele modulus is much higher (i.e. $\phi \gg 1$), the use of only asymptotic Sherwood number may lead to significant error. In the latter case ($\phi \gg 1$), the concentration gradient in the washcoat is mostly near the fluid-washcoat interface. Therefore, if we select an artificial layer at a distance $\delta_1 \left(\sim \frac{1}{\phi} \right)$, the Thiele modulus in the first layer Ω_1 based on its thickness is less than unity, and hence, the asymptotic Sherwood number can be utilized for this layer. In addition, all the reactant is

expected to be practically consumed in Ω_1 and remains negligible in the second layer Ω_2 . In other words, concentration gradient in the second layer is practically negligible and hence, asymptotic Sherwood number can be utilized in this layer as well.

Similarly, for multicomponent system, the washcoat domain Ω_w is divided into the two artificial domain Ω_1 and Ω_2 such that the Thiele modulus matrix in Ω_1 has all eigenvalues less than unity. It can be achieved by evaluating the largest eigenvalue λ_{\max} of Thiele modulus Φ^2 (which can be obtained in few steps using power-method) and selecting the thickness of the first artificial layer Ω_1 as $\delta_1 \sim \frac{1}{\sqrt{|\lambda_{\max}|}}$. This enables the use of asymptotic Sherwood number in both domains, which may be sufficient to capture the diffusional limitation, especially when the Thiele modulus matrix is diagonally dominant.

Thus, decomposing the single washcoat layer in the two artificial domain based on largest eigenvalue of the Thiele modulus matrix can avoid the computation of functions of Thiele modulus matrices and significantly reduce the computation time. The ROM with domain decomposition corresponds to that of a dual-layer monolith containing the two artificial layers Ω_1 and Ω_2 of the washcoat as shown in *Fig. 6.1*. For such systems, ROM can be obtained by following our earlier work: Ratnakar et al., (2018), Sarkar et al., (2020)), which can be expressed as follows: The species and energy balance in the flow channel (Ω_f) and energy balance in washcoat (Ω_w) remains the same as in 1+1D model along with corresponding boundary and initial conditions. But the species balance in the two artificial layers are represented as

$$\varepsilon_w \frac{\partial \langle \mathbf{C}_1 \rangle}{\partial t} = \frac{1}{\delta_1} (\mathbf{j}_0 - \mathbf{j}_1) + \boldsymbol{\nu}^T \mathbf{r}(\langle \mathbf{C}_1 \rangle, T_w) \quad \text{in } \Omega_1 \quad (6.13)$$

$$\text{and } \varepsilon_w \frac{\partial \langle \mathbf{C}_2 \rangle}{\partial t} = \frac{1}{\delta_2} \mathbf{j}_1 + \boldsymbol{\nu}^T \mathbf{r}(\langle \mathbf{C}_2 \rangle, T_w) \quad \text{in } \Omega_2, \quad (6.14)$$

where δ_1 and δ_2 are the mean thicknesses of artificial layers Ω_1 and Ω_2 , respectively

and are given by

$$h^* = \sqrt{\frac{Sh_{i\infty}}{\lambda_{\max}}}; \delta_1 = h^* \delta_w \text{ and } \delta_2 = (1 - h^*) \delta_w. \quad (6.15)$$

λ_{\max} being the largest absolute eigenvalue of Φ^2 ; h^* is the relative thickness of the first artificial layer to the total washcoat layer (when $h^* > 1$, use only one layer), which essentially represents the boundary-layer for the case of very high concentration-gradient near the fluid-washcoat interface; \mathbf{J}_0 and \mathbf{J}_1 are the interface mass-flux vectors at the fluid-washcoat ($\partial\Omega_{f1}$) interface and artificial intermediate interface ($\partial\Omega_{12}$), respectively that can be given in terms the transfer and cross-transfer coefficients as follows (Ratnakar et al. [8], Sarkar et al., [35]):

$$\mathbf{C}_s - \langle \mathbf{C}_1 \rangle = \mathbf{k}_{i1}^{-1} \mathbf{j}_0 + \widehat{\mathbf{k}}_{i1}^{-1} \mathbf{j}_1 \quad (6.16)$$

$$\text{and } \langle \mathbf{C}_1 \rangle - \langle \mathbf{C}_2 \rangle = \widehat{\mathbf{k}}_{e1}^{-1} \mathbf{j}_0 + \left(\mathbf{k}_{i1}^{-1} + \widehat{\mathbf{k}}_{i2}^{-1} \right) \mathbf{j}_1, \quad (6.17)$$

where these coefficients are required to be evaluated only asymptotically, i.e.,

$$\mathbf{k}_{i1} = \frac{\mathbf{D}_{e1} \mathbf{S} \mathbf{h}_{i1}}{\delta_1} = \frac{Sh_{i1,\infty}}{\delta_1} \mathbf{D}_{e1}, \quad (6.18)$$

$$\widehat{\mathbf{k}}_{i1} = \frac{\mathbf{D}_{e1} \widehat{\mathbf{S}} \mathbf{h}_{i1}}{\delta_1} = \frac{\widehat{Sh}_{i1,\infty}}{\delta_1} \mathbf{D}_{e1}, \quad (6.19)$$

$$\mathbf{k}_{e1} = \frac{\mathbf{D}_{e1} \mathbf{S} \mathbf{h}_{e1}}{\delta_1} = \frac{Sh_{e1,\infty}}{\delta_1} \mathbf{D}_{e1}, \quad (6.20)$$

$$\widehat{\mathbf{k}}_{e1} = \frac{\mathbf{D}_{e1} \widehat{\mathbf{S}} \mathbf{h}_{e1}}{\delta_1} = \frac{\widehat{Sh}_{e1,\infty}}{\delta_1} \mathbf{D}_{e1} \quad (6.21)$$

$$\text{and } \mathbf{k}_{i2} = \frac{\mathbf{D}_{e2} \mathbf{S} \mathbf{h}_{i2}}{\delta_2} = \frac{Sh_{i2,\infty}}{\delta_2} \mathbf{D}_{e2}. \quad (6.22)$$

The inlet, exit and initial conditions are the same as the 1+1D model. Thus, it can be seen from (Eqs. 6.18-6.22) that the proposed approach is free from the evaluation of non-linear functions of Thiele modulus matrices.

In addition, diffusivity matrices in the flow channel and washcoat are usually

diagonal (for most applications). For example, the diffusivity of a j^{th} species in the flow channel can be obtained using Fuller correlation which can be simplified (Reid et al. (1987)) as

$$D_{f,j} = a_j \times 10^{-10} \times T_f^{1.75} \quad [m^2/s], \quad (6.23)$$

where a_j is a constant for j^{th} component at a given pressure (representing the measure of its atomic volume). Similarly, diffusivity of j^{th} species in the washcoat can be expressed as

$$D_{w,j} = \frac{\varepsilon_w}{\tau_w} 97 r_p \sqrt{\frac{T_w}{M_{w,j}}}, \quad (6.24)$$

assuming the Knudsen diffusion regime, where ε_w , τ_w and r_p are the porosity, tortuosity and mean pore radius (in m) of the washcoat; and $M_{w,j}$ is the molecular weight of j^{th} species (in g/mol). Thus, it can be seen from *Eqs.* (6.18 - 6.22) suggest that the transfer coefficients are diagonal matrices. Further, in the absence of homogeneous reaction in the flow channel, the external mass-transfer coefficient in the flow channel (k_{e0}) is also a diagonal matrix. Therefore, the evaluation of interfacial fluxes j_0 and j_1 from the local equations (*Eq.* 6.16, 6.17) are even easier and can be performed element-wise. In the next section, we validate this approach even when reactions are very fast.

6.3 Validation of the Workflow with Linear Kinetics.

While the accuracies and validity of the proposed approach may not be proved rigorously for general case of non-linear kinetics, we can, however, investigate these aspects for linear kinetics, especially for transient short monolith model or for steady-states. [Note: even the transient long channel models with linear kinetics are equivalent to the steady-state in Laplace domain with modified rate constant]. Therefore, in this section, we consider the steady-state linear model with single and multicomponent systems, where rate constant can be very high. To simplify further, we consider only species balance through a parallel channels with neglect

the axial dispersion/diffusion in both phases, which reduces the 1+1D model in following form:

$$\frac{d\mathbf{C}_f}{d\tau} = \frac{-1}{R\Omega_f} \mathbf{j}_0, \quad 0 < x < L; \quad \text{and} \quad (\mathbf{C}_f)_{x=0} = \mathbf{C}_f^{in}, \quad (6.25)$$

$$\frac{\partial^2 \mathbf{C}_w}{\partial y^2} = \Phi^2 \mathbf{C}_w, \quad 0 < y < 1; \quad (\mathbf{C}_w)_{y=0} = \mathbf{C}_s \quad (6.26)$$

$$\text{and} \quad \left(\frac{\partial \mathbf{C}_w}{\partial y} \right)_{y=1} = \mathbf{0}, \quad (6.27)$$

with the interfacial flux given by

$$\mathbf{j}_0 = \mathbf{k}_{e0} (\mathbf{C}_f - \mathbf{C}_s) = -\frac{\mathbf{D}_e}{\delta_w} \left(\frac{\partial \mathbf{C}_w}{\partial y} \right)_{y=0}. \quad (6.28)$$

where $\tau = \frac{x}{u_f}$ is the space time coordinate in the flow channel and y is the dimensionless transverse coordinate in the washcoat.

6.3.1 Exact solution of 1+1D Model

The exact solution for washcoat concentration can be obtained by solving Eq. (6.26) that can be expressed as

$$\mathbf{C}_w = \cosh[\Phi(1-y)] (\cosh[\Phi])^{-1} \mathbf{C}_s, \quad (6.29)$$

which leads to the expression for flux (from Eq. 6.26) as

$$\mathbf{j}_0 = \frac{\mathbf{D}_w}{\delta_w} \Phi \tanh[\Phi] \mathbf{C}_s, \quad (6.30)$$

and effectiveness factor matrix as

$$\mathbf{H} = \Phi^{-1} \tanh[\Phi]. \quad (6.31)$$

Thus, the interface flux \mathbf{j}_0 can be solved in terms of fluid phase concentration \mathbf{C}_f by using *Eq.s.* (6.28 and 6.30) as $\mathbf{j}_0 = \mathbf{U}\mathbf{C}_f$ and thus, the fluid phase concentration can be expressed as follows:

$$\mathbf{C}_f = \exp\left[-\frac{\tau}{R_{\Omega_f}}\mathbf{U}\right]\mathbf{C}_f^{in}; \quad \mathbf{U}^{-1} = \mathbf{k}_e^{-1} + (\Phi \tanh[\Phi])^{-1} \delta_w \mathbf{D}_e^{-1}. \quad (6.32)$$

6.3.2 Solution of ROM

Similarly, since the ROM consisting of global *Eq.s.* (6.25, 6.13, 6.14) and local *Eq.s.* (6.16-6.22) are linear in interface fluxes and concentrations, they can also be solved exactly. This solution can be expressed as follows:

$$\mathbf{C}_f = \exp\left[-\frac{\tau}{R_{\Omega_f}}\mathbf{U}\right]\mathbf{C}_f^{in}; \quad \mathbf{U}^{-1} = \mathbf{k}_e^{-1} + \mathbf{A}^* \delta_w \mathbf{D}_e^{-1}, \quad (6.33)$$

while the interface flux at the fluid-washcoat interface is given by

$$\mathbf{J}_0 = \frac{\mathbf{D}_e}{\delta_w} (\mathbf{A}^*)^{-1} \Phi^2 \mathbf{C}_s, \quad (6.34)$$

and effectiveness factor matrix is given by

$$\mathbf{H} = (\mathbf{A}^*)^{-1}. \quad (6.35)$$

Here the matrix \mathbf{A}^* depends on Thiele modulus matrix as follows:

$$\begin{aligned} \mathbf{A}^* &= \mathbf{A}_1 - \mathbf{A}_2 \mathbf{A}_4^{-1} \mathbf{A}_3, \\ \mathbf{A}_1 &= h \Phi^2 \mathbf{S} \mathbf{h}_{1,int}^{-1} + \frac{1}{h} \mathbf{I}, \\ \mathbf{A}_2 &= h \Phi^2 \widehat{\mathbf{S}} \mathbf{h}_{1,int}^{-1} - \frac{1}{h} \mathbf{I}, \\ \mathbf{A}_3 &= h \Phi^2 \widehat{\mathbf{S}} \mathbf{h}_{1,ext}^{-1} - \frac{1}{h} \mathbf{I} \end{aligned}$$

$$\text{and } \mathbf{A}_4 = h\Phi^2\mathbf{S}\mathbf{h}_{e1}^{-1} + (1-h)\Phi^2\mathbf{S}\mathbf{h}_{i2}^{-1} - \left(\frac{1}{h} + \frac{1}{1-h}\right)\mathbf{I},$$

where $h = \frac{\delta_1}{\delta_1 + \delta_2} = \frac{\delta_1}{\delta_w}$ is the dimensionless thickness of the first artificial layer, which is chosen from *Eq.* (6.15) when h^* is less than unity. In this work, we have chosen h as follows:

$$h = \min[h^*, 0.5].$$

i.e., if $h = h^*$ when $h^* < 0.5$, otherwise $h = 0.5$ (i.e. at the middle of the washcoat). It should be noted from *Eq.* (6.32 and 6.33) or *Eqs.* (6.30 and 6.34) that the solution from 1+1D model and ROM is in similar form where the matrix \mathbf{A}^* is equivalent to $(\Phi^{-1} \tanh[\Phi])^{-1}$, i.e. inverse of effectiveness factor matrix.

6.3.3 Comparison for Single-component system

The exact solutions presented above can easily be simplified for a single components. In practice, we are mainly interested in the exit conversion of the solutes, therefore present the two important quantities: the effectiveness factor in the washcoat (from *Eqs.* 6.31 and 6.35) and the dimensionless interfacial flux $\frac{\delta_w}{D_e} j_0$ at the fluid-washcoat interface. *Fig.* 6.2 shows the former while *Fig.* 6.3 shows the latter. In these figures, the solid red lines are obtained from solution of 1+1D model while the blue dashed lines are obtained from solution of our proposed ROM where only asymptotic transfer coefficients are used. *Fig.* 6.2 is well known "effectiveness factor plot" in chemical engineering literature. While good match between proposed ROM and detailed model is expected for lower ϕ (i.e., for slow reactions) due to smaller concentration gradients in the washcoat, these figures show that the proposed ROM leads to very good results even when Thiele modulus is much higher (i.e., $\phi \gg 1$) that correspond to fast reactions (or higher temperatures).

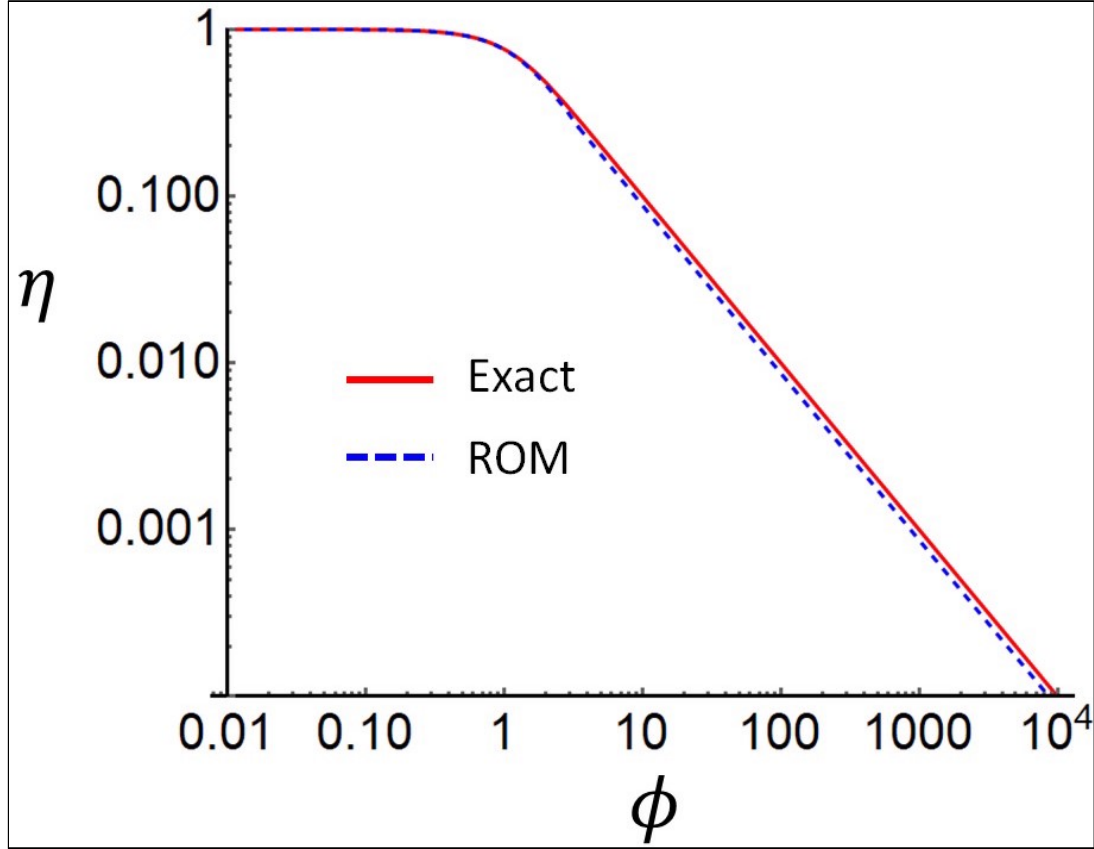
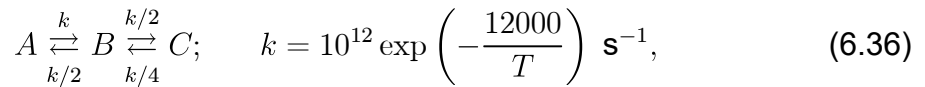


Figure 6.2: Effectiveness factor of the washcoat from the exact solution and the proposed ROM-coupled with domain decomposition using only asymptotic transfer coefficients.

6.3.4 Comparison for multicomponent system

In this section, we consider a reversible reaction scheme between three species (A , B and C) with linear kinetics:



and compare the exit concentrations of each species from 1+1D model and proposed ROM. The geometric, transport and kinetic parameters used in numerical calculations are listed in *Table 6.1*.

Since, we are interested in validation for fast reactions, temperature T is taken as a parameter such that the rate constant k can vary and comparison can be made

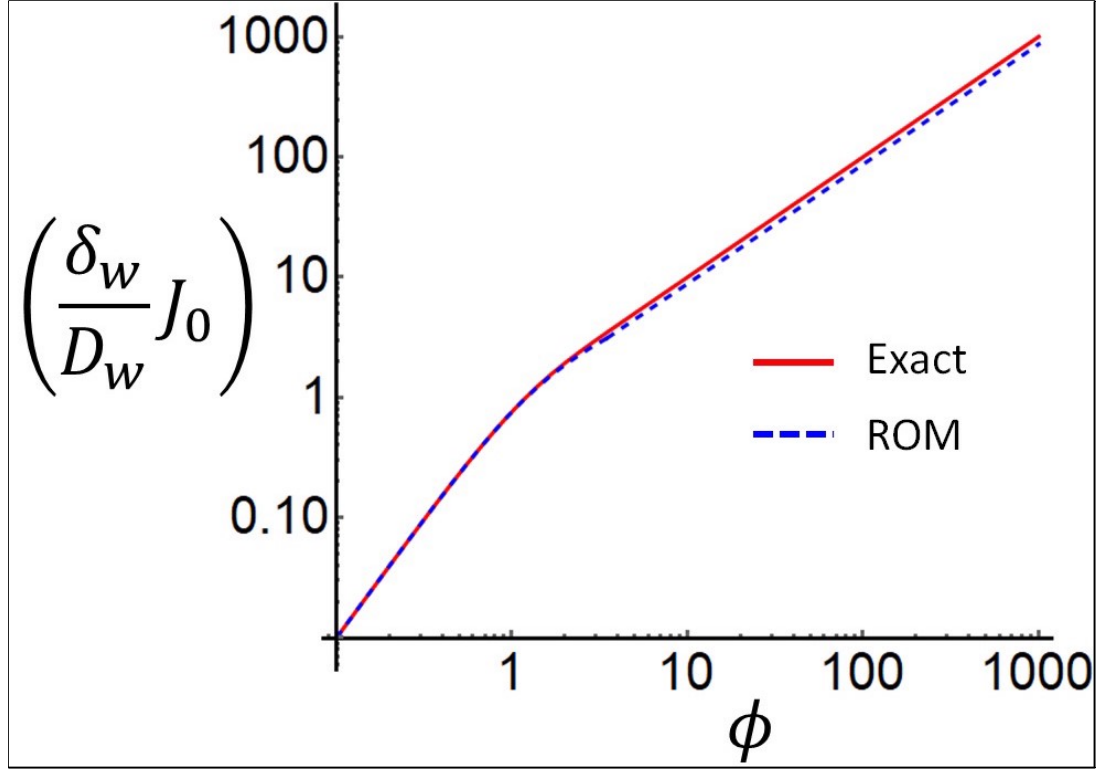


Figure 6.3: Dimensionless interface flux at the fluid-washcoat interface from the exact solution and the proposed method using only asymptotic transfer coefficients.

for each rate constants, especially corresponding to high Thiele modulus values. Note that with transport parameters provided in *Table 6.1*, the largest eigenvalue of Thiele modulus matrix corresponding to reaction scheme (*Eq. 6.36*) is given by

$$\lambda_{\max} = \frac{1.10837 \times 10^{11}}{\sqrt{T}} \exp\left(\frac{-12000}{T}\right), \quad (6.37)$$

which may vary from about 0.2 to 3×10^5 when temperature is varied from 500K to 1300K.

Considering the inlet mole fraction \mathbf{X}_f^{in} of the three species as given in *Table 6.1*, the exit mole fractions \mathbf{X}_f^{exit} are calculated from 1+1D model and proposed method, which are plotted in *Fig. 6.4*. The solid line corresponds to prediction from 1+1D while the dashed line corresponds to prediction from proposed method.

Table 6.1: Numerical constants and parameters used in model simulation

Constant	Value
L	3.0×10^{-2} m
u_f	20 m/s
R_Ω	181×10^{-6} m
δ_w	30×10^{-6} m
δ_s	63.5×10^{-6} m
r_p	10×10^{-9} m
ϵ_w	0.41
τ_w	8
Sh_∞	3
\widehat{Sh}_∞	6
$[\chi_{f,j}^{in}]_{A,B,C}$	[0.99, 0.005, 0.005]
$[a_j]_{A,B,C}$	[9.56, 44.5, 8.78]
$[M_{wj}]_{A,B,C}$	[28, 2, 30]

It can be seen from this *Fig. 6.4* that the predictions from the proposed method is acceptable and captures the washcoat diffusion effects even when reaction is fast (at higher temperature). Since the reaction scheme considered here is reversible with different rate constants for forward and backward reactions, the Thiele modulus matrix is not symmetric and may have negative or complex eigenvalue in general. Even in those cases, the proposed method can easily be utilized because it always require Φ^2 for evaluation rather than Φ (as compared to previously developed ROM in literature). Thus, the example considered here validates the proposed methodology not only for slow reactions but also for fast reactions as well when reaction network may be even more complicated. In addition, the computation time with proposed method was 1.7s as compared to 188s for $1 + 1D$ model, increasing the simulation speed by about 100 times. In addition, it should be noted that this example was considered in our previous work (see example #3 in chapter

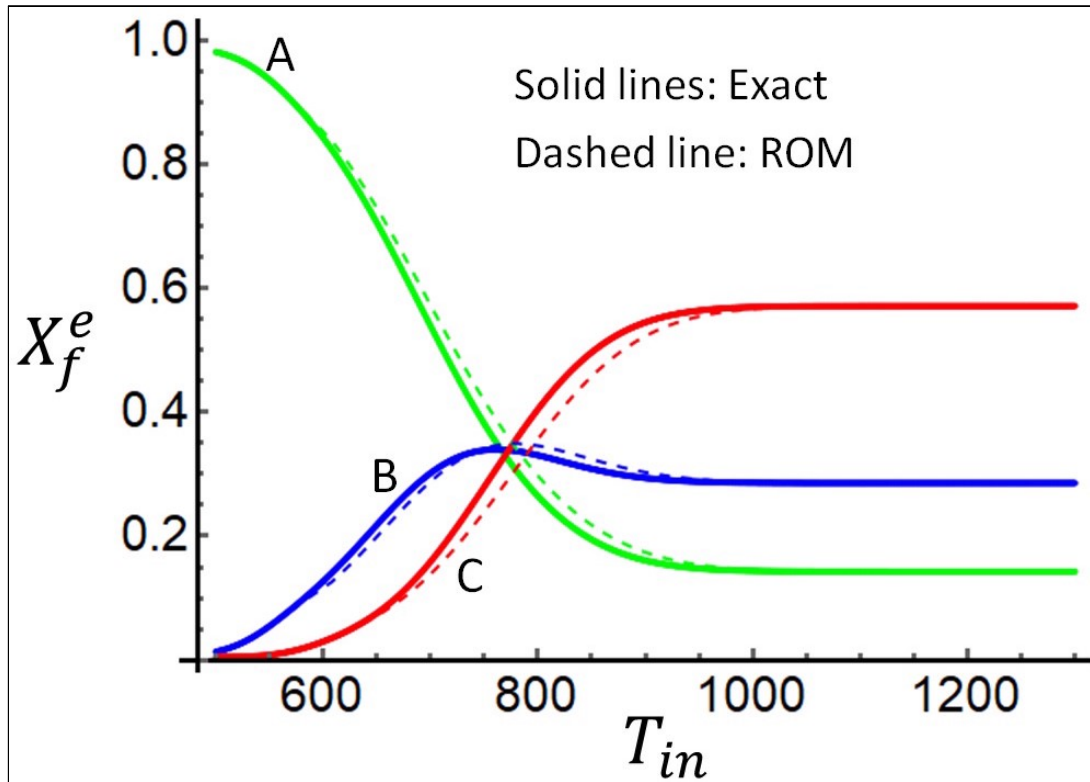


Figure 6.4: Exit concentrations (dimensionless) from 1+1D model and proposed ROM for linear kinetics.

l), where we showed that even the use of Thiele modulus dependent transfer coefficient with diagonal approximation of Φ (with computation time of 1.6s) was not adequate for prediction of exit concentration and led to significant error ($> 300\%$ relative error). And, the computation time from ROM with accurate Thiele modulus dependent transfer coefficient was about 5.5s for this case. In other words, the proposed approach works better than the ROM containing Thiele modulus dependent transfer coefficient with diagonal approximation (but without domain decomposition) in terms of accuracy while computation time is more or a less the same. But the current approach has reduced the computation time by about factor 3 as compared to ROM with proper Thiele modulus dependent transfer coefficients. Now we consider a nonlinear kinetics in the next section.

6.4 Real time simulation of three-way catalytic converter

This section presents the applicability of the proposed method for realistic system of TWC where reaction rates may be highly non-linear. We consider the four reaction model provided in *Table 6.2*, which may contain negative order kinetics with respect to NO . The rate expressions and kinetic parameters as listed in this

Table 6.2: Four reaction model for TWC: rates and kinetic parameters

Reaction scheme:					
#	Reactions			Rates	
1	$CO + 0.5O_2 \longrightarrow CO_2$			$r_1 = \frac{1}{G}K_1X_{CO}X_{O_2}$	
2	$H_2 + 0.5O_2 \longrightarrow H_2O$			$r_2 = \frac{1}{G}K_2X_{H_2}X_{O_2}$	
3	$C_3H_6 + 4.5O_2 \longrightarrow 3CO_2 + 3H_2O$			$r_3 = \frac{1}{G}K_3X_{HC}X_{O_2}$	
4	$NO + CO \longrightarrow CO_2 + 0.5N_2$			$r_4 = K_4X_{NO}X_{CO}$	
Kinetic parameters:					
#	K_i^0	E_i/R	K_{ai}^0	E_{ai}/R	$(-\Delta H)$
	mol.m ⁻³ s ⁻¹ K	K	mol.m ⁻³ s ⁻¹ K	K	kJmol ⁻¹
1	1×10^{19}	10825	65.5	-961	283
2	1×10^{19}	10825	2080	-361	242
3	2×10^{19}	11427	3.98	-11611	1926
4	$4 \times 10^{14*}$	10825	4.79×10^5	3733	373
*unit of K_4^0 is mol.m ⁻³ s ⁻¹					
$G = T(1 + K_{a1}X_{CO} + K_{a1}X_{HC})^2(1 + K_{a3}X_{CO}^2X_{HC}^2)(1 + K_{a4}X_{NO}^{0.7})$					
$K_{ai} = K_{ai}^0 \exp(\frac{-E_{ai}}{RT});$					
$K_i = K_i^0 \exp(\frac{-E_i}{RT})$					

table are obtained from Joshi et al., [2] and Tu et al., [19]. The diffusivity of all five species (CO , H_2 , NO , HC , O_2) in the flow channel and washcoat can be calculated from *Eqs. (6.23 and 6.24)*, component specific parameters a_j along with various other parameters are listed in *Table 6.3* for numerical computation in this

example. 6.1).6.1.

Table 6.3: Numerical constants and parameters used in model simulation

Constant	Value	Constant	Value
L	$7.85 \times 10^{-2} \text{ m}$	k_f	$0.0386 \text{ W} \cdot \text{m}^{-1} \cdot \text{K}^{-1}$
u_f	2 m/s	k_w	$1.5 \text{ W} \cdot \text{m}^{-1} \cdot \text{K}^{-1}$
R_Ω	$181 \times 10^{-6} \text{ m}$	Cp_f	$1068 \text{ J} \cdot \text{kg}^{-1} \cdot \text{K}^{-1}$
δ_w	$30 \times 10^{-6} \text{ m}$	Cp_w	$1000 \text{ J} \cdot \text{kg}^{-1} \cdot \text{K}^{-1}$
δ_s	$63.5 \times 10^{-6} \text{ m}$	ρ_w	$2000 \text{ kg} \cdot \text{m}^{-3}$
r_p	$10 \times 10^{-9} \text{ m}$	Sh_∞	3
ϵ_w	0.41	\widehat{Sh}_∞	6
τ_w	8	Nu_∞	3
T_f^{in}	550 K	\widehat{Nu}_∞	6
T_f^0	300 K	T_w^0	300 K
$X_{f,CO}^{in}$	1%	a_{CO}	9.56
X_{f,O_2}^{in}	0.85%	a_{O_2}	9.55
X_{f,H_2}^{in}	500 ppm	a_{H_2}	44.5
X_{f,H_2}^{in}	0.3%	a_{NO}	8.78
$X_{f,NO}^{in}$	300 ppm	\mathbf{X}_w^0	$\mathbf{0}$
\mathbf{X}_f^0	$\mathbf{0}$		

Corresponding to these parameters (Table 6.3) and four reaction scheme (Table 6.2), the simulation results are plotted in Figs. 6.5 to 6.8.

Figs. 6.5 and 6.6 show the temporal profiles of dimensionless exit concentrations \mathbf{X}_f^e and exit temperature T_f^e , respectively, where results from 1+1D model are plotted as solid lines while results from our approach is plotted as dashed lines. Similarly, Fig. 6.7 show the axial (spatial) profiles of the dimensionless exit concentrations \mathbf{X}_f at various times from both 1+1D model (solid lines) and our approach (dashed lines). These figures show very good match between the two (within acceptable accuracies). The comparison can be visualized better from

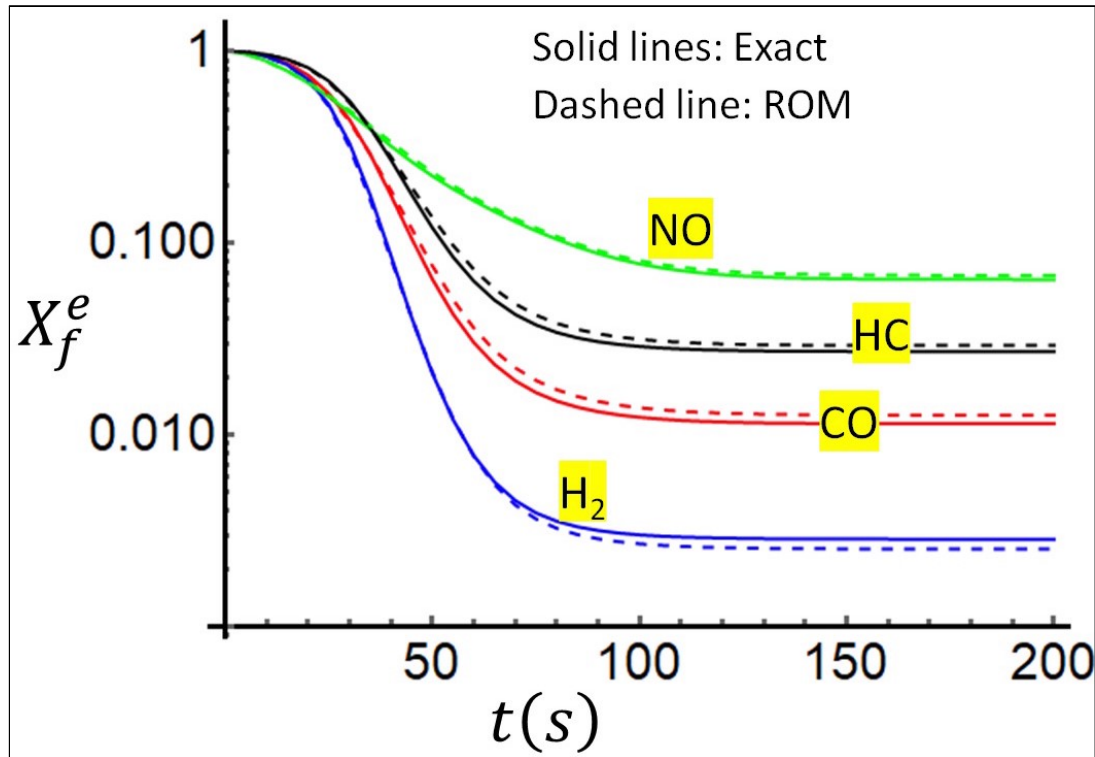


Figure 6.5: Temporal profile of dimensionless exit concentrations X_f^e for TWC obtained from 1+1D model (solid lines) and proposed method (dashed line) for CO , H_2 , NO and hydrocarbon (HC).

cross-plot shown in *Fig. 6.8* where horizontal axis represents the exit concentrations of each species from 1+1D model and vertical axis represents the same from our approach. It can be seen from this figure that all the numerical data points are aligned with the unit-slope line (i.e. $y = x$), within relative deviation of within 6%, validating the accuracies and validity of our approach for the example considered here.

The 1+1D model here is solved by using 30 equally-spaced mesh points in flow direction while 10 geometrically-spaced mesh points in transverse direction, which assured the grid-insensitive solution. The computation time corresponding to 1+1D model was about 1623s. The same number equally-spaced mesh points were used in flow direction to obtain numerical solution from the proposed ROM, which required computation time of about 4.7s, i.e. 300 times faster than the 1+1D.

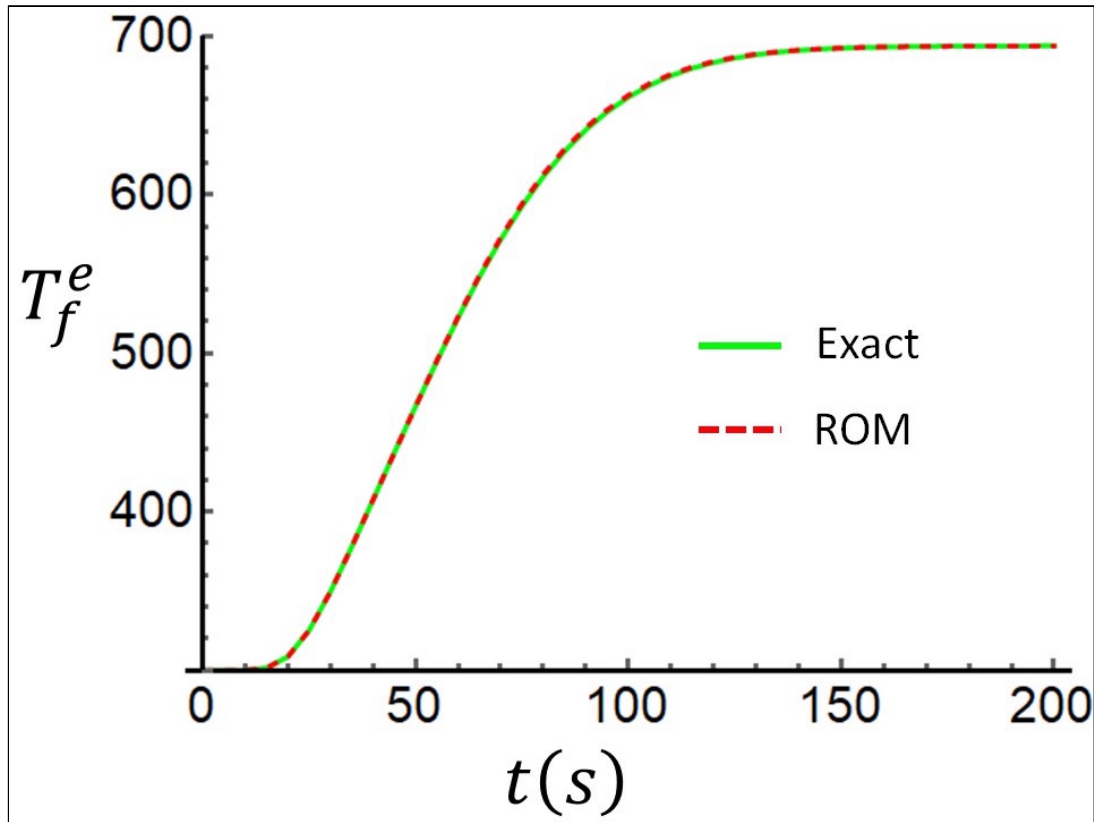


Figure 6.6: Temporal profile of exit fluid temperature T_f^e for TWC obtained from 1+1D model (solid lines) and proposed method (dashed line) for CO , H_2 , NO and hydrocarbon (HC).

For the same example considered in our earlier work (see Example #1 in chapter II), it was shown that the computation time from ROM with diagonal approximation was about 3.2s while from ROM with proper representation was about 23s. Thus, the proposed approach does not only simplifies the model calculation and enables the use of asymptotic transfer coefficient, but also increases the computation speed by roughly 2 order of magnitude as compared to 1+1D model and by about factor 5 as compared to the ROM with Thiele modulus dependent transfer coefficients, for the current example. For the more complicated case of complex network with highly non-linear kinetics and larger number of species, the increase in computation speed from our approach is expected to be even faster.

Remark: It should also be noted that the accuracy of our approach can further

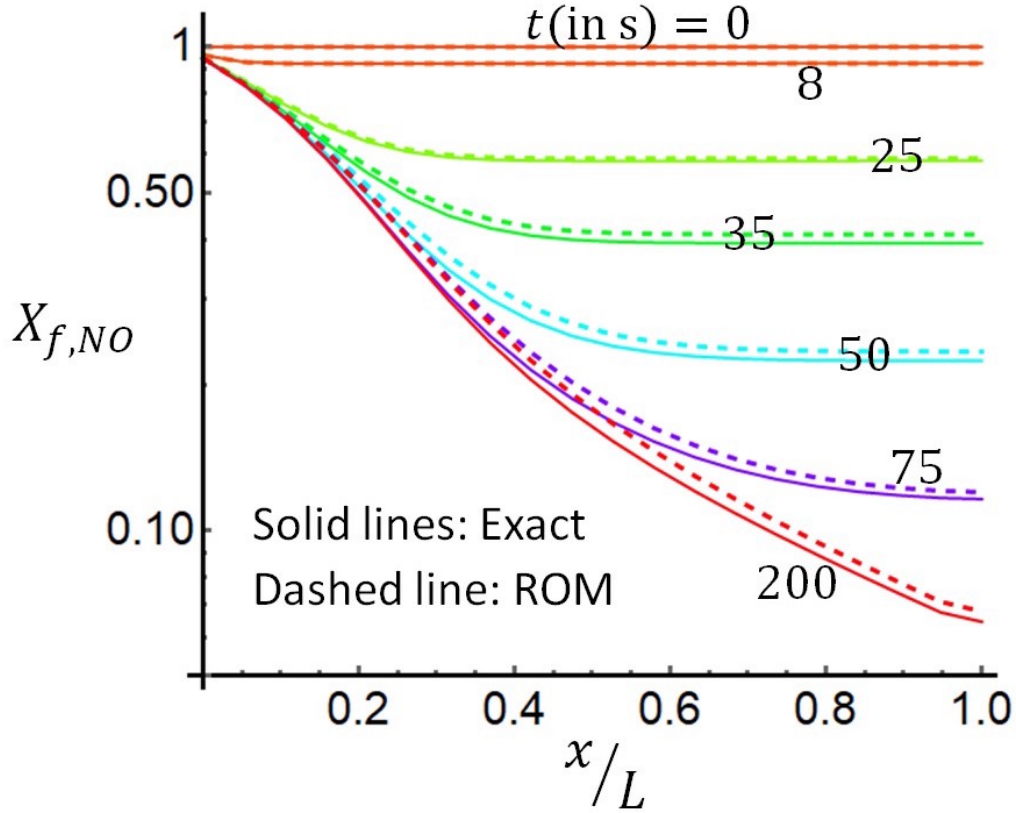


Figure 6.7: Axial profiles of dimensionless exit concentrations X_f of NO versus dimensionless axial coordinate (x/L) obtained from 1+1D model (solid lines) and proposed method (dashed line) for TWC at various times.

be increased, when we consider the transfer coefficient as a linear function of Φ^2 , i.e.

$$\mathbf{Sh}_\Omega = Sh_{\Omega\infty}\mathbf{I} + \lambda\Phi_\Omega^2 \quad (6.38)$$

$$\text{and } \widehat{\mathbf{Sh}}_\Omega = \widehat{Sh}_{\Omega,\infty}\mathbf{I} + \Phi_\Omega^2, \quad (6.39)$$

for any domain Ω . Eq. 6.38 is the Taylor series expansion of exact Sherwood number \mathbf{Sh}_Ω to the first term in Φ_Ω^2 (from Eq. 6.1 or 6.4) that is good only when eigenvalues of Φ_Ω^2 are less than unity, which is satisfied in our approach due to the domain decomposition (leading to maximum eigenvalue λ_{\max} of $\Phi_{\Omega_1}^2$ less than unity). On the other hand, Eq. 6.4 is valid for any Φ_Ω^2 and is not restricted to the magnitude of

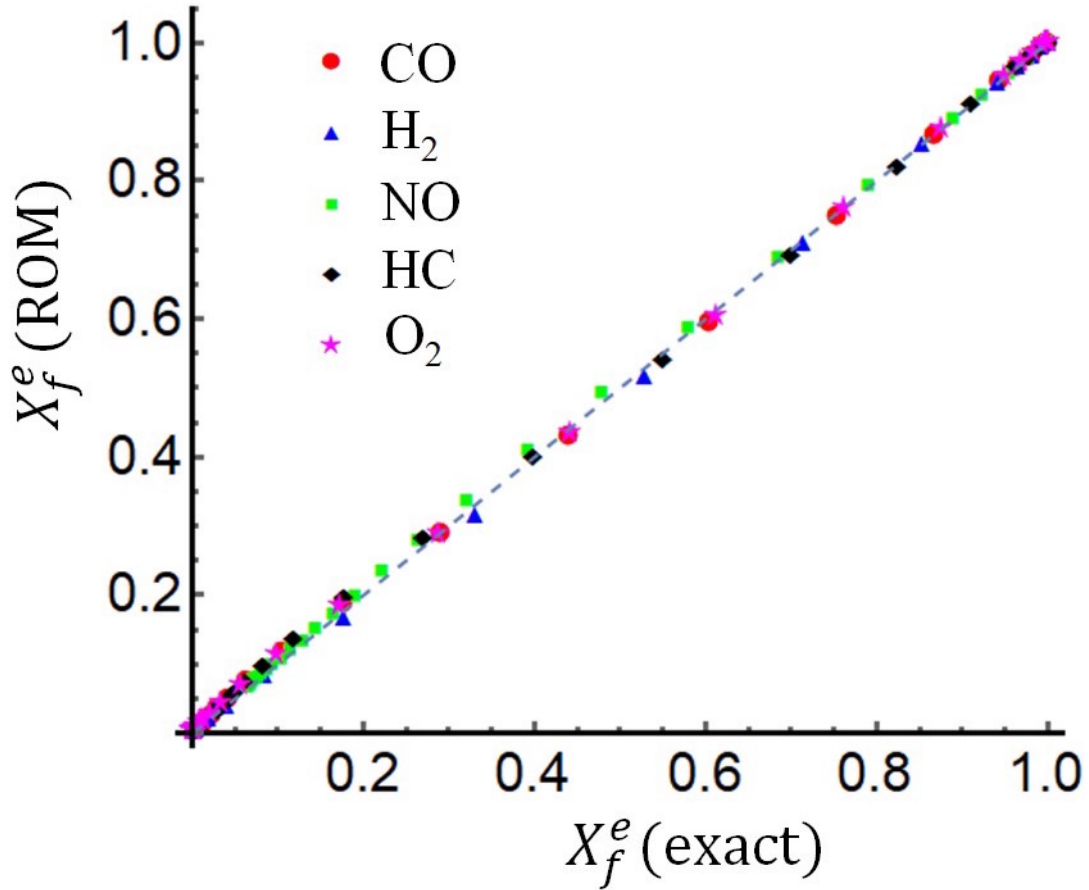


Figure 6.8: Cross-plot between exit dimensionless concentrations X_f^e of all species obtained from 1+1D model (solid lines) and proposed method (dashed line) for TWC.

its eigenvalues. Using these two approximation may increase the overall accuracy of the simulation while no additional evaluation of function of Thiele modulus matrix is required. However, only drawback in using these approximations (Eqs. 6.38 or 6.39) is that the transfer coefficient matrices may not be diagonal and may add up a little to the computation time in solving for fluxes. However, it is still much more efficient than using the non-linear function of matrices as their computation can be $O(N^4)$, where N is the number of species.

6.5 Conclusions and Discussion

In this chapter, we proposed a novel approach based on coupling of reduced order model (ROM) with domain decomposition method for describing the reactive flow in monolith reactors. First, it should be pointed out that washcoat diffusional effects must be captured in order to evaluate the performance of the monolith reactor, and if neglected then the simulation can lead to significant errors. Several reduced order model have been developed for this purposes, however, the ROM containing Thiele modulus dependent transfer coefficients are only ones which capture the washcoat diffusional effects properly (see chapter 2 and 3 for detailed discussion). This requires evaluation of function of Thiele modulus matrices. While this approach has shown to decrease the computation time significantly (2-3 orders of magnitude for simpler systems and several order of magnitude for larger systems), the one major cost in computation is the evaluation of (non-linear) functions of Thiele modulus matrices. In this work, we resolve that issue and decrease the computation time even further by deploying the domain decomposition method with ROM, while keeping the acceptable accuracy in numerical computation. This approach essentially decouples the boundary layer (i.e. higher gradient zone near the fluid-washcoat interface) captures the washcoat diffusional effects with sufficient accuracy within the boundary-layer. Since the main objective of this work is presenting the methodology for faster real time simulation, we have illustrated it here with only simple examples of only few (less than four) reactions. Even in these simple cases, it is shown that the proposed approach leads to acceptable accuracies (even for faster reactions) and can speed-up the transient simulation two to three orders of magnitude as compared to 1+1D model, thus capturing the washcoat diffusional effects. Even though it is not possible to prove theoretically, our experience indicates that the speed-up factor could be much higher (several orders of magnitude higher) for realistic cases when they contain complex reaction

network with highly non-linear kinetics, or larger number of species and/or reactions. The reason for increased computation speed and retained accuracy is due to the simplification of transfer coefficients with asymptotic values and proper domain decomposition, which captures the washcoat diffusional effects in the boundary-layer near fluid-washcoat interface and avoids the calculation of function of Thiele modulus matrices (which could have complex features such as negative or complex eigenvalues).

Chapter 7

Summary and Suggestions for Future Work

7.1 Summary

The main contribution of this work is the presentation of a novel and accurate reduced order model with local property dependent internal and external mass transfer coefficients for real time simulations of monolith reactors. In chapter 3, we compared the accuracy of the present approach with other reduced order models in the literature and with exact (numerical) solution of the detailed washcoat diffusion model and illustrated the application of the reduced order models to three-way catalytic converter in three different cases. First, it should be pointed out that completely neglecting washcoat diffusional effects as is done in some literature studies could lead to very large error (as much as a factor ten or higher in predicting the exit concentrations of some species as illustrated in example 1). The proposed method for including the washcoat diffusional effect is based on the calculation of the internal mass transfer coefficient matrix that depends on the local Thiele matrix. We showed that the use of local property dependent transfer coefficients in terms of the Jacobian of the reaction rate vector leads to the best accuracy followed by its diagonal approximation, followed by the asymptotic (slow reaction) approximation for the internal Sherwood number. It is shown that the proposed method has sufficient accuracy for most practical applications, especially in the washcoat diffusion-controlled regime, while speeding up the calculations by orders of magnitude compared to detailed washcoat diffusion models.

In chapter 4, we presented a novel and accurate procedure with local property dependent internal and external mass transfer coefficient matrices for real time simulations of monolith reactors with dual washcoat layers, this approach extends the Thiele matrix method for accurately describing the washcoat diffusional

effects in single layered systems. It combines the vector form of the multi-scale averaged model with calculation of the local property dependent internal, external and cross-Sherwood number matrices for multi-component systems. We illustrated the usefulness of the reduced order model using the example of a dual-layered model system with first washcoat layer of selective catalytic reduction (SCR) catalyst and second washcoat layer of lean NO_x trap (LNT) catalyst. We determined the mesh independent solutions of the full 1+1D detailed model and compared the same with that obtained with the reduced order model and we showed that the proposed method has the same accuracy as the mesh independent detailed solution while speeding up calculations by about three orders of magnitude for the example studied, and possibly by several more orders of magnitude for real systems with complex and detailed kinetic models to describe the storage and reactions in the catalytic layers.

Moreover, micro kinetics are more often used to develop and improve reaction schemes as they are more detailed than global kinetics, but the time consuming problem of estimating parameters with microkinetic reaction scheme and the accuracy of the estimated parameters has always been a difficult problem to solve. With the goal to speed up the calculations and that the parameters should be used directly for accurate full-scale transient simulations. In chapter 5, we presented a novel procedure of computing washcoat diffusional effects in reduced order models with local property dependent internal and external transfer coefficients for the reaction system with detailed micro-kinetics. We extended the Thiele matrix approach to the case of detailed micro-kinetics with the example of H₂/CO/C₃H₆ oxidation over Pt/Al₂O₃ catalyst, the large number of reactions make the simulation of detailed 1+1D model very time consuming, but our reduced order model with Thiele matrix approximation is shown to be more efficient than other cases because Φ^2 becomes diagonal which leads to an easier calculation of the internal

mass transfer coefficient matrix.

The main contribution of chapter 6 is the presentation of a novel approach based on coupling of reduced order model (ROM) with domain decomposition method for describing the reactive flow in monolith reactors. From previous chapters, we find that except with the case of micro kinetics model and without homogeneous reactions in the monolith channel, the determination of cross-transfer and transfer coefficient (\mathbf{K}_{int} and $\widehat{\mathbf{K}}_{int}$) for multicomponent systems require evaluation of non-linear functions of Thiele modulus matrices which can be cumbersome and computationally costly for large multi-component systems. So the method we propose in chapter 6 is to avoid solving matrix function of Thiele matrix and use only asymptotic values to calculate the mass transfer coefficients, but this method is different from the conventional asymptotic approximation which was proposed by Kumar et al., (2012). This approach essentially decouples the boundary layer (i.e. higher gradient zone near the fluid-washcoat interface) captures the washcoat diffusional effects with sufficient accuracy within the boundary-layer and use asymptotic Sherwood numbers in each of the layers.

7.2 Suggestions for Future Work

We now discuss some limitations of the Thiele matrix approach for including washcoat diffusional effects in reduced order models. First, we note that while it leads to exact results for linear kinetics, the error may not be neglected for strongly nonlinear kinetics, especially when there is a large difference between the interfacial and washcoat averaged concentrations. The error may be reduced when external mass transfer effects become significant and interfacial concentrations are smaller. Second, this approach assumes that the washcoat thickness is small and uniform so that species diffusion is mainly unidirectional. If this is not the case (or for thicker and/or irregular two or three-dimensional washcoat shapes), additional error could arise in using an effective one-dimensional model. Finally, it should be

pointed out that the problem of nonlinear diffusion–reaction is an extremely complex one and can display various spatio-temporal patterns depending on the type of kinetics used. The low-dimensional model as well as the approach presented here are either not valid or breakdown for the case of autocatalytic kinetics that could lead to multiple steady-states and spatial patterns. In such cases, we have to resort back to detailed models to determine the system behavior.

For the new approach proposed in chapter 6, while the methodology may work for most practical cases, it must be kept in mind that it is still based on ROM and may have the limitations inherent to dimension-reductions. For example, while it may lead to accurate results for linear kinetics or slower reactions, it may still lead to significant error for strongly non-linear kinetics, especially when kinetic order is negative, or when boundary-layer thickness may not be uniform, or when time-scales for intermediate components appearing and disappearing are much smaller. In such cases, the detailed model is the only choice. However, whenever, length and time-scale separation is evident, ROM is applicable and proposed workflow can be utilized to increase for real time simulations. This approach can also be extended to other transport-reacting systems such as packed-bed reactors, other tubular/catalytic reactors and porous catalyst.

There are several possible extensions of the work presented here but we discuss only a few of them. The first of these is to the modeling of packed-bed catalytic reactors, where the problem of diffusion and reaction in the catalyst particles can be approximated (and coupled to the fluid and solid phase balances) as shown in this work. Second is the extension of Thiele matrix approach to non-isothermal case with dual layered monolith reactors. As the temperature gradients within the catalytic layers in most practical systems are small (and only axial and gas to catalyst temperature gradients are significant), the extension only requires addition of energy balances for the gas and solid phases (as illustrated in earlier studies for

single layered systems). A third possible extension is to more than two washcoat layers or to cases where the catalytic activity varies with axial or transverse positions. In chapter 4, we used the kinetics derived from a model with less mesh points in the washcoat diffusion-disguised regime. Hence, one of the interesting extensions would be investigating how much the kinetics constants will be changed with different number of mesh points to maintain a same exit species mole fraction. Another extension worthy of discussion is to elaborate the physical meaning of the Thiele matrix square with complex eigenvalues.

For the extension work of micro-kinetics based model, one obvious extension of the calculations presented in chapter 5 is for more detailed micro-kinetic models that include multiple adsorption/desorption and/or reaction sites. Another possible extension is to monolith reactors with more than a single washcoat layer or to cases where the catalytic activity varies with axial or transverse positions.

References

1. Balakotaiah, V., 2008. "On the relationship between Aris and Sherwood numbers and friction and effectiveness factors." *Chemical Engineering Science* 63,5802–5812.
2. Joshi, S.Y., Harold, M.P., Balakotaiah, V., 2009. "Low-dimensional models for real time simulations of catalytic monoliths." *AIChE Journal* 55, 1771-1783.
3. Kumar, P., Makki, I., Kerns, J., Grigoriadis, K., Franchek, M., & Balakotaiah, V., 2012. "A low-dimensional model for describing the oxygen storage capacity and transient behavior of a three-way catalytic converter." *Chemical Engineering Science* 73, 373-387.
4. Bissett, E. J., "An asymptotic solution for washcoat pore diffusion in catalytic monoliths." 2015. *Emission Control Sci. Tech.* 1, 3-16.
5. Gundlapally, S.R., Dudgeon, R., Wahiduzzaman, S., 2018. "Efficient solution of washcoat diffusion0reaction problem for real-time simulations." *Emission Control Sci. Tech.* 4(2) 90–102.
6. Ratnakar, R.R., Bhattacharya, M., Balakotaiah, V., 2012. "Reduced order models for describing dispersion and reaction in monoliths." *Chemical Engineering Science* 83, 77-92.
7. Ratnakar, R.R., Balakotaiah, V., 2015. "Reduced order multimode transient models for catalytic monoliths with micro-kinetics." *Chemical Engineering Journal* 260, 557–572.
8. Ratnakar, R.R., Dadi, R.K. and Balakotaiah, V., 2018. "Multi-scale reduced

- order models for transient simulation of multi-layered monolith reactors." *Chemical Engineering Science* 352, 293.
9. Kumar, P., Gu, T., Grigoriadis, K., Franchek, M., & Balakotaiah, V., 2014. "Spatio-temporaldynamics of oxygen storage and release in a three-way catalytic converter." *Chemical Engineering Science* 111, 180-190.
 10. Ting, AWL., Li, M., Harold, M.P., Balakotaiah, V., 2017. "Fast cycling in a non-isothermal monolithic lean NO_x trap using H₂ as reductant: Experiments and modeling." *Chemical Engineering Journal* 326, 419-435.
 11. Ting, AWL., Balakotaiah, V., Harold, M.P., 2019. "Fast cycling NO_x storage and reduction: Modeling and analysis of reaction pathways, transport and reductant effects." *Chemical Engineering Journal* 370, 1493-1510.
 12. Daneshvar, K., Dadi, R.K., Luss, D., Balakotaiah, V., Sung, B. K., Kalamaras, C. M., Epling, W. S., 2017. "Experimental and modeling study of CO and hydrocarbons light-off on various Pt-Pd/ γ -Al₂O₃ diesel oxidation catalysts." *Chemical Engineering Journal* 323, 347–360.
 13. Mozaffari, B., Tischer, S., Votsmeier, M., Deutschmann, O., 2016. "A one-dimensional modeling approach for dual-layer monolithic catalysts." *Chemical Engineering Science* 139, 196-210.
 14. Rink, J., Mozaffari, B., Tischer, S., Deutschmann, O., Votsmeier, M., 2017. "Real-time Simulation of Dual-Layer Catalytic Converters Based on the Internal Mass Transfer Coefficient Approach." *Topics in Catalysis* 60, 225-229.
 15. Gundlapally, S.R., Balakotaiah, V., 2011. "Heat and mass transfer correlations and bifurcation analysis of catalytic monoliths with developing flows." *Chemical Engineering Science* 66, 1879-1892.

16. Gu, T., Balakotaiah, V., 2016. "Impact of heat and mass dispersion and thermal effects on the scale-up of monolith reactors." *Chemical Engineering Journal* 284, 513-535.
17. Joshi, S.Y., Harold, M.P., Balakotaiah, V., 2009. "On the use of internal mass transfer coefficients in modeling of diffusion and reaction in catalytic monoliths." *Chemical Engineering Science*. 64 (23), 4976-4991.
18. Reid, R. C., Prausnitz, J.M., &Sherwood, T.K., 1977. "The properties of gases and liquids." McGraw-Hill. (3rd edition).
19. M. Tu, R. R. Ratnakar, V. Balakotaiah, 2020."Reduced order models with local property dependent transfer coefficients for real time simulations of monolith reactors." *Chemical Engineering Journal* 383 (2020) 123074.
20. J.R. Picardo, S. Pushpavanam, "Low-dimensional modeling of transport and reactions in two-phase stratified flow." *Ind. Eng. Chem. Res.* 54 (2015) 10481–10496.
21. B. Shakya, M.P. Harold, V. Balakotaiah. "Modeling and analysis of dual-layer NO_x storage and reduction and selective catalytic reduction monolithic catalyst." *Chemical Engineering Journal* 237 (2014) 109–122.
22. P. S. Dhillon, M. P. Harold, D. Wang, A. Kumar, S. Y. Joshi. "Modeling and analysis of transport and reaction in washcoated monoliths: Cu-SSZ-13 SCR and dual-layer Cu-SSZ-13 + Pt/Al₂O₃ ASC." *Royal Society of Chemistry* (2019) 1103-1115
23. R. K. Dadi, K. Daneshvar, D. Luss, V. Balakotaiah, C. M. Kalamaras, W. Epling. "Comparison of light-off performance of Pt-Pd/ γ -Al₂O₃ dual layer and dual brick diesel oxidation catalysts." *Chemical Engineering Journal* 335 (2018) 1004–1017.

24. Nibbelke, R.H., Nievergeld, A.J.L., Hoebink, J.H.B.J., Marin, G. B. (1998). "Development of a transient kinetic model for the CO oxidation by O₂ over a Pt/Rh/CeO₂/γ-Al₂O₃ three-way catalyst." *Applied Catalysis B: Environmental* 19 (1998) 245-259.
25. Harmsen, J. M. A., Hoebink, J.H.B.J., Schouten, J.C.(2001). "Acetylene and carbon monoxide oxidation over a Pt/Rh/CeO₂ /γ-Al₂O₃ automotive exhaust gas catalyst: kinetic modelling of transient experiments." *Chemical Engineering Science* 56 (2001) 2019-2035.
26. KOČÍ, P., KUBÍČEK, M., MAREK, M.(2004). "MULTIFUNCTIONAL ASPECTS OF THREE-WAY CATALYST Effects of Complex Washcoat Composition." *Chemical Engineering Research and Design*, 82(A2): 284–292.
27. Rankovic, N., Nicolle, A., Berthout, D., Patrick D., C.(2011). "Kinetic Modeling Study of the Oxidation of Carbon Monoxide Hydrogen Mixtures over Pt/Al₂O₃ and Rh/Al₂O₃ Catalysts." |*J. Phys. Chem. C* 2011, 115, 20225–20236.
28. Keller K., Lott P., Stotz H., Maier, L., Deutschmann, O.(2020). "Microkinetic Modeling of the Oxidation of Methane Over PdO Catalysts—Towards a Better Understanding of the Water Inhibition Effect." *Catalysts* 2020, 10, 922; doi:10.3390/catal10080922.
29. Stotz, H., Maier, L., Boubnov, A., Gremminger, A.T., Grunwaldt, J.-D., Deutschmann, O.(2019). "Surface reaction kinetics of methane oxidation over PdO." *Journal of Catalysis* 370 (2019) 152–175.
30. Balakotaiah, V., Gupta N., West D. H., (2000). "A simplified model for analyzing catalytic reactions in short monoliths." *Chemical engineering science*, 5 (2000) 5367-5383.

31. Kota, A. S., Dadi, R.K., Luss, D., Balakotaiah, V. (2017). "Analysis of light-off during oxidation of reactant mixtures on Pt/Al₂O₃ using micro-kinetic models." *Chemical Engineering Science* 166 (2017) 320–333.
32. Joshi, S. Y., Ren, Y., Harold, M. P., & Balakotaiah, V. (2012). "Experimental and theoretical investigation of controlling regimes during lean oxidation of methane and propylene on Pt/Al₂O₃ monolithic reactors." *Industrial & engineering chemistry research*, 51(22), 7482-7492.
33. Irandoust, S., & Andersson, B. (1988). "Monolithic catalysts for nonautomobile applications." *Catalysis Reviews Science and Engineering*, 30(3), 341-392.
34. Alam, I., West, D. H., & Balakotaiah, V. (2015). "Bifurcation analysis of thermally coupled homogeneous–heterogeneous combustion." *Chemical Engineering Journal*, 280, 293-315.
35. Sarkar, B., Ratnakar, R. R., & Balakotaiah, V. (2020). "Multi-scale coarse-grained continuum models for bifurcation and transient analysis of coupled homogeneous-catalytic reactions in monoliths." *Chemical Engineering Journal*, 407, 126500.
36. Ratnakar, R. R., & Balakotaiah, V. (2015). "Reduced-order transient models for describing thermal gradients in catalytic monoliths." *Industrial & Engineering Chemistry Research*, 54(42), 10260-10274.
37. R. R. Ratnakar, M. Tu, V. Balakotaiah, 2021. "A novel approach for computing washcoat diffusional effects in reduced order model for monolith reactors." in preparation, ECST.
38. P.S. Metkar, M.P. Harold, V. Balakotaiah, "Experimental and kinetic modeling study of NH₃-SCR of NO_x on Fe-ZSM5. Cu-chabazite and combined Fe- and

Cuzeolite monolithic catalysts." *Chemical Engineering Science* 87 (2013) 51–66.

Appendices

Appendix A: Calculation of matrix functions and some details of Thiele matrix approach

The purpose of this Supplementary Material is to give some details of the Thiele matrix based approach to the simplification of multi-component washcoat diffusion problem. We present these details only for the case of slab (flat plate or thin washcoat) geometry and global kinetics. Additional details and extensions may be found in the references cited.

Effectiveness Factor and Sherwood Matrices:

For the case of N_r reactions among N species occurring in a washcoat of thickness δ_c , the diffusion-reaction problem is described by

$$\mathbf{D}_e \frac{d^2 \mathbf{c}_{wc}}{dy^2} = \mathbf{r}(\mathbf{c}_w) = -\boldsymbol{\nu}^T \hat{\mathbf{r}}(\mathbf{c}_{wc}); 0 < y < \delta_c \quad (\text{S-1})$$

$$\text{and } \mathbf{c}_{wc} = \mathbf{c}_s @ y = 0; \frac{d\mathbf{c}_w}{dy} = \mathbf{0} @ y = \delta_c, \quad (\text{S-2})$$

where \mathbf{D}_e is the matrix of effective diffusivities, $\boldsymbol{\nu}$ is the $(N_r \times N)$ stoichiometric coefficient matrix, $\hat{\mathbf{r}}(\mathbf{c}_{wc})$ is the $(N_r \times 1)$ vector of reaction rates and $\mathbf{r}(\mathbf{c}_{wc})$ is the $(N \times 1)$ vector of species consumption (or production) rates. Linearization of Eqs. S-1 and S-2 at the fluid-washcoat interfacial concentration \mathbf{c}_s and solving the resulting vector equation as described in [1] gives

$$\mathbf{c}_{wc}(z) = \mathbf{c}_s - [\mathbf{I} - (\cosh \boldsymbol{\Phi})^{-1} \cosh(\boldsymbol{\Phi}(1-z))] \cdot \mathbf{J}^{-1} \cdot \mathbf{r}(\mathbf{c}_s), \quad (\text{S-3})$$

where

$$z = \frac{y}{\delta_c}, \quad \mathbf{J} = \frac{\partial \mathbf{r}}{\partial \mathbf{c}_{wc}} \Big|_{\mathbf{c}_{wc}=\mathbf{c}_s} \quad (\text{S-4})$$

$$\text{and } \boldsymbol{\Phi}^2 = \delta_c^2 \mathbf{D}_e^{-1} \cdot \mathbf{J}. \quad (\text{A.1})$$

Using *Eq. S-3*, we can determine the average concentration in the washcoat

$$\langle \mathbf{c}_{wc} \rangle = \mathbf{c}_s - [\mathbf{I} - \Phi^{-1} \tanh \Phi] \cdot \mathbf{J}^{-1} \cdot \mathbf{r}(\mathbf{c}_s), \quad (\text{S-6})$$

the interfacial flux vector

$$\mathbf{j}_{fw} = \frac{\mathbf{D}_e}{\delta_c} [\Phi \tanh \Phi] \cdot \mathbf{J}^{-1} \cdot \mathbf{r}(\mathbf{c}_s) \quad (\text{S-7})$$

$$\text{and } = \mathbf{k}_{mi} \cdot (\mathbf{c}_s - \langle \mathbf{c}_{wc} \rangle), \quad (\text{S-8})$$

and the Sherwood matrix

$$\mathbf{Sh}_i = \delta_c \mathbf{D}_e^{-1} \cdot \mathbf{k}_{mi} = [(\Phi \tanh \Phi)^{-1} - \Phi^{-2}]^{-1}. \quad (\text{S-9})$$

If the objective is to predict the effluent concentration vector from the monolith reactor, then it is sufficient to evaluate the interfacial flux vector using *Eq. S-7* and we do not need to evaluate either the average concentration vector $\langle \mathbf{c}_w \rangle$ or the Sherwood matrix. However, this requires that the matrix \mathbf{J} be non-singular, and this may not be the case in many applications. For example, when $N > N_r$, which may be the case in some applications, \mathbf{J} has $N - N_r$ zero eigenvalues, which are due to the existence of stoichiometric invariants. Hence, we rewrite *Eq. S-7* as

$$\mathbf{j}_{fw} = \delta_c \mathbf{D}_e \cdot \mathbf{H} \cdot \mathbf{D}_e^{-1} \cdot \mathbf{r}(\mathbf{c}_s), \quad (\text{S-10})$$

where

$$\mathbf{H} = \Phi^{-1} \tanh \Phi, \quad (\text{S-11})$$

is the effectiveness factor matrix. For the scalar single first-order reaction case,

Eqs. S-22 and S-11 reduce to the well known expressions [1]

$$Sh_i = \left[\left(\frac{1}{\Phi \tanh \Phi} \right) - \frac{1}{\Phi^2} \right]^{-1} \quad (\text{S-12})$$

$$\text{and } \eta = \frac{\tanh \Phi}{\Phi}. \quad (\text{S-13})$$

The advantage of these expressions is that both these functions have finite limits as $\Phi \rightarrow 0$ and are even in Φ . Thus, their matrix equivalents *Eqs. S-7 and S-9* can be computed easily as explained below.

Calculation of the Sherwood Matrix:

First we demonstrate that the Sherwood matrix is a real-valued matrix even when Φ^2 may have negative or complex eigenvalues. The Sherwood matrix in terms of the shape normalized Thiele matrix may be expressed as follows:

$$\mathbf{Sh}_i = Sh_{i\infty} \mathbf{I} + \Phi \tanh[\Lambda^* \Phi], \quad (\text{S-14})$$

where Φ^2 may have zero, positive, negative or complex eigenvalues because the rate constant matrix may not be diagonal or symmetric. When Φ^2 has negative or complex eigenvalues, Φ is multivalued with complex elements. However, we will show here that \mathbf{Sh}_i matrix will be a real-valued matrix. For this, we denote $\mathbf{A} = \Phi^2$ and consider a scalar function $g(x)$ as follows:

$$g(x) = Sh_{i\infty} + \sqrt{x} \tanh[\Lambda^* \sqrt{x}], \quad (\text{S-15})$$

Thus, the Sherwood matrix can be given by $\mathbf{Sh}_i = g(\Phi^2) = g(\mathbf{A})$.

Note that since $g(x)$ is an even function in \sqrt{x} , it will be a real-valued for real x and may be complex-valued for complex x . Now, the Cayley-Hamilton theorem may be used to show that the Sherwood matrix is real-valued. Assume that \mathbf{A} is $N \times N$ and let $\lambda_1, \lambda_2, \dots, \lambda_N$ be the N eigenvalues of \mathbf{A} . Thus, any function of matrix

\mathbf{A} can be written as follows:

$$g(\mathbf{A}) = a_0 \mathbf{I} + \sum_{k=1}^{N-1} a_k \mathbf{A}^k, \quad (\text{S-16})$$

where coefficients a_k depend on the eigenvalues of \mathbf{A} and the scalar function g , and can be obtained by solving the linear equations:

$$g(\lambda_j) = a_0 + \sum_{k=1}^{N-1} a_k \lambda_j^k, \quad j = 1, 2, \dots, N. \quad (\text{S-17})$$

When the eigenvalues are not distinct, then repeated eigenvalues satisfy the equation(s) obtained by differentiating Eq.(S-17). If the algebraic multiplicity of an eigenvalue (i.e. number of repetition) is p , then Eq.(S-17) is differentiated $(p - 1)$ times, which gives the required number of additional equations to obtain the coefficients a_0 to a_{N-1} , uniquely. However, the analysis presented below is applicable whether the eigenvalues are repeated or not, therefore, we will assume distinct eigenvalues for ease of explanation. In this case, Eq.(S-17) can be written in matrix-vector form as follows:

$$\mathbf{B}\alpha = \gamma \Rightarrow \alpha = \mathbf{B}^{-1}\gamma, \quad (\text{S-18})$$

where the matrix \mathbf{B} and vectors α and γ are given as follows:

$$\mathbf{B} = \begin{bmatrix} 1 & \lambda_1 & \lambda_1^2 & \dots & \lambda_1^{N-1} \\ 1 & \lambda_2 & \lambda_2^2 & \dots & \lambda_2^{N-1} \\ \vdots & \vdots & \vdots & \dots & \vdots \\ 1 & \lambda_N & \lambda_N^2 & \dots & \lambda_N^{N-1} \end{bmatrix}, \alpha = \begin{bmatrix} a_0 \\ a_1 \\ \vdots \\ a_{N-1} \end{bmatrix} \quad \text{and} \quad \gamma = \begin{bmatrix} g(\lambda_1) \\ g(\lambda_2) \\ \vdots \\ g(\lambda_N) \end{bmatrix}. \quad (\text{S-19})$$

Thus, Eqs.(S-16) and (S-18) suggest that when the vector α is real then the Sherwood matrix will be a real-valued matrix (since \mathbf{A}^k is real for $0 \leq k \leq N - 1$).

We now consider the various possibilities.

(a) All eigenvalues are real

We note that when all λ_j are real, matrix \mathbf{B} and vector $\boldsymbol{\gamma}$ defined in Eq.S-19 are real-valued, therefore vector $\boldsymbol{\alpha} = \mathbf{B}^{-1}\boldsymbol{\gamma}$ is also real-valued. Thus, when Φ^2 matrix has real eigenvalues (negative or positive), the Sherwood matrix is real-valued.

(b) Some eigenvalues are complex

In this case, the complex eigenvalues will exist in conjugate pairs. Let us assume that λ_1 and λ_2 are the two complex eigenvalues such that complex conjugate of λ_1 is λ_2 , i.e. $\overline{\lambda_1} = \lambda_2$, where $\overline{(\cdot)}$ denotes the complex conjugate. Thus, Eq.S-17 corresponding to λ_1 and λ_2 can be written as follows:

$$g_1 = g(\lambda_1) = a_0 + \sum_{k=1}^{N-1} a_k \lambda_1^k \quad (\text{S-20})$$

$$\text{and } g_2 = g(\lambda_2) = a_0 + \sum_{k=1}^{N-1} a_k \lambda_2^k. \quad (\text{S-21})$$

Since $\overline{\lambda_1} = \lambda_2$, we can write $\lambda_2^k = \overline{\lambda_1^k} = \overline{\lambda_1^k}$ and $g_2 = g(\lambda_2) = g(\overline{\lambda_1}) = \overline{g(\lambda_1)} = \overline{g_1}$. Thus Eq. S-21 can be rewritten as follows:

$$\overline{g_1} = g_2 = a_0 + \sum_{k=1}^{N-1} a_k \overline{\lambda_1^k}. \quad (\text{S-22})$$

Eqs. S-21 and S-22 can be used in pairs to obtain equations with real coefficients as follows:

$$\text{Re}(g_1) = \frac{g_1 + \overline{g_1}}{2} = a_0 + \sum_{k=1}^{N-1} a_k \frac{\lambda_1^k + \overline{\lambda_1^k}}{2} = a_0 + \sum_{k=1}^{N-1} a_k \text{Re}(\lambda_1^k). \quad (\text{S-23})$$

Similarly,

$$\text{Im}(g_1) = \frac{g_1 - \overline{g_1}}{2i} = a_0 + \sum_{k=1}^{N-1} a_k \frac{\lambda_1^k - \overline{\lambda_1^k}}{2i} = a_0 + \sum_{k=1}^{N-1} a_k \text{Im}(\lambda_1^k), \quad (\text{S-24})$$

where $\text{Re}(\cdot)$ and $\text{Im}(\cdot)$ denotes the real and imaginary part of the complex number. Thus, the two complex equations can be transformed into two real equations. A similar transformation can be made for all pairs of complex eigenvalues. This leads to the modified but real-valued matrix \mathbf{B} and r.h.s. vector γ . Thus, the coefficient vector $\alpha = \mathbf{B}^{-1}\gamma$ and hence the Sherwood matrix are real-valued. [Remark: This procedure of rewriting the equations can be avoided if complex algebra is used. In this case, the computed Sherwood matrix may have small imaginary contributions in the entries due to round-off errors. This issue can be dealt with by simply taking only the real part of the entries].

(c) Several zero eigenvalues

When has $k (\geq 1)$ zero (or close to zero) eigenvalues, the calculation of the Sherwood matrix becomes simpler as in this case, the first k constants in Eq. S-16 are already determined explicitly and we only need to solve $(N - k)$ linear equations for the remaining constants. Examples illustrating this case are provided in the main article.

As a numerical example, we consider the case of Example 1 discussed in the article ($N = 5, N_r = 4$) with washcoat thickness of $30 \mu\text{m}$ and $T_{in} = 500 \text{ K}$. For the case of concentrated inlet conditions, the (square of the) Thiele matrix (with species ordering $1 = \text{CO}, 2 = \text{H}_2, 3 = \text{HC}, 4 = \text{NO},$ and $5 = \text{O}_2$) may be calculated

as

$$\Phi^2 = \begin{pmatrix} -0.1661 & 0 & -98.0 & -148.0 & 8.884 \\ -0.6188 & 2.018 & -7.857 & -11.87 & 0.7123 \\ -0.3744 & 0 & 2.572 & -7.180 & 0.4309 \\ 1.457 & 0 & 0 & 48.57 & 0 \\ -2.797 & 4.036 & -57.99 & -131.0 & 7.866 \end{pmatrix}. \quad (\text{S-25})$$

The eigenvalues of Φ^2 are $\{0, 4.187 \pm 0.2886i, 7.985, 43.24\}$. Using the above procedure (with $Sh_{i\infty} = 3$ and $\Lambda = 0.2$), the Sherwood matrix becomes

$$\mathbf{Sh}_i = \begin{pmatrix} 3.244 & -0.0858 & -17.37 & -17.75 & 1.667 \\ -0.0966 & 3.386 & -1.490 & -1.512 & 0.1431 \\ -0.0550 & -0.00417 & 3.492 & -0.8629 & 0.0811 \\ 0.1816 & 0.0011 & 0.1859 & 9.332 & -0.0181 \\ -0.2785 & 0.7091 & -10.33 & -15.90 & 4.496 \end{pmatrix}. \quad (\text{S-26})$$

We note that the Sherwood matrix has both positive and negative entries and some off diagonal elements are larger in absolute value compared to the diagonal elements. Using the diagonal approximation gives

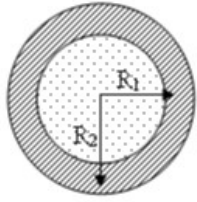
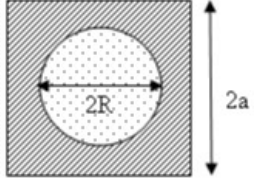
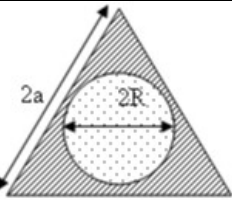
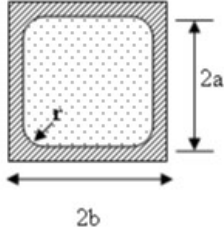
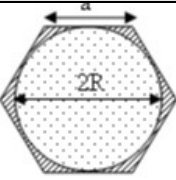
$$\mathbf{Sh}_i = \begin{pmatrix} 4.605 & 0 & 0 & 0 & 0 \\ 0 & 3.393 & 0 & 0 & 0 \\ 0 & 0 & 4.337 & 0 & 0 \\ 0 & 0 & 0 & 9.161 & 0 \\ 0 & 0 & 0 & 0 & 4.427 \end{pmatrix}. \quad (\text{S-27})$$

Comparing *Eqs.* S-26 and S-27, we observe that the diagonal approximation estimates the diagonal elements of \mathbf{Sh}_i with acceptable accuracy but completely misses the off-diagonal elements that are due to the coupling between the reactions.

Washcoat geometry shapes and related asymptotic Sherwood numbers

We note that the small and large Φ asymptotes of Eq. S-14 match with the exact expression for any value of Λ^* . However, the specific value of Λ^* for a given geometry is obtained by matching the numerically computed values at the transition point ($Sh_{i\infty} = \Phi$). The Λ^* value for a given washcoat geometry may also be obtained by comparing the Taylor series expansions of the exact expression for the Sherwood number with that given by Eq. S-14. For example, for the case of thin washcoat (slab geometry), the first approach gives $\Lambda^* = 0.18$ while the Taylor series matching gives $\Lambda^* = \frac{1}{5}$. The values listed in the table are obtained using the first approach.

Table A.1: Effective diffusion lengths, asymptotic internal Sherwood number and Λ for some common channel and washcoat shapes for the case of first order kinetics

Channel Shape	R_{Ω_1}	δ_{Ω_c}	$Sh_{i\infty}$ and Λ^*												
	a	b-a	$Sh_{i\infty} = 3$ and $\Lambda^* = 0.18$												
	$R_1/2$	$(R_2^2 - R_1^2)/(2R_1)$	<table border="1"> <thead> <tr> <th>R_2/R_1</th> <th>$Sh_{i\infty}$</th> <th>Λ^*</th> </tr> </thead> <tbody> <tr> <td>1.01</td> <td>3.0125</td> <td>0.20</td> </tr> <tr> <td>1.1</td> <td>3.153</td> <td>0.19</td> </tr> <tr> <td>1.2</td> <td>3.311</td> <td>0.18</td> </tr> </tbody> </table>	R_2/R_1	$Sh_{i\infty}$	Λ^*	1.01	3.0125	0.20	1.1	3.153	0.19	1.2	3.311	0.18
R_2/R_1	$Sh_{i\infty}$	Λ^*													
1.01	3.0125	0.20													
1.1	3.153	0.19													
1.2	3.311	0.18													
	$R/2$	$(4a^2 - \pi R^2)/(2\pi R)$	<table border="1"> <thead> <tr> <th>a/R</th> <th>$Sh_{i\infty}$</th> <th>Λ^*</th> </tr> </thead> <tbody> <tr> <td>1</td> <td>0.826</td> <td>0.45</td> </tr> <tr> <td>1.1</td> <td>1.836</td> <td>0.46</td> </tr> <tr> <td>1.2</td> <td>2.533</td> <td>0.31</td> </tr> </tbody> </table>	a/R	$Sh_{i\infty}$	Λ^*	1	0.826	0.45	1.1	1.836	0.46	1.2	2.533	0.31
a/R	$Sh_{i\infty}$	Λ^*													
1	0.826	0.45													
1.1	1.836	0.46													
1.2	2.533	0.31													
	$R/2$	$(\sqrt{3}a^2 - \pi R^2)/(2\pi R)$	<table border="1"> <thead> <tr> <th>a/R</th> <th>$Sh_{i\infty}$</th> <th>Λ^*</th> </tr> </thead> <tbody> <tr> <td>1.7321</td> <td>0.84</td> <td>0.42</td> </tr> <tr> <td>1.9245</td> <td>1.45</td> <td>0.53</td> </tr> <tr> <td>2.4744</td> <td>2.92</td> <td>0.31</td> </tr> </tbody> </table>	a/R	$Sh_{i\infty}$	Λ^*	1.7321	0.84	0.42	1.9245	1.45	0.53	2.4744	2.92	0.31
a/R	$Sh_{i\infty}$	Λ^*													
1.7321	0.84	0.42													
1.9245	1.45	0.53													
2.4744	2.92	0.31													
	$\frac{(4a^2 - 4r^2 + \pi r^2)}{(2\pi r + 8a - 8r)}$	$\frac{(4b^2 - 4a^2 + 4r^2 - \pi r^2)}{(2\pi r + 8a - 8r)}$	<table border="1"> <thead> <tr> <th>b/a</th> <th>b/r</th> <th>$Sh_{i\infty}$</th> <th>Λ^*</th> </tr> </thead> <tbody> <tr> <td>1.11</td> <td>5</td> <td>2.65</td> <td>0.21</td> </tr> <tr> <td>1.25</td> <td>10</td> <td>3.09</td> <td>0.20</td> </tr> </tbody> </table>	b/a	b/r	$Sh_{i\infty}$	Λ^*	1.11	5	2.65	0.21	1.25	10	3.09	0.20
b/a	b/r	$Sh_{i\infty}$	Λ^*												
1.11	5	2.65	0.21												
1.25	10	3.09	0.20												
	$R/2$	$(3\sqrt{3}a^2 - 2\pi R^2)/(4\pi R)$	<table border="1"> <thead> <tr> <th>a/R</th> <th>$Sh_{i\infty}$</th> <th>Λ^*</th> </tr> </thead> <tbody> <tr> <td>1.155</td> <td>0.814</td> <td>0.50</td> </tr> <tr> <td>1.17</td> <td>1.16</td> <td>0.76</td> </tr> <tr> <td>1.2</td> <td>1.74</td> <td>0.54</td> </tr> </tbody> </table>	a/R	$Sh_{i\infty}$	Λ^*	1.155	0.814	0.50	1.17	1.16	0.76	1.2	1.74	0.54
a/R	$Sh_{i\infty}$	Λ^*													
1.155	0.814	0.50													
1.17	1.16	0.76													
1.2	1.74	0.54													

Where washcoat and flow area are designated as shown below:



Appendix B: Vector form of the reduced order model for a dual layered monolith reactor

We review here briefly the vector form of the reduced order model for a dual layered monolith reactor. A schematic diagram of the channel cross-section for a square channeled monolith with dual washcoat layers is shown in *Fig. S1*. Denoting \mathbf{c}_{fm} as the cup-mixing concentration vector for flow channel, \mathbf{c}_{s1} as the fluid-washcoat interfacial concentration vector, $\langle \mathbf{c}_{w1} \rangle$ as the volume averaged concentration vector in layer 1, \mathbf{c}_{s2} as the concentration vector at the interface between layers, $\langle \mathbf{c}_{w2} \rangle$ as the volume averaged concentration vector in layer 2, \mathbf{j}_1 as the species flux vector at the fluid-washcoat interface, \mathbf{j}_2 as the species flux vector at the interface between layers (with \mathbf{j}_1 and \mathbf{j}_2 having units of $\frac{mol}{m^2 \cdot s}$), the various local equations may be written as (Ratnakar et al.[8]).

$$\mathbf{c}_{fm} - \mathbf{c}_{s1} = \mathbf{k}_{e0}^{-1} \cdot \mathbf{j}_1, \quad (\text{B.1})$$

$$\mathbf{c}_{s1} - \langle \mathbf{c}_{w1} \rangle = \mathbf{k}_{i1}^{-1} \cdot \mathbf{j}_1 + \widehat{\mathbf{k}}_{i1}^{-1} \cdot \mathbf{j}_2, \quad (\text{B.2})$$

$$\langle \mathbf{c}_{w1} \rangle - \mathbf{c}_{s2} = \widehat{\mathbf{k}}_{e1}^{-1} \cdot \mathbf{j}_1 + \mathbf{k}_{e1}^{-1} \cdot \mathbf{j}_2 \quad (\text{B.3})$$

$$\text{and } \mathbf{c}_{s2} - \langle \mathbf{c}_{w2} \rangle = \mathbf{k}_{i2}^{-1} \cdot \mathbf{j}_2, \quad (\text{B.4})$$

where \mathbf{k}_{e0} is the external mass transfer coefficient matrix for layer 1, \mathbf{k}_{i1} is the internal mass transfer coefficient matrix for layer 1, $\widehat{\mathbf{k}}_{i1}$ is the cross-coupling internal mass transfer coefficient matrix for layer 1, $\widehat{\mathbf{k}}_{e1}$ is the cross-coupling external mass transfer coefficient matrix for layer 1, \mathbf{k}_{e1} is the external mass transfer coefficient matrix for layer 1, \mathbf{k}_{i2} is the internal mass transfer coefficient matrix for layer 2. We can eliminate the interfacial concentration vectors \mathbf{c}_{s1} and \mathbf{c}_{s2} by adding *Eqs. B.1*

and B.2 and *Eqs.* B.3 and B.4, this gives

$$\mathbf{c}_{fm} - \langle \mathbf{c}_{w1} \rangle = \mathbf{k}_{01}^{-1} \cdot \mathbf{j}_1 + \widehat{\mathbf{k}}_{i1}^{-1} \cdot \mathbf{j}_2, \quad (\text{B.5})$$

$$\langle \mathbf{c}_{w1} \rangle - \langle \mathbf{c}_{w2} \rangle = \widehat{\mathbf{k}}_{e1}^{-1} \cdot \mathbf{j}_1 + \mathbf{k}_{02}^{-1} \cdot \mathbf{j}_2, \quad (\text{B.6})$$

$$\mathbf{k}_{01}^{-1} = \mathbf{k}_{e0}^{-1} + \mathbf{k}_{i1}^{-1} \quad (\text{B.7})$$

$$\text{and } \mathbf{k}_{02}^{-1} = \mathbf{k}_{e1}^{-1} + \mathbf{k}_{i2}^{-1}. \quad (\text{B.8})$$

We note that these local equations contain four mass transfer coefficient matrices which have simple meaning. For example, \mathbf{k}_{01} is the overall mass transfer coefficient matrix for transfer of species at the first interface (fluid and layer 1) while \mathbf{k}_{02} is the overall mass transfer coefficient matrix for transfer of species at the second interface (layer 1 and layer 2). The cross-coupling mass transfer coefficient matrices $\widehat{\mathbf{k}}_{i1}$ and $\widehat{\mathbf{k}}_{e1}$ which depend only the properties of layer 1 arise due to non-zero fluxes at both boundaries of layer 1.

In terms of mole fractions, the local equations may be expressed as

$$\mathbf{X}_{fm} - \langle \mathbf{X}_{w1} \rangle = \mathbf{k}_{01}^{-1} \cdot \mathbf{J}_1 + \widehat{\mathbf{k}}_{i1}^{-1} \cdot \mathbf{J}_2 \quad (\text{B.9})$$

$$\text{and } \langle \mathbf{X}_{w1} \rangle - \langle \mathbf{X}_{w2} \rangle = \widehat{\mathbf{k}}_{e1}^{-1} \cdot \mathbf{J}_1 + \mathbf{k}_{02}^{-1} \cdot \mathbf{J}_2, \quad (\text{B.10})$$

where flux vectors \mathbf{J}_i have units of m/s .

We can express the mass transfer coefficients matrices in terms of the respective Sherwood matrices. For example,

$$\mathbf{k}_{i1} = \frac{1}{\delta_{c1}} \mathbf{D}_{e1} \cdot \mathbf{Sh}_{i1}, \quad (\text{B.11})$$

where δ_{c1} is the effective thickness of layer 1 and \mathbf{D}_{e1} is the diagonal matrix of species effective diffusivities in layer 1. The schematic *Figs.* S1 and S2 indicate the various effective layer thickness values, interfacial fluxes and concentrations.

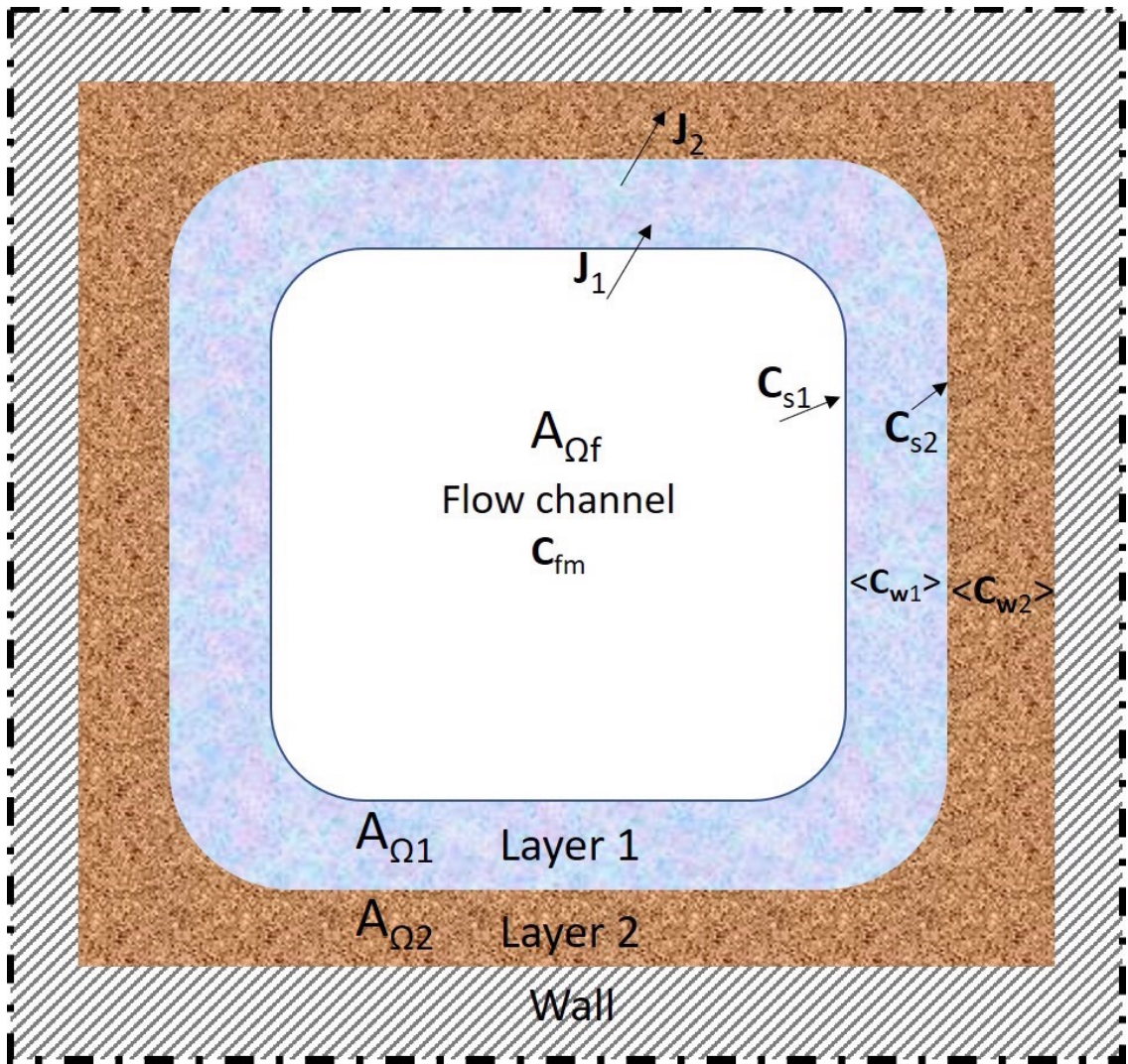
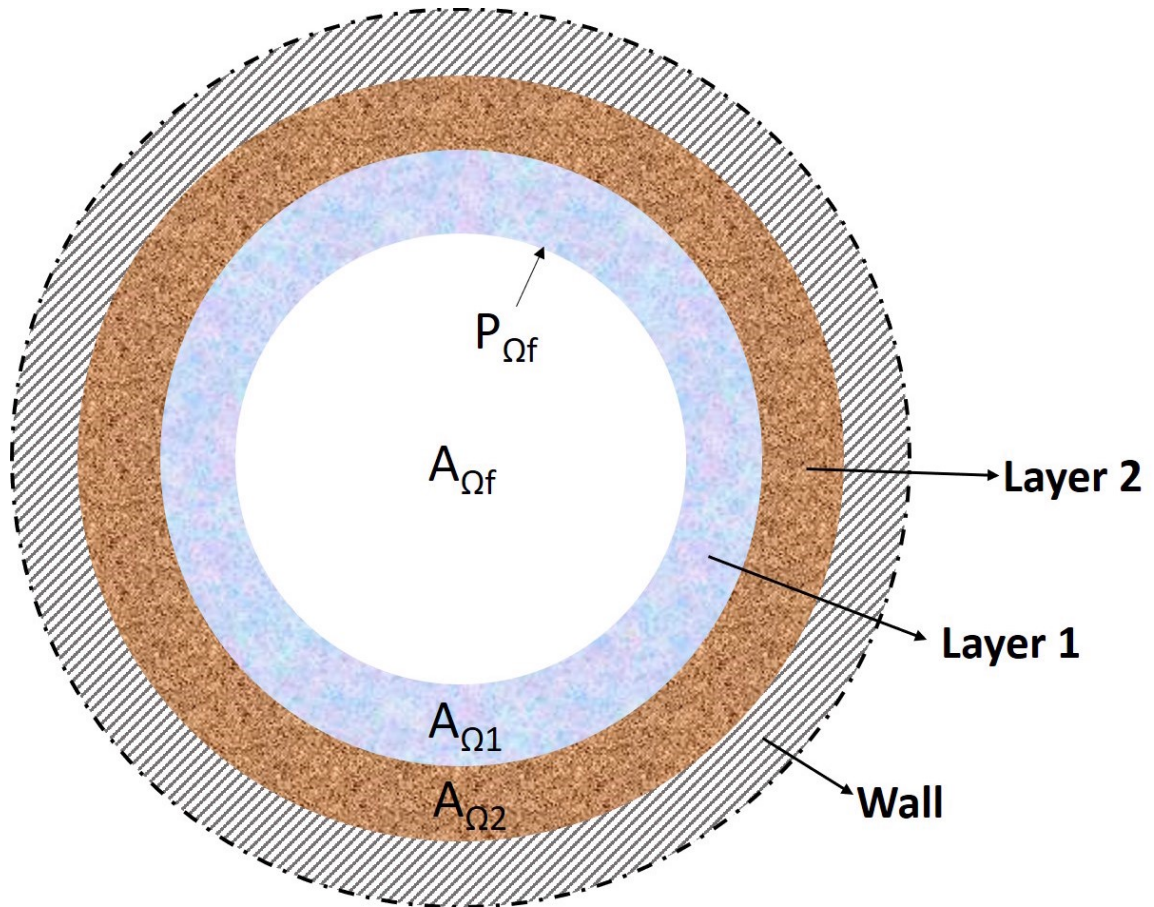


Figure B.1: Figure S1: Schematic cross-section of a monolith channel with dual washcoat layers and various concentration modes.

When the flow geometry is close to a circular cross-section and the layer thickness is small compared to the hydraulic diameter of the channel, the irregular cross-section shown in figure S1 may be approximated by that shown in figure S2 with effective thickness for each layer.

As explained in the main article, all the Sherwood matrices can be computed in terms of the Thiele matrices defined at the interfacial mole fractions:



Effective length scale:

$$R_{\Omega} = A_{\Omega_f} / P_{\Omega_f}$$

$$\delta_{C1} = A_{\Omega_1} / P_{\Omega_f}$$

$$\delta_{C2} = A_{\Omega_2} / P_{\Omega_f}$$

Figure B.2: Figure S2: Schematic cross-section of a monolith channel with dual washcoat layers and various length scales.

$$\Phi_1^2 = \delta_{c1}^2 (\mathbf{D}_{e,1})^{-1} \left(-\frac{1}{C_T} \frac{d(\boldsymbol{\nu}_1^T \mathbf{r}_{g1}(\mathbf{X}_{w1}, \boldsymbol{\theta}_{w1}))}{d\mathbf{X}_{w1}} \right)_{\mathbf{x}=\mathbf{x}_{s1}}$$

and $\Phi_2^2 = \delta_{c2}^2 (\mathbf{D}_{e,2})^{-1} \left(-\frac{1}{C_T} \frac{d(\boldsymbol{\nu}_2^T \mathbf{r}_{g2}(\mathbf{X}_{w2}, \boldsymbol{\theta}_{w2}))}{d\mathbf{X}_{w2}} \right)_{\mathbf{x}=\mathbf{x}_{s2}}, \quad (\text{B.12})$

However, since \mathbf{X}_{s1} and \mathbf{X}_{s2} are not known, they can be approximated by the relations

$$\mathbf{X}_{s1} = \mathbf{X}_{fm} + \mathbf{k}_{e0}^{-1} \cdot \mathbf{J}_1 = \langle \mathbf{X}_{w1} \rangle + \mathbf{k}_{i1}^{-1} \cdot \mathbf{J}_1 + \widehat{\mathbf{k}}_{i1}^{-1} \cdot \mathbf{J}_2 \quad (\text{B.13})$$

$$\text{and } \mathbf{X}_{s2} = \langle \mathbf{X}_{w2} \rangle + \mathbf{k}_{i2}^{-1} \cdot \mathbf{J}_2 = \langle \mathbf{X}_{w1} \rangle + \mathbf{k}_{i1}^{-1} \cdot \mathbf{J}_1 + \widehat{\mathbf{k}}_{i1}^{-1} \cdot \mathbf{J}_2, \quad (\text{B.14})$$

with the quantities on the right hand side of *Eqs.*(B-14) and (B-15) evaluated either at a previous time or axial mesh point.

As mentioned in the main article, the Thiele (and Sherwood) matrices are of order three for the LNT layer during storage. Though *NO* oxidation can occur in the SCR layer, the rate of this reaction (at or below $T = 370$ °C) is so low that the SCR layer effectively acts as an inert diffusion layer during the *NOx* storage phase. During the storage phase, only the first four reaction steps shown table 6 of LNT reaction scheme occur and the relevant gas phase species are *NO*, *NO₂* and *O₂*. Hence, the Jacobian was calculated based on the partial derivatives of the net rate of *NO*, *NO₂* and *O₂* (or the species formation vector). As a numerical example, with an LNT layer thickness of 30 μm and $T = 370$ °C, the (square of the) Thiele matrix (with species ordering 1 = *NO*, 2 = *NO₂* and 3 = *O₂*) in the simulations shown in figure 8 at $t=0$ s (composition in LNT layer is: 5% *O₂*, 500 ppm *NO*) may be calculated as

$$\Phi_2^2 = \delta_c^2(\mathbf{D}_e)^{-1} \left(-\frac{\mathbf{J}}{C_T} \right) = \begin{bmatrix} -4.90 \times 10^2 & -3.25 \times 10^5 & 0.4 \times 10^2 \\ 6.1 \times 10^2 & 4.079 \times 10^5 & -0.5 \times 10^2 \\ -2.7 \times 10^2 & -1.74 \times 10^5 & 0.2 \times 10^2 \end{bmatrix}.$$

at $t=12$ s (composition in LNT layer is: 4.96% O_2 , 4.67 ppm NO , 4.71 ppm NO_2) may be calculated as

$$\Phi_2^2 = \delta_c^2(\mathbf{D}_e)^{-1} \left(-\frac{\mathbf{J}}{C_T} \right) = \begin{bmatrix} 1.22 \times 10^4 & -1.21 \times 10^4 & 0.47 \\ 1.51 \times 10^4 & 1.95 \times 10^4 & -0.33 \\ -0.66 \times 10^4 & -0.56 \times 10^4 & 0.31 \end{bmatrix}.$$

The largest eigenvalue of Φ^2 is 4×10^5 at $t=0$ s and is about 2×10^4 at $t=12$ s.

In the simulations with cycling input condition, both LNT and SCR layers become active with NOx storage, and regeneration/reduction steps. In this case, Φ_2^2 is a 5×5 matrix corresponding to the gas phase species NO , NO_2 , O_2 , H_2 and NH_3 ; Φ_1^2 is also a 5×5 matrix that includes NH_4NO_3 but excludes H_2 . As a numerical example, with an LNT layer thickness of $20 \mu\text{m}$, SCR layer thickness of $10 \mu\text{m}$ and $T = 300$ °C (corresponding to the simulations shown in figure 7 of the article), the matrices Φ_2^2 (with species ordering 1 = NO , 2 = NO_2 , 3 = O_2 , 4 = H_2 and 5 = NH_3) and Φ_1^2 (with species ordering 1 = NO , 2 = NO_2 , 3 = O_2 , 4 = NH_3 and 5 = NH_4NO_3) at $t=184$ s (and composition in SCR layer is: 2.5% O_2 , 0.16% H_2 , composition in LNT layer is: 2.5% O_2 , 0.14% H_2 , 100 ppm NH_3) may be calculated as

$$\Phi_2^2 = \begin{bmatrix} 4.50 \times 10^4 & -2.30 \times 10^3 & 0.002 & 7.64 \times 10^{-4} & 0.01 \\ -1.13 \times 10^4 & 2.87 \times 10^3 & -0.002 & 0 & 0 \\ 0.49 \times 10^4 & -1.24 \times 10^3 & 0.001 & 0 & 0 \\ 2.24 \times 10^4 & 0 & 0 & 0.14 & 0 \\ -2.64 \times 10^4 & 0 & 0 & -0.10 & 0.16 \end{bmatrix},$$

$$\Phi_1^2 = \begin{bmatrix} 0.36 & -5.47 \times 10^{-5} & 2.80 \times 10^{-11} & 0 & 0 \\ -7.49 \times 10^{-5} & 0.057 & -3.47 \times 10^{-11} & 0 & 0 \\ 0.09 & -7.31 \times 10^{-5} & 1.36 \times 10^{-6} & 0 & 0 \\ 0 & 0 & 0 & 373.36 & 0 \\ 0 & -0.01 & 0 & 0 & 0.26 \end{bmatrix}.$$

We note that Φ_1^2 is a diagonally dominant matrix but Φ_2^2 is not. The largest eigenvalue of Φ_2^2 is about 4.5×10^4 while in Φ_1^2 is about 373, so the washcoat diffusion limitations occur mainly in the LNT layer and the number of mesh points required to obtain an accurate solution is determined mainly by the square root of largest eigenvalue in Φ_2^2 .

Mesh selection in dual layer numerical calculations

The mesh point distribution in the dual layered washcoat is shown in *Fig. S3*. We denote N_1 and N_2 as the number of interior mesh points in layer 1 and 2, respectively; Δy_1 is the mesh size in layer 1 and equals to $\frac{\delta_{c1}}{N_1+1}$, Δy_2 is the mesh size in layer 2 and equals to $\frac{\delta_{c2}}{N_2+1}$. For uniform mesh $\Delta y_1 = \Delta y_2$, hence $\frac{\delta_{c1}}{N_1+1} = \frac{\delta_{c2}}{N_2+1} = \Delta y$. Also, for uniform mesh, Δy is equal to $\frac{\delta_{c1}+\delta_{c2}}{N_1+N_2+2}$. The total number of mesh points N (interior and boundary points) is $N_1 + N_2 + 3$, and now $\Delta y = \frac{\delta_{c1}+\delta_{c2}}{N-1}$. Thus, if N is fixed and δ_{c1} and δ_{c2} are known, we can determine the mesh size and

number of points in each layer by the relations

$$\begin{aligned}\Delta y &= \frac{\delta_{c1} + \delta_{c2}}{N - 1}, \\ N_1 + 1 &= \frac{\delta_{c1}}{\Delta y} = (N - 1) \frac{\delta_{c1}}{\delta_{c1} + \delta_{c2}} \\ \text{and } N_2 + 1 &= \frac{\delta_{c2}}{\Delta y} = (N - 1) \frac{\delta_{c2}}{\delta_{c1} + \delta_{c2}}.\end{aligned}$$

Example: δ_{c2} is 20 μm , δ_{c1} is 10 μm . When $N = 10$

$$\begin{aligned}\Delta y &= \frac{30}{9} = 3.33 \mu\text{m}, \\ N_1 + 1 &= \frac{\delta_{c1}}{\Delta y} = 3 \Rightarrow N_1 = 2 \\ \text{and } N_2 + 1 &= \frac{\delta_{c2}}{\Delta y} = 6 \Rightarrow N_2 = 5,\end{aligned}$$

When $N = 100$

$$\begin{aligned}\Delta y &= \frac{30}{99} \mu\text{m}, \\ N_1 + 1 &= \frac{\delta_{c1}}{\Delta y} = 33 \Rightarrow N_1 = 32 \\ \text{and } N_2 + 1 &= \frac{\delta_{c2}}{\Delta y} = 66 \Rightarrow N_2 = 65.\end{aligned}$$

Illustration of mesh structure:

- 10 mesh points
- Evenly distributed

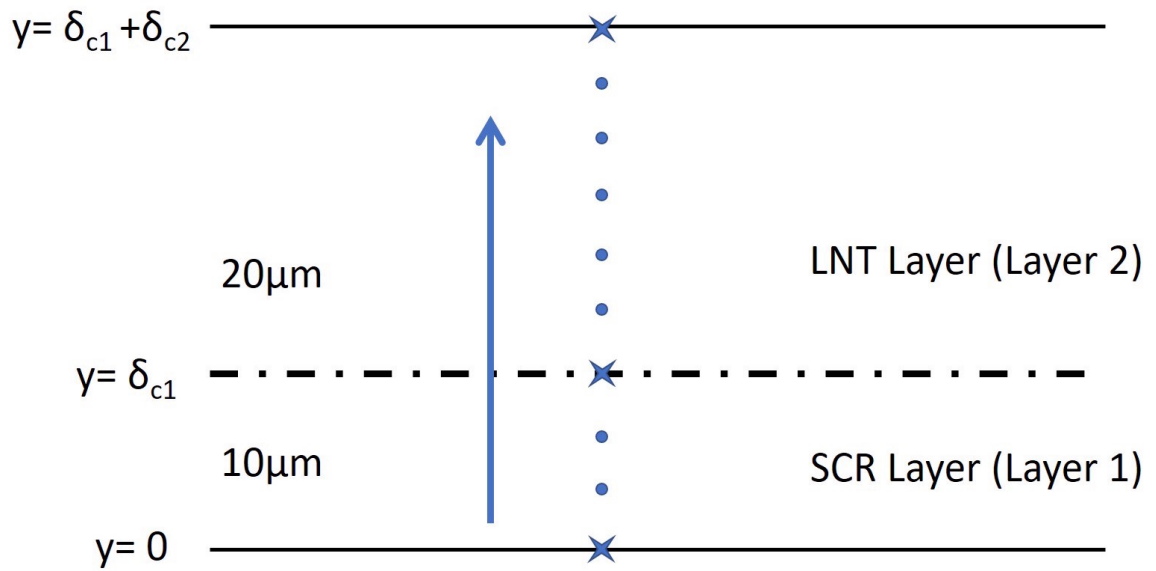
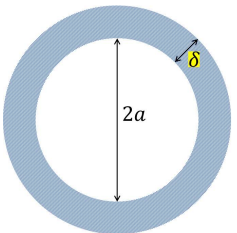
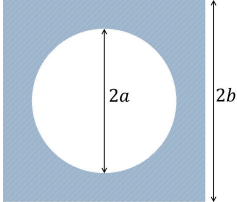
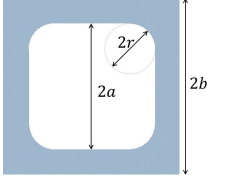
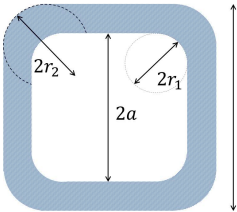


Figure B.3: Figure S3: Mesh point distribution in the washcoat layer

Appendix C: Asymptotic Sherwood and Cross-Sherwood Numbers for Standard Geometries

This section presents the asymptotic values of internal Sherwood and cross-Sherwood numbers for standard washcoat geometries in *Table C.1* that can be utilized with our proposed model. For example, when squared monolith with rounded square flow channel are considered, they can be divided into two washcoat layers with an artificial rounded square boundary. This leads to the washcoat layer 1 having internal and external rounded square boundaries, and the washcoat layer 2 having internal rounded square boundary but external square boundary. Thus, the asymptotic Sherwood numbers for these two layers can easily be obtained from the *Table C.1* below.

Table C.1: Effective diffusion lengths, asymptotic internal Sherwood and cross-Sherwood numbers for some common washcoat shapes

Channel Shape	$\delta_{\Omega w} = \frac{2A_{\Omega w}}{P_{\Omega_1} + P_{\Omega_2}}$	$Sh_{\Omega\infty}$																																				
	δ	<table border="1"> <thead> <tr> <th>$Sh_{i\infty}$</th> <th>$\widehat{Sh}_{int,\infty}$</th> <th>$Sh_{ext,\infty}$</th> <th>$\widehat{Sh}_{ext,\infty}$</th> </tr> </thead> <tbody> <tr> <td>3</td> <td>6</td> <td>3</td> <td>6</td> </tr> </tbody> </table>	$Sh_{i\infty}$	$\widehat{Sh}_{int,\infty}$	$Sh_{ext,\infty}$	$\widehat{Sh}_{ext,\infty}$	3	6	3	6																												
$Sh_{i\infty}$	$\widehat{Sh}_{int,\infty}$	$Sh_{ext,\infty}$	$\widehat{Sh}_{ext,\infty}$																																			
3	6	3	6																																			
	$(b - a)$	<table border="1"> <thead> <tr> <th>b/a</th> <th>$Sh_{i\infty}$</th> <th>$\widehat{Sh}_{int,\infty}$</th> <th>$Sh_{ext,\infty}$</th> <th>$\widehat{Sh}_{ext,\infty}$</th> </tr> </thead> <tbody> <tr> <td>1.01</td> <td>3.00</td> <td>5.97</td> <td>3.00</td> <td>6.03</td> </tr> <tr> <td>1.1</td> <td>3.00</td> <td>5.73</td> <td>3.00</td> <td>6.30</td> </tr> <tr> <td>1.2</td> <td>3.01</td> <td>5.51</td> <td>3.01</td> <td>6.61</td> </tr> <tr> <td>1.5</td> <td>3.05</td> <td>5.04</td> <td>3.04</td> <td>7.56</td> </tr> </tbody> </table>	b/a	$Sh_{i\infty}$	$\widehat{Sh}_{int,\infty}$	$Sh_{ext,\infty}$	$\widehat{Sh}_{ext,\infty}$	1.01	3.00	5.97	3.00	6.03	1.1	3.00	5.73	3.00	6.30	1.2	3.01	5.51	3.01	6.61	1.5	3.05	5.04	3.04	7.56											
b/a	$Sh_{i\infty}$	$\widehat{Sh}_{int,\infty}$	$Sh_{ext,\infty}$	$\widehat{Sh}_{ext,\infty}$																																		
1.01	3.00	5.97	3.00	6.03																																		
1.1	3.00	5.73	3.00	6.30																																		
1.2	3.01	5.51	3.01	6.61																																		
1.5	3.05	5.04	3.04	7.56																																		
	$\frac{(b^2 - \frac{\pi}{4}a^2)}{(b + \frac{\pi}{4}a)}$	<table border="1"> <thead> <tr> <th>b/a</th> <th>$Sh_{i\infty}$</th> <th>$\widehat{Sh}_{int,\infty}$</th> <th>$Sh_{ext,\infty}$</th> <th>$\widehat{Sh}_{ext,\infty}$</th> </tr> </thead> <tbody> <tr> <td>1.1</td> <td>1.53</td> <td>11.82</td> <td>2.24</td> <td>8.72</td> </tr> <tr> <td>1.2</td> <td>2.00</td> <td>6.60</td> <td>2.69</td> <td>6.61</td> </tr> <tr> <td>1.5</td> <td>2.55</td> <td>4.63</td> <td>2.96</td> <td>6.87</td> </tr> </tbody> </table>	b/a	$Sh_{i\infty}$	$\widehat{Sh}_{int,\infty}$	$Sh_{ext,\infty}$	$\widehat{Sh}_{ext,\infty}$	1.1	1.53	11.82	2.24	8.72	1.2	2.00	6.60	2.69	6.61	1.5	2.55	4.63	2.96	6.87																
b/a	$Sh_{i\infty}$	$\widehat{Sh}_{int,\infty}$	$Sh_{ext,\infty}$	$\widehat{Sh}_{ext,\infty}$																																		
1.1	1.53	11.82	2.24	8.72																																		
1.2	2.00	6.60	2.69	6.61																																		
1.5	2.55	4.63	2.96	6.87																																		
	$\frac{b^2 - a^2 + (1 - \frac{\pi}{4})r_1^2}{b + a - (1 - \frac{\pi}{4})r_1}$	<table border="1"> <thead> <tr> <th>b/a</th> <th>r/a</th> <th>$Sh_{i\infty}$</th> <th>$\widehat{Sh}_{int,\infty}$</th> <th>$Sh_{ext,\infty}$</th> <th>$\widehat{Sh}_{ext,\infty}$</th> </tr> </thead> <tbody> <tr> <td>1.1</td> <td>0.1</td> <td>2.75</td> <td>5.65</td> <td>2.99</td> <td>5.57</td> </tr> <tr> <td>1.1</td> <td>0.2</td> <td>2.47</td> <td>6.03</td> <td>2.96</td> <td>5.56</td> </tr> <tr> <td>1.5</td> <td>0.1</td> <td>3.69</td> <td>4.52</td> <td>4.90</td> <td>11.05</td> </tr> <tr> <td>1.5</td> <td>0.2</td> <td>3.69</td> <td>4.55</td> <td>2.93</td> <td>11.23</td> </tr> <tr> <td>1.5</td> <td>0.5</td> <td>3.83</td> <td>4.69</td> <td>2.97</td> <td>13.14</td> </tr> </tbody> </table>	b/a	r/a	$Sh_{i\infty}$	$\widehat{Sh}_{int,\infty}$	$Sh_{ext,\infty}$	$\widehat{Sh}_{ext,\infty}$	1.1	0.1	2.75	5.65	2.99	5.57	1.1	0.2	2.47	6.03	2.96	5.56	1.5	0.1	3.69	4.52	4.90	11.05	1.5	0.2	3.69	4.55	2.93	11.23	1.5	0.5	3.83	4.69	2.97	13.14
b/a	r/a	$Sh_{i\infty}$	$\widehat{Sh}_{int,\infty}$	$Sh_{ext,\infty}$	$\widehat{Sh}_{ext,\infty}$																																	
1.1	0.1	2.75	5.65	2.99	5.57																																	
1.1	0.2	2.47	6.03	2.96	5.56																																	
1.5	0.1	3.69	4.52	4.90	11.05																																	
1.5	0.2	3.69	4.55	2.93	11.23																																	
1.5	0.5	3.83	4.69	2.97	13.14																																	
	$\frac{b^2 - a^2 - (1 - \frac{\pi}{4})(r_2^2 - r_1^2)}{b + a - (1 - \frac{\pi}{4})(r_2 + r_1)}$	<table border="1"> <thead> <tr> <th>$\frac{b}{a}$</th> <th>$\frac{r_1}{a} = \frac{r_2}{b}$</th> <th>$Sh_{i\infty}$</th> <th>$\widehat{Sh}_{int,\infty}$</th> <th>$Sh_{ext,\infty}$</th> <th>$\widehat{Sh}_{ext,\infty}$</th> </tr> </thead> <tbody> <tr> <td>1.1</td> <td>0.2</td> <td>2.9</td> <td>5.9</td> <td>3.0</td> <td>6.1</td> </tr> <tr> <td>1.1</td> <td>0.5</td> <td>2.9</td> <td>5.9</td> <td>3.0</td> <td>6.3</td> </tr> <tr> <td>1.5</td> <td>0.2</td> <td>2.8</td> <td>4.8</td> <td>3.0</td> <td>6.5</td> </tr> <tr> <td>1.5</td> <td>0.5</td> <td>2.9</td> <td>5.0</td> <td>3.1</td> <td>7.1</td> </tr> </tbody> </table>	$\frac{b}{a}$	$\frac{r_1}{a} = \frac{r_2}{b}$	$Sh_{i\infty}$	$\widehat{Sh}_{int,\infty}$	$Sh_{ext,\infty}$	$\widehat{Sh}_{ext,\infty}$	1.1	0.2	2.9	5.9	3.0	6.1	1.1	0.5	2.9	5.9	3.0	6.3	1.5	0.2	2.8	4.8	3.0	6.5	1.5	0.5	2.9	5.0	3.1	7.1						
$\frac{b}{a}$	$\frac{r_1}{a} = \frac{r_2}{b}$	$Sh_{i\infty}$	$\widehat{Sh}_{int,\infty}$	$Sh_{ext,\infty}$	$\widehat{Sh}_{ext,\infty}$																																	
1.1	0.2	2.9	5.9	3.0	6.1																																	
1.1	0.5	2.9	5.9	3.0	6.3																																	
1.5	0.2	2.8	4.8	3.0	6.5																																	
1.5	0.5	2.9	5.0	3.1	7.1																																	